Current-induced scour beneath elevated subsea pipelines

by

Jun Yi Lee

B.Eng. (Hons)

University of Tasmania

Submitted in fulfilment of the requirements for the degree of

Doctor of Philosophy

University of Tasmania

September 2018

Statements and declarations

Declaration of originality

This thesis contains no material which has been accepted for a degree or diploma by the University or any other institution, except by way of background information and duly acknowledged in the thesis, and to the best of my knowledge and belief no material previously published or written by another person except where due acknowledgement is made in the text of the thesis, nor does the thesis contain any material that infringes copyright.

Authority of access

This thesis may be made available for loan and limited copying and communication in accordance with the Copyright Act 1968.

Signed: Date: 7 July 2018

……

……..

Jun Yi Lee

Candidate

University of Tasmania

Statement regarding published work contained in thesis

The publishers of the papers comprising Chapters 4, 5, 6 and 7 hold the copyright for that content, and access to the material should be sought from the respective journals. The remaining non published content of the thesis may be made available for loan and limited copying and communication in accordance with the Copyright Act 1968.

Statement of co-authorship

The following people and institutions contributed to the publication of work undertaken as part of this thesis:

Jun Y. Lee, University of Tasmania	**= Candidate**
Alexander L. Forrest, University of California – Davis, Supervisor	**= Author 1**
Fauzi A. Hardjanto, University of Tasmania, Supervisor	**= Author 2**
Shuhong Chai, University of Tasmania, Supervisor	**= Author 3**
Remo Cossu, University of Queensland	**= Author 4**
Zhi Q. Leong, University of Tasmania	**= Author 5**
Jasmin B.T. McInerney, University of California – Davis	**= Author 6**

Author details and their roles:

Paper 1, Predicting scour beneath subsea pipelines from existing small free span depths under steady currents:

Lee, J. Y., McInerney, J., Cossu, R., Leong, Z. Q., & Forrest, A. L. (2017). Predicting scour beneath subsea pipelines from existing small free span depths under steady currents. *Journal of Ocean Engineering and Science*, 2(2), 61-75. DOI: 10.1016/j.joes.2017.03.001

Located in Chapter 4

The initial idea and aim of the paper was formulated by the candidate, Authors 1, 4 and 5. The funding for the work was partly attained with the assistance of Author 1. The main numerical simulations were planned and performed by the candidate, with advice from Author 5. The complementary circulating water channel experiments and field survey was planned and executed by Author 6, with the assistance of the candidate. The analysis of the

data was conducted by the candidate. The equation for scour prediction was formulated by the candidate and Author 1. The paper was initially drafted by the candidate, and multiple revisions were produced upon obtaining critical feedback from all authors regarding the interpretation and presentation of the results.

The percentage of the contribution made by the candidate was 80% while the co-authors contributed the remaining 20%.

Paper 2, Current-induced scour beneath initially elevated subsea pipelines:

Lee, J. Y., Hardjanto, F. A., Cossu, R., Chai, S., Leong, Z. Q., & Forrest, A. L. (2019). Current-induced scour beneath initially elevated subsea pipelines. *Applied Ocean Research*, 82, 309-324. DOI: 10.1016/j.apor.2018.11.011

Located in Chapter 5

The initial idea and aim of the paper was formulated by the candidate and Author 2. The funding for the work was partly attained with the assistance of Author 5. The parametric study was designed and performed by the candidate, with advice from Authors 1, 2 and 5. The data was analysed by the candidate. The equations for predicting the maximum dimensionless seabed shear stress and equilibrium scour depth were developed by the candidate and Author 2. The paper was initially drafted by the candidate, and multiple revisions were produced upon obtaining critical feedback from all authors regarding the interpretation and presentation of the results.

The percentage of the contribution made by the candidate was 90% while the co-authors contributed the remaining 10%.

Paper 3, Development of current-induced scour beneath elevated subsea pipelines:

Lee, J. Y., Forrest, A. L., Hardjanto, F. A., Chai, S., Cossu, R., & Leong, Z. Q. (2018). Development of current-induced scour beneath elevated subsea pipelines. *Journal of Ocean Engineering and Science*, 3(4), 265-281. DOI: 10.1016/j.joes.2018.09.001

Located in Chapter 6

The initial idea and aim of the paper was formulated by the candidate, Authors 1, 2, 3 and 4. The funding for the work was partly attained by Authors 1 and 2. The experimental data was analysed by the candidate. The improved manner of non-dimensionalising the scour time scale was formulated by the candidate. The empirical formula for predicting the non-dimensional scour time scale was developed by the candidate. The paper was initially drafted

by the candidate, and multiple revisions were produced upon obtaining critical feedback from all authors regarding the interpretation and presentation of the results.
The percentage of the contribution made by the candidate was 90% while the co-authors contributed the remaining 10%.

Paper 4, Two-phase model for simulating current-induced scour beneath subsea pipelines at different initial elevations:

Lee, J. Y., McInerney, J. B., Hardjanto, F. A., Chai, S., Cossu, R., Leong, Z. Q., & Forrest, A. L. (2018). Two-Phase Model for Simulating Current-Induced Scour Beneath Subsea Pipelines at Different Initial Elevations. In *ASME 2018 37th International Conference on Ocean, Offshore and Arctic Engineering* (pp. V009T10A021-V009T10A021). American Society of Mechanical Engineers. DOI:10.1115/OMAE2018-77245
Located in Chapter 7
The initial idea and aim of the paper was formulated by the candidate, Authors 1 and 2. The funding for the work was partly attained with the assistance of Authors 2 and 3. The design and execution of the numerical simulations were done by the candidate, with advice from Authors 2 and 5. The data was analysed by the candidate. The paper was initially drafted by the candidate, and multiple revisions were produced upon obtaining critical feedback from all authors regarding the interpretation and presentation of the results.
The percentage of the contribution made by the candidate was 90% while the co-authors contributed the remaining 10%.

We the undersigned agree with the above stated “proportion of work undertaken” for each of the above published (or submitted) peer-reviewed manuscripts contributing to this thesis:

Signed:

	---	---
	Fauzi Hardjanto	Shuhong Chai
	Supervisor	Head of School
	Australian Maritime College	Australian Maritime College
	University of Tasmania	University of Tasmania
Date:	7 July 2018	7 July 2018

"*There is an art to science, and science in art; the two are not enemies, but different aspects of the whole.*"

- Isaac Asimov

Boston University

Acknowledgements

This work is funded by the National Centre for Maritime Engineering and Hydrodynamics at the University of Tasmania, and Tasmanian Gas Pipeline Pty. Ltd. Given the opportunity to conduct this fascinating research, I sincerely thank my academic supervisors, Alexander Forrest, Fauzi Hardjanto, and Shuhong Chai; and research advisors, Remo Cossu and Zhi Leong. I also wish to thank Barry Parsons, from Tasmanian Gas Pipeline Pty. Ltd. and Andrew Hargrave from Adetra Pty Ltd. The generous assistance and advice from Fabian Bombardelli, Katie Stagl, Jasmin McInerney, Bill Sluis, Daret Kehlet, Vanessa Lucieer, Nathan Kemp, Isak Bowden-Floyd, Michael Underhill, Alan Faulkner, Karl Manzer, Christopher Coppard, Supun Randeni, and the Dell Richey II fishing vessel crew, in obtaining field measurements and conducting laboratory experiments are greatly appreciated. I would also like to acknowledge the Australian Maritime College and Tasmanian Partnership for Advanced Computing for providing access to their high performance computing facilities. Last but not least, I am grateful for the support from my caring family and friends, as I would not be able to complete this thesis without them.

Abstract

The erosion of sediment, or scour, around marine structures is a common occurrence. Scour around subsea pipelines may lead to excessive bending moments and/or vortex-induced vibrations; thus potentially compromising the structural integrity of the pipe. However, when a pipeline is installed along an uneven seabed, certain sections may be elevated with respect to the seabed. Small initial pipe elevations can result in high flow amplification beneath the pipe, which induces a high capacity for scour to occur, and increase the initial gap between the pipe and the seabed. A recent survey of a subsea pipeline revealed multiple incidences of free spanning, whereby a significant number of spans had maximum seabed gaps less than 30% of the outer pipe diameter. Rectification works are challenging and expensive; therefore, this work focused on predicting scour beneath subsea pipelines under steady currents with a particular emphasis on quantifying the influence of the initial pipe elevation.

Few existing empirical formulae have included the influence of the pipe elevation. In this work, a combination of experimental, numerical and field investigations has been undertaken; through which the data obtained in this work and from published literature are used to develop new empirical formulae for predicting: (1) the maximum dimensionless seabed shear stress beneath the pipe; (2) the equilibrium scour depth; and, (3) the scour time scale, which includes a suggestion for a new non-dimensional form of the time scale. The key variables of interest are: (1) the pipe-elevation-to-diameter ratio; (2) upstream dimensionless seabed shear stress; and, (3) the pipe Reynolds number. A scalar objective function is used to quantify the influence of the aforementioned variables in deriving a new set of empirical formulae.

Upon the validation of a single-phase rigid seabed model with published experimental data, a large parametric study is performed to compute the seabed shear stress beneath the pipe. The numerical data is used to develop an equation for predicting the maximum dimensionless seabed shear stress, which can be compared to the critical shear stress to estimate the initiation of scour beneath the pipe. Subsequently, sediment flume experiments are conducted

to investigate the influence of the pipe elevation on the development of scour beneath the pipe. The experimental data from the present study as well as from the published literature are used to derive empirical formulae for predicting the equilibrium scour depth and scour time scale. The recent derivations suggest that the maximum seabed shear stress, equilibrium scour depth, and time scale, are significantly influenced by the pipe elevation and upstream seabed shear stress. However, the Reynolds number effects are small compared to the other parameters.

In addition to a review of existing empirical formulae for scour prediction, a comprehensive review of existing numerical modelling techniques has been performed; through which the practical options for modelling scour are identified, employed, verified and validated. A single-phase rigid seabed model is found to be appropriate for performing a large parametric study to predict the maximum seabed shear stress for predicting the initiation of scour. A two-phase Eulerian-Eulerian model is deemed to be practical for predicting the equilibrium scour depth with reasonable accuracy, but not the time scale.

This thesis focused on predicting two-dimensional current-induced scour beneath elevated subsea pipelines. The pipe elevation has not been considered in existing formulae for predicting the initiation of scour. Subsequently, the severity of scour can be estimated via the prediction of the equilibrium scour depth and the scour time scale. This would be beneficial when the flow condition may not necessarily result in a deep scour hole, or when the time required for a substantial scour depth to develop is significantly longer than the storm period. Ultimately, this body of work aims to improve the design and management of subsea pipelines.

Contents

List of figures

List of tables

List of symbols

a	Amplitude of the orbital motion of the fluid particles	[m]
C_D	Drag coefficient	
C_h	Heat capacity	[kg·m^2·K^{-1}·s^{-2}]
C_k	Correction factor	
C_{pm}	Mean pressure coefficient	
C_r	Courant number	
D	External pipe diameter	[m]
D_*	Dimensionless sediment grain size	
d_{50}	Median diameter of sediment grains	[m]
e	Coefficient of restitution	
E	Comparison error	
e_m	Pipe embedment depth	[m]
e_o	Pipe elevation with respect to the far-field seabed	[m]
eta	Constant for the *JohnsonJacksonSchaeffer* frictional stress model	
f_i	Value predicted via a curve-fitted equation	
Fr_j	Constant for the *JohnsonJacksonSchaeffer* frictional stress model	[N·m^{-2}]
f_w	Friction factor	
g	Gravitational acceleration	[m·s^{-2}]
g_0	Radial distribution function	
G_{max}	Maximum seabed gap	[m]
G_s	Seabed gap; the summation of the pipe elevation and scour depth directly beneath the pipe	[m]
H	Local wave height	[m]
h	Mean water depth	[m]

h_{gs}	Inter-phase heat transfer coefficient	
I	Identity matrix	
I_t	Turbulence intensity	[%]
J_s	Dissipation or generation rate of granular energy due to interaction with the fluid phase	$[kg \cdot m^{-3} \cdot s^{-1}]$
k	Turbulent kinetic energy	$[J \cdot kg^{-1}]$
K_b	Equivalent sand roughness parameter	[m]
KC	Keulegan–Carpenter number	
K_{gs}	Inter-phase momentum transfer	$[kg \cdot m^{-3} \cdot s^{-1}]$
KP	Kilometre point	
k_s	Nikuradse roughness	[m]
L_c	Sediment container length	[m]
L_w	Local wave length	[m]
n	Sediment porosity	
P	Dynamic pressure	[Pa]
p	Constant for the *JohnsonJacksonSchaeffer* frictional stress model	
p_∞	Pressure taken at the leading edge of the flat plate (i.e. 36D upstream from the pipe)	[Pa]
P_a	Absolute pressure which is shared among both phases	[Pa]
p_f	Normal fluid pressure along the flat plate	[Pa]
P_{fric}	Normal frictional stress	[Pa]
p_k	Order of accuracy	
p_{kest}	Estimate for the theoretical order of accuracy	
P_s	Solids pressure or granular particle pressure	[Pa]
q	Conductive heat flux	$[W \cdot m^{-2}]$
r	Equivalent sand grain roughness height	[m]
R^+	Roughness parameter	
R^2	Squared correlation coefficient	
Re	Reynolds number	
Re_p	Particle Reynolds number	
Re_y	Wall-distance-based Reynolds number	
r_k	Grid refinement ratio	

S	Scour depth	[m]
s	Specific gravity	
S_{eq}	Equilibrium scour depth directly beneath the vertical centreline of the pipe	[m]
S_{ij}	Mean strain rate tensor	[s^{-1}]
S_m	Invariant measure of the strain rate	[s^{-1}]
S_{max}	Maximum scour depth	[m]
S_r	Strain rate parameter	
S_s	Strain rate for the sediment phase	
t	Time	[s]
T	Temperature	[K]
T_e	Scour time scale	[s]
T_e^*	Non-dimensional scour time scale associated with T_e	
T_p	Scour time scale	[s]
T_p^*	Non-dimensional scour time scale associated with T_p	
T_q^*	New dimensionless scour time scale proposed in this work	
U	Mean computed flow velocity	[$m \cdot s^{-1}$]
u	Local flow velocity	[$m \cdot s^{-1}$]
u_*	Friction velocity	[$m \cdot s^{-1}$]
u_{35}	Stream-wise velocity beneath the pipe measured at 0.035 m above the seabed	[$m \cdot s^{-1}$]
U_∞	Free-stream current velocity	[$m \cdot s^{-1}$]
U_c	Critical velocity for sediment entrainment	[$m \cdot s^{-1}$]
U_{cr}	Critical current velocity for scour onset	[$m \cdot s^{-1}$]
U_D	Uncertainty of the benchmark data	
U_f	Mean velocity of the fluid phase	[$m \cdot s^{-1}$]
U_G	Grid uncertainty	
U_{in}	Incoming current velocity	[$m \cdot s^{-1}$]
u_m	Amplitude of the oscillatory velocity	[$m \cdot s^{-1}$]
U_o	Depth-averaged flow velocity	[$m \cdot s^{-1}$]
U_{rp}	Modified Ursell parameter	
U_s	Mean velocity of the sediment phase	[$m \cdot s^{-1}$]
$\overline{U'U'}$	Reynolds stress tensor	[Pa]

U_V	Validation uncertainty	
u_x, U_x	Stream-wise flow velocity	[m·s^{-1}]
U_y	Cross-stream flow velocity in the vertical *y* direction	[m·s^{-1}]
x, X	Stream-wise distance from the vertical centreline of the pipe	[m]
x_{aft}	Distance between the downstream forward-facing step and the pipe	[m]
x_{fwd}	Distance between the upstream backward-facing step and the pipe	[m]
x_{inlet}	Distance between the downstream forward-facing step and the inlet boundary	[m]
y,Y	Elevation from the far-field seabed	[m]
y^+	Non-dimensional wall distance for a wall-bounded flow	
$\overline{y}$	Mean of the simulated or measured values	
y_i	Simulated or measured value	
y_{sed}	Sediment box depth	[m]
y_1	Distance from the wall boundary to the first node	[m]
z_o	Seabed roughness height	[m]
z_p	Pipe surface roughness height	[m]
α_f	Volume fraction of the fluid phase	
α_s	Volume fraction of the sediment phase	
$\alpha_{s,max}$	Maximum particle packing limit	
$\alpha_{s,min}$	Threshold for friction	
γ	Contact angle for the pipe	[°]
γ_s	Dissipation rate of granular energy due to inelastic particle-particle collisions	[kg·m^{-3}·s^{-1}]
δ_{in}	Incoming boundary layer thickness	[m]
$\delta^*_{RE_{k_1}}$	Numerical error	
Δt	Time step	[s]
Δx	Minimum length of a computational cell	[m]
$\Delta\tau_{max}$	Relative change in τmax	[%]
ε	Rate of dissipation of turbulence energy	[J·kg^{-1}·s^{-1}]
$\varepsilon_{k_{21}}$	Difference between the result computed using a ‘fine’ mesh and a ‘medium’ mesh	

$\varepsilon_{k_{32}}$	Difference between the result computed using a 'medium' mesh and a 'coarse' mesh	
η_{max}	Maximum apparent erosion rate	[m·s^{-1}]
θ	Dimensionless seabed shear stress or Shields parameter	
Θ	Granular temperature	[m^2·s^{-2}]
θ_∞	Upstream dimensionless seabed shear stress	
θ_{cr}	Critical dimensionless seabed shear stress	
θ_{cw}	Dimensionless seabed shear stress due to currents and waves	
θ_{cz}	Dimensionless seabed shear stress due to currents and waves	
θ_{eff}	Effective dimensionless seabed shear stress	
θ_{max}	Maximum dimensionless seabed shear stress	
κ	0.4, von Kármán constant	
κ_s	Thermal conductivity of granular energy	[kg·m^{-1}·s^{-1}]
$\lambda_A \Delta C_{p0}$	Exit pressure gradient coefficient	
λ_s	Bulk viscosity	[Pa·s]
μ_f	Dynamic viscosity	[Pa·s]
μ_f	Fluid dynamic viscosity	[Pa·s]
μ_f^{eff}	Effective dynamic viscosity	[Pa·s]
μ_{fric}	Frictional shear viscosity	[Pa·s]
μ_s	Shear viscosity	[Pa·s]
μ_t	Dynamic turbulent viscosity	[Pa·s]
ν	Fluid kinematic viscosity	[m^2·s^{-1}]
ν_t	Kinematic eddy viscosity	[m^2·s^{-1}]
ρ, ρ_f	Fluid density	[kg·m^{-3}]
ρ_s	Particle density	[kg·m^{-3}]
τ_∞	Upstream seabed shear stress	[Pa]
τ_b	Seabed shear stress	[Pa]
τ_c	Seabed shear stress due to a steady current	[Pa]
τ_{cw}	Seabed shear stress due to a combination of currents and waves	[Pa]
τ_f	Combined Reynolds and viscous stress for the fluid phase	[Pa]
τ_{max}	Local maximum seabed shear stress beneath the pipe	[Pa]
τ_{mean}	Mean seabed shear stress	[Pa]

τ_s	Shear stress tensor for the sediment phase	[Pa]
τ_w	Seabed shear stress due to waves	[Pa]
φ	Flow incidence angle	[°]
φ_{fric}	Angle of internal friction	[°]
ω	Specific turbulent dissipation rate, turbulent frequency	[s^{-1}]

List of abbreviations

2-D	Two-dimensional
3-D	Three-dimensional
ADCP	Acoustic Doppler current profiler
ADV	Acoustic Doppler velocimeter
AUV	Autonomous underwater vehicle
CFD	Computational fluid dynamics
cosh	Hyperbolic cosine function
coth	Hyperbolic cotangent function
CWC	Circulating water channel
DEM	Discrete element method
DNV	Det Norske Veritas
DNV GL	Det Norske Veritas and Germanischer Lloyd
DOI	Digital object identifier
exp	Exponential function
GPS	Global positioning system
GPU	Graphics processing unit
INS	Inertial navigation system
LBM	Lattice Boltzmann method
LES	Large eddy simulation
MATLAB	Matrix laboratory
NS	Navier-Stokes
OpenFOAM	Open Source Field Operation and Manipulation
PVC	Polyvinyl chloride
RANS	Reynolds-averaged Navier-Stokes
ROV	Remotely operated vehicle
sech	Hyperbolic secant function

SST	Shear stress transport
tanh	Hyperbolic tangent function
TGP	Tasmanian gas pipeline
US	United States
UTC	Coordinated universal time

Chapter 1
Introduction

This chapter provides background information on scour around pipelines, research objectives, contributions, scope of this work, and an outline of this thesis. This chapter aims to inform the reader of the extent of the problem, the measures taken to develop potential solutions for the problem, and the implications of the outcome of this work.

1.1 Background

Subsea pipeline networks across the globe, which stretch up to tens of thousands of kilometres along the ocean floor, are said to be the lifeline of the oil industry [1]. A common occurrence and problem for subsea pipelines is scour. Scour can be defined as flow-induced sediment transport in the form of bed load and suspended load, which is influenced by the geometry of a marine structure [2]; in the context of this work, this is a subsea pipeline which is laid on the seabed. The stability of a marine structure may be undermined by scour. Figure 1.1 shows a subsea cable with multiple free spans. When a scour hole beneath a pipe has developed to a certain extent, the pipe may experience excessive bending moments, which may compromise its structural integrity; and/or, vortex-induced vibrations and a potential accumulation of fatigue damage [3]. It is therefore important to predict the conditions pertaining to the initiation and development of scour underneath subsea pipelines.

When a subsea pipeline is installed along an uneven seabed, certain sections of the pipeline may be elevated above the seabed, where it is not possible for the pipeline to conform to the natural bathymetry [1, 4]. Scour may occur due to flow amplification at a small gap in between the pipe and the seabed, where a smaller clearance has been found to result in higher seabed shear stress amplification [5], which suggests a higher capacity for scour to occur

beneath the pipe. Furthermore, storm events may not last as long as the period required for the scour hole to reach an equilibrium state [6], and hence a pipeline may have multiple spans with gaps in between the pipe and the seabed. Rectification works, such as rock dumping, are challenging to perform and can lead to a substantial increase in project costs (e.g. approximately $US1.2 million per kilometre [7]). Therefore, this work focused on scour underneath subsea pipelines, with a particular focus on the influence of the pipe elevation.

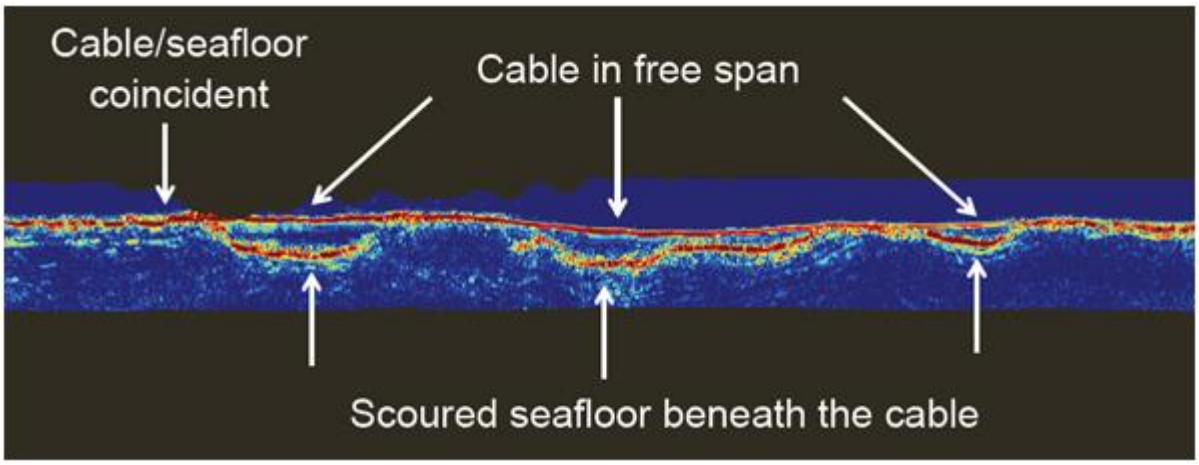

Figure 1.1: Sub-bottom profile data showing the location of a subsea cable with respect to the seabed. © Pangeo Subsea (https://www.pangeosubsea.com/sub-bottom-imager/)

Following the initiation of the scouring process beneath a rigid pipeline, the scour hole would develop with time and eventually reach an equilibrium state, provided that the flow condition remained constant. Aside from the lack of consideration of the pipe elevation, e_o (refer to Figure 1.2), in terms of predicting the occurrence of scour, previous research which focused on the development of scour beneath pipelines for which $e_o/D > 0$ had also been sparse; a comprehensive literature review on these topics is presented in Chapter 2.

In brief, Sumer and Fredsøe [1] proposed an empirical formula in which the equilibrium scour depth beneath the pipe, S_{eq}, is solely a function of e_o/D. However, Moncada-M and Aguirre-Pe [8] showed that the inclusion of a Froude number term yielded a high correlation to their experimental results, which largely involved a small water-depth-to-pipe-diameter ratio (i.e. $h/D < 4$). The aforementioned empirical formulae were developed based on live-bed experiments, for which the upstream seabed shear stress exceeded the critical shear stress for the sediment. Hence, there is sediment transport occurring upstream and along the entire sand bed. It is then interesting to note that the equilibrium scour depth had been reported to be

dependent on the upstream dimensionless seabed shear stress, θ_∞, and the Reynolds number, *Re* [9], whilst the effects of these parameters have not been quantified. In addition, the effect of e_o/D on the scour time scale, which is the time required for a significant scour depth to develop, had not been investigated as well. Therefore, this work also focused on quantifying the influence of the aforementioned parameters on the equilibrium scour depth and scour time scale.

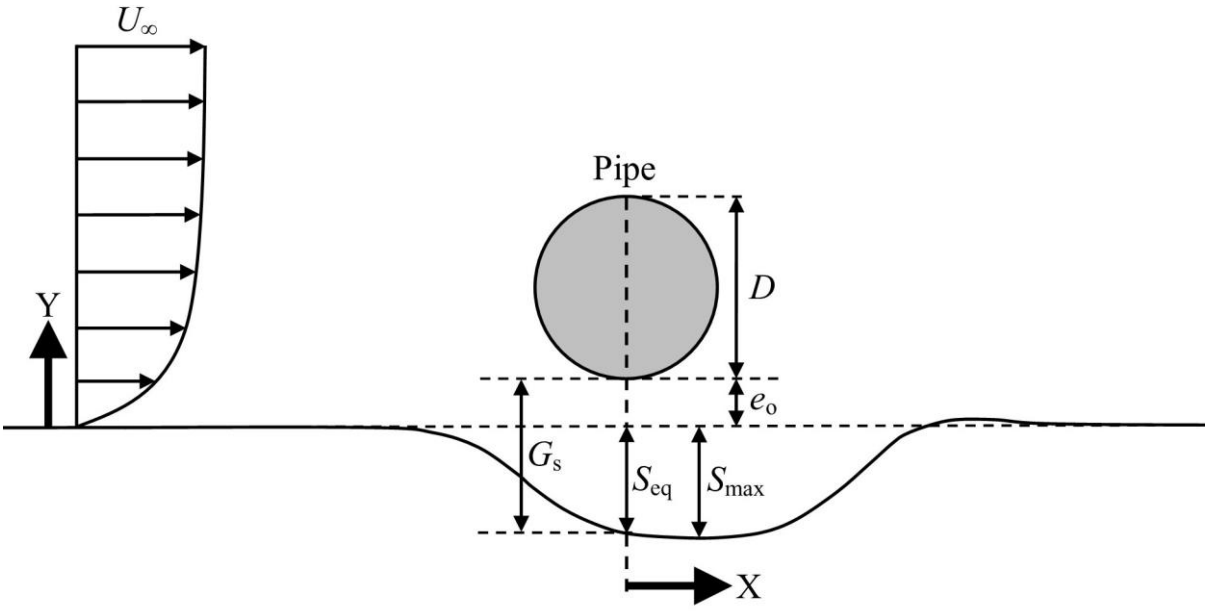

Figure 1.2: A two-dimensional sketch illustrating a scour hole beneath a pipe, wherein U_∞ is the free-stream current velocity; D is the external pipe diameter; e_o is the elevation of the pipe with respect to the average far-field seabed; S_{eq} is the equilibrium scour depth directly beneath the pipe, which may not be the same as the maximum scour depth, S_{max}; and, the seabed gap, G_s, is defined as the summation of e_o and the scour depth directly beneath the pipe.

To date, although there are several models for scaling general sediment transport experiments, achieving perfect similitude remains a physical impossibility [10]. With scaled sediment, the sediment grain size will be so small that they exhibit cohesive properties, which are not characteristic of the sediment at its full scale [11]. Having smaller sediment with cohesive properties will result in scour propagation timescales to be falsely exaggerated [12], compared to predictions made via empirical formulae developed for non-cohesive sediment (e.g. [13]). Quantifying the influence of the Reynolds number becomes particularly important, when excessive fluid viscous forces are introduced in scaled experiments, or in other words, scale effects [10].

With regards to subsea pipelines, the diameter can range from 0.2 m to more than 1 m in diameter [1], where the Reynolds number often range from 3×10^5 to 1.5×10^6 [6]; however, the range may be from 5×10^3 to 5×10^4 in laboratory experiments (e.g. [3, 8, 12]). Due to the spatial and time scales associated with studying the mechanics of scour around a full-scale pipeline, it is often logistically impractical to rely on field measurements. With some notable exceptions (e.g. [7]), limited field data have been obtained and published. To address this paucity of data, numerical simulations offer a viable alternative as the restrictions in terms of the size of the computational domain would depend on the available computational resources. This served as a motivation to review available numerical modelling techniques to identify practical options for simulating scour, after which these practical options are then employed in this work to assess their capabilities.

1.2 Research questions and objectives

The extent of which the aforementioned parameters (e.g. pipe elevation, Reynolds number, etc.) affect scour beneath subsea pipelines are not completely understood; however, scouring may result in significant repercussions on asset management. This work focused on quantifying the effects of the pipe elevation with respect to the far-field seabed, e_o/D, upstream dimensionless seabed shear stress, θ_∞, and Reynolds number, Re, on the maximum dimensionless seabed shear stress beneath the pipe, the equilibrium scour depth, as well as the scour time scale. In addition, the state of present numerical modelling techniques are reviewed, and numerical simulations are performed to model scour beneath pipelines with various e_o/D ratios. The broader applications may involve assisting the development of accurate risk models and amendments to industry standards for the design and maintenance of subsea pipelines.

The work presented in this thesis aims to address the following major research questions:

- How would having a small initial pipe elevation or seabed gap affect the occurrence of scour beneath a pipe?
- To what extent does θ_∞ and Re influence the maximum seabed shear stress and equilibrium scour depth underneath a pipe for $e_o/D > 0$?
- To what extent does θ_∞, Re and e_o/D affect the scour time scale?

- What is the state-of-the-art in terms of practical numerical modelling techniques for simulating scour beneath subsea pipelines?

Subsequently, the main objectives in addressing the outlined problems, and to answer the aforementioned research questions are:

- Obtain field measurements of seabed gaps underneath a pipeline, and perform full-scale numerical simulations to predict the maximum dimensionless seabed shear stress beneath the pipe.
- Perform numerical simulations at various scales and obtain experimental data, to develop new empirical formulae for predicting the maximum dimensionless seabed shear stress and equilibrium scour depth underneath the pipe, in which the effects of θ_∞, Re and e_o/D are quantified.
- Conduct experiments and compile experimental data from published literature, to develop a new empirical formula for predicting the non-dimensional scour time scale, through which the effects of θ_∞, Re and e_o/D are quantified.
- Review existing numerical modelling techniques, and subsequently apply, verify and validate a practical option for simulating scour beneath subsea pipelines.

1.3 Present contributions and novel aspects

The work presented in this thesis have been accomplished with reference to the aforementioned research objectives, in order to provide the following contributions to the field of scour around subsea pipelines:

- A better understanding of the state of pipelines in the field, as there are limited field data available in published literature, and a new means of predicting the occurrence of scour beneath a pipeline with $e_o/D > 0$, which relies on the maximum dimensionless seabed shear stress beneath the pipe.
- A new empirical formula for predicting the maximum dimensionless seabed shear stress beneath subsea pipelines, where scour is expected to occur when the maximum shear stress exceeds the critical dimensionless seabed shear stress, θ_{cr}; where the effects of θ_∞, Re and e_o/D have been quantified.

- A new empirical formula for predicting the equilibrium scour depth beneath subsea pipelines, in which the effects of θ_∞, Re and e_0/D have been quantified.
- A new empirical formula for predicting the scour time scale, in which the effects of θ_∞, Re and e_0/D have been quantified.
- A new equation for non-dimensionalising the scour time scale, which enabled existing empirical formulae to attain higher correlation coefficients with respect to experimental data.
- A comprehensive review of present numerical modelling techniques, as well as the application, verification and validation of an open-source two-phase computational fluid dynamics (CFD) model, which considers fluid-particle and particle-particle interactions, for simulating current-induced scour beneath subsea pipelines at different pipe elevations.

1.4 Research methodology and scope

Existing empirical formulae which have been developed for predicting the initiation of the scouring process, the equilibrium scour depth, and the scour time scale, have been identified and knowledge gaps have been uncovered. This is accompanied by a comprehensive review of the numerical modelling techniques which have been used to simulate scour beneath subsea pipelines under steady currents. A novel combination of field, experimental and numerical work have been undertaken, through which rich collections of data have enabled the development of new empirical formulae, for predicting scour beneath subsea pipelines with the consideration of the effects of the pipe elevation with respect to the far-field seabed. Previous research on this topic have been sparse, and it is therefore the primary focus of this work.

This work focused on predicting two-dimensional scour beneath subsea pipelines for different elevations under steady currents. Three-dimensional effects may be worth investigating; however, experiments conducted by Azamathulla *et al.* [14] suggested that the equilibrium scour depth was at maximum when the flow was perpendicular to the pipe's axial length. In addition, the difference in scour depth with respect to flow incidence angles is insignificant. Investigating the influence of waves is not within the scope of this work, because unidirectional currents have been found to result in deeper scour depths as compared

to that under the effect of waves or a combination of current and wave action [15]. Nevertheless, three-dimensional scour and the influence of waves could be an interesting extension of this work in the future.

1.5 Thesis outline

This thesis consists of several chapters that reflect the overall research methodology and objectives. In Chapter 2, a detailed literature review is presented, wherein the existing empirical formulae for predicting the initiation of scour, the equilibrium scour depth, and the scour time scale are evaluated. Subsequently, the current state of numerical modelling techniques, which have been used to simulate scour beneath subsea pipelines, are compared to identify practical options for predicting the initiation and development of scour beneath pipelines.

Chapter 3 provides a general description of the various methods which have been employed in this work, wherein a combination of experimental, numerical, and field investigations have been conducted. The specific test conditions are not described in this chapter, as they are presented in the subsequent chapters.

In Chapter 4, field measurements are obtained to gauge the incidence of small seabed gaps between a pipeline and the seabed, for which a higher capacity for scour to occur underneath the pipe can be expected. A new manner of predicting the occurrence of scour beneath a pipeline with $e_o/D > 0$ is introduced. This is based on computing the maximum dimensionless seabed shear stress beneath the pipe via CFD, and comparing the predicted value to the critical shear stress for the sediment.

Chapter 5 presents an extensive parametric study that involved computing the seabed shear stresses beneath pipelines at various scales using a single-phase CFD model. A new equation is proposed for predicting the maximum seabed shear stress beneath the pipe, which builds on the work done in Chapter 4, in terms of quantifying the influence of the Reynolds number. Subsequently, a new empirical formula is developed based on a collection of experimental data, for predicting the equilibrium scour depth, wherein the influence of θ_∞ and Re on S_{eq}/D is quantified.

Chapter 6 focused on predicting the development of scour via sediment flume experiments. This chapter presents a new manner of non-dimensionalising the time scale, which is found to improve the correlation of existing formulae with the experimental data. Subsequently, a new empirical formula is proposed for predicting the non-dimensional scour time scale, in which the effects of θ_∞, Re and e_o/D are quantified. Finally, full-scale predictions of the equilibrium scour depth and time scale are made. The seabed gaps predicted using the equation which is proposed in Chapter 5 is compared with the field measurements that are obtained in Chapter 4.

In Chapter 7, an open-source two-phase numerical model is employed to take a closer look into multiphase modelling, by simulating scour beneath a pipeline with $e_o/D > 0$ under a steady current. The numerical model is selected based on the literature review in Chapter 2, where an Eulerian-Eulerian model is deemed to be the most practical option for modelling scour beneath a pipe. The numerical model is verified and validated by experimental results. The numerical results agreed well with the equation proposed in Chapter 5, in terms of predicting the equilibrium scour depth. However, the computed scour time scale is found to be inaccurate. Nevertheless, relatively short computation times and negligible mesh dependency have been observed.

Chapter 8 provides a summary of the research scope and the main findings, as well as the implications of this work and recommendations for future work.

Chapter 2

Literature review

This chapter reviews existing empirical formulae which have been developed for predicting the initiation of scour beneath subsea pipelines, the equilibrium depth, and the scour time scale. This is complemented by a discussion on potential scale effects. Subsequently, present numerical modelling techniques which have been employed to simulate scour beneath pipelines are reviewed, to identify practical options that can be used in this work.

2.1 Two-dimensional scour beneath pipelines

2.1.1 Initiation of scour

The mechanics of scour beneath pipes with initial partial embedment or bottom-seated pipes (i.e. zero embedment) had been studied extensively via laboratory experimentation (e.g. [3, 16]). The onset process is illustrated in Figure 2.1, wherein a steady current is flowing from left to right. Initially, when there is a flow-induced pressure difference between the upstream and downstream sides of a pipe, water can flow through the voids in between the sediment particles beneath the pipe (i.e. seepage flow). Eventually, a mixture of water and sediment will be discharged at the immediate downstream side of the pipe (i.e. referred to as piping) [16]. This is followed by a "jet period" (i.e. tunnel erosion) where sediment is syphoned violently underneath the pipe [3]. As more sediment is eroded, the scour hole would deepen. When the scour depth exceeds the equivalent of 30% of the pipe diameter, periodic vortex shedding can occur in the wake of the pipe [3, 17], which leads to further erosion downstream of the pipe, and may lead to vortex-induced vibrations.

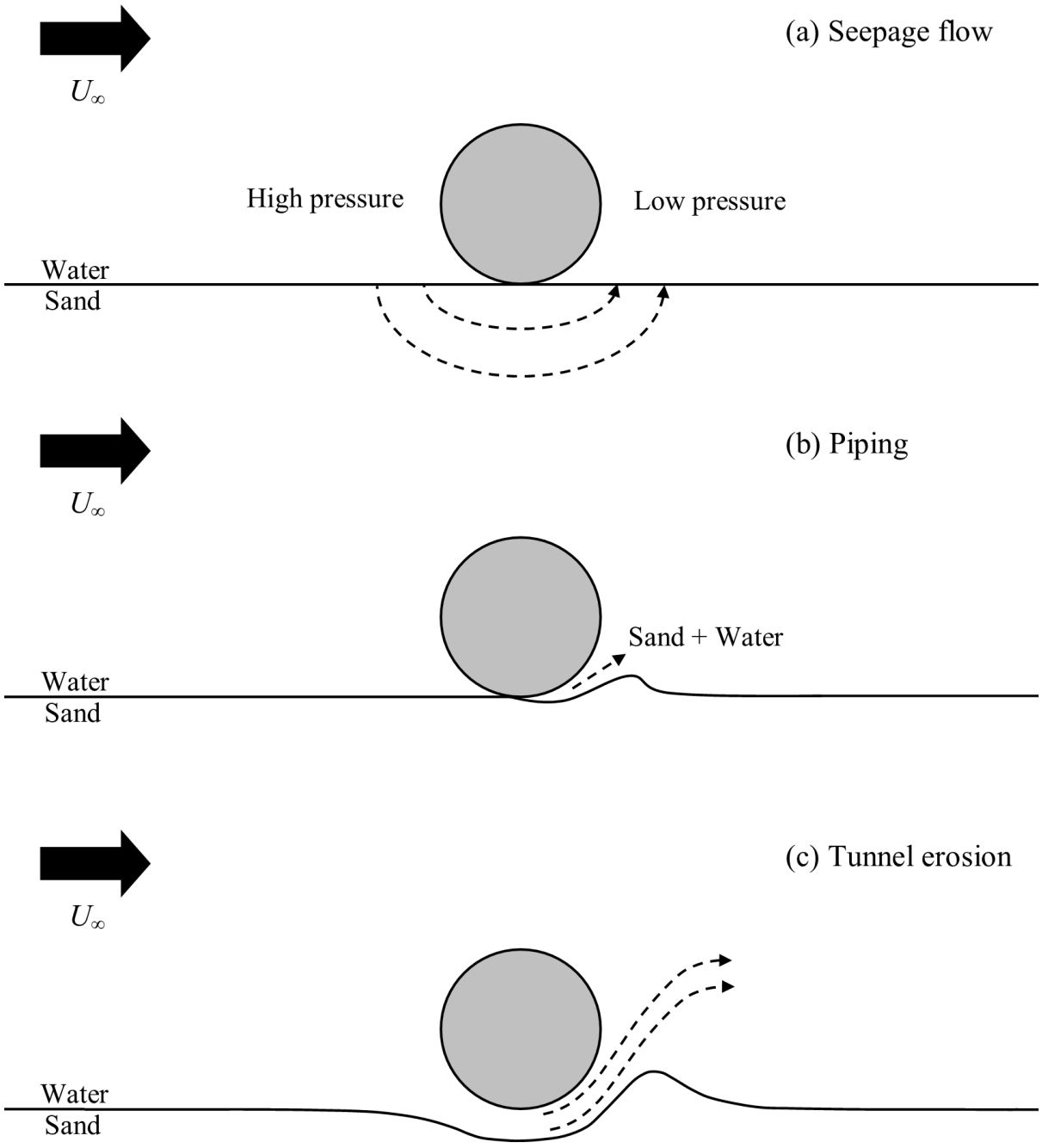

Figure 2.1: Two-dimensional view of the scour onset process beneath a bottom-seated pipe in a steady current: (a) seepage flow; (b) piping; and, (c) tunnel erosion.

Several empirical relationships have been derived based on two-dimensional studies, to estimate the critical far-field current velocity for scour onset around a pipe with initial partial embedment (e.g. Sumer *et al.* [18]), without the consideration of the pipe elevation, e_o. A comparison of closed-form equations, which are available in the literature for the prediction of scour onset, is presented in Table 2.1. Based on the correlation with experimental data,

Sumer *et al.* [18] derived an equation, to estimate the critical current velocity for scour onset, U_{cr}; g is gravitational acceleration; D is the external pipe diameter; n is sediment porosity; s is the specific gravity of the sediment; and, e_m is the initial pipe embedment or burial depth. However, the effects of e_o/D had not been considered.

Table 2.1: Comparison of equations for predicting the initiation of scour, listed in chronological order.

Reference	Equation
Steady currents:	
Sumer *et al.* [18]; 2001	$\frac{U_{cr}{}^2}{gD(1-n)(s-1)} = 0.025\exp\left[9\left(\frac{e_m}{D}\right)^{0.5}\right]$
Currents and/or waves:	
Zang *et al.* [19]; 2009	$\frac{u_m^2}{gD(s-1)(1-n)} \geq \frac{\gamma}{\lambda_A \Delta C_{p0}}\left(1-\exp\left(-0.018KC^{1.5}\right)\right)$ where $KC = \frac{2\pi a}{D}$.
DNV GL [20]; 2017	$U_{cr} = \sqrt{0.08\frac{g(s-1)d_{50}}{f_w}}$ where $f_w = 0.04\left(\frac{a}{K_b}\right)^{-0.25}$ for waves, and $f_w = 0.005$ for currents.

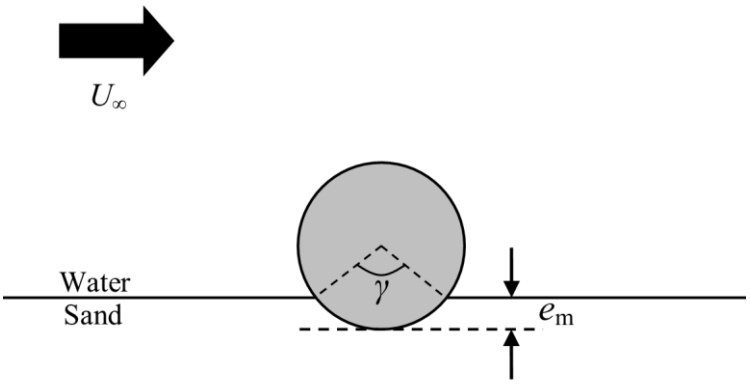

Figure 2.2: Illustration of the terms, e_m, which is the initial pipe embedment depth, and γ, which is the contact angle defined in Zang *et al.* [19].

Zang *et al.* [19] extended this work using numerical simulations, to estimate the critical flow velocity, due to currents and/or waves, at which scour onset around a pipe with initial partial embedment is likely to occur; u_m is the amplitude of the oscillatory velocity, γ is the contact

angle for the pipe, $\lambda_A \Delta C_{p0}$ is the exit pressure gradient coefficient, and KC is the Keulegan–Carpenter number, in which a is the amplitude of the orbital motion of the fluid particles. While the equation proposed by Zang *et al.* [19] is more comprehensive, it is not easily solved with $\lambda_A \Delta C_{p0}$. Furthermore, this equation is also only applicable to partially embedded pipes, and thus there is a need to investigate the effects of e_o/D.

The equations from Sumer *et al.* [18] and Zang *et al.* [19] are not cited in the latest version of industrial standards (e.g. [20, 21]). DNV GL [20] presented a general equation to predict the critical flow velocity leading to the onset of scour under steady currents or waves, but not both combined. d_{50} is the median sediment grain size; f_w is a friction factor, which has different values, depending on the flow condition; and, K_b is the equivalent sand roughness parameter. This is the extent of the description on 'seabed stability' in DNV GL [20], without the inclusion of the influence of the geometry of a marine structure (e.g. external pipe diameter). Although there is a new guideline on pipe-soil interaction [22], its contents are confidential.

2.1.2 Equilibrium scour depth

During the tunnel erosion stage (Figure 2.1c), the magnitude of the seabed shear stress underneath the pipe can be on the order of three to five times the upstream seabed shear stress [1]. This is a result of flow amplification, and thus there is a high rate of sediment transport in this region. However, it is later shown that this amplification ratio can be significantly higher, especially for the clear-water condition (i.e. where the upstream seabed shear stress is below the critical shear stress); this is discussed in Chapter 5. Nonetheless, although the scour hole will deepen as more erosion occurs, the scour depth will eventually reach an equilibrium depth, provided that the upstream flow condition remains constant. This is because, as the scour depth increases, the magnitude of the seabed shear stress beneath the pipe decreases. The seabed shear stress would eventually reduce to a value below the threshold for sediment transport to occur; or, there is an equivalent amount of sediment being transported into and out of the scour hole, and the net transport rate underneath the pipe would be practically nil [9].

Several equations have been proposed for the prediction of the equilibrium scour depth, S_{eq}. A comparison is presented in Table 2.2, in which the equations are listed in a chronological

order. Kjeldsen *et al.* [23] formulated an equation via flume experiments, where $U_o^2/2g$ is the velocity head. However, this equation appears to have been developed for bottom-seated pipelines (i.e. $e_o/D = 0$), and the influence of the sediment properties had not been considered. Bijker and Leeuwestein [24] modified the aforementioned equation based on more experimental data, and quantified the influence of the median sediment grain size, d_{50}, which seems to be relatively small. However, the proposed equation is still not fully non-dimensional.

Table 2.2: Comparison of equations for predicting the equilibrium scour depth, listed in chronological order.

Reference	Equation
Steady currents:	
Kjeldsen *et al.* [23]; 1973	$S_{eq} = 0.972\left(\frac{U_o^{\,2}}{2g}\right)^{0.2} D^{0.8}$
Bijker and Leeuwestein [24]; 1984	$S_{eq} = 0.929\left(\frac{U_o^{\,2}}{2g}\right)^{0.26} D^{0.78} d_{50}^{-0.04}$
Ibrahim and Nalluri [25]; 1986	$\frac{S_{eq}}{D} = \begin{cases} 4.706\left(\frac{U_o}{U_c}\right)^{0.89}\left(\frac{U_o}{\sqrt{gh}}\right)^{1.43} + 0.06, & \text{clear-water} \\ 0.084\left(\frac{U_o}{U_c}\right)^{-0.3}\left(\frac{U_o}{\sqrt{gh}}\right)^{-0.16} + 1.33, & \text{live-bed} \end{cases}$
Fredsøe *et al.* [13]; 1992	$\frac{S_{eq}}{D} = 0.6 \pm 0.1$
Moncada-M and Aguirre-Pe [8]; 1999	$\frac{S_{eq}}{D} = 0.9\tanh\left(1.4\frac{U_o}{\sqrt{gh}}\right) + 0.55$, $\frac{S_{eq}}{D} = \frac{2U_o}{\sqrt{gh}}\operatorname{sech}\left(1.7\frac{e_o}{D}\right)$
Sumer and Fredsøe [1]; 2002	$\frac{S_{eq}}{D} = 0.625\exp\left(-0.6\frac{e_o}{D}\right)$
Currents and waves:	
Zhang *et al.* [26]; 2016	$S_{eq} = \left(S_c^2 + S_w^2\right)^{0.5}$ where $S_c = 0.972\left(\frac{U_0^{\,2}}{2g}\right)^{0.2} D^{0.8}$ [23], and $\frac{S_w}{D} = 0.1\sqrt{KC}$ [9].

Ibrahim and Nalluri [25] extended this work by proposing two non-dimensional equations: one for the clear-water condition, and, another for the live-bed condition. In these equations, U_o is the undisturbed mean flow velocity, U_c is the critical velocity for sediment entrainment, and h is the water depth. The clear-water condition refers to the scenario whereby the upstream seabed shear stress is lower than the critical value for sediment transport to occur upstream (i.e. $\theta_\infty < \theta_{cr}$); conversely, for the live-bed condition, the upstream seabed shear stress is greater than the critical value (i.e. $\theta_\infty > \theta_{cr}$). However, there are contradicting exponents in the two equations proposed by Ibrahim and Nalluri [25]. Furthermore, having $S_{eq}/D > 0$ when $U_o = 0$ m/s may not be practically sound.

Subsequently, Fredsøe *et al.* [13] claimed that the dimensionless equilibrium scour depth, S_{eq}/D, due to steady currents is 0.6 for all practical purposes. Moncada-M and Aguirre-Pe [8], who investigated scour beneath pipelines in river crossings, later showed that S_{eq}/D is significantly influenced by the Froude number and e_o/D. This may be the case due to the fact that the experiments mostly involved a water depth ratio, h/D, of less than 4. Nevertheless, this is the first time the effects of e_o/D have been included in an equation for the prediction of S_{eq}/D.

Sumer and Fredsøe [1] also reported that the equilibrium scour depth can be significantly influenced by e_o/D. However, e_o/D is the only term which has been included in the equation, with the notion that it is only applicable for the live-bed condition. Therefore, there is a need to quantify the influence of these parameters on S_{eq}/D for both clear-water and live-bed conditions, as Sumer and Fredsøe [9] have reported that the equilibrium scour depth is also dependent on θ_∞ and Re.

More recently, Zhang *et al.* [26] attempted to formulate an equation which can be used to predict the equilibrium scour depth due to a combination of currents and waves. A correlation between the equation from Sumer and Fredsøe [9] for waves, and the equation from Kjeldsen *et al.* [23] for currents have been proposed. However, the influence of e_o/D had not been included. In addition, it is worth noting that investigating the influence of waves is not within the scope of this work, because unidirectional currents have been found to result in deeper scour depths as compared to that under the effect of waves or a combination of current and wave action [15].

On a separate note, Chao and Hennessy [27] proposed an iterative method to compute the scour depth based on potential flow theory. However, this method only provides a prediction of the order of magnitude of the scour depth. The limitation in the accuracy can be attributed to the negligence of fluid viscosity, and consequently, the absence of flow separation occurring downstream of the pipe [15].

Chiew [15] and Dey and Singh [28] proposed more comprehensive iterative methods to predict the equilibrium scour depth, whereby the iteration process involves estimating a scour depth that would result in a seabed shear stress beneath the pipe, which is equal to the critical shear stress for the sediment. Thus, it is assumed that the scour hole will not develop any further as the shear stress is equal to or below the critical value. However, this may only be valid for the clear-water condition; otherwise, even the upstream seabed shear stress would exceed the critical value for the live-bed condition. Therefore, developing a closed-form equation for the prediction of S_{eq}/D is one of the aims of this work.

2.1.3 Time scale

The development of the scour hole beneath the pipe in time is also of technical interest. The following equation is commonly used to describe the development of the scour depth beneath a pipe [13]:

$$S(t) = S_{eq}\left\{1-\exp\left(-\frac{t}{T_e}\right)\right\} \tag{2.1}$$

wherein $S(t)$ is the change in the absolute value of the scour depth beneath the pipe with time; S_{eq} is the equilibrium scour depth; t is time in seconds; and, T_e had been defined as the time required for substantial scour to develop. A non-dimensional form of the time scale, T_e^*, had also been proposed [13]:

$$T_e^* = \frac{\left[g(s-1)d_{50}^3\right]^{\frac{1}{2}}}{D^2}T_e \tag{2.2}$$

where g is gravitational acceleration; s is the specific gravity of the sediment; d_{50} is the median sediment grain size; and, D is the external pipe diameter. Using Eq. (2.1) and Eq. (2.2) as the foundation, several empirical formulae have been developed to predict the non-dimensional scour time scale (Table 2.3). Fredsøe *et al.* [13] analysed experimental data [3, 23], and reported that the time scale mainly decreased with the upstream dimensionless seabed shear stress, θ_∞; thus suggesting that the time taken for the scour depth to reach a considerable depth would reduce as the upstream seabed shear stress increased. Hence, Fredsøe *et al.* [13] proposed an equation where the non-dimensional time scale, T_e^*, is inversely proportional to θ_∞.

Dogan and Arisoy [29] resumed Fredsøe *et al.*'s [13] work by quantifying the effects of the Keulegan–Carpenter (KC) number on the scour time scale. Two additional equations have been proposed, which are presented in Table 2.3, as they resulted in a better correlation with experimental data, as compared to the equation with just the θ_∞ term. However, different coefficients have been suggested for the clear-water and live-bed cases. The clear-water case refers to a condition in which θ_∞ is less than the critical shear stress for the sediment, whilst conversely, the live-bed case refers to a condition in which θ_∞ exceeds the critical shear stress. Subsequently, two additional equations are proposed, wherein the KC number is replaced with the modified Ursell parameter, U_{rp} [30]. However, the associated correlation coefficient is lower than that for the equations with the KC number. In addition, the influence of the pipe elevation, e_o, had not been considered.

Larsen *et al.* [31] noted that the scour time scale due to wave-plus-current flow conditions had not been studied, at that time. Hence, a deformable seabed model (described in Section 2.2) was employed to simulate wave-plus-current scour beneath a pipe. Based on the simulation results, an equation for predicting the non-dimensional scour time scale was proposed. The parameter, m, represents the current's magnitude, where U_{cp} is the current velocity at the centre of the pipeline, and U_{mo} is the maximum free-stream velocity of the oscillating flow. The proposed far-field Shields parameter, θ_{cw}, is a function of the dimensionless seabed shear stress due to currents, θ_{cur}, and the dimensionless shear stress due to waves, θ_w. Interestingly, Larsen *et al.* [31] reported that the scour time scale under wave-plus-current flow was larger as compared to pure current conditions. This suggests that the scour hole beneath the pipe can develop at a faster rate under pure current conditions.

Table 2.3: Comparison of equations for predicting the non-dimensional scour time scale, listed in chronological order.

Reference	Equation
Steady currents:	
Fredsøe *et al.* [13]; 1992	$T_e^* = \frac{1}{50}\theta_\infty^{-\frac{5}{3}}$ where $T_e^* = \frac{\left[g(s-1)d_{50}^3\right]^{\frac{1}{2}}}{D^2}T_e$
Mohr *et al.* [12]; 2016	$T_e = \begin{cases} 2.8\frac{S_{eq}}{\eta_{max}}\frac{D}{L_c}, & \text{non-cohesive} \\ \frac{S_{eq}}{\eta_{max}}, & \text{cohesive} \end{cases}$
Waves:	
Dogan and Arisoy [29]; 2015	$T_e^* = \begin{cases} 4.36\times10^{-6}\theta_\infty^{-2.4}KC^{2.4}, & \text{clear-water} \\ 4.63\times10^{-5}\theta_\infty^{-1.5}KC^{2.5}, & \text{live-bed} \end{cases}$ $T_e^* = \begin{cases} 2.88\times10^{-6}\theta_\infty^{-2.65}U_{rp}, & \text{clear-water} \\ 7.40\times10^{-6}\theta_\infty^{-3.0}U_{rp}^{0.75}, & \text{live-bed} \end{cases}$
Currents and waves:	
Larsen *et al.* [31]; 2016	$T_e^* = \Gamma(m)\theta_{cw}^{-\frac{5}{3}}$ where $\Gamma(m) = \frac{1}{50} + 0.015\left[\exp\left(-350(m-0.5)^2\right) + \exp\left(-25(m-0.53)^2\right)\right]$ $m = U_{cp}/\left(U_{cp}+U_{mo}\right)$ $\theta_{cw} = \theta_m + \theta_w$ $\theta_m = \theta_{cur}\left(1+1.2\left(\frac{\theta_w}{\theta_{cur}+\theta_w}\right)^{3.2}\right)$
Zhang *et al.* [26]; 2016	$T_p^* = 0.02\theta_{cz}^{-1.5}$ where: $T_p \approx 1.29T_e$ $\tau_{cz} = \sqrt{\left(\tau_{mean}+\tau_w\cos\varphi\right)^2 + \left(\tau_w\sin\varphi\right)^2}$ $\frac{\tau_{mean}}{\tau_c} = 1+1.2\left(\frac{\tau_w}{\tau_c+\tau_w}\right)^{3.2}$

Zang *et al.* [32]; 2017	$T_e^* = \frac{1}{50}\theta_{eff}^{-\frac{5}{3}} \exp\left(\left(2.6\frac{e_m}{D}\right)^2\right)$ where $\theta_{eff} = \sqrt{\left(\theta_\infty \cos\varphi\right)^2 + \left(j\theta_\infty \sin\varphi\right)^2}$

Mohr *et al.* [12] studied the effect of the type of sediment on the scour time scale under steady flow conditions. The equation from Fredsøe *et al.* [13] was found to perform well in terms of predicting the time scale for non-cohesive sediment (e.g. coarse sand). However, it under-predicted the time scale for cohesive sediment (e.g. very fine sand with a high clay content). Therefore, two new equations have been proposed for predicting the dimensional scour time scale: one for non-cohesive sediment, whereby the transport of sediment is mainly in the form of bed load; and, the other for cohesive sediment, which is largely transported via suspension. With reference to Table 2.3, η_{max} is the maximum apparent erosion rate, D is the pipe diameter, and L_c is the stream-wise length of the sediment container. These equations have been derived based on a control volume analysis. The erosion rate is calculated based on the upstream seabed shear stress and a critical shear stress, which is determined from erosion testing conducted in Mohr *et al.* [12]. However, there may be potential limitations as physical erosion testing would be required to obtain η_{max}, and L_c would be very large for field conditions.

Zhang *et al.* [26] conducted experiments for the live-bed condition, involving steady currents and waves, and reported that a higher correlation with the experimental data was attained by replacing θ_∞ with θ_{cz}, where θ_{cz} is a function of the upstream shear stress due to steady currents and the upstream shear stress due to waves, and φ is the flow incidence angle. This meant that, for the case of steady currents, θ_{cz} would be equivalent to θ_∞. This equation was also developed based on experiments conducted with bottom-seated pipes (i.e. $e_o/D = 0$), and with the flow being perpendicular to the pipe for all cases. Nevertheless, it is worth mentioning that Zhang *et al.* [26] found the following equation from Whitehouse [2] to be capable of attaining a very high correlation coefficient, in terms of describing the development of the scour depth:

$$S(t) = S_{eq}\left\{1 - \exp\left[-\left(\frac{t}{T_p}\right)^{C_p}\right]\right\} \tag{2.3}$$

where C_p is a constant, for which the value is determined via a least-square fit, and if $C_p = 1$, then Eq. (2.3) would be equivalent to Eq. (2.1). Eq. (2.3) is later used in this work to estimate the dimensional scour time scale, T_p, where the best fit of T_p and C_p are found for each test case.

More recently, Zang *et al.* [32] investigated the influence of the initial partial embedment depth, e_m, and the angle of the incident flow, φ, on the scour time scale, for the live-bed condition. The equation shown in Table 2.3 included an effective dimensionless shear stress, θ_{eff}, and the embedment ratio, e_m/D, where θ_{eff} would be equivalent to θ_∞ for the case of having the flow perpendicular to the pipeline. This is the first equation wherein the initial vertical position of the pipe with respect to the far-field seabed had been considered for predicting the time scale. However, it would not be appropriate to apply the equation from Zang *et al.* [32] to the prediction of the scour time scale beneath a pipe with an initial elevation, e_o. Therefore, this work investigated the influence of e_o/D on the scour time scale, with a particular focus on the clear-water condition, which had not been considered in previous studies. In addition, the Reynolds number effect is also considered, since it had been reported to influence the equilibrium scour depth [9].

2.1.4 Scale effects

Although laboratory experiments provide a good platform for studying the mechanics of scour, they are limited by the dimensions of the associated experimental facilities. In general, scaled experiments tend to exhibit scale effects as excessive fluid viscous forces are introduced [10]. As subsea pipelines that form multiple fluid transportation networks across the globe can range from 0.2 m to more than 1 m in diameter [1], the pipe diameter can be larger by an order of magnitude as compared to the model-scale experiments. However, the median sediment grain size will not be as vastly different, and may even be the same in some cases. If the sediment grain size is scaled with the pipe diameter, the sediment will be so small that they will exhibit cohesive properties (i.e. for $d_{50} < 63$ μm), which are not characteristic of the sediment at its full scale [11]. In addition, even if non-cohesive sediments are used, the critical shear stress associated with the onset of sediment transport also differs significantly for different grain sizes [33, 34]. Therefore, it would be beneficial to consider the scale effects on scour beneath pipelines.

Based on the typical range of external diameters of subsea pipelines, the corresponding Reynolds numbers, *Re*, often range from 3×10^5 to 1.5×10^6 [6], whilst the range may be from 5×10^3 to 5×10^4 in laboratory experiments (e.g. [3, 8, 12]). A compilation of experimental data from various sources suggests that there is a slight decrease in the equilibrium scour depth when $10^5 < Re < 3 \times 10^5$ [9]. In addition, the scour process is also dependent on the upstream Shields parameter [9], which is a function of the flow velocity and sediment properties. With regards to the Shields parameter, there is a rapid increase in the equilibrium scour depth with the Shields parameter for the clear-water case, whilst the scour depth decreases with the Shields parameter for the live-bed case [23]. However, it is physically impossible to simultaneously maintain the upstream Shields parameter and the pipe Reynolds number while scaling, and hence there will be scale effects when one of the non-dimensional scaling parameters is ignored.

Table 2.4: Range of experimental conditions considered by previous researchers, listed in chronological order.

Reference	Pipe diameter (mm)	Median sediment grain size (mm)	Flow velocity (m/s)	Water depth (mm)
Ibrahim and Nalluri [25]; 1986	25, 50, 75	0.425, 0.80, 1.50	0.19 - 0.48 (current)	32 - 300
Mao [3]; 1986	50, 100	0.36	0.25 - 1.13 (current)	250, 350
Sumer and Fredsøe [9]; 1990	10, 20, 30, 50	0.18, 0.36, 0.58	0.099 - 3.23 (wave)	400
Chiew [15]; 1991	32, 50, 63	0.33, 0.61, 0.80, 1.70	N/A	50, 70, 100, 150, 180
Çevik and Yüksel [30]; 1999	32.3, 49, 77, 114	1.28	N/A	650
Dogan and Arisoy [29]; 2015	63, 90, 110	0.55, 1.85, 3.75	0.259 - 0.477 (wave)	650
Mohr *et al.* [12]; 2016	40	0.015, 0.025, 0.08, 0.12, 0.18, 0.19, 0.54	N/A	200
Zhang *et al.* [26]; 2016	50, 196	0.24, 0.60	0.09 - 1.10 (current) 0.22 - 0.80 (wave)	190, 1100

Table 2.4 presents a typical range of boundary conditions that have been considered by some researchers for investigating scour equilibrium; though it is unfortunate that the upstream current velocity is often not reported in these studies. Table 2.4 suggests that when the pipe diameter is large, there is a risk that the water depth would not be sufficient to minimise the

free surface effects. In addition, the influence of the pipe diameter on scour differs from the influence of the current velocity (discussed in Chapter 5). Thus, increasing the current velocity to have the same Reynolds number as in the full-scale condition may not be equivalent to having a larger pipe diameter. Therefore, a proper investigation involving a wider range of parameters is required to accurately quantify the influence of the Shields parameter and pipe Reynolds number on scour.

To date, scale effects have mainly been investigated numerically. Liang *et al.* [6] investigated the influence of having a computational domain that is eight times larger, whilst maintaining the upstream friction velocity, in which it is assumed that θ_∞ is held constant, and the Reynolds number had been increased due to having a larger pipe diameter. It was found that, for the same non-dimensional time-scale, the scour depth beneath the larger pipe is 10 to 15% shallower. Assuming that the influence of the change in water depth is negligible, and given that there is a sufficient amount of time for the scour profile to develop, a smaller scour depth can be expected for a larger pipe diameter. Interestingly, the time required to reach an equilibrium state at full-scale is predicted to be an order of magnitude longer (e.g. more than two days, if it takes one to a few hours at model-scale). Therefore, an equilibrium scour depth may not be achieved during a single extreme weather event if it did not occur for a sufficiently long period of time.

In terms of obtaining real-world measurements, limited field data have been published, with some notable exceptions involving the Australian North West Shelf [7, 35]. Pinna *et al.* [35] observed a higher number of free spans than expected, instead of having most of the pipe being buried. At a water depth of approximately 130 m, scour is mainly induced by tidal and soliton currents, instead of large storm events [7]. Interestingly, without the influence of surface gravity waves and storms in deep waters, scour developed in such a way where the most common distance between each span and percentage of the pipeline in a span remained relatively constant for about five years [7]. However, this may only be true at the Australian North West Shelf. To address this paucity of data, numerical modelling offers a practical alternative as the simulations can be performed at various scales.

2.2 Numerical modelling techniques

The preference for the use of numerical models to simulate scour has been growing as they can eliminate the need for scaling, which may be an issue for laboratory experiments. At present, the different methods used to model scour beneath pipelines can be categorised into: (1) single-phase models; (2) multi-phase models; and, (3) other less conventional methods such as machine learning algorithms.

2.2.1 Single-phase models

In terms of single-phase models, scour is mainly predicted via: (1) correlating the computed flow velocities around the pipe to the initiation of scour with a rigid seabed; or, (2) by having a deformable seabed. For both methods, the flow velocities are typically modelled using the Reynolds-averaged Navier-Stokes (RANS) approach and a two-equation linear eddy viscosity turbulence model (e.g. standard k-ε turbulence model [36]); the difference mainly lies in the way in which sediment transport is taken into account in different numerical models. The governing equations for the RANS approach are presented in Chapter 3.

2.2.1.1 Rigid seabed

The least computationally expensive technique is to calculate the shear stress acting on the seabed, τ_b, based on the computed friction velocity, u_*, via $\tau_b = \rho u_*^2$ [37]. Several numerical studies [38-42] have demonstrated that computational fluid dynamics (CFD) can be used to accurately model flow around a cylinder close to a flat bed; however, these studies did not focus on scouring around the pipe. Only a few studies have investigated the amplification of the seabed shear stress underneath a pipe due to flow amplification [5, 43]. The amplification factor, or the maximum seabed shear stress normalised by the upstream seabed shear stress, τ_{max}/τ_∞, is found to increase with a smaller e_o/D, whereby a higher amplification factor suggests a higher capacity for scour. However, having a high amplification factor would not necessarily lead to the occurrence of scour, where the maximum shear stress beneath the pipe had not exceeded the critical shear stress; further discussion on this matter can be found in Chapter 5. Therefore, in this work, the calculated seabed shear stress is converted into the

Shields parameter [34], to predict the initiation of scour. This involved comparing the predicted Shields parameter to the critical value for the particular sediment grain size.

Zang *et al.* [19] employed the two-dimensional RANS approach with the *k-ω* turbulence model to compute the flow velocity and pressure around a pipe with initial partial embedment, and modelled seepage flow beneath the pipe (Figure 2.1a) via Laplace's equation. This is made possible by first computing the pressure distribution along the seabed via RANS, which is then used as a boundary condition to calculate the pressure distribution within the seabed. A range of flow conditions have been considered to develop the equation which is presented in Table 2.1 for the prediction of scour onset around an initially embedded pipe due to currents and/or waves. Zang *et al.* [19] used the numerical model that is introduced in Zhao *et al.* [44], which appeared to be an in-house model. Nevertheless, these rigid seabed models are more appropriate for predicting the onset of scour, and are limited in terms of predicting the evolution of the seabed profile over time.

2.2.1.2 Deformable seabed

A deformable seabed or morphologic model (e.g. [6, 31, 45-48]) can be used to simulate the development of scour around subsea pipelines, but is more computationally intensive than a rigid seabed model. Figure 2.3 depicts a snapshot of a deforming mesh, as a result of the morphologic model employed in Liang *et al.* [48]. In brief, the elevation of the seabed is periodically updated based on the sediment transport rate, which is calculated based on the computed flow velocities. The flow velocities are typically computed via RANS, or the Large Eddy Simulation (LES) approach which involves a sub-grid scale model (e.g. Smagorinsky [49]), whilst the suspended and bed load transport rates are generally calculated using an additional transport equation (e.g. Exner equation [50]) and an empirical formula (e.g. [51]), respectively. The governing equations and numerical solution procedure may vary between different models; a review on morphologic models can be found in Sumer [52]. It is worth noting that this may resemble a quasi-two-phase model, wherein the suspended load transport is included; however, the fluid-particle and particle-particle interaction underneath the seabed are not considered.

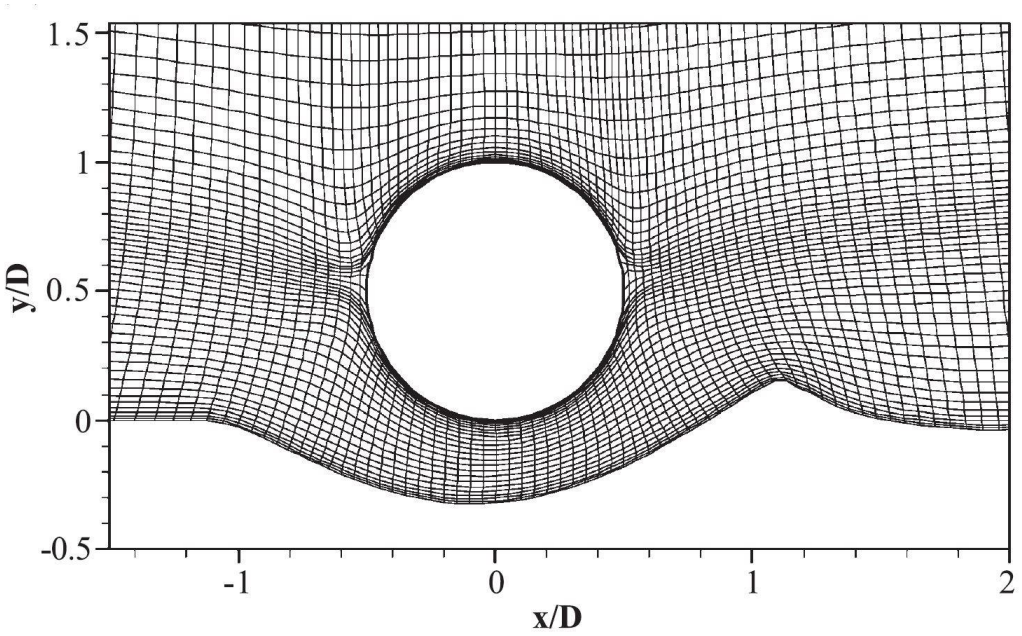

Figure 2.3: A snapshot of a deforming mesh, representing a scouring seabed beneath a pipe; figure extracted from Liang *et al.* [48].

Liang *et al.* [6] successfully implemented a sand slide model to avoid having slopes that exceed the angle of repose for the sediment, and investigated the influence of the pipe Reynolds number on the equilibrium scour depth. As mentioned in Section 2.1.4, the scour depth has been reported to be shallower for a larger Reynolds number, even for the same non-dimensional time-scale. More recently, a similar numerical model has also been employed to simulate wave-plus-current scour beneath pipelines [31]; however, these deformable seabed models neglect fluid-particle interaction and particle-particle interaction below the seabed. In addition, it seemed that an initial scour hole (e.g. 0.15D [31]) is usually required to successfully initiate the scour process. Therefore, it is hypothesised that multi-phase models may be more physically accurate as these interactions are taken into account. In addition, a two-phase model, which has been employed in this work, is shown to be practical, in terms of producing accurate predictions within a reasonable timeframe (discussed in Chapter 7).

2.2.2 Two-phase models

Two-phase models can be grouped into models that either use: (1) the Eulerian-Eulerian approach whereby the fluid phase and sediment phase are treated as inter-penetrating continua; or, (2) the Eulerian-Lagrangian approach, by which the motion of the fluid phase is

treated as a continuous medium, whilst the sediment phase is treated as a discrete phase by tracking the motion of individual sediment grains. There are also three-phase models, in which air, water, and sediment are considered for shallow water conditions (e.g. [53]). However, a three-phase model is not considered in this work to model scour in very shallow waters (e.g. $h/D < 2$), because scour beneath subsea pipelines is the primary focus in this work. Therefore, a two-phase Eulerian-Eulerian model is employed, in which the fluid phase is modelled as a Newtonian fluid with a constant viscosity, whilst the sediment phase is also modelled as a "fluid", but with a non-uniform viscosity; further details are presented in Chapter 3.

2.2.2.1 Eulerian-Eulerian models

An example of an output of a two-phase Eulerian-Eulerian model is shown in Figure 2.4, whereby tunnel erosion beneath a pipeline in a unidirectional flow is simulated. As seen in Figure 2.4, a non-dimensional volume fraction is used in Eulerian-Eulerian models to represent the dimensionless sediment concentration in every cell. The continuity and momentum equations for both the fluid phase and sediment phase are also typically solved using either the RANS or LES approach; though the models employed for turbulence modelling and the inter-phase momentum transfer would differ among different models. It seemed that the stresses of the sediment phase can either be modelled as: (1) a function of the sediment concentration, fluid properties and flow velocity (e.g. [54]); or, (2) via kinetic theory for granular flow [55]. The inter-phase momentum transfer is generally computed using an empirical drag model (e.g. [56]), since the drag force is the dominant contributor to the inter-phase momentum transfer term in dense fluid-solid systems [57]. A comprehensive review of CFD models for fluid-solid interaction is available in Van Wachem *et al.* [58].

Zhao and Fernando [59] appeared to be the first to use a two-phase model to simulate scour beneath a pipeline, whereby the stresses of the sediment phase are modelled using kinetic theory for granular flow. The Eulerian-Eulerian approach is employed, and the predicted equilibrium scour depth seemed to be in good agreement with the experimental measurement from Mao [3]. However, the scour depth has been over-predicted during the tunnel erosion stage, which is thought to be caused by having an initial gap between the pipe and the seabed at the beginning of the simulation to initialise the scour process. The gap is generated using a

sinusoidal function with an amplitude of 0.1*D*, whereas the pipe in the experiment [3] is bottom-seated (i.e. $e_o/D = 0$).

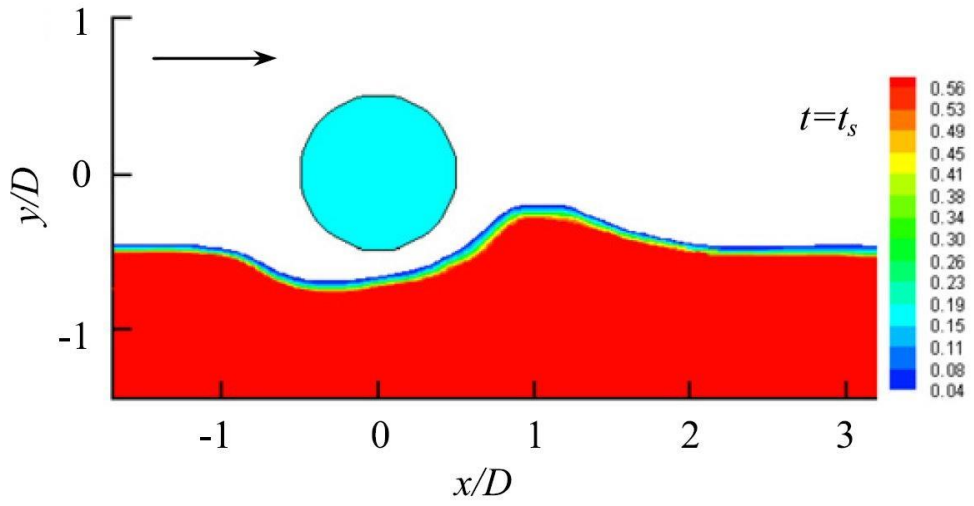

Figure 2.4: The seabed profile represented by the dimensionless sediment volume fraction during tunnel erosion, which is modelled using a two-phase Eulerian-Eulerian model with a steady current flowing from left to right; figure reproduced from Yeganeh-Bakhtiary *et al.* [60].

In addition, an unrealistic accumulation of sediment near the pipe has been reported in Zhao and Fernando [59] when the two-phase model is employed. Hence, a different numerical solution procedure has been implemented, in which the velocity of the fluid phase is first solved without the influence of the sediment, and the solution of the fluid phase is then used to calculate the resulting sediment motion. Nonetheless, the unrealistic accumulation of sediment near the pipe may be caused by the use of the frictional viscosity model from Schaeffer [61], which is developed for "quasi-static flow". Savage [62] stated that there are strain rate fluctuations which exist even in purely quasi-static flow, which will reduce the shear stress, but has not been considered in the model from Schaeffer [61]. It is hypothesised that this issue can be addressed by using the *JohnsonJacksonSchaeffer* frictional stress model [57], in which the frictional viscosity model proposed by Schaeffer [61] is combined with the normal frictional stress model from Johnson and Jackson [63]. This new model has been implemented in recent two-phase models for modelling sediment transport (e.g. [64]).

More recently, Yeganeh-Bakhtiary *et al.* [60] successfully simulated tunnel erosion underneath a pipeline using a two-phase Eulerian-Eulerian model (Figure 2.4). Several notable differences as compared to Zhao and Fernando [59] include: (1) only tunnel erosion

is modelled, and not scour equilibrium; (2) a "pure" two-phase calculation is performed, as opposed to constraining the sediment phase to first obtain a solution for the fluid velocities; (3) instead of adopting kinetic theory for granular flow, the inter-granular stresses are modelled as a function of the sediment concentration, fluid properties and flow velocity, where it seemed that the effects of the particle velocity fluctuations are ignored; (4) a fully-orthogonal mesh is used, which is trimmed at the surface of the pipe, and thus the boundary layer and flow separation may not be adequately modelled due to the non-uniform mesh around the pipe; and, (5) the initial seabed gap is smaller (i.e. one cell height), and the initial seabed profile is flat, instead of having a small sinusoidal profile beneath the pipe. A more accurate seabed profile during the tunnel erosion stage is predicted, and it is reported that having an initial sinusoidal profile has led to an over-predicted scour depth.

Unfortunately, it is unclear whether modelling scour equilibrium is not pursued due to a longer computation time, or the results would not be accurate. Furthermore, both Zhao and Fernando [59] and Yeganeh-Bakhtiary *et al.* [60] used the k-ε turbulence model [36] for the fluid phase, which is notorious for its poor performance in the near-wall region, and this would affect flow separation at the surface of the pipe. Therefore, in this work, a two-phase Eulerian-Eulerian model is employed, in which the k-ω SST turbulence model [65] is used for the fluid phase, while the *JohnsonJacksonSchaeffer* frictional stress model [57] is employed for the sediment phase; further details are presented in Chapter 3.

2.2.2.2 Eulerian-Lagrangian models

In regard to Eulerian-Lagrangian models, individual sediment grains can be included in the computational domain, and the trajectory of each grain would be calculated. For Eulerian-Eulerian models, the calculation of particle-particle interactions is influenced by the mesh resolution. Having the fluid phase represented by a continuous medium, and the sediment phase represented by Lagrangian particles, can potentially provide a more physically accurate solution. However, this also translates to longer computational run times and the need for an immensely larger amount of memory [66]. A well-written review on discrete particle simulations has been published in Zhu *et al.* [67].

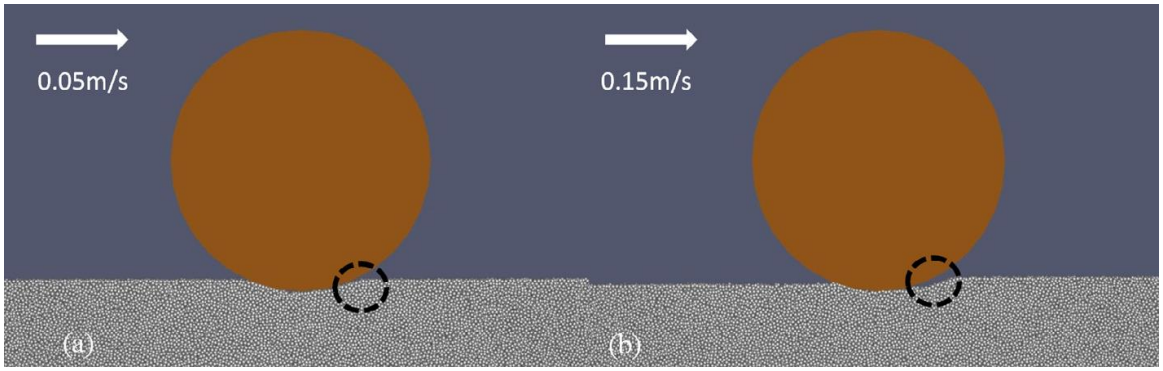

Figure 2.5: Piping at different upstream current velocities which is modelled using CFD-DEM; figure extracted from Zhang *et al.* [68].

Figure 2.5 depicts an example of an Eulerian-Lagrangian simulation of the onset of scour beneath a pipeline, where a coupled computational fluid dynamics-discrete element method (CFD-DEM) model [68] is employed. For this CFD-DEM model, turbulence associated with the fluid phase is modelled using the standard k-ε turbulence model [36], while the drag force acting on the particles is modelled using the drag model from Di Felice [69], and a linear spring model [70] is employed to account for inter-particle collisions. It is stated that periodic boundaries, which are parallel to the flow direction in Figure 2.5, had to be implemented in between 10 layers of particles, to limit the total number of particles in the simulation. When a particle exits one of the periodic boundaries, it would enter through the other periodic boundary which is on the opposite side of the domain. In addition, the computational time step had to be very small (i.e. 10^{-6} s), to ensure that every inter-particle collision is modelled whilst maintaining numerical stability.

Yeganeh-Bakhtiary *et al.* [66] successfully implemented a two-dimensional CFD-DEM model to predict scour equilibrium underneath a pipeline, wherein the particles are represented by rigid disks with uniform diameters. The particle diameter had been set to 2 mm, instead of 0.36 mm which is used in the experiment conducted in Mao [3]. This greatly reduced the number of particles needed (i.e. 6,240), as compared to having 110,000 particles in Zhang *et al.* [68]. However, the equilibrium scour depth had been under-predicted, which might be a result of having inaccurate sediment properties, or further calibration of the coefficients associated with DEM may be required. In a more recent study which involved models similar to that in Zhang *et al.* [68], Yang *et al.* [71] adopted a small computational domain and large sediment particle size (i.e. 1 mm in diameter) to reduce the computational

load. Scour would occur at the upstream edge of the sediment container, and this may affect the scour profile around the pipe when the computational domain is not sufficiently large (discussed in Chapter 7). Therefore, an Eulerian-Lagrangian model is not employed in this work because it might not be more accurate than Eulerian-Eulerian models, yet it requires more computational resources as compared to Eulerian-Eulerian models [72].

2.2.3 Less conventional models

This section describes the less conventional models which have been employed to model scour underneath pipelines. This discussion includes alternative modelling techniques such as the Lattice Boltzmann method and machine learning algorithms.

2.2.3.1 Lattice Boltzmann method (LBM)

The LBM is put into context because it has been employed to simulate general sediment transport via coupling with the aforementioned DEM (e.g. [73]), as well as scour below a pipeline (e.g. [74]). In brief, the LBM involves discretising the Boltzmann equation, which is a balance equation for fluid particle density, and is derived based on gas kinetic theory. It is worth noting that the aforementioned kinetic theory for granular flow is also derived from gas kinetic theory to model sediment particle collisions. The Boltzmann equation describes the evolution of a particle distribution function, which describes the probability of finding a fluid particle at a given space, velocity and time. This differs from the Navier-Stokes (NS) equation, as the NS equation is a balance equation for momentum, which is derived at the macroscopic scale; whereas the Boltzmann equation is derived based on a statistical description in between the microscopic and macroscopic scale (i.e. mesoscopic scale). Further information on the LBM can be found in Viggen [75].

The attention received by the LBM can be attributed to: (1) it supposedly describes fluid flow at a more detailed level (i.e. mesoscopic scale); and, (2) solvers based on the LBM (e.g. Palabos) may offer superior parallel efficiency as compared to solvers based on the NS equation (e.g. OpenFOAM). Alam and Cheng [74] utilised the LBM to model scour beneath a pipe, where a sample output is shown in Figure 2.6. The motion of the sediment particles is set to be governed by the critical Shields parameter. This model predicted an equilibrium

scour depth that matched Mao's [3] experimental measurement relatively well; however, the scour depth has been under-predicted at the early stages.

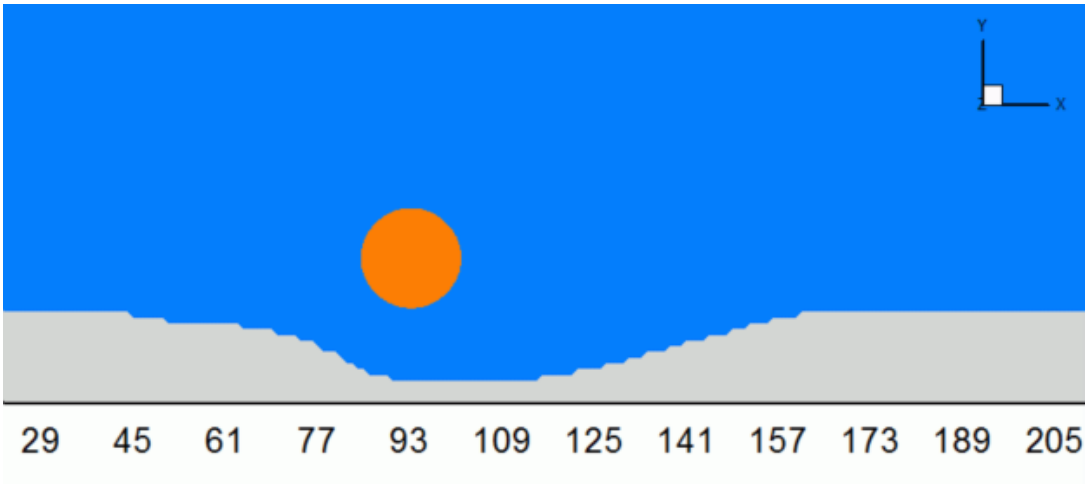

Figure 2.6: Equilibrium scour profile modelled using LBM; figure extracted from Alam and Cheng [74].

Unfortunately, the LBM is generally not favoured over the conventional NS-based approach, which could be due to the fact that turbulence is not a result of velocity fluctuations at the molecular level, but rather, a superposition of macroscopic bulks of the fluid (i.e. eddies) [76]. The LBM has been successfully implemented in simulating turbulent flow using graphics processing units (GPUs) (e.g. [77]). However, having the solution from an open channel flow as an initial condition significantly affected the outcome. Although the aforementioned two-phase Eulerian-Eulerian model employs kinetic theory for granular flow to describe inter-particle collisions, the mass and momentum equations for both the fluid phase and sediment phase are still solved based on the NS equation. It is also worth mentioning that recent comparisons [78, 79] have shown that NS-based solvers can be more efficient than LBM-based solvers. This is because the LBM typically involves transporting 9 variables for 2-D isothermal simulations, and 19 variables in 3-D; in contrast, conventional NS-based solvers only transport 3 variables for 2-D simulations and 4 variables for 3-D simulations. In summary, it appears that LBM-based solvers may be more appropriate when vast computational resources (e.g. large GPU clusters) are available, for performing transient scale-resolving simulations (e.g. Large Eddy Simulation), at the mesoscopic scale.

2.2.3.2 Machine learning algorithms

A machine learning algorithm (e.g. artificial neural network) is generally an algorithm that is used to make predictions via pattern recognition, filtering and so on, based on a large sample of data. Recent predictions of scour depths made by Najafzadeh *et al.* [80] displayed a high correlation coefficient based on comparisons with experimental data. The group method of data handling (GMDH) network is used to approximate the relations between several dimensionless parameters (e.g. dimensionless embedment depth) for scour prediction, based on published data. However, it appears that only data from two sources have been used to train the network. In addition, this method may only be appropriate for predicting a certain variable of interest; for example, the maximum scour depth, and not the profile of a scoured seabed. Further information on neural networks can be found in Maren *et al.* [81].

2.3 Research gaps and contributions of this thesis

In summary, scour prediction is of technical interest, because scour can lead to occurrences that may compromise the structural integrity of subsea pipelines (e.g. vortex-induced vibrations). However, previous work which focused on the influence of the pipe elevation on scour (e.g. the initiation of scour and the scour time scale) have been sparse. The influence of the pipe elevation had previously been considered for predicting the equilibrium scour depth. However, the experiments have only been conducted under live-bed conditions, and the influence of the Reynolds number had not been quantified. Furthermore, there is a paucity of published field data. Therefore, it will be beneficial to not only conduct more field investigations, but also to assess the applicability of numerical models to simulate scour.

Table 2.5 presents an overview of the aforementioned numerical modelling techniques. In general, single-phase models omit fluid-particle interaction and particle-particle interaction within the sediment layer; though they require less computational effort for performing large parametric studies. Multi-phase models account for more physical phenomena which enable the evolution of the seabed profile to be modelled, but consequently, require more computational resources. Therefore, the single-phase rigid seabed model is deemed to be practical for modelling the initiation of scour, whilst the two-phase Eulerian-Eulerian model is deemed to be practical for modelling the development of scour. Other less conventional

methods such as artificial neural networks may only be appropriate when large datasets are available for training the network.

Table 2.5: Brief comparison of different scour modelling techniques.

Model type	Fluid-sediment interaction	Particle-particle interaction	Computational effort	Brief comments
Rigid seabed	No	No	Less demanding	Appropriate for modelling scour onset
Deformable seabed	Limited	No	Demanding	Less physically accurate than two-phase models
Eulerian-Eulerian	Yes	Yes	Demanding	Results may be affected by mesh resolution
Eulerian-Lagrangian	Yes	Yes	Very demanding	Might not be more accurate than Eulerian-Eulerian models
LBM-based	Possible	Possible	Very demanding	May be less computationally efficient than NS-based models
Machine learning algorithms	Depends on input data	Depends on input data	Less demanding	Require very large datasets to obtain meaningful results

In this thesis, a novel combination of field, experimental and numerical investigations is used, to predict the initiation, equilibrium depth and time scale of scour beneath elevated subsea pipelines. The field investigation is conducted to collect seabed gap data for a pipeline, to identify the range of detected seabed gaps beneath the pipeline. Sediment flume experiments are conducted to measure the equilibrium scour depths and scour time scales for a range of initial pipe elevations. A single-phase rigid seabed model is used to predict the initiation of scour beneath pipelines with a small initial elevation from the seabed by calculating the maximum seabed shear stress beneath the pipe. A two-phase Eulerian-Eulerian model is then employed to simulate the development of scour beneath elevated pipelines, whereby the implementation of this open-source solver, *twoPhaseEulerFoam*, for this application is new.

The result of the aforementioned studies, with the consideration of key variables of interest (i.e. θ_∞, Re and e_0/D), is the development of new empirical formulae for the prediction of the initiation, equilibrium depth and time scale of scour. As the influence of the pipe elevation on the initiation of scour and scour time scale has not been considered in existing formulae, the formulae proposed in this thesis are the first to account for the effects of e_0/D. Although this has been taken into account in terms of predicting the equilibrium scour depth, the formula

proposed in this thesis considers the effects of θ_∞ and *Re*, which is shown to be an improvement (i.e. via attaining a higher correlation coefficient) to existing formulae where these effects have not been considered.

Chapter 3
Methodology

This chapter provides a general description of the main methods which have been employed in this work. The methods involved a combination of experimental, numerical, and field investigations. In addition to the data collected via the aforementioned investigations, experimental data from published literature have also been compiled. As a result, this enabled the development of new empirical formulae for predicting: (1) the maximum seabed shear stress beneath the pipe; (2) the equilibrium scour depth; and, (3) the scour time scale, for elevated subsea pipelines under steady currents.

3.1 Laboratory experiments

Laboratory experimentation can be considered as the primary method in this work. Experiments have been conducted in a sediment flume to study the effects of the pipe elevation on the development of scour beneath the pipe. In addition, experiments have also been conducted in a circulating water channel, which involved measuring the flow between a pipe and a flat plate, mainly for validating a numerical model that was used in this work.

3.1.1 Sediment flume

Experiments were conducted in a sediment flume with a test section of 6.82 m in length, 0.46 m in width, and 0.61 m in depth at the University of California, Davis, to investigate the effects of the pipe elevation, e_o/D, on the equilibrium scour depth and scour time scale. A sketch of a cross-section of the sediment flume, which had an open top section, is shown in Figure 3.1. A steady flow would enter the flume from a tank, which was located at a height of about 15 m, via gravity, whereby the flow rate and water depth were controlled by the

opening and the height of the tailgate. A 2.62 m long and 0.15 m deep sandbox, which was filled with Cemex #0/30 sand with a median grain size, d_{50}, of approximately 0.52 mm, was supported by 6 mm-thick Perspex which were attached to the bottom and sides of the flume.

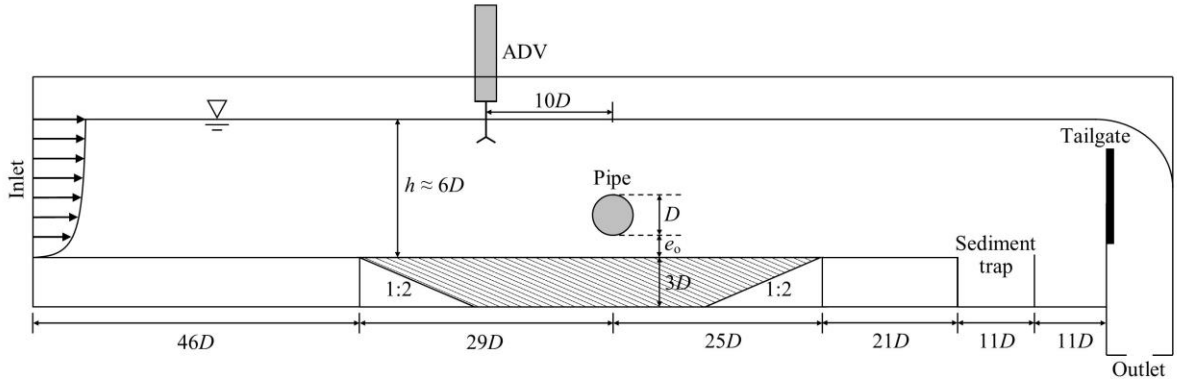

Figure 3.1: Sketch of the sediment flume experimental setup, where the external pipe diameter, *D*, is 48 mm.

A smooth PVC pipe with an external diameter, *D*, of 48 mm and thickness of 2 mm was rigidly positioned at various elevations above the sand bed. The pipe was positioned sufficiently far downstream from the inlet to ensure that the flow is fully developed when it encountered the pipe. The development of the scour depth directly beneath the vertical centreline of the pipe was measured using a transparent 30 cm ruler with an accuracy of ±1 mm. A Panasonic Lumix DMC-GF1 camera was set to capture the scour process every second, where the accuracy of the scour time scale measurement was estimated to be ±1 s. In addition, the scour depths have also been manually recorded every two minutes for the first ten minutes, and then every five minutes until the scour depth only deepens by 1 mm or less. Similar to Mohr *et al.* [12], the scour depth was observed to be slightly deeper at the side walls of the flume. Therefore, the scour depths at the middle of the pipe have been recorded, instead of the scour depths at the side walls, to remove this boundary effect.

The flow velocities were measured using a Nortek Vector Current Meter, which is an ADV that relies on the Doppler effect, at a rate of 32 Hz; further details on ADVs can be found in Voulgaris and Trowbridge [82]. With reference to Figure 3.1, the ADV was placed 10*D* upstream from the pipe to measure the flow velocities at various heights for every test case. The mean stream-wise flow velocities were attained by averaging the velocities, which were

recorded for over one minute, and were found to agree well with the law of the wall; further discussions can be found in Chapter 6. The accuracy for water velocity measurements was reported to be ±0.5% of the measured value, whilst the temperature sensor had an accuracy of ±0.1 °C [83]. As tap water was used with a mean water temperature of approximately 22 °C, hence the water density, ρ, and kinematic viscosity, ν, were taken to be 997.7735 kg/m^3 and 9.5653 × 10^{-7} m^2/s, respectively [84]. The results that were obtained using this sediment flume are presented in Chapter 6.

3.1.2 Circulating water channel

Flow experiments were conducted in a circulating water channel (CWC) of 17.2 m in length, 5.0 m wide and 2.5 m deep at the University of Tasmania, to investigate the flow velocity between a pipe and a flat bed. This was primarily done to validate a single-phase numerical model, which is used to compute the maximum seabed shear stress on a flat seabed in the vicinity of a pipe; further details on this numerical model are presented in a subsequent section of this chapter. The maximum seabed shear stress is used to predict the conditions pertaining to the initiation of scouring of the flat seabed underneath the elevated pipe, while the sediment flume experiments mentioned in Section 3.1.1 are focused on the development of the scour hole beneath the pipe.

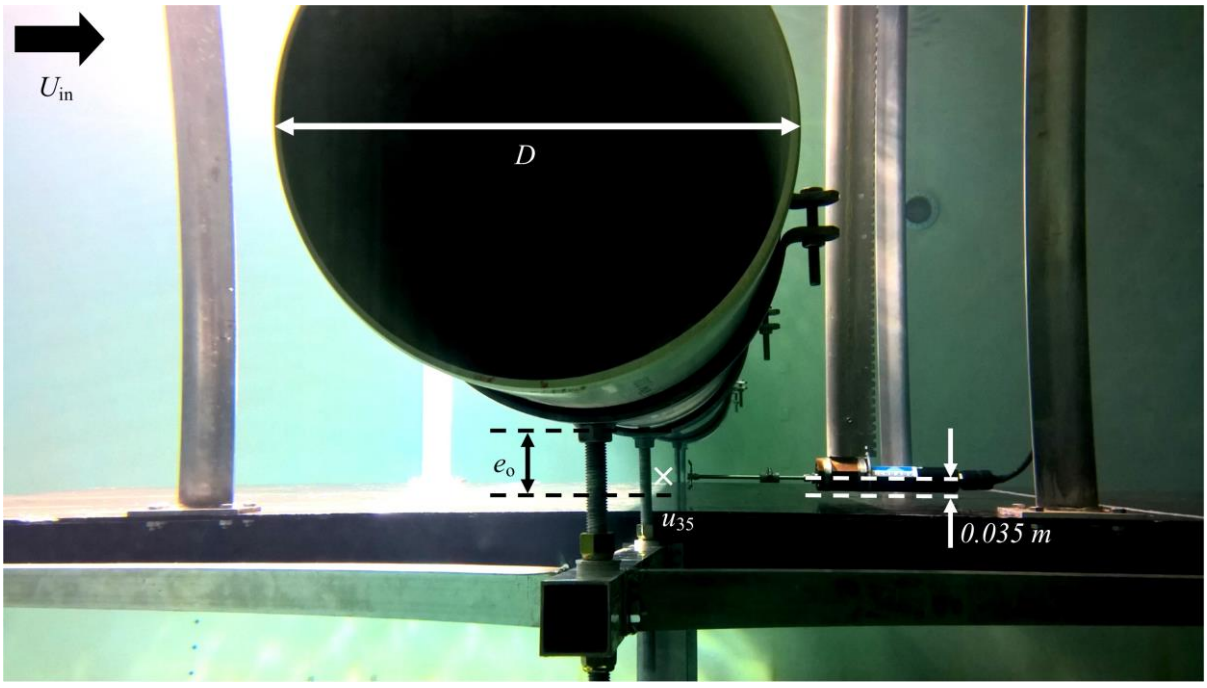

Figure 3.2: Angled cross-stream view of the CWC experimental setup.

Figure 3.2 presents an angled side view of the experimental setup, which is slightly distorted, especially at the edges, due to light refraction off the glass. A PVC pipe 4 m in length with an external diameter, D, of 0.3 m and thickness of 0.005 m is elevated by 0.1 m (i.e. $e_o/D = 1/3$) above a 3.15 m long, 1.70 m wide and 0.003 m thick aluminium flat plate. The vertical centreline of the pipe is placed on the centreline of the flat plate, thus being 1.6 m from the leading edge of the plate (i.e. more than 5D). The test rig was situated in the middle of the CWC and bolted to the walls.

The flow velocity beneath the centreline of the pipe was measured using a Sontek Acoustic Doppler Velocimeter (ADV) at 0.035 m above the flat plate, and at a rate of 50 Hz. The ADV probe has an acoustic transmitter and three receivers, 9×10^{-8} m^3 sampling volume, 1×10^{-4} m/s resolution, and an accuracy of 1% of measured velocity [85]. The ADV probe was located slightly downstream, and thus the receivers are positioned at 0.05 m downstream from the vertical centreline of the pipe. This was done to ensure that the flow velocity at 0.035 m above the flat plate, u_{35}, is measured within the sampling volume.

The incoming current velocities, U_{in}, were determined based on a calibration curve derived prior to the experiments. During the calibration process, the ADV was placed several metres upstream of the pipe to measure the incoming flow velocity for a range of pump revolution speeds. The vertical level at which U_{in} was measured in the circulating water channel was approximately equal to the vertical height of the centreline of the pipe. It is also worth noting that due to physical limitations, it was not possible to directly measure the shear velocity, u_*, or have a smaller pipe elevation; this was one of the motivations for adopting a numerical model to model flow and scour beneath pipelines with small pipe elevations. The results that were obtained using this circulating water channel are presented in Chapter 4.

3.2 Numerical modelling

Numerical modelling was another significant part of this work, as it offered an alternative to laboratory experiments, which was particularly beneficial in terms of investigating scale effects. Based on the literature review in Chapter 2, a single-phase fixed seabed model was employed to compute the maximum seabed shear stress beneath the pipe, whilst a two-phase Eulerian-Eulerian model was utilised to simulate the development of scour beneath the pipe.

The aim of adopting a single-phase model to calculate the seabed shear stress for a flat seabed, was for predicting the initiation of scour, where the maximum seabed shear stress can be compared to the critical shear stress. In terms of the evolution of the seabed profile due to scour, the two-phase Eulerian-Eulerian model was required to simulate the fluid-particle and interparticle interactions.

3.2.1 Single-phase model

In regard to fundamental sediment transport, the classic Shields parameter, θ, is commonly used to predict the initiation of sediment transport, as well as to categorise different regimes of sediment transport. The Shields parameter is a non-dimensional representation of the seabed shear stress, τ_b, which is calculated using Eq. (3.1) [34]:

$$\theta = \frac{\tau_b}{(\rho_s - \rho) g d_{50}} \tag{3.1}$$

where ρ_s is the particle density; ρ is the fluid density; g is gravitational acceleration; and, d_{50} is the median sediment grain size. By the same token, one can assume that, when the local maximum Shields parameter underneath a pipeline, θ_{max}, exceeds the equivalent of the critical Shields parameter for a given median grain size, θ_{cr}, then the occurrence of scour beneath the pipe can be expected. A wide range of θ_{cr} values for different median grain sizes are available in literature (e.g. [33, 34, 86]). Furthermore, it can also be calculated using Eq. (3.2) [87]:

$$\theta_{cr} = \frac{0.30}{1+1.2D_*} + 0.055\left[1 - \exp\left(-0.02D_*\right)\right] \tag{3.2}$$

where D_*, which is the dimensionless form of the sediment grain size, can be calculated using Eq. (3.3) [87]:

$$D_* = \left[\frac{g(s-1)}{\nu^2}\right]^{1/3} d_{50} \tag{3.3}$$

where s is the specific gravity of the sediment and ν is the kinematic viscosity of the liquid.

In this work, the seabed shear stress, τ_b, was calculated from the friction velocity, u_*, via $\tau_b = \rho u_*^2$ [37]. The velocities of the fluid flowing over a rough seabed were computed using a CFD solver, STAR-CCM+ V10 [37], whereby the Reynolds-averaged form of the single-phase incompressible isothermal continuity and momentum equations were solved:

$$\nabla \cdot U = 0 \tag{3.4}$$

$$\frac{\partial U}{\partial t} + \nabla \cdot (UU) = -\frac{1}{\rho}\nabla P + \nabla \cdot (\nu \nabla U) - \overline{U'U'} \tag{3.5}$$

where U is the mean velocity; P is the dynamic pressure; and, the Reynolds stress tensor, $\overline{U'U'}$, represents the velocity fluctuations about the mean value, which was modelled via the Boussinesq approximation [88]:

$$-\overline{U'U'} = \nu_t \left(\nabla U + (\nabla U)^T\right) - \frac{2}{3}k\mathrm{I} \tag{3.6}$$

where ν_t is the kinematic eddy viscosity; the superscript in Eq. (3.6), T, indicates a transpose; k is the turbulent kinetic energy; and, I is an identity matrix. In this case, a linear eddy viscosity model was employed to solve ν_t as a function of k, and the turbulence frequency or specific dissipation rate, ω. The k-ω Shear Stress Transport (SST) turbulence model [65] was used because it performs well for complex flows which involve separation [89]. The k-ω SST model combines the k-ω model [90], which is adequate for modelling boundary layer flow, and the k-ε model [36], which is appropriate for the fully-turbulent region outside of the boundary layer. The k-ω SST model has been shown to accurately model turbulent flow around a cylinder (e.g. [91]), as well as flow around a wall-mounted cylinder (e.g. [39]). The latest formulation of the k-ω SST model is given as [92]:

$$\frac{\partial(\rho k)}{\partial t} + \nabla \cdot (\rho U k) = P_k - \beta^* \rho k \omega + \nabla \cdot \left[(\mu + \sigma_k \mu_t)\nabla k\right] \tag{3.7}$$

$$\frac{\partial(\rho\omega)}{\partial t}+\nabla\cdot(\rho U\omega)=\frac{\alpha}{\nu_{\mathrm{t}}}P_{\mathrm{k}}-\beta\rho\omega^{2}+\nabla\cdot\left[(\mu+\sigma_{\omega}\mu_{\mathrm{t}})\nabla\omega\right]+2(1-F_{1})\frac{\rho\sigma_{\omega 2}}{\omega}\nabla k\nabla\omega \quad (3.8)$$

$$\alpha=\alpha_{1}F_{1}+\alpha_{2}(1-F_{1}) \quad (3.9)$$

$$\nu_{\mathrm{t}}=\frac{a_{1}k}{\max(a_{1}\omega,S_{\mathrm{m}}F_{2})} \quad (3.10)$$

$$P_{k}=\min\left(\mu_{\mathrm{t}}\nabla U\cdot\left(\nabla U+(\nabla U)^{T}\right),10\beta^{*}\rho k\omega\right) \quad (3.11)$$

$$F_{1}=\tanh\left\{\left\{\min\left[\max\left(\frac{\sqrt{k}}{\beta^{*}\omega y},\frac{500\nu}{y^{2}\omega}\right),\frac{4\rho\sigma_{\omega 2}k}{CD_{\mathrm{k}\omega}y^{2}}\right]\right\}^{4}\right\} \quad (3.12)$$

$$F_{2}=\tanh\left[\left[\max\left(\frac{2\sqrt{k}}{\beta^{*}\omega y},\frac{500\nu}{y^{2}\omega}\right)\right]^{2}\right] \quad (3.13)$$

$$CD_{\mathrm{k}\omega}=\max\left(2\rho\sigma_{\omega 2}\frac{1}{\omega}\nabla k\nabla\omega,10^{-10}\right) \quad (3.14)$$

where the fluid density, ρ, is held constant due to incompressibility; y is the distance to the nearest wall; and, S_{m} is an invariant measure of the strain rate, which is the square root of the double inner product of the mean strain rate tensor, S_{ij}:

$$S_{\mathrm{m}}=\sqrt{2S_{\mathrm{ij}}S_{\mathrm{ij}}} \quad (3.15)$$

$$S_{\mathrm{ij}}=\frac{1}{2}(\nabla\cdot U) \quad (3.16)$$

where the subscripts, i and j, are spatial indices. The blending functions, F_1 and F_2, are set to unity inside the boundary layer to activate the original k-ω model, and becomes zero for the

region outside of the boundary layer to activate the *k*-ε model. The values of the constants are presented in Table 3.1.

Table 3.1: Values of the constants in the *k*-ω SST model [92].

β^*	α_1	β_1	σ_{k1}	$\sigma_{\omega1}$	α_2	β_2	σ_{k2}	$\sigma_{\omega2}$
0.09	5/9	0.075	0.85	0.5	0.44	0.0828	1.0	0.856

In terms of taking the seabed roughness into account, STAR-CCM+ [37] adopted an approach for defining a rough wall boundary condition which is similar to that in Yoon and Patel [93], wherein the specific dissipation rate, ω, for a rough surface is [94]:

$$\omega = \frac{u_*^2 S_r}{\nu} \tag{3.17}$$

where S_r, which is a strain rate parameter, is calculated via:

$$S_r = \begin{cases} \left(\frac{50}{R^+}\right)^2 \; if \; 5 \le R^+ \le 25 \\ \left(\frac{100}{R^+}\right) if \; 25 \le R^+ \end{cases} \tag{3.18}$$

where R^+ is a roughness parameter, which is defined as:

$$R^+ = \frac{r u_*}{\nu} \tag{3.19}$$

whereby r is the equivalent sand-grain roughness height. This roughness height was estimated through a combination of the following assumptions: (1) the flow is hydrodynamically rough [87], and hence $r = k_s/30$, where k_s is the Nikuradse roughness; and subsequently, (2) $k_s = 2.5 d_{50}$ (see Soulsby and Humphery [95] for further details). u_* is computed iteratively, whereby a 'reference velocity' is first specified via [37]:

$$u_* = \sqrt{g\nu u / y + (1-g)\beta^{*1/2} k} \tag{3.20}$$

where the blending function, $g = \exp(-Re_y/11)$, is dependent on the wall-distance-based Reynolds number, Re_y, which is calculated via $Re_y = (k)^{1/2}y/\nu$; u is the velocity parallel to the wall. With the k-ω SST turbulence model selected, the kinematic eddy viscosity, ν_t, is calculated based on the turbulent kinetic energy, k, and the specific dissipation rate, ω. This would influence the final computed flow velocities, as ν_t is used to model the Reynolds stress tensor, $\overline{U'U'}$, in the momentum equation.

In summary, the Reynolds averaged Navier-Stokes (RANS) approach was employed to model flow over a rough seabed using the k-ω SST turbulence model, to calculate the maximum Shields parameter underneath the pipe, θ_{max}. When $\theta_{max} > \theta_{cr}$, then scour can be expected to occur. Further information on the numerical solution procedure can be found in CD-adapco [37]. The results that were obtained using this single-phase CFD model are presented in Chapter 4 and Chapter 5.

3.2.2 Two-phase model

The aforementioned single-phase model offers a direct correlation between the flow velocities and the initiation of scour, as well as relatively good computational efficiency for large parametric studies. However, it lacks the ability to describe fluid-particle interaction and particle-particle interaction. Therefore, a two-phase Eulerian-Eulerian model was employed (i.e. *twoPhaseEulerFoam*), by which both phases are treated as inter-penetrating continua. This native OpenFOAM solver is commonly used for modelling fluidised bed reactors involving gas-particle flow (e.g. [96]), and more recently, for modelling scour [97]. In this work, *twoPhaseEulerFoam* in OpenFOAM v1612+ was adopted. It is worth mentioning that this two-phase Eulerian-Eulerian model, which accounts for inter-particle stresses, was not available in STAR-CCM+. Although STAR-CCM+ has an Eulerian-Lagrangian model (i.e. CFD-DEM), it was not employed due to the high computational cost, as a high number of particles would be required; this matter was discussed in Chapter 2.

The RANS approach was also employed, and the continuity equations for the fluid phase and sediment phase, respectively, are [98]:

$$\frac{\partial\left(\alpha_{\mathrm{f}}\rho_{\mathrm{f}}\right)}{\partial t}+\nabla\cdot\left(\alpha_{\mathrm{f}}\rho_{\mathrm{f}}U_{\mathrm{f}}\right)=0 \tag{3.21}$$

$$\frac{\partial\left(\alpha_{\mathrm{s}}\rho_{\mathrm{s}}\right)}{\partial t}+\nabla\cdot\left(\alpha_{\mathrm{s}}\rho_{\mathrm{s}}U_{\mathrm{s}}\right)=0 \tag{3.22}$$

where α is the volume fraction or phase concentration, ρ is the density of the phase, and U is the mean velocity, for which the subscripts, f and s, denote the fluid phase and sediment phase, respectively. The volume fractions have the following relationship, whereby $\alpha_{\mathrm{f}} + \alpha_{\mathrm{s}} = 1$. This solver is originally implemented based on incompressible equations from Rusche [99]; however, in newer versions of OpenFOAM (i.e. version 2.3.0 and above), the flow is deemed to be compressible with the addition of heat transfer models. Nonetheless, both the fluid density and particle density were held constant in this work, and heat transfer was neglected.

The momentum equations for the fluid phase and sediment phase, respectively, are:

$$\frac{\partial\left(\alpha_{\mathrm{f}}\rho_{\mathrm{f}}U_{\mathrm{f}}\right)}{\partial t}+\nabla\cdot\left(\alpha_{\mathrm{f}}\rho_{\mathrm{f}}U_{\mathrm{f}}U_{\mathrm{f}}\right)=-\alpha_{\mathrm{f}}\nabla P_{\mathrm{a}}+\nabla\cdot\left(\alpha_{\mathrm{f}}\tau_{\mathrm{f}}\right)+\alpha_{\mathrm{f}}\rho_{\mathrm{f}}g-K_{\mathrm{gs}}\left(U_{\mathrm{f}}-U_{\mathrm{s}}\right) \tag{3.23}$$

$$\frac{\partial\left(\alpha_{\mathrm{s}}\rho_{\mathrm{s}}U_{\mathrm{s}}\right)}{\partial t}+\nabla\cdot\left(\alpha_{\mathrm{s}}\rho_{\mathrm{s}}U_{\mathrm{s}}U_{\mathrm{s}}\right)=-\alpha_{\mathrm{s}}\nabla P_{\mathrm{a}}+\nabla\cdot\left(\alpha_{\mathrm{s}}\tau_{\mathrm{s}}\right)-\nabla P_{\mathrm{s}}+\alpha_{\mathrm{s}}\rho_{\mathrm{s}}g+K_{\mathrm{gs}}\left(U_{\mathrm{f}}-U_{\mathrm{s}}\right) \tag{3.24}$$

where the pressure, P_{a}, is the absolute pressure which is shared among both phases, and is different from the dynamic pressure shown in Eq. (3.5) wherein only the pressure difference mattered. τ_{f} is the combined Reynolds and viscous stress for the fluid phase, for which the Reynolds stress was modelled using the aforementioned Boussinesq approximation, but with the flow being treated as a compressible flow in this case [99]:

$$\tau_{\mathrm{f}}=\mu_{\mathrm{f}}^{\mathrm{eff}}\left(\nabla U_{\mathrm{f}}+\left(\nabla U_{\mathrm{f}}\right)^{\mathrm{T}}-\frac{2}{3}\left(\nabla\cdot U_{\mathrm{f}}\right)\mathrm{I}\right)-\frac{2}{3}\rho_{\mathrm{f}}k_{\mathrm{f}}\mathrm{I} \tag{3.25}$$

where the "effective viscosity" of the fluid phase, $\mu_f^{eff} = \mu_f + \mu_t$; μ_f is the dynamic viscosity of the fluid, and μ_t is the dynamic turbulent viscosity which was modelled using the aforementioned *k-ω* SST turbulence model.

K_{gs} is the inter-phase momentum transfer term, which was modelled using the *WenYu* [56] drag model:

$$K_{gs} = \frac{3}{4} C_D \frac{(1-\alpha_s)\alpha_s \rho_f |U_f - U_s|}{d_s} (1-\alpha_s)^{-2.65} \tag{3.26}$$

where d_s is the particle diameter, which is assumed to be equal to d_{50}, and the drag coefficient, C_D, is calculated via:

$$C_D = \begin{cases} \dfrac{24}{Re_p (1-\alpha_s)} \left[1 + 0.15 \left((1-\alpha_s) Re_p \right)^{0.687} \right], & \text{if } (1-\alpha_s) Re_p < 1{,}000 \\ 0.44, & \text{if } (1-\alpha_s) Re_p \geq 1{,}000 \end{cases} \tag{3.27}$$

in which the particle Reynolds number, Re_p, was calculated using:

$$Re_p = \frac{d_s \rho_f |U_f - U_s|}{\mu_f} \tag{3.28}$$

The *WenYu* [56] drag model was selected because it is derived based on multiple experimental datasets, that of their own as well as from other sources, of settling solid particles in a liquid, wherein a wide range of sediment volume fractions (i.e. $0.01 \leq \alpha_s \leq 0.63$) have been considered.

In the momentum equation for the sediment phase, Eq. (3.24), there is a shear stress tensor, τ_s, as well as a solids pressure or granular particle pressure, P_s. These terms were derived based on the kinetic theory for granular flow. It appeared that the *kineticTheory* model in *twoPhaseEulerFoam* has primarily been coded based on the Ph.D. thesis of van Wachem [72].

The shear stress tensor was modelled via:

$$\tau_s = \mu_s\left(\nabla U_s + \left(\nabla U_s\right)^T\right) + \left(\lambda_s - \frac{2}{3}\mu_s\right)\left(\nabla \cdot U_s\right)\mathrm{I} \tag{3.29}$$

where μ_s is the shear viscosity, and λ_s is the bulk viscosity.

The granular particle pressure, P_s, which represents the normal forces due to particle-particle interactions, was calculated using the *Lun* granular pressure model [55]:

$$P_s = \rho_s \alpha_s \Theta + 2 g_0 \rho_s \alpha_s^2 \Theta\left(1+e\right) \tag{3.30}$$

where Θ is the 'granular temperature', which is introduced to account for the particle velocity fluctuations. The first term in Eq. (3.30) represents the effective stresses in the sediment phase due to particle streaming or propagation through the fluid (i.e. kinetic contribution); the second term represents the contribution due to collisions, wherein e is the coefficient of restitution for the sediment particles, which is set to 0.91 [100]. g_0 is the radial distribution function, for which the *SinclairJackson* [101] radial distribution function was used:

$$g_0 = \left[1 - \left(\frac{\alpha_s}{\alpha_{s,max}}\right)^{\frac{1}{3}}\right]^{-1} \tag{3.31}$$

where the maximum particle packing limit, $\alpha_{s,max}$, was set to 0.62, because the *WenYu* drag model is only applicable for sediment volume fractions up to 0.63. It is worth noting that the *SinclairJackson* [101] radial model has been reported to tend toward the correct limit at closest packing [58].

The granular temperature, Θ, was calculated via the following transport equation [58]:

$$\frac{3}{2}\left[\frac{\partial\left(\alpha_s \rho_s \Theta\right)}{\partial t} + \nabla \cdot \left(\alpha_s \rho_s U_s \Theta\right)\right] = \left(-P_s \mathrm{I} + \tau_s\right) : \nabla U_s + \nabla \cdot \left(\kappa_s \nabla \Theta\right) - \gamma_s - J_s \tag{3.32}$$

wherein the first term on the right-hand side of Eq. (3.32) represents the generation of fluctuating energy due to shear in the sediment phase; the second term represents the

diffusion of the fluctuating energy along the gradient of Θ. It is worth mentioning that, in Van Wachem *et al.* [58], there are two typographical errors: (1) the granular particle pressure, P_s, is incorrectly presented as ∇P_s; and, (2) the second term on the right-hand side (i.e. the laplacian term) had a minus sign, instead of a plus sign.

κ_s is the thermal conductivity of granular energy, and the thermal conductivity model from Gidaspow [102] was employed:

$$\kappa_s = 2\alpha_s^2 \rho_s d_s g_0 (1+e)\sqrt{\frac{\Theta}{\pi}} + \frac{9}{8}\sqrt{\Theta\pi}\rho_s d_s g_0 \left(\frac{1}{2}+\frac{e}{2}\right)\alpha_s^2 + \frac{15}{16}\sqrt{\Theta\pi}\alpha_s \rho_s d_s + \frac{25}{64}\sqrt{\Theta\pi}\frac{\rho_s d_s}{(1+e)g_0} \tag{3.33}$$

The thermal conductivity model describes the conductivity of granular energy, which also accounts for the kinetic contribution and the collision contribution. It is worth mentioning that a comparison of different models showed that they predicted the same thermal conductivity at high sediment volume fractions [58] (i.e. $\alpha_s > 0.3$), and hence the selection of a thermal conductivity model was not expected to significantly influence the results.

γ_s is the dissipation rate of granular energy due to inelastic particle-particle collisions, and can be modelled via [55]:

$$\gamma_s = 12(1-e^2)\frac{\alpha_s^2 \rho_s g_0}{d_s\sqrt{\pi}}\Theta^{\frac{3}{2}} \tag{3.34}$$

J_s is the dissipation or generation rate of granular energy due to interaction with the fluid phase, and it was calculated via the following equation [103]:

$$J_s = \beta\left(3\Theta - \frac{\beta d_s (U_f - U_s)^2}{4\alpha_s \rho_s \sqrt{\pi\Theta}}\right) \tag{3.35}$$

In regard to the shear viscosity, μ_s, which is introduced in Eq. (3.29), the *Gidaspow* [102] shear viscosity model was selected:

$$\mu_s = \frac{4}{5}\alpha_s^2 \rho_s d_s g_0 (1+e)\sqrt{\frac{\Theta}{\pi}} + \frac{1}{15}\sqrt{\Theta\pi}\rho_s d_s g_0 (1+e)\alpha_s^2 + \frac{1}{6}\sqrt{\Theta\pi}\rho_s d_s \alpha_s + \frac{10}{96}\sqrt{\Theta\pi}\frac{\rho_s d_s}{(1+e)g_0} \tag{3.36}$$

wherein the first term on the right-hand side of Eq. (3.36) represents the collisional contribution, and the rest represents the kinetic contribution to the shear viscosity of the sediment phase. Similar to the thermal conductivity model, although there are several shear viscosity models available, they would all yield the same shear viscosity at high sediment volume fractions [58].

The bulk viscosity, λ_s, was modelled via [55]:

$$\lambda_s = \frac{4}{3}\alpha_s^2 \rho_s d_s g_0 (1+e)\sqrt{\frac{\Theta}{\pi}} \tag{3.37}$$

where there is general agreement on the use of the aforementioned model to describe the resistance of the particle suspension against compression.

When the sediment volume fraction is high (e.g. $\alpha_s > 0.5$), it will be necessary to consider the frictional stresses between the particles due to multi-particle contact, because the assumption that particle collisions are instantaneous no longer hold true [104]. In *twoPhaseEulerFoam*, additional frictional stresses are simply added to the stresses predicted via kinetic theory when the sediment volume fraction exceeds a threshold value, $\alpha_{s,min}$, and thus the total stresses were calculated via:

$$P_{s,new} = P_s + P_{fric} \tag{3.38}$$

$$\mu_{s,new} = \mu_s + \mu_{fric} \tag{3.39}$$

where P_{fric} and μ_{fric} represent the normal frictional stress and frictional shear viscosity, respectively. They were computed using the *JohnsonJacksonSchaeffer* frictional stress model [57]:

$$P_{\text{fric}} = 0.1\alpha_{\text{s}} Fr_{\text{j}} \frac{\left(\alpha_{\text{s}} - \alpha_{\text{s,min}}\right)^{eta}}{\left(\alpha_{\text{s,max}} - \alpha_{\text{s}}\right)^{p}} \tag{3.40}$$

$$\mu_{\text{fric}} = \frac{P_{\text{fric}}\sqrt{2}\sin\phi_{\text{fric}}}{2\sqrt{S_{\text{s}} : S_{\text{s}} + \frac{\Theta}{d_{\text{s}}^2}}} \tag{3.41}$$

where Fr_{j}, *eta*, and *p* are constants, and they were set to 0.05, 2, and 5, respectively; φ_{fric} is the angle of internal friction; and, S_{s} is the strain rate for the sediment phase:

$$S_{\text{s}} = \frac{1}{2}\left(\nabla U_{\text{s}} + \left(\nabla U_{\text{s}}\right)^{\text{T}}\right) - \frac{1}{3}\left(\nabla \cdot U_{\text{s}}\right)\text{I} \tag{3.42}$$

As mentioned in Section 2.2.2.1, the *JohnsonJacksonSchaeffer* frictional stress model combines the frictional viscosity model proposed by Schaeffer [61] and the normal frictional stress model from Johnson and Jackson [63].

For the sake of completeness, the energy equations for the fluid phase and sediment phase, respectively, are [105]:

$$\frac{\partial\left(\alpha_{\text{f}}\rho_{\text{f}}C_{\text{hf}}T_{\text{f}}\right)}{\partial t} + \nabla\cdot\left(\alpha_{\text{f}}\rho_{\text{f}}C_{\text{pf}}T_{\text{f}}U_{\text{f}}\right) = \nabla\cdot q_{\text{f}} - h_{\text{gs}}\left(T_{\text{f}} - T_{\text{s}}\right) \tag{3.43}$$

$$\frac{\partial\left(\alpha_{\text{s}}\rho_{\text{s}}C_{\text{hs}}T_{\text{s}}\right)}{\partial t} + \nabla\cdot\left(\alpha_{\text{s}}\rho_{\text{s}}C_{\text{hs}}T_{\text{s}}U_{\text{s}}\right) = \nabla\cdot q_{\text{s}} + h_{\text{gs}}\left(T_{\text{f}} - T_{\text{s}}\right) \tag{3.44}$$

where C_{h} is the heat capacity for the phase; *T* is the phase's temperature; h_{gs} is the inter-phase heat transfer coefficient; and, *q* is the conductive heat flux. The inter-phase heat transfer coefficient is typically modelled using the *RanzMarshall* heat transfer model [106]. Nevertheless, heat transfer was neglected in this work, and the energy equations were not solved by setting the maximum number of iterations to zero in the *fvSolution* dictionary.

Table 3.2: Summary of the selected models and constants for *twoPhaseEulerFoam*.

Model/constant	Selection/value
Fluid phase closure	*kOmegaSST* [65]
Sediment phase closure	*kineticTheory* [72]
Drag model	*WenYu* [95]
Granular temperature transport equation	Eq. (3.32) [58]
Shear viscosity model	*Gidaspow* [102]
Thermal conductivity of granular energy model	*Gidaspow* [102]
Coefficient of restitution, e	0.91 [100]
Granular particle pressure model	*Lun* [55]
Radial distribution function	*SinclairJackson* [101]
Maximum particle packing limit, $\alpha_{s,max}$	0.62
Frictional stress model	*JohnsonJacksonSchaeffer* [57]
Threshold for friction, $\alpha_{s,min}$	0.50 [100]
Constant in Eq. (3.40), Fr_j	0.05 (N/m^2) [100]
Constant in Eq. (3.40), *eta*	2 [100]
Constant in Eq. (3.40), p	5 [100]
Angle of internal friction, φ_{fric}	28.5^o [100]

In summary, the models and constants selected for performing two-phase simulations are presented in Table 3.2. Further information on the numerical solution procedure can be found in Rusche [99], while a comprehensive review on kinetic theory models and is presented in Van Wachem *et al.* [58]. The results that were obtained using *twoPhaseEulerFoam* are presented in Chapter 7.

3.3 Field investigation

A field survey was conducted for the southernmost 5 km section of the Tasmanian Gas Pipeline (TGP), off the Northern Tasmanian coast in South Eastern Australia (Figure 3.3a). The TGP transports natural gas across the Bass Strait with an offshore section over 300 km long, and has an annual capacity of 47 PJ [107] (see Table 3.3 for the design parameters and operating conditions). The field survey was conducted to obtain the following:

- Ensemble-averaged water column velocities at 50 m east of the pipeline
- Median grain size of the sediment in the vicinity of the surveyed site
- Approximated maximum seabed gaps or seabed gaps of each span along the surveyed pipe length

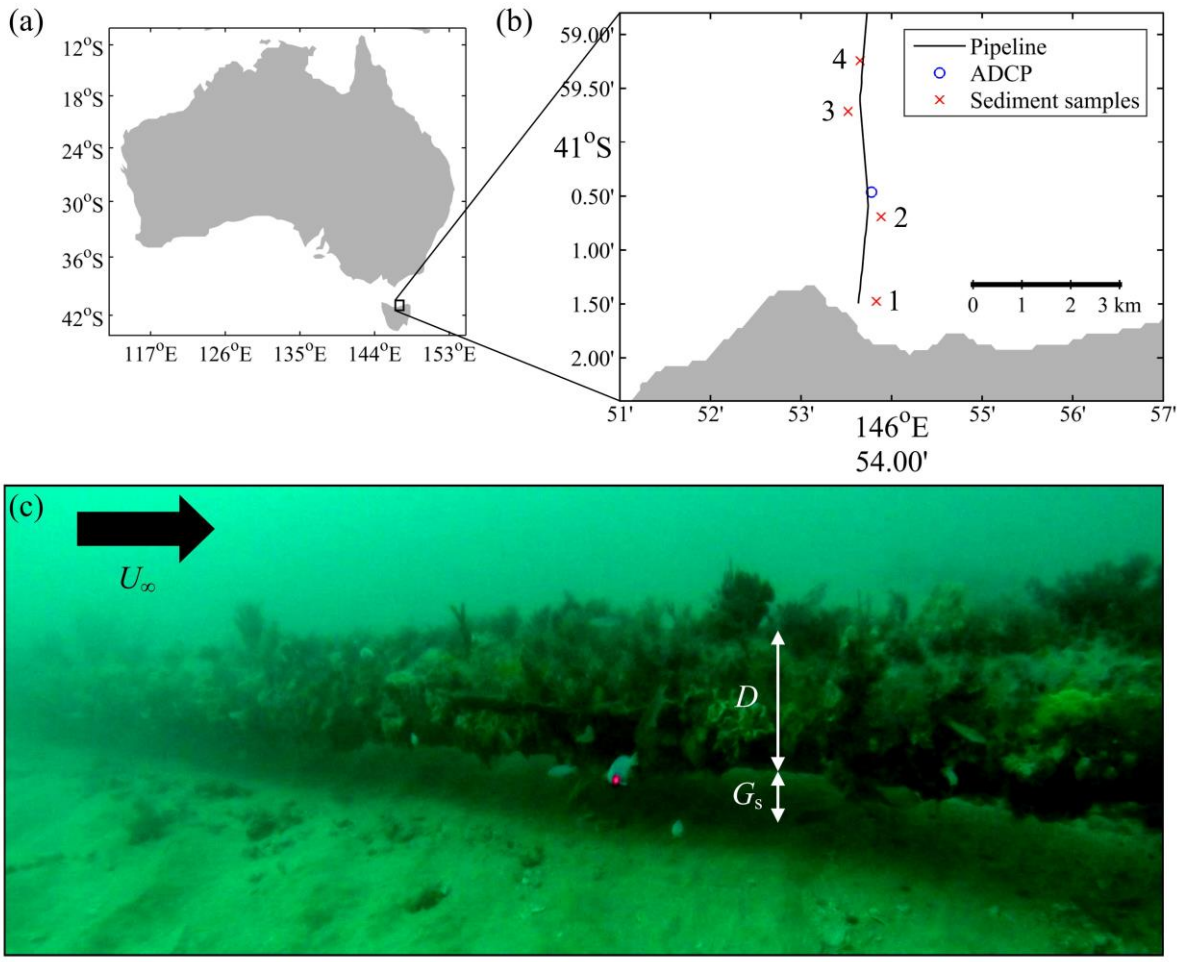

Figure 3.3: (a) Surveyed site location with respect to Australia plotted using the Miller projection. (b) Location of a near-shore stretch of the Tasmanian Gas Pipeline (TGP), acoustic Doppler current profiler (ADCP) mooring and sediment sampling points. (c) Snapshot of Remotely Operated Vehicle (ROV) footage obtained while conducting a visual inspection of the TGP at several kilometres off the coast of Northern Tasmania in May 2015. The key parameters here are the upstream flow velocity, U_∞, the seabed gap, G_s, and the external pipe diameter, D.

A Teledyne Sentinel V 500 kHz 4-beam Acoustic Doppler Current Profiler (ADCP) was deployed at a location 50 m east of the pipeline (Figure 3.3b), at which the average water depth was found to be approximately 23 m. The key ADCP profile settings were: 25 m range, 0.50 m cell size, 50 cells and 1.0 m blanking distance. The resolution and accuracy were 0.001 and ±0.003 m s^{-1} respectively [108]. Transient water column velocity data over a period of eight days (i.e. from 25 May 2015 4:53:38 UTC to 2 June 2015 22:28:38 UTC) had been ensemble-averaged over five-minute intervals.

A total of four sediment samples have been collected within safe distances from the TGP (Figure 3.3b), as recommended by the pipeline operator. A Large Ekman Bottom Grab sediment sampler with dimensions of 0.23 m × 0.23 m × 0.23 m was used to collect the sediment samples. The sediments were oven-dried, and subsequently, filtered through a set of sieves on a sieve shaker. The amount of sediment in each sieve was then measured to produce a particle size distribution curve for each sample. A median particle size, d_{50}, was then estimated from the particle size distributions. The d_{50} was used to calculate the Nikuradse roughness, k_s, and subsequently, the associated seabed roughness height, z_o, to be incorporated in the CFD computations which are performed in Chapter 4.

Video footage of the TGP was obtained using a SeaBotix LBV300 explorer class Remotely Operated Vehicle (ROV) (Figure 3.3c). Several key parameters for this field investigation are the seabed gap, G_s, external pipe diameter, D, and the upstream flow velocity, U_∞, which was measured at 2 m above the seabed. Due to physical constraints, the lowest elevation from the seabed at which the velocity can be measured was 1.5 m. This is due to the 0.5 m clearance between the seabed and the top of the ADCP that was attached to an anchored steel frame, in addition to the ADCP's 1.0 m blanking distance.

Table 3.3: Design parameters and operating conditions of the Tasmanian Gas Pipeline [107].

Parameter	Details
Pipeline length	301.6 km
External diameter	355.6 mm
Pipe wall thickness	11.1 mm
Pipe wall thickness (shore crossing)	12.7 mm
Nominal concrete weighted coating	38 mm
Grade	X65
Maximum Allowable Operating Pressure (MAOP)	15.3 MPa(g)
Offshore pipeline average design temperature	13 °C
Marine sediment type	Fine and medium grained quartzose sands
Median grain size	0.12 to 0.25 mm
Current speeds during 5 year return period storms	0.30 and 0.79 m/s
Current speeds during 100 year return period storms	0.41 to 1.03 m/s

A Gavia Scientific Autonomous Underwater Vehicle (AUV) with a 500 kHz Kongsberg GeoAcoustics GeoSwath+ interferometric sonar module was employed to produce acoustic backscatter images of the TGP and the seabed. This was primarily done to identify and geo-reference free spans, and to approximate the maximum seabed gaps along the 5 km stretch of the TGP. Interferometric sonar exploits the phase of the reflected sound waves (i.e. acoustic

return) and the return range, to estimate the position of the reflector (see Gostnell and Yoos [109] for further details). Further details regarding the application of acoustic backscatter imagery are presented in McInerney *et al.* [110]. Although a Global Positioning System (GPS) receiver is unreliable underwater [111], with a Kearfott T-24 Inertial Navigation System (INS) on board the AUV, the position drift is less than 0.1% of the distance travelled [112]. Therefore, there is a high level of confidence in the accuracy of the survey data. The field data are presented in Chapter 4.

3.4 Summary

Field measurements were obtained to gauge the incidence of small seabed gaps beneath the Tasmanian Gas Pipeline. Laboratory experiments were conducted in a circulating water channel to investigate flow velocities beneath an elevated pipe, whilst sediment flume experiments were conducted to investigate the effects of the pipe elevation on the equilibrium scour depth and the scour time scale. A single-phase numerical model was used to predict the occurrence of scour beneath pipelines with small elevations, whilst a two-phase numerical model was used to take a closer look at multiphase modelling, and to simulate the development of scour. Based on the results, new empirical formulae were proposed for the prediction of two-dimensional current-induced scour beneath elevated pipelines, where the development of these equations is described in the subsequent chapters.

Chapter 4

Scour beneath pipelines with small elevations[1]

In this chapter, field measurements are obtained to gauge the incidence of small seabed gaps between the Tasmanian Gas Pipeline and the seabed, for which a higher capacity for scour to occur underneath the pipe can be expected. The small seabed gaps are assumed to be equivalent to small pipe elevations, as the seabed is observed to be relatively flat. Subsequently, two-dimensional full-scale computational fluid dynamics (CFD) simulations are performed using the Reynolds-averaged Navier–Stokes approach and the Shear Stress Transport k-ω turbulence model, to model steady flow around the Tasmanian Gas Pipeline with small elevations, upon attaining a good agreement between model-scale CFD data and experimental data. A significant incidence of small seabed gaps is observed from the field data. The computed maximum seabed shear stress is found to increase in a relatively linear fashion with the upstream seabed shear stress, but decrease in a non-linear fashion as the pipe was raised higher from the bed. As existing formulae for predicting the occurrence of scour are only applicable to partially embedded pipelines, an equation is developed to predict the dimensionless maximum seabed shear stress beneath the pipe, which can be compared with the critical shear stress, to estimate the occurrence of scour beneath the pipe with a small elevation.

[1] A version of this chapter has been published as: Lee, J. Y., McInerney, J., Cossu, R., Leong, Z. Q., & Forrest, A. L. (2017). Predicting scour beneath subsea pipelines from existing small free span depths under steady currents. *Journal of Ocean Engineering and Science*, 2(2), 61-75. DOI: 10.1016/j.joes.2017.03.001.

4.1 Introduction

Subsea pipelines transport oil or natural gas across vast distances along the seabed. The marine sediment beneath the pipeline can be eroded by current and/or wave action. Sediment erosion, commonly referred to as scour, can lead to free span formation in the vicinity of a subsea pipeline [1]; however, the time required to reach an equilibrium scour depth in the field is much longer than storm periods [6]. Thus, a pipeline may have multiple spans with small seabed gaps (defined as $G_s/D < 0.3$ in this work) upon experiencing strong currents. Furthermore, when a pipeline is laid on an uneven seabed, certain sections may have an initial elevation with respect to the far-field seabed.

Small pipe elevations (i.e. $e_o/D < 0.3$) are of interest because shear stress amplification is higher at smaller gaps [5]. Scour can occur when flow is accelerated underneath the pipe, which will widen and deepen existing free spans. Free spans can be permanent [113], and rectification works are often required (e.g. installing grout bags), where the risk of vortex-induced vibration causing fatigue is high. In addition, installing grout bags, which are relatively large, under a pipeline with a small seabed gap is often impractical. Therefore, it is necessary to predict the occurrence of scour beneath a pipeline with existing small seabed gaps, G_s, or an elevation with respect to the far-field seabed, e_o.

In this chapter, a small seabed gap is assumed to be equivalent to a small pipe elevation for practical purposes, as the seabed is observed to be relatively flat based on the field investigation (Figure 3.3c). Computational fluid dynamics (CFD) simulations are performed to compute the local maximum seabed shear stress beneath the pipe for small elevations and a range of current velocities. An equation is fitted to the full-scale CFD results, which can be used to calculate the maximum dimensionless seabed shear stress beneath the pipeline, based on the upstream dimensionless shear stress and pipe elevation ratio. The predicted maximum shear stress can then be compared to the critical shear stress for the median sediment grain size, to predict whether scour will occur.

4.2 Methods

The main results were obtained using the single-phase numerical model which was described in Chapter 3. Field measurements were obtained to provide supplementary data to perform the CFD simulations, while experimental data provide a benchmark for CFD modelling; further details on the field investigation and laboratory experiments can be found in Chapter 3. A trend line equation was then fitted to the full-scale CFD data, which can be used to predict the occurrence of scour beneath the Tasmanian Gas Pipeline (TGP) in areas with small pipe elevations.

4.2.1 Numerical computations

A finite-volume-method-based CFD solver, STAR-CCM+ V10, was used to compute the mean flow velocities around a pipe close to a flat seabed, using the 2-D RANS approach and the k-ω SST turbulence model. There were three stages in regard to CFD modelling: (1) verification was completed to estimate the numerical uncertainty; (2) comparisons between model-scale CFD and experimental data from the CWC experiments and Jensen *et al.* [114] were conducted; and, (3) a full-scale computational domain was employed, where an external pipe diameter of 0.5 m was used, representing the TGP, and all cases were within the bound of $e_o/D < 0.3$, where periodic vortex shedding in the wake of the pipe has not been observed in previous experiments [3, 17].

4.2.1.1 Boundary conditions

A large 2-D computational domain was employed for the simulation cases (Figure 4.1). A block-structured approach was adopted to generate the computational grids (a sample grid is highlighted in blue). As the seabed appeared to be relatively flat based on the ROV footage (Figure 3.3c), it was assumed, for simplicity, to be flat in the CFD simulations as well. In addition, a small seabed gap, G_s, was assumed to be equivalent to a small pipe elevation, e_o. For the full-scale simulations, the inlet and outlet boundaries were set to 100D away from the pipe to minimise artificial blockage effects. However, for the model-scale simulations, the dimensions of the computational domain was set to match the CWC experiments and that of Jensen *et al.* [114], to account for certain flow features such as the bed boundary layer

thickness. The water depth, h, was set to a large value, where $h = 101D + 0.28D$. h was also held constant for all full-scale cases to maintain the far field conditions (e.g. inlet velocity profile) for different values of e_o.

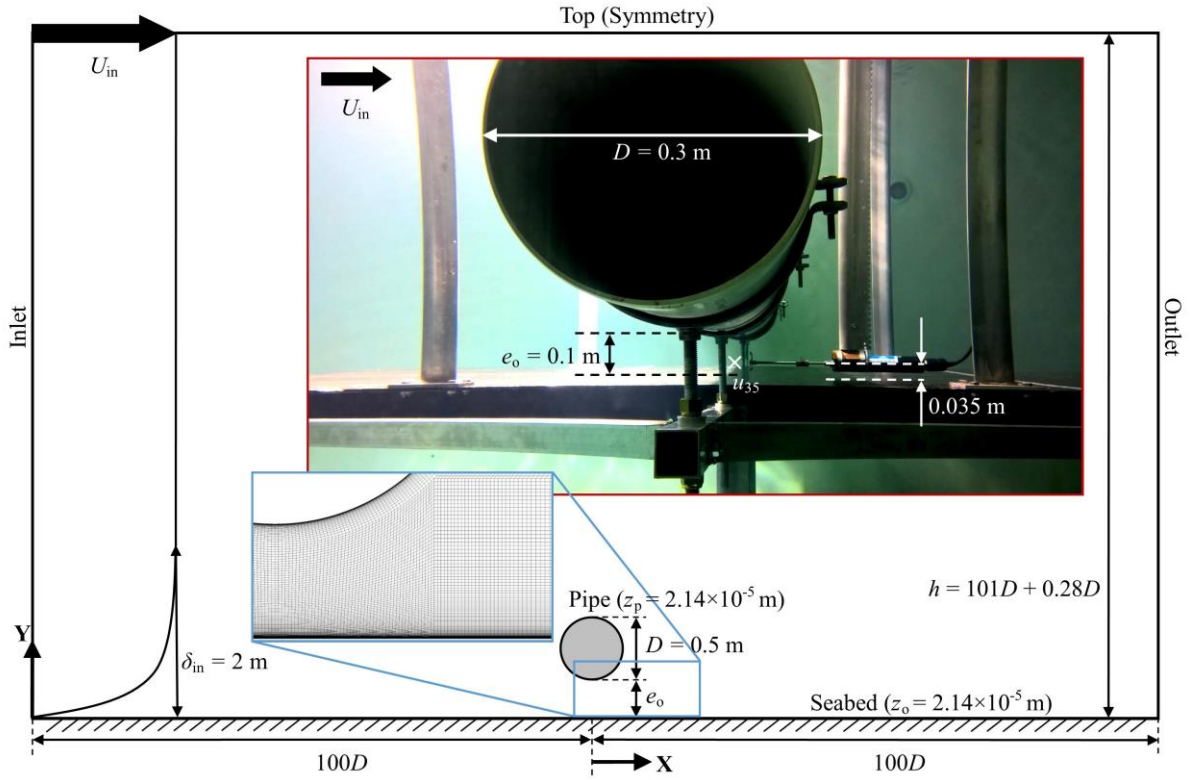

Figure 4.1: Angled cross-stream view of the circulating water channel (CWC) experimental setup shown in a red box, within a schematic diagram illustrating the full-scale domain employed for CFD computations. A close-up view of the mesh between the pipe and the seabed, for $e_o/D = 0.28$, is shown in a blue box.

The inlet velocity profile was defined using Eq. (4.1) [87]:

$$U_x(y) = \frac{u_*}{\kappa} \ln\left(\frac{y}{z_o}\right) \tag{4.1}$$

where U_x is the stream-wise flow velocity; $\kappa = 0.4$ is the von Kármán constant [87]; y is the elevation from the seabed; the incoming boundary layer thickness, δ_{in}, is set to 2 m for all cases; and, z_o is the bed roughness height. Therefore, at $z \geq 2$ m, the inlet velocity, U_{in}, would be equivalent to the free-stream velocity. Previous studies [19, 38] have demonstrated that, although the dimensionless inlet boundary layer thickness, δ_{in}/D, has a significant effect on

the flow field around the pipe, it diminishes when $\delta_{in}/D > 1$ [38]. Thus, as δ_{in} = 2 m in this case, which means that $\delta_{in}/D = 4$, its effects are negligible; moreover, it is also expected to be large in the field. As the average water temperature recorded by the ADCP is 14°C, a seawater density, ρ, of 1026.236 kg/m^3 and fluid kinematic viscosity, ν, of 1.2205 × 10^{-6} m^2/s was used [84].

The turbulent quantities such as the turbulence kinetic energy, k, and the specific turbulence dissipation rate, ω, were calculated by STAR-CCM+ using the specified turbulence intensity, I_t, and turbulent viscosity ratio, μ_t/μ. A constant inlet turbulence intensity, I_t, of 1% was applied, as well as a turbulent viscosity ratio, μ_t/μ, of 10, which were the values recommended by STAR-CCM+ while using the k-ω SST model. As the pipe and seabed were set to be rough walls, was specified using the method presented in Section 3.2.1.

Table 4.1: Boundary conditions employed for the CFD computations

Boundary	Parameter	Condition/Value
Inlet	Stream-wise velocity	$U_x(y) = \frac{u_*}{\kappa}\ln\left(\frac{y}{z_o}\right)$ for $z_o \le y \le \delta_{in}$ $U_x(y) = U_{in}$ for $y > \delta_{in}$
	Cross-stream velocity	$U_y(y) = 0$
	Turbulence intensity	I_t = 1%
	Turbulent viscosity ratio	μ_t/μ = 10
	Turbulence kinetic energy	Calculated
	Specific turbulence dissipation rate	Calculated
Outlet	Gauge pressure	0 Pa
	Turbulence intensity	I_t = 1%
	Turbulent viscosity ratio	μ_t/μ = 10
	Turbulence kinetic energy	Calculated
	Specific turbulence dissipation rate	Calculated
Pipe	Shear stress specification	No-slip
	Turbulence kinetic energy	Calculated
	Specific turbulence dissipation rate	$\omega = \frac{u_*^2 S_r}{\nu}$
Seabed	Shear stress specification	No-slip
	Turbulence kinetic energy	Calculated
	Specific turbulence dissipation rate	$\omega = \frac{u_*^2 S_r}{\nu}$
Top	Shear stress specification	Symmetry plane

The outlet boundary was assigned as a pressure outlet, at which the relative pressure was set to zero. The turbulence intensity and turbulent viscosity ratio were kept similar to that as specified at the inlet boundary. The top boundary was assigned as a symmetry plane, whereby

the shear stress is zero, and the velocity and pressure were extrapolated from the adjacent cells.

The seabed roughness height was estimated via a combination of the following assumptions: (1) the flow is hydrodynamically rough [87], and hence $z_o = k_s/30$, where k_s is the Nikuradse roughness; and subsequently, (2) $k_s = 2.5d_{50}$ (see Soulsby and Humphery [95] for further details). Assuming that the median particle size is 0.257 mm, $z_o \approx 2.14 \times 10^{-5}$ m, which is close to $z_o = 2.08 \times 10^{-5}$ m for $d_{50} = 0.25$ mm with reference to Det Norske Veritas [115], and hence these assumptions are assumed to be reasonable. d_{50} was assumed to be 0.257 mm because that was the mean value which was obtained from the field investigation (Figure 4.3). As for modelling the CWC and Jensen *et al.*'s [114] experiments, the seabed was defined as a smooth boundary because a smooth bottom was used in the experiments.

Surface roughness was taken into account for both the seabed and the pipe in the CFD computations. The pipe roughness height, z_p, was assumed to be the same as the bed roughness height (i.e. $z_p \approx 2.14 \times 10^{-5}$ m), which represents an un-coated steel pipe [116] for simplicity. This does not represent the effects of marine growth on the pipe. Nevertheless, previous experimental results [9] showed that increasing the pipe roughness from smooth to $z_p/D = 0.1$ did not influence the scour profile.

The test conditions for the main full-scale CFD simulations are listed in Table 4.2, corresponding to the TGP with an external diameter of 0.5 m. Three pipe elevation ratios were investigated, whereby small e_o/D ratios (i.e. $e_o/D < 0.3$) are of interest. A small pipe elevation was assumed to be equivalent to a small seabed gap, G_s, as the seabed was seen to be relatively flat (Figure 3.3c). The lower end of the velocity range corresponds to the mean flow velocity recorded by the ADCP, which translates to a very low upstream dimensionless seabed shear stress (i.e. $\theta_\infty < \theta_{cr}$). The middle range corresponds to the maximum velocity recorded by the ADCP, while the higher end corresponds to the current speeds occurring during 100 year return period storms [107].

Table 4.2: Parameters considered for the main numerical simulations performed at full-scale.

Pipe elevation ratio, e_o/D	External pipe diameter, D (m)	Seabed roughness height, z_o (m)	Pipe roughness height, z_p (m)	Current velocity, U_{in} (m/s)
0.07	0.5	2.14×10^{-5}	2.14×10^{-5}	0.05
0.07	0.5	2.14×10^{-5}	2.14×10^{-5}	0.10
0.07	0.5	2.14×10^{-5}	2.14×10^{-5}	0.20
0.07	0.5	2.14×10^{-5}	2.14×10^{-5}	0.40
0.07	0.5	2.14×10^{-5}	2.14×10^{-5}	0.80
0.14	0.5	2.14×10^{-5}	2.14×10^{-5}	0.05
0.14	0.5	2.14×10^{-5}	2.14×10^{-5}	0.10
0.14	0.5	2.14×10^{-5}	2.14×10^{-5}	0.20
0.14	0.5	2.14×10^{-5}	2.14×10^{-5}	0.40
0.14	0.5	2.14×10^{-5}	2.14×10^{-5}	0.80
0.14	0.5	1.00×10^{-5}	2.14×10^{-5}	0.10
0.14	0.5	1.00×10^{-6}	2.14×10^{-5}	0.10
0.14	0.5	2.14×10^{-5}	1.00×10^{-5}	0.10
0.14	0.5	2.14×10^{-5}	1.00×10^{-6}	0.10
0.28	0.5	2.14×10^{-5}	2.14×10^{-5}	0.05
0.28	0.5	2.14×10^{-5}	2.14×10^{-5}	0.10
0.28	0.5	2.14×10^{-5}	2.14×10^{-5}	0.20

4.2.1.2 Verification and validation

Verification was performed to estimate the numerical uncertainty associated with the CFD simulations, by observing the changes in the computed results with an increase in the number of cells (i.e. spatial resolution of the grid in the *x* and *y* directions). The grid was refined by increasing the number of grid points surrounding the pipe by a factor of 2, which was followed by the adjacent grid lines and refinement around the seabed. The test conditions of the grid independence study are presented in Table 4.3. The maximum seabed shear stress beneath the pipe, τ_{max}, was used as a reference to observe the influence of grid refinement.

Table 4.3: Test matrix for the grid independence study.

Grid nodes on pipe	Number of cells	Pipe elevation, e_o/D	Pipe diameter, D (m)	Seabed roughness, z_o (m)	Pipe roughness, z_p (m)	Inlet velocity, U_{in} (m/s)
200	44,860	0.14	0.5	2.14×10^{-5}	2.14×10^{-5}	0.20
400	148,758	0.14	0.5	2.14×10^{-5}	2.14×10^{-5}	0.20
800	494,306	0.14	0.5	2.14×10^{-5}	2.14×10^{-5}	0.20

The generalised Richardson extrapolation method was employed to estimate the numerical error, $\delta^*_{RE_{k_1}}$ [117-121]:

$$\delta^*_{\mathrm{RE}_{\mathrm{k}_1}} = \frac{\varepsilon_{\mathrm{k}_{21}}}{r_{\mathrm{k}}^{p_{\mathrm{k}}} - 1} \tag{4.2}$$

where p_{k}, the order of accuracy, was calculated via:

$$p_{\mathrm{k}} = \frac{\ln\left(\varepsilon_{\mathrm{k}_{32}} / \varepsilon_{\mathrm{k}_{21}}\right)}{\ln\left(r_{\mathrm{k}}\right)} \tag{4.3}$$

wherein $\varepsilon_{\mathrm{k}_{21}}$ is the difference between the result computed using a 'fine' mesh and a 'medium' mesh; $\varepsilon_{\mathrm{k}_{32}}$ is the difference between the result computed using a 'medium' mesh and a 'coarse' mesh; and, r_{k} is the grid refinement ratio.

Subsequently, the numerical uncertainty or, more specifically, the grid uncertainty, U_{G}, was estimated via [117-119]:

$$U_{\mathrm{G}} = \begin{Bmatrix} \left[9.6\left(1-C_{\mathrm{k}}\right)^2 + 1.1\right]\left|\delta^*_{\mathrm{RE}_{\mathrm{k}_1}}\right|, & \left|1-C_{\mathrm{k}}\right| < 0.125 \\ \left[2\left|1-C_{\mathrm{k}}\right| + 1\right]\left|\delta^*_{\mathrm{RE}_{\mathrm{k}_1}}\right|, & \left|1-C_{\mathrm{k}}\right| \geq 0.125 \end{Bmatrix} \tag{4.4}$$

which is valid when C_{k} is larger than unity [117-119]. C_{k} is a correction factor, which has been included to account for the effects of higher-order terms, and it was estimated using:

$$C_{\mathrm{k}} = \frac{r_{\mathrm{k}}^{p_{\mathrm{k}}} - 1}{r_{\mathrm{k}}^{p_{\mathrm{kest}}} - 1} \tag{4.5}$$

where p_{kest} is an estimate for the theoretical order of accuracy, which was assumed to be unity [119].

The error associated with the number of iterations was neglected, because the number of iterations has been set to result in root mean squared residuals either below or on the order of 10^{-5} for all simulations, which was deemed to be sufficiently small to have negligible effects

on the solution [122]. Furthermore, the error associated with blockage effects was also deemed to be insignificant because a very large computational domains was used.

The validation uncertainty, U_V, was calculated via [118, 119]:

$$U_V = \sqrt{U_G^2 + U_D^2} \tag{4.6}$$

where U_D is the uncertainty of the benchmark data (e.g. experimental uncertainty). The ideal scenario would be having the difference between the experimental and numerical value (i.e. the comparison error, E) being less than the validation uncertainty; otherwise, both the comparison error and validation uncertainty would be reported nonetheless, to quantify the accuracy of the numerical model.

The numerical simulation setup was validated by comparing model-scale results with experimental data, both from the circulating water channel (CWC) experiments and from Jensen *et al.* [114]. The CWC experimental setup is presented in Chapter 3, while the test conditions for validation are listed in Table 4.4. The experiment conducted by Jensen *et al.* [114] involved having a smooth cylinder with an external diameter of 0.03 m, conducted in an open water flume tank of 10 m in length, 0.3 m wide and 0.3 m deep. The water depth was held constant at 0.23 m, while the flow velocity corresponded to a Reynolds number of 6×10^3.

Table 4.4: Test matrix for circulating water channel experiments.

Pipe elevation, e_o (m)	Pipe diameter, D (m)	Inlet velocity, U_{in} (m/s)	Pipe Reynolds number, Re
D/3	0.3	0.18	4.43×10^4
D/3	0.3	0.24	6.01×10^4
D/3	0.3	0.30	7.60×10^4
D/3	0.3	0.37	9.18×10^4
D/3	0.3	0.43	1.08×10^5
D/3	0.3	0.49	1.23×10^5
D/3	0.3	0.56	1.39×10^5

4.2.2 Predicting scour

The upstream dimensionless seabed shear stress, θ_∞, was adopted to represent the upstream condition, because firstly, the scour rate has been experimentally shown to be influenced by the upstream dimensionless seabed shear stress. As reported in Mao [3], the scour rate beneath the pipe at the early stage is higher at larger values of θ_∞. Secondly, although the influence of the upstream dimensionless seabed shear stress on the equilibrium scour depth is weak in the case of live-bed scour, its effect is significant when its value is less than the critical dimensionless seabed shear stress [1]. Hansen [123] and Mao [3] showed that there is a steep gradient in the equilibrium scour depth when $\theta < \theta_{cr}$. Thus, Sumer and Fredsøe [1] also stated that the effect of θ should be taken into consideration in the case of clear-water scour. Thirdly, the Shields parameter have been used for scaling laboratory experiments investigating sediment for many years [124]. Finally, the upstream dimensionless seabed shear stress is a dimensionless parameter that encompasses both the local flow speed and the sediment grain size. Therefore, it is suitable to be used to represent the upstream condition.

The current velocity was represented in the upstream dimensionless seabed shear stress, θ_∞, using Eq. (4.8), which was derived by substituting Eq. (4.7) into Eq. (3.1), via $\tau_b = \rho u_*^2$ [37]:

$$u_* = \frac{\kappa U_{in}}{\ln\left(y/z_o\right)} \tag{4.7}$$

$$\theta_\infty = \left[\frac{\kappa U_{in}}{\ln\left(y/z_0\right)}\right]^2 \times \frac{1}{\left(\frac{\rho_s}{\rho} - 1\right) g d_{50}} \tag{4.8}$$

where the sediment density, ρ_s, is assumed to be 2650 kg/m^3 [87]. The maximum dimensionless seabed shear stress, θ_{max}, which was the key parameter of interest, was calculated based on the maximum seabed shear stress beneath the TGP, τ_{max}, that was computed via CFD. Thus, by fitting trend lines to the CFD data, the equation for the prediction of scour occurring beneath the TGP in areas with small elevations under steady currents can be derived. The equation for the trend lines was assumed to be a function of θ_∞ and e_o/D:

$$\theta_{\max} = \frac{\tau_{\max}}{(\rho_s - \rho) g d_{50}} = \left(\left[\frac{\kappa U_{in}}{\ln(y/z_0)} \right]^2 \times \frac{1}{\left(\frac{\rho_s}{\rho} - 1 \right) g d_{50}} \right)^{C_1} \times \left(\frac{e_0}{D} \right)^{C_2} \quad (4.9)$$

wherein e_0/D is a user-defined value; and, C_1 and C_2 are constants. The exponents, C_1 and C_2, were iteratively solved using unconstrained nonlinear optimisation (see Lagarias *et al.* [125] for further details). The optimisation process involved the exponents being initially assumed to be 1. The differences between the data computed via CFD and the values calculated using Eq. (4.9) were then squared, and a scalar objective function, *fminsearch*, was used to compute the values for C_1 and C_2 that would result in the smallest difference via MATLAB, which resembled the 'least squares' approach.

4.3 Results

4.3.1 Field observations

A field survey was conducted for the southernmost 5 km section of the Tasmanian Gas Pipeline (TGP), as per the pipeline operator's request; further inspection was not conducted due to logistical challenges. Significant free spanning was observed from the video footage obtained via the Remotely Operated Vehicle (ROV) (Figure 3.3c), and acoustic backscatter images obtained using the Autonomous Underwater Vehicle (AUV). ROV footage such as that presented in Figure 3.3c suggest that the TGP had significant seabed gaps and span lengths, and was covered in marine growth. The seabed gap, G_s, appears to be relatively small as compared to the pipe diameter, D (i.e. approximately equal to or less than 0.3D). The sandy seabed also appeared to be relatively flat.

As only visual observations can be made from the ROV footage, the AUV was used to produce acoustic backscatter images to identify and geo-reference free spans, and subsequently, estimate the maximum seabed gaps. Figure 4.2a reveals the maximum seabed gaps, G_{max}, along the 5 km stretch of the TGP. *KP* is Kilometre Point, where an increase in *KP* is proportional to the proximity to the Northern Tasmanian coast. This indicated multiple incidences of free spanning along this relatively short stretch of the TGP. Figure 4.2b

presents the same dataset normalised over the external pipe diameter, D, which is not constant along this 5 km stretch. Figure 4.2c shows the histogram of maximum seabed gaps detected along the surveyed pipe length. The data revealed that over the 5 km stretch of the TGP, more than 12% of the spans had G_{max}/D ratios smaller than 0.3.

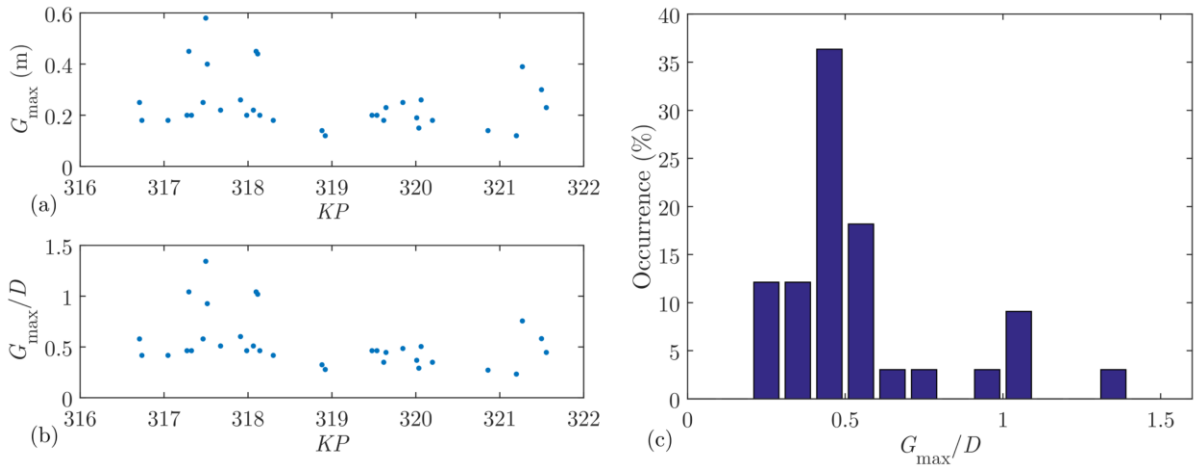

Figure 4.2: (a) Maximum seabed gaps, G_{max}, plotted against Kilometre Point, *KP*. The increase in *KP* indicates the proximity to the Northern Tasmanian coast. (b) Maximum seabed gaps normalised over external pipe diameter, G_{max}/D. (c) Histogram of maximum seabed gaps detected along the surveyed pipe length.

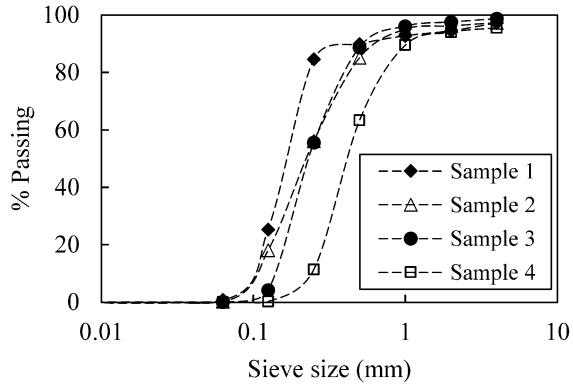

Figure 4.3: Particle size distribution of marine sediment samples collected at the locations illustrated in Figure 3.3b.

In addition to the pipeline inspection, sediment samples have also been collected within safe distances from the TGP (Figure 3.3b), as recommended by the pipeline operator. Figure 4.3 presents the particle size distribution for each sediment sample, which is produced by

measuring the amount of sediment in each sieve. The sample number corresponds to the order of collection as shown in Figure 3.3b. Due to logistical challenges, only four sediment samples have been obtained successfully. The sieve size corresponding to 50% passing can be observed from Figure 4.3. This can be related to the median particle size for the individual sample. By taking the average of the sieve size at 50% passing for all samples, the median particle size, d_{50}, is estimated to be approximately 0.257 mm.

4.3.2 Verification and validation results

A grid independence study was performed to investigate the influence of grid refinement around the pipe and the seabed on the variables of interest, following the procedure presented in Chapter 3. Figure 4.4 suggests that the changes in the pipe's drag coefficient, C_D, local flow velocity profile beneath the pipe and bed shear stresses along the seabed are minimal, with a grid refinement ratio of 3.32. As seen in Figure 4.4a, C_D decreased by 0.58% and then by 0.09%, due to an increase in number of cells around the pipe and the seabed. With reference to Figure 4.4b, the maximum stream-wise velocity beneath the pipe, u_x, increased by 0.48% and then by 0.00% with grid refinement. Similarly, the maximum bed shear stress beneath the pipe, τ_{max}, only increased by 0.90% and then by 0.16% with refinement of the grid (Figure 4.4c). Thus, by adopting τ_{max} as the main variable of interest, the resulting numerical uncertainty was estimated to be 0.35%, as the 'medium' refinement level was used for the remaining CFD simulations.

Figure 4.5 presents the CFD and Circulating Water Channel (CWC) experimental results at $e_o = D/3$, comparing the stream-wise velocities measured at 0.035 m above the seabed, u_{35}. The error bars for the CFD data are plotted based on the numerical uncertainty which was estimated to be 0.35%. The standard deviations were used to plot the error bars associated with the CWC data. The mean difference between the CFD and experimental data was approximately 11.1%. This was smaller than the validation uncertainty, U_V, of approximately 1.1%, whereby the experimental uncertainty was assumed to be 1%, which is the accuracy of the ADV [85]. The potential reasons for this discrepancy are discussed in Section 4.4.

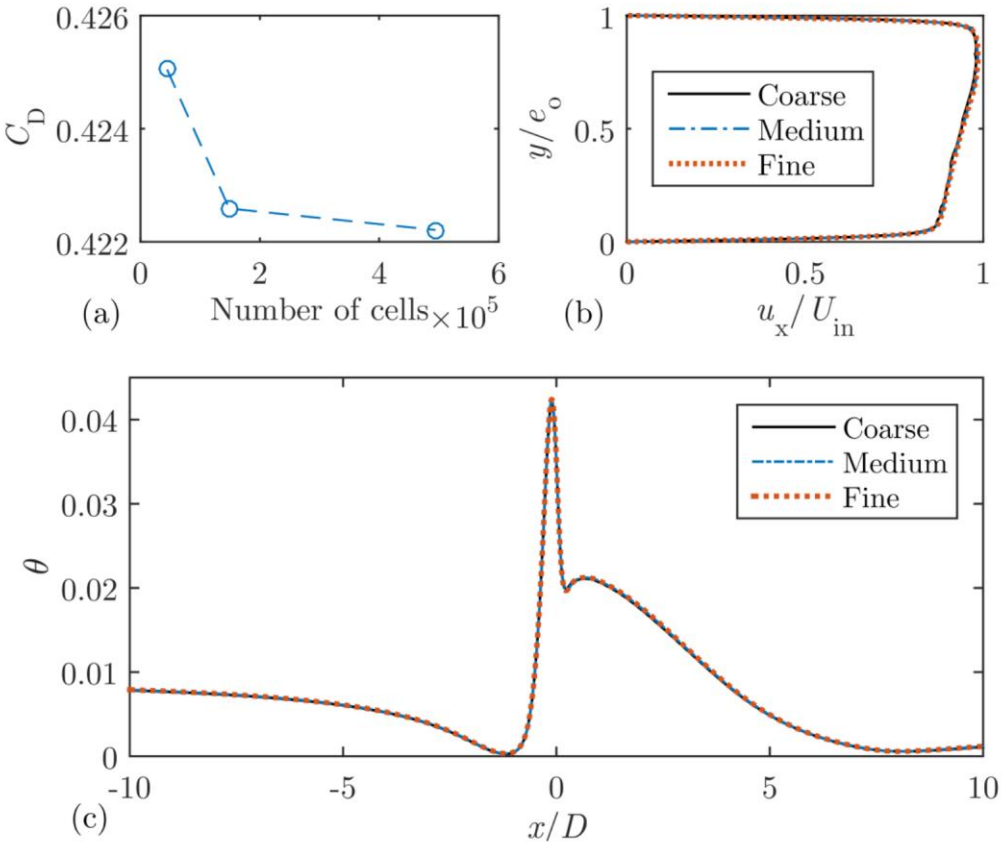

Figure 4.4: Grid independence study: (a) drag coefficient for the pipe versus number of cells in the domain; (b) elevation from the seabed, y, normalised over the pipe elevation, e_o, plotted against mean local stream-wise velocities in the x-direction, u_x, normalised over inlet velocity, U_{in}, for different grid densities; (c) dimensionless bed shear stress, θ, distributions along the seabed computed using different grid resolutions.

Further assessment of the accuracy of the CFD model was performed by modelling the experimental setup of Jensen *et al.* [114]. This was done to further support the assumption that a steady-state solution was sufficient for modelling flow around a pipe close to the flat bed. Figure 4.6 presents the mean velocities computed via RANS, superimposed on measurements extracted from Jensen *et al.* [114]. The results displayed a good agreement at $Re = 6 \times 10^3$. This correlation between numerical and experimental data resembled that of Akoz and Kirkgoz [39], in which it was reported that the *k-ω* SST model is adequate for modelling flow around a wall-mounted circular cylinder. The mean difference between the computed velocities and measurements from Jensen *et al.* [114] was approximately 4.6%. As the experimental uncertainty has not been reported in Jensen *et al.* [114], it was not possible

to estimate the validation uncertainty; nonetheless, the good qualitative agreement between the computed and measured velocity profiles were worth noting.

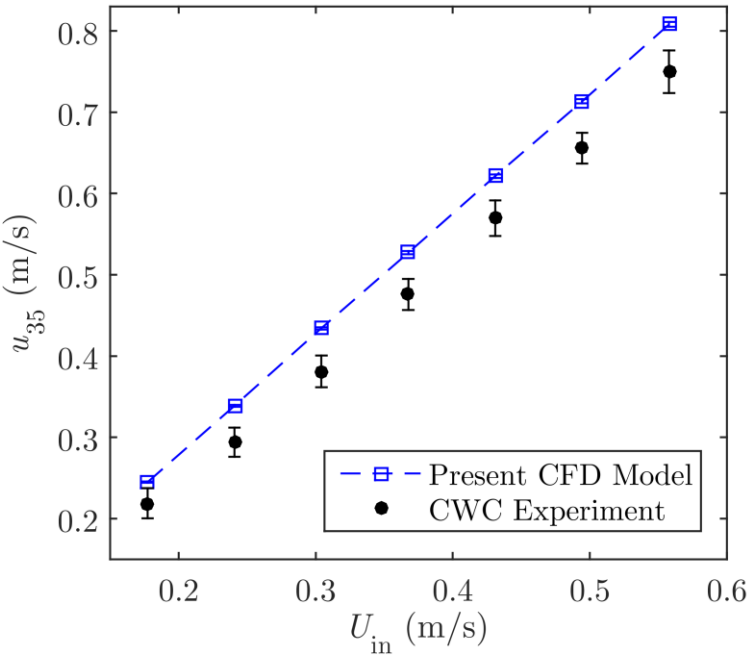

Figure 4.5: Computed and measured velocity beneath the pipe at 0.035 m from the aluminium flat plate , u_{35}, plotted against the inflow free-stream velocity, U_{in}, at a e_o = 0.1 m, corresponding to e_o = D/3, where D = 0.3 m.

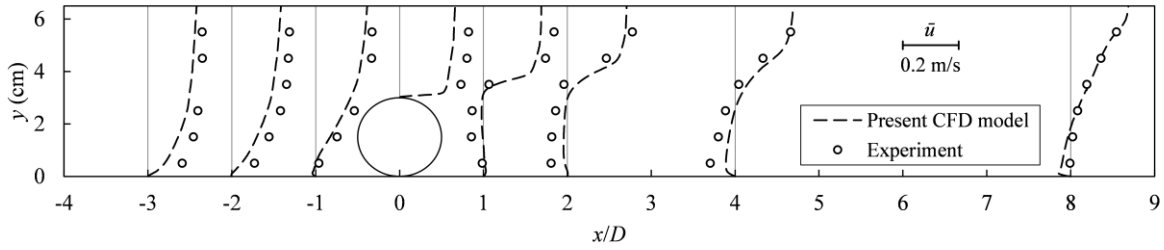

Figure 4.6: Comparing mean stream-wise velocities in the x-direction computed using the present CFD model with experimental measurements extracted from Jensen *et al.* [114] for $Re = 6 \times 10^3$.

4.3.3 Full-scale CFD results

Upon attaining a high level of confidence in the numerical setup, the simulations corresponding to the conditions in Table 4.2 were performed to predict the occurrence of scour beneath the TGP. Figure 4.7a shows the stream-wise velocity, u_x, normalised by inlet

velocity, U_{in}, with reference to the elevation from the seabed, y, normalised over the pipe elevation, e_o, for e_o/D = 0.07 and 0.05 m/s ≤ U_{in} ≤ 0.80 m/s. Figure 4.7b shows the velocity profiles for e_o/D = 0.14, while Figure 4.7c shows the plots for e_o/D = 0.28. It can be seen that the flow beneath the pipe was further accelerated as U_{in} increased. With reference to Figure 4.7d, it seems that even at a constant U_{in} of 0.05 m/s, when e_o/D increases, the flow no longer resembled flow between two flat plates and became increasingly asymmetrical about y/e_o = 0.5. Higher inlet velocities at e_o/D = 0.28 have not been considered, because the solution did not converge to result in root mean squared residuals below the order of $O(10^{-4})$.

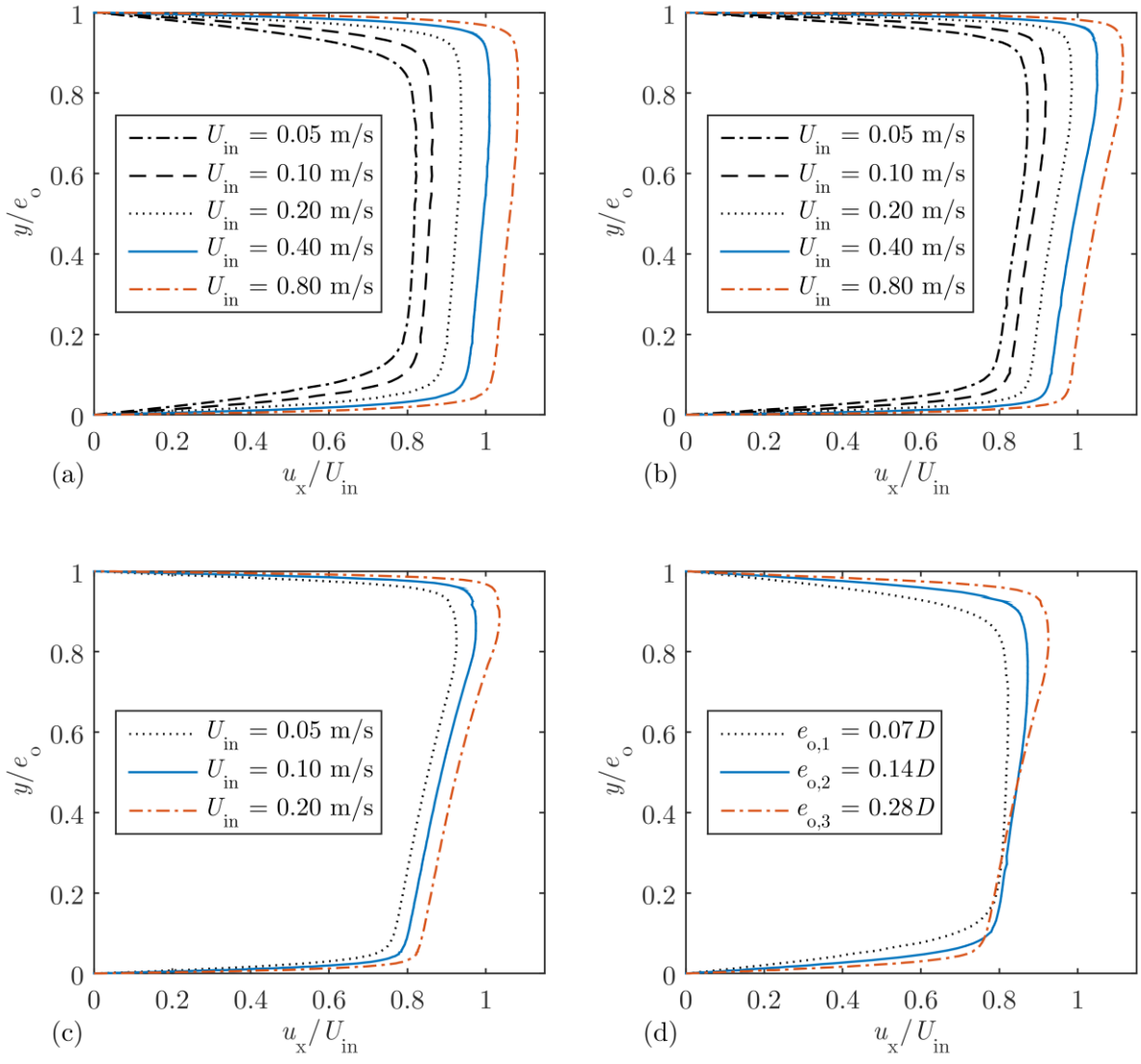

Figure 4.7: (a) Elevation from the seabed, y, normalised over pipe elevation, e_o; plotted against mean local stream-wise velocities in the x-direction, u_x, normalised over inlet velocity, U_{in}, where e_o/D = 0.07. (b) e_o/D = 0.14. (c) e_o/D = 0.28. (d) U_{in} = 0.05 m/s.

Figure 4.8a presents the seabed shear stress, τ, distributions for e_o/D = 0.07. The distance along the seabed, x, was normalised over the pipe diameter, D, where the pipe was located at x/D = 0. The method of computing the seabed shear stress is presented in Chapter 3. The seabed shear stress distribution was seen to increase nonlinearly with an increase in the inlet velocity. In addition, there are highly nonlinear changes in the seabed shear stresses in the vicinity of the pipe. Furthermore, the maximum seabed shear stress appears to always occur beneath the pipe. Figure 4.8b and Figure 4.8c reveal a similar trend for e_o/D = 0.14 and e_o/D = 0.28, respectively, while Figure 4.8d compares the influence of e_o/D on the seabed shear stress distribution, at a constant inlet velocity of U_{in} = 0.05 m/s. Although the upstream seabed shear stresses were the same in Figure 4.8d, the maximum seabed shear stress decreased as e_o/D increased.

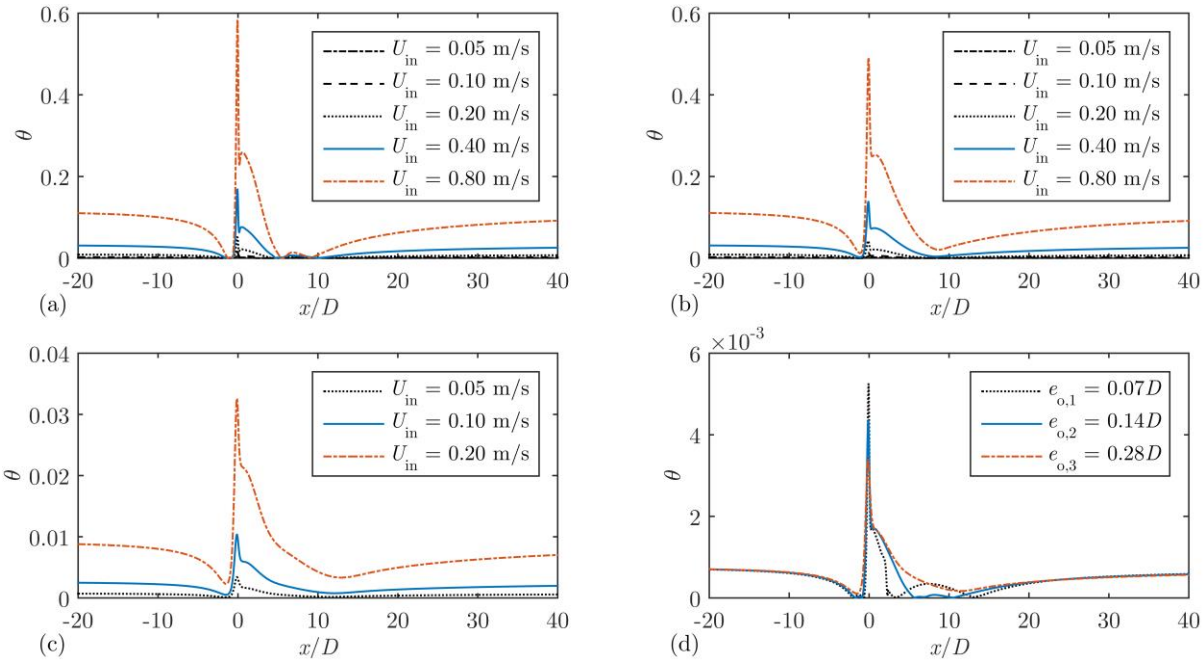

Figure 4.8: (a) Shields parameter, θ, distributions for e_o/D = 0.07. The distance along the seabed, x, is normalised over the pipe diameter, D, where the pipe is located at x/D = 0. (b) e_o/D = 0.14. (c) e_o/D = 0.28. (d) U_{in} = 0.05 m/s.

The effect of the bed and pipe surface roughness heights on the seabed shear stresses have been briefly investigated. Figure 4.9a shows the seabed shear stress distributions for several seabed roughness heights, z_o; where e_o/D = 0.14 and U_{in} = 0.1 m/s. The differences in the datasets were hardly noticeable. Figure 4.9b shows the change in maximum seabed shear stress beneath the pipe, $\Delta\tau_{max}$, relative to τ_{max} for the largest seabed roughness length. It was

clear that the differences are small as they were below the order of $O(10^{-3})$. Similarly, for several pipe roughness heights that have been investigated, Figure 4.9c and Figure 4.9d also show little difference between the seabed shear stresses for different pipe roughness heights, z_p, where e_o/D = 0.14 and U_{in} = 0.1 m/s. The range investigated in this study included seabed roughness heights ranging from silt to fine sand [115], and pipe roughness heights ranging from painted steel pipes to un-coated steel pipes [116]. These roughness heights were also selected for numerical stability, as the seabed roughness height should be smaller than the cell height at the bed and pipe boundaries [37].

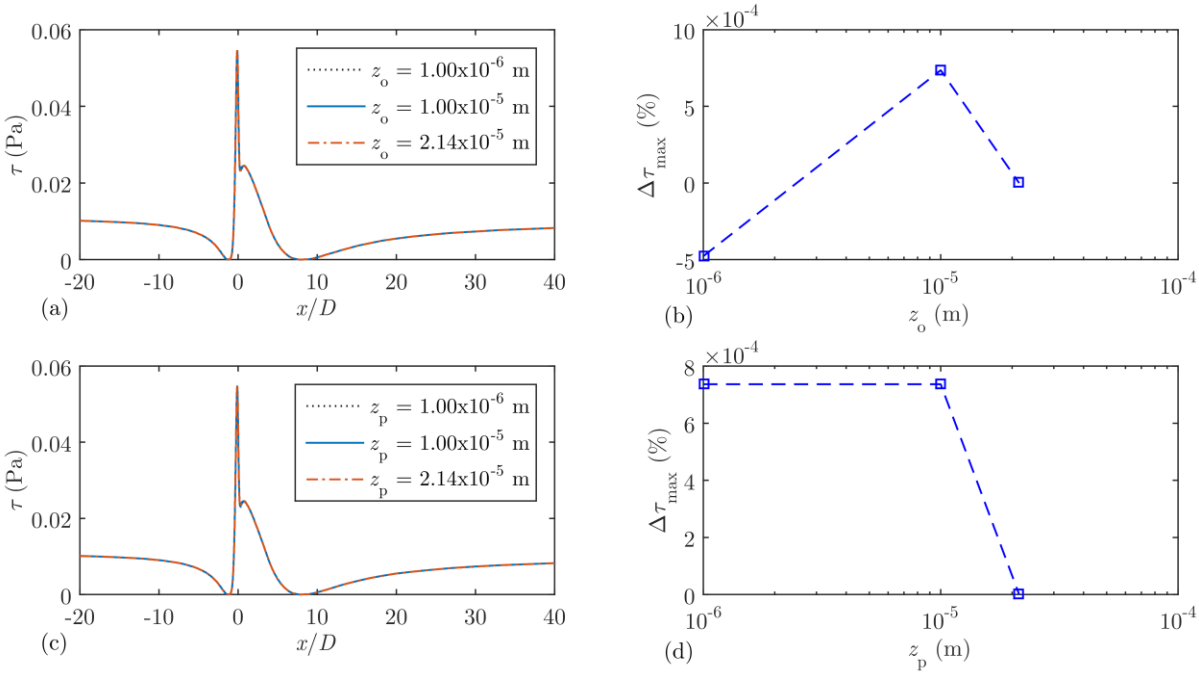

Figure 4.9: (a) Seabed shear stress distributions for different seabed roughness heights, z_o; e_o/D = 0.14, and U_{in} = 0.1 m/s. (b) Relative difference in maximum seabed shear stress beneath the pipe, $\Delta\tau_{max}$, vs. z_o. (c) Seabed shear stress distributions along the seabed for different pipe roughness heights, z_p; e_o/D = 0.14, and U_{in} = 0.1 m/s. (d) $\Delta\tau_{max}$ vs. z_p.

Figure 4.10a shows the maximum seabed shear stress beneath the pipe, τ_{max}, for all cases, which seemed to be increasing nonlinearly with the inlet velocity, U_{in}, but decreasing with an increase in e_o/D. Figure 4.10b shows the seabed shear stress amplification factor in the form of the Shields parameter, plotted against the inlet velocity, U_{in}. The seabed shear stress amplification factor, τ_{max}/τ_∞, has been a variable of interest in previous studies [5, 43], and hence it was investigated as well. This amplification factor was seen to decrease nonlinearly with U_{in}, which was contrary to the trend in Figure 4.10a (i.e. τ_{max} increasing nonlinearly with

increasing U_{in}). However, the amplification factor was also seen to decrease with an increase in e_o/D, when U_{in} was held constant.

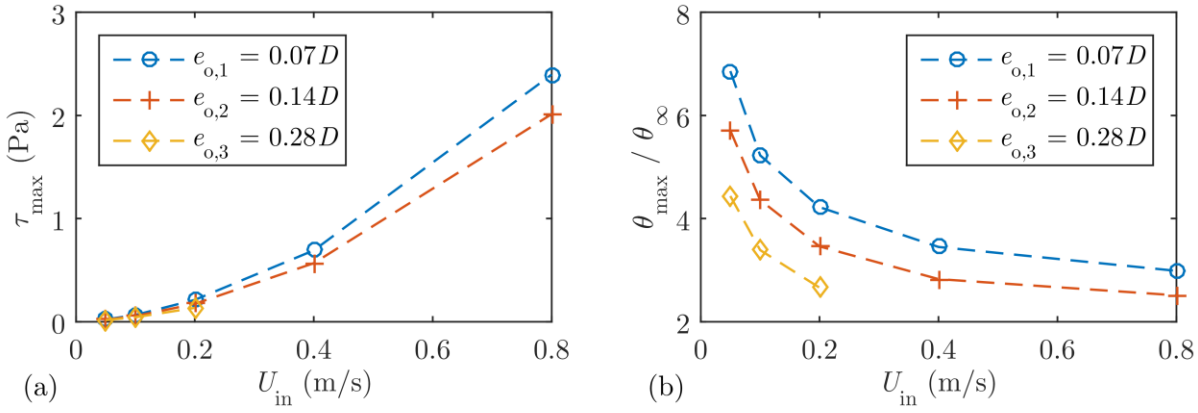

Figure 4.10: (a) Maximum seabed shear stress beneath the pipe, τ_{max}, plotted against inlet velocity, U_{in}. (b) Maximum dimensionless seabed shear stress normalised over upstream dimensionless seabed shear stress, $\theta_{max}/\theta_\infty$, plotted against U_{in}.

4.3.4 Scour prediction

Figure 4.11a presents the maximum dimensionless seabed shear stress, θ_{max}, plotted against the inlet velocity, U_{in}, at different e_o/D ratios. Based on the median grain size (estimated via Figure 4.3), the critical dimensionless seabed shear stress (i.e. $\theta_{cr} = 0.048$) was obtained from Barton *et al.* [33] and plotted as the red horizontal line. When $\theta_{max} > \theta_{cr}$, then scour beneath the TGP is likely to occur. With reference to Figure 4.11a, $\theta_{max} > \theta_{cr}$ when $U_{in} = 0.2$ m/s and $e_o/D = 0.07$. This occurred at a low current velocity, which was below that of the maximum eastward horizontal flow velocity of 0.32 m/s and maximum northward velocity of 0.21 m/s recorded by the ADCP. In addition, similar to the maximum seabed shear stress beneath the pipe (Figure 4.10a), the maximum dimensionless seabed shear stress increased nonlinearly with the increase in U_{in}, while it decreased with an increase in e_o/D.

In Figure 4.11b, the inlet velocity, U_{in}, was converted to the upstream dimensionless seabed shear stress, θ_∞, using Eq. (4.8). θ_{max} was plotted against θ_∞ with logarithmic axes, and similar to Figure 4.11a, the red horizontal line represents the critical dimensionless seabed shear stress. The trend lines were plotted with an assumed power law relationship, where the exponents in Eq. (4.9) were iteratively solved using unconstrained nonlinear optimisation (see Section 4.2.2 for further details). The result of the optimisation process was the

converged values of the exponents (i.e. C_1 = 0.864 and C_2 = -0.333). Hence, Eq. (4.9) can be written as:

$$\theta_{max} = \frac{\tau_{max}}{(\rho_s - \rho) g d_{50}} = \left(\left[\frac{\kappa U_{in}}{\ln(y/z_0)} \right]^2 \times \frac{1}{\left(\frac{\rho_s}{\rho} - 1 \right) g d_{50}} \right)^{0.864} \times \left(\frac{e_o}{D} \right)^{-0.333} \quad (4.10)$$

With reference to the CFD data, Eq. (4.10) corresponded to a squared correlation coefficient, R^2, of 0.9986. The good fit can be observed in Figure 4.11b, as more than 99% of the total variation of the CFD data can be reproduced using Eq. (4.10).

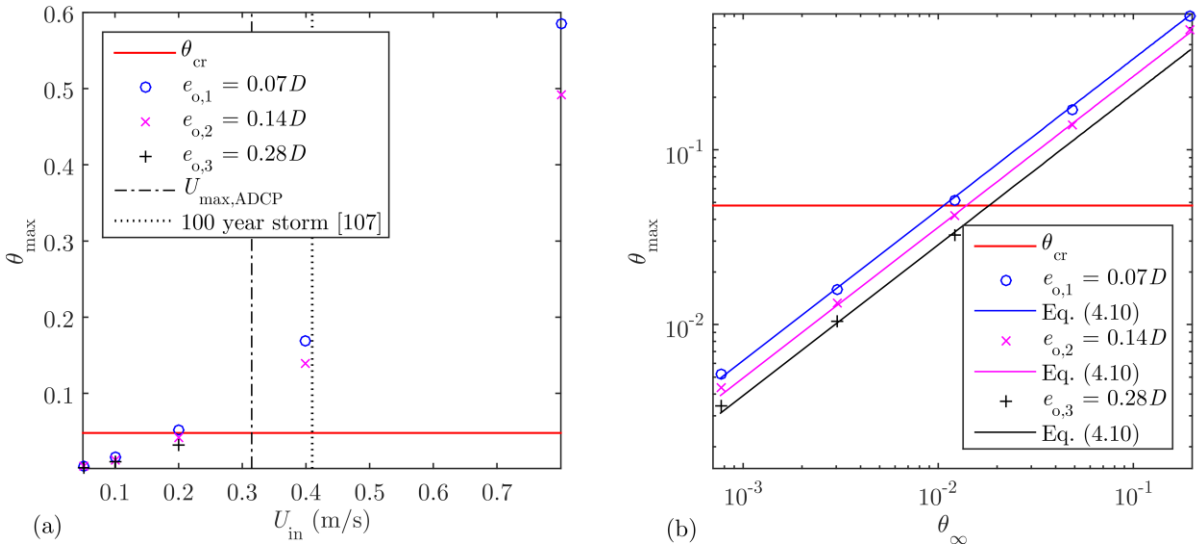

Figure 4.11: (a) Maximum dimensionless seabed shear stress beneath the pipe, θ_{max}, versus inlet velocity, U_{in}, at several e_o/D ratios. (b) θ_{max} versus upstream dimensionless seabed shear stress, θ_∞; the trend lines are plotted using Eq. (4.10), where R^2 = 0.9986.

4.4 Discussion

The field investigation provided an insight into the number of spans and seabed gaps along the TGP, far field ensemble-averaged velocities and median sediment grain size in the vicinity of the surveyed area. A significant amount of free spanning was observed along the 5 km stretch of the surveyed area (Figure 4.2). In addition, more than 12% of the detected spans have G_{max}/D ratios smaller than 0.3. Thus, a significant amount of small seabed gaps

can be expected along the TGP, considering the fact that the TGP is over 300 km long. Therefore, it will be beneficial to be able to predict whether scour will occur beneath the TGP in areas with small pipe elevations, at which the seabed shear stresses were higher, and it is often impractical to perform rectification works.

As the seabed appeared to be relatively flat in Figure 3.3c, a flat boundary was used to represent the seabed in the CFD simulations for simplicity. In addition, the seabed topography along the path at which the TGP was laid was also reported to be relatively featureless [107]. Although there appeared to be a significant amount of marine growth on the pipe (Figure 3.3c), previous experimental investigations on pipe roughness, representing marine growth, appear to pose an insignificant influence on the scour profile [9]. Thus, the effects of hard and soft marine growth have not been included in the scope of this work.

The median particle size, d_{50}, was estimated to be approximately 0.257 mm, based on the particle size distributions (Figure 4.3). Therefore, it was assumed that the sediment in the surveyed area was mainly comprised of non-cohesive medium sand [33]. This is in agreement with the range reported in [107], wherein the sediment in the vicinity of the TGP has been reported to be primarily comprised of fine and medium grained quartzose sands. Interestingly, the particle size distribution was seen to slightly shift towards the right as the sample number increased. With reference to the sampling locations (Figure 3.3b), this suggested that the sediment closer to the shore were generally smaller in size; however, this could only be true for the surveyed area.

With regards to the grid independence study (Figure 4.4), the numerical results computed with a ‘medium’ mesh (i.e. 400 grid points on the pipe) were deemed to be grid-independent, as the changes in the results due to grid refinement were very small (i.e. less than 1%). As for the comparison between the CFD and CWC results (Figure 4.5), the discrepancies between the CFD and experimental data, E, have exceeded the validation uncertainty, U_V, which was not ideal. The difference between the datasets was hypothesised to stem from: (1) the combined effects of modelling uncertainties (e.g. boundary conditions, turbulence model, fluid properties, etc. [120]), in addition to the numerical uncertainties; and, (2) the pressure field generated by the strut that was used to hold the ADV in the CWC (Figure 4.1), which has not been included in the CFD simulations. Nevertheless, both CFD and CWC results have a similar gradient, especially at higher inlet velocities. The simulation setup was still deemed

to be reliable, because there was a good agreement between the CFD and experimental data in Figure 4.6, in conjunction with a very small numerical uncertainty.

Full-scale CFD computations have been performed upon establishing a reliable numerical model. With reference to Figure 4.7, it can be seen that the dimensionless flow velocity, u_x/U_{in}, increased with an increase in U_{in}, whilst e_o/D was held constant. The flow beneath the pipe was further accelerated as U_{in} increased, which suggested a nonlinear increase in the seabed shear stresses beneath the pipe, as $\tau = \rho u_*^2$ [87]; this nonlinear increase in the seabed shear stress was reflected in Figure 4.8. With reference to Figure 4.7a, a symmetrical flow pattern was observed at a low U_{in}; however, as U_{in} increased, the velocities at the upper region of the velocity profile (i.e. the region closer to the pipe) became higher relative to the velocities near the seabed. This can be attributed to two occurrences as the flow became increasingly turbulent: (1) the viscous region of the boundary layer attached to the pipe's surface decreases in thickness; and, (2) flow separation on the pipe's bottom surface was delayed, pushing the separation point further downstream [126]. A similar situation was observed in Figure 4.7b and Figure 4.7c.

It is interesting to note that, although the flow velocity beneath the pipe was higher relative to the upstream velocity at the same vertical height from the seabed, it was not significantly higher than the free-stream velocity at the inlet boundary, U_{in}. As observed in Figure 4.7, u_x/U_{in} was less than unity in many cases. This occurrence can be explained by the velocity contour plot shown in Figure 4.12. It can be seen that the cylinder or pipe was well within the boundary layer developing along the flat seabed, because the incoming boundary layer thickness, δ_{in}, was set to 2 m in the CFD simulations. Hence, the flow velocity in between the pipe and the seabed can be lower than U_{in}.

There were highly nonlinear changes in the seabed shear stresses in the vicinity of the pipe (Figure 4.8), suggesting that the presence of the pipe posed a significant influence on the seabed shear stresses. The fact that the maximum seabed shear stress appeared to always occur beneath the pipe, implied that the capacity for scour to occur is maximum at the point beneath the pipe. These seabed shear stress distributions are in good agreement with the shear distributions presented in Ong *et al.* [41], who analysed the applicability of the *k-ε* turbulence model for different Reynolds numbers, but did not focus on the scour process underneath the pipe. Figure 4.8d shows that although the upstream seabed shear stresses are the same, the

maximum seabed shear stress increased as e_o/D decreased, indicating that the capacity for scour to occur increases with a decrease in e_o/D.

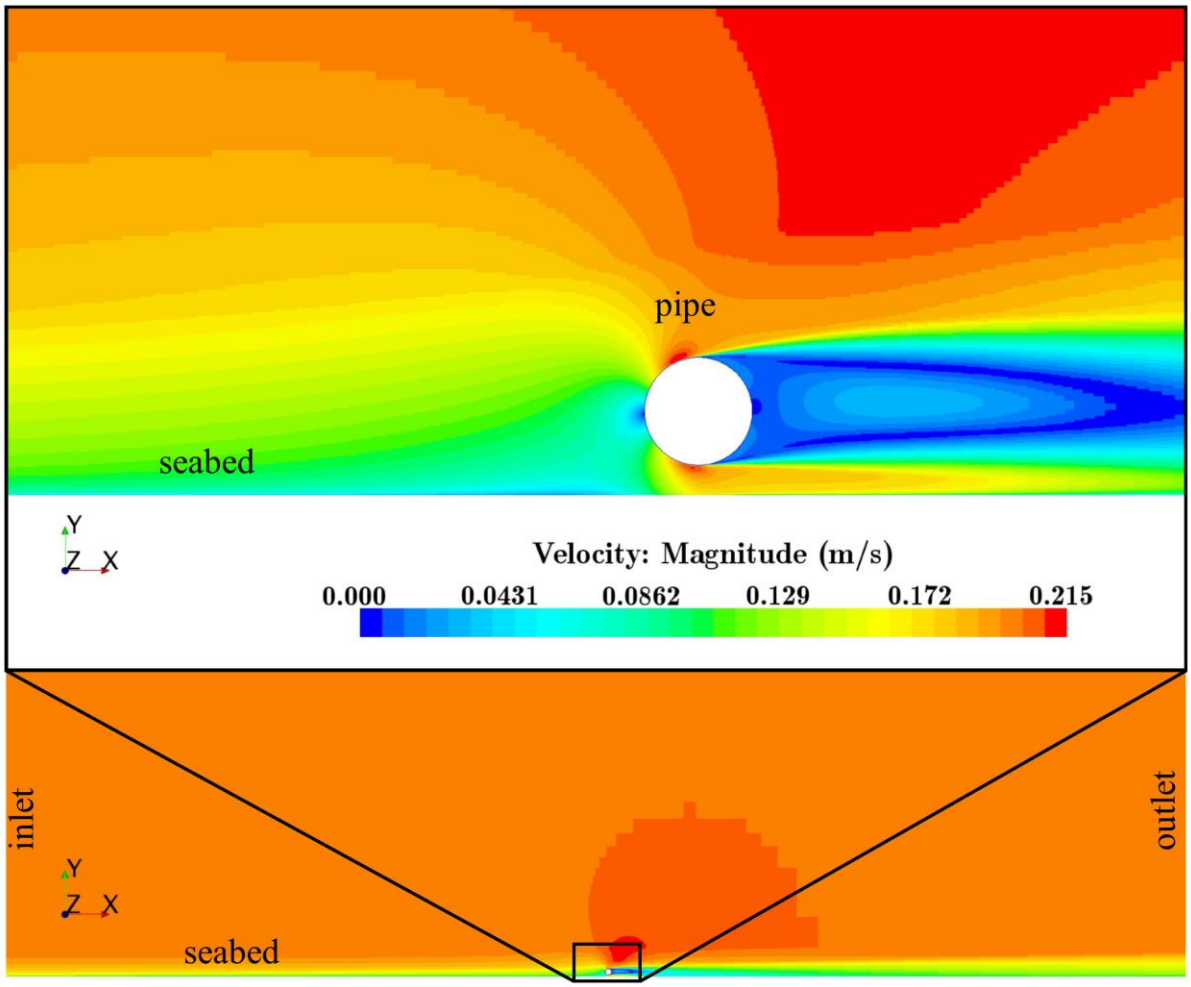

Figure 4.12: Velocity contour plot for a full-scale case: D = 0.5 m, e_o/D = 0.28, U_{in} = 0.20 m/s, and δ_{in} = 2 m, where a close-up view of the flow velocity around the pipe is shown in a black box.

The maximum seabed shear stress beneath the pipe, τ_{max}, was seen to increase nonlinearly with U_{in}, but decrease with an increase in e_o/D (Figure 4.10a). This suggested that the capacity for scour increases with the increase in U_{in}, and with decreasing e_o/D. Griffiths *et al.* [5] reported that the amplification factor decreased with the pipe elevation, which agreed with Figure 4.10b, where the amplification factor was seen to increase with a decrease in e_o/D, at a constant U_{in}. This occurrence can be attributed to the decrease in maximum seabed shear stress beneath the pipe as e_o/D increases, whilst the upstream seabed shear stress remained constant due to a constant U_{in}. As the Shields parameter is a dimensionless form of the bed

shear stress, an increase in e_o/D with a constant U_{in} also resulted in a decrease in θ_{max} and, subsequently, a decrease in the amplification factor.

Figure 4.10b shows that the amplification factor was also a function of current velocity, U_{in}, where it decreased nonlinearly with U_{in}; this was not discussed in Griffiths *et al.* [5]. However, Figure 4.7 shows that the ratio of the velocity beneath the pipe over the incoming flow velocity, u_x/U_{in}, increases with the increase in U_{in}. This may be attributable to the reduction in the boundary layer thickness as U_{in} increased. Thus, the upstream velocity at the same vertical height as the pipe would be lower than U_{in}, while the upstream seabed shear stress is calculated based on the upstream friction velocity, and not U_{in}. Nevertheless, a high amplification may not necessarily result in scour occurring when the maximum shear stress is below the critical shear stress. Therefore, this study focused on predicting the maximum Shields parameter beneath the TGP under steady currents, where it can be compared to the critical Shields parameter for the median sediment grain size.

Figure 4.11a shows that even at a small U_{in}, which was below the maximum flow velocity recorded by the ADCP, the maximum Shields parameter beneath the TGP has exceeded the critical Shields parameter. Thus, the occurrence of scour beneath the TGP in areas with small pipe elevations (i.e. $e_o/D < 0.3$) can be expected, due to the fact that flow velocities as high as 0.32 m/s were recorded. At higher current velocities (e.g. during a storm event), the occurrence of scour beneath the TGP will likely be more severe. These findings can be related to the significant amount of free spanning that was observed along the 5 km stretch of the surveyed area (Figure 4.2). Overall, the Shields parameter approach appeared to be a more reliable method for scour prediction, as compared to using the shear stress amplification factor.

The high squared correlation coefficient, R^2, of 0.9986 implied that Eq. (4.10) can be used, with high confidence, to calculate the maximum Shields parameter beneath the TGP in areas with a small e_o/D under steady currents. Eq. (4.10) is valid for $e_o/D < 0.3$, where there was no periodic vortex shedding in the wake of the pipe [3, 17], and the friction velocity beneath the pipe was constant over time [40, 41]. Hence, $e_o/D = 0.28$ was selected as the upper limit because the presence of periodic vortex shedding at higher pipe elevations could produce different results. Nevertheless, $e_o/D < 0.3$ is of interest not only because the capacity for scour is higher at smaller pipe elevations, but also, performing rectification works such as installing

grout bags are often impractical. The additional option to conduct inexpensive RANS-based CFD simulations to modify Eq. (4.10) is also available.

4.5 Summary

A combination of numerical, experimental and field work was undertaken to predict the occurrence of scour beneath the Tasmanian Gas Pipeline (TGP) in areas with small pipe elevations under steady currents. Two-dimensional full-scale CFD computations were performed by incorporating information attained through field measurements. A good agreement between model-scale CFD data and experiments was demonstrated. A range of e_o/D ratios and steady current velocities, U_{in}, were considered in the numerical simulations. A trend line equation was fitted to the full-scale CFD data using unconstrained nonlinear optimisation, which resulted in a very high correlation coefficient. The following conclusions can be drawn from this work:

- A significant occurrence of spans with small maximum seabed gaps (i.e. $G_{max}/D < 0.3$) is detected during the field survey, thus supporting the need to develop an equation to predict whether scour will occur under those circumstances.
- The seabed is observed to be relatively flat, and hence a small seabed gap is assumed to be equivalent to a small pipe elevation in this case.
- The maximum seabed shear stress beneath the pipe increases nonlinearly with U_{in}, but decreases with an increase in e_o/D. Hence, the capacity for scour increases with an increase in U_{in}, but decreases with an increase in e_o/D.
- The shear stress amplification factor decreases nonlinearly with U_{in}; thus, it does not accurately reflect the occurrence of scour and it may not be an appropriate tool for scour prediction.
- Eq. (4.10) is developed to calculate the maximum Shields parameter beneath the pipe, θ_{max}, based on the upstream Shields parameter, θ_∞, and e_o/D; θ_{max} can be compared to the critical Shields parameter, θ_{cr}, for the particular sediment grain size.
- Eq. (4.10) can be used to predict the occurrence of scour beneath the TGP in areas with a small e_o/D under steady currents, and is valid for $e_o/D < 0.3$, where there is no periodic vortex shedding in the wake of the pipe [3, 17], and the bed shear stress beneath the pipe is constant over time [40, 41].

- High horizontal flow velocities recorded by the Acoustic Doppler Current Profiler suggest that the occurrence of scour beneath the TGP is likely, based on the maximum Shields parameter computed via CFD.

Chapter 5

Reynolds number effect on the seabed shear stress and equilibrium scour depth[2]

This chapter focused on quantifying the effects of the upstream dimensionless seabed shear stress, θ_∞, and Reynolds number, *Re*, on: (1) the maximum dimensionless seabed shear stress beneath the pipe, θ_{max}, to be compared to the critical shear stress in order to determine whether scour would occur and progress towards an equilibrium state; and, (2) the dimensionless equilibrium scour depth beneath the pipe, S_{eq}/D. Using a 2-D Reynolds averaged Navier-Stokes (RANS) approach along with the k-ω Shear Stress Transport (SST) turbulence model, a parametric study involving 243 computational fluid dynamics (CFD) simulations is conducted. The simulation results are used to develop a closed-form equation for the prediction of θ_{max}. Subsequently, experimental measurements of S_{eq}/D have been compiled from published literature, to develop a new closed-form equation for the prediction of S_{eq}/D with a high correlation to the experimental data. In summary, this chapter presents two closed-form equations for the prediction of θ_{max} and S_{eq}/D for pipelines with $e_o/D \geq 0$, which are applicable for both clear-water and live-bed conditions; the effects of θ_∞ and *Re* have been included, albeit *Re* having a small influence as compared to the other parameters.

[2] A version of this chapter has been published as: Lee, J. Y., Hardjanto, F. A., Cossu, R., Chai, S., Leong, Z. Q., & Forrest, A. L. (2019). Current-induced scour beneath initially elevated subsea pipelines. *Applied Ocean Research*, 82, 309-324. DOI: 10.1016/j.apor.2018.11.011.

5.1 Introduction

It is of technical interest to predict the conditions driving the occurrence of scour and the equilibrium scour depth, S_{eq}/D; however, subsea pipelines may have an initial elevation with respect to the far-field seabed, e_o, at certain sections, upon installation along an uneven seabed [1]; see Figure 1.2 for the definition of terms. The capacity for scour to occur beneath the pipe is higher at smaller values of e_o/D, because there is flow amplification and a corresponding increase in the seabed shear stress beneath the pipe [5, 127]. Furthermore, performing rectification works in such situations, such as installing grout bags or rock dumping, is both challenging and will lead to a substantial increase in project costs. Therefore, this chapter investigated the local maximum dimensionless seabed shear stress beneath the pipe, θ_{max}, to be used as a determinant of whether scour would progress towards an equilibrium state for a particular flow condition, with reference to the critical dimensionless shear stress, θ_{cr}, and subsequently, the corresponding S_{eq}/D would be of interest.

Novel experiments [3, 16, 18, 128, 129] and numerical computations [19, 68] have been conducted, through which a few empirical formulae have been proposed to predict the occurrence of scour around pipelines with a partial embedment (i.e. $e_o/D < 0$). While these equations are useful predictors, their application to pipelines with a positive e_o/D is inappropriate. There have been a few studies (e.g. [5]) which investigated the amplification of the seabed shear stress underneath a pipeline with $e_o/D \geq 0$; however, a high amplification may not necessarily result in scour occurring when the maximum shear stress is below the critical shear stress. An equation has been introduced in Chapter 4 to predict the maximum dimensionless seabed shear stress underneath pipelines as a primary function of e_o/D, to complement field measurements [127]:

$$\theta_{max} = \theta_{\infty}^{\,0.864}\left(\frac{e_o}{D}\right)^{-0.333} \tag{5.1}$$

where θ_{∞} is the upstream dimensionless seabed shear stress, and e_o/D is the normalised elevation of the bottom of the pipe with respect to the far-field seabed. This chapter builds on this work by quantifying the influence of the pipe Reynolds number on θ_{max}, as only a narrow

range of pipe Reynolds numbers were considered in [127]. In particular, a wide range of external pipe diameters are considered, as subsea pipelines that form multiple fluid transportation networks across the globe range from 0.2 m to more than 1 m in diameter [1].

With regards to predicting the equilibrium scour depth, S_{eq}, for steady currents, several equations have been proposed over the years; a comprehensive review of the existing empirical formulae is presented in Chapter 2. Moncada-M and Aguirre-Pe [8] and Sumer and Fredsøe [1] have proposed empirical formulae for the prediction of S_{eq}/D, wherein the effects of e_o/D have been included; however, they are only applicable for the live-bed condition. Therefore, as Sumer and Fredsøe [9] have indicated that the equilibrium scour depth is also dependent on the upstream dimensionless seabed shear stress and pipe Reynolds number, this chapter focused on quantifying the influence of these parameters on S_{eq}/D for both clear-water and live-bed conditions.

An extensive parametric study is performed, wherein a range of external pipe diameters, dimensionless pipe elevation with respect to the far-field seabed, seabed roughness heights, incoming boundary layer thicknesses, and incoming free-stream current velocities, are investigated numerically. Based on the simulation results, the influence of the Reynolds number on the maximum dimensionless seabed shear stress beneath the pipeline, θ_{max}, is quantified, and an equation with a better correlation for the prediction of θ_{max} is proposed. In addition, published experimental data have been compiled and fitted with a newly developed equation, to quantify the influence of θ_∞ and Re on the equilibrium scour depth, S_{eq}, and consequently, a higher correlation for the prediction of S_{eq}/D is obtained as compared to existing formulae, as this work considered both clear-water and live-bed conditions.

5.2 Methods

5.2.1 Overview

Firstly, verification and validation were performed by: (1) employing three different mesh densities to quantify the corresponding change in the computed maximum seabed shear stress beneath the pipe, τ_{max}; and, (2) using the same RANS approach to model an experiment conducted by Bearman and Zdravkovich [17]. Secondly, 243 CFD simulations were

performed to compute the seabed shear stresses underneath pipelines of various diameters and e_o/D, under various flow conditions. The simulation results were used to quantify the influence of the Reynolds number on the maximum dimensionless seabed shear stress beneath the pipe, θ_{max}. The correlation of Eq. (5.1) from Lee *et al.* [127] with the simulation results was compared against a new equation, which was introduced in this paper for predicting θ_{max}. The aim of predicting θ_{max} was to compare the predicted value with the critical dimensionless shear stress, θ_{cr}, to determine whether scour would occur underneath the pipe. Finally, experimental measurements [3, 8, 12] of the equilibrium scour depth beneath the pipe, S_{eq}/D, for various conditions were extracted, and subsequently, a new equation for predicting S_{eq}/D was proposed whilst quantifying the influence of θ_∞ and Re on S_{eq}/D. The numerical model in this chapter focused on the initiation of scour, while published experimental data were used to develop a separate empirical formula to predict the equilibrium scour depth beneath the pipe.

5.2.2 Computational fluid dynamics

5.2.2.1 General modelling approach

Numerous 2-D steady RANS simulations were performed using a finite-volume-based solver, STAR-CCM+ V10, to compute the seabed shear stresses beneath the pipe, whereby the same numerical model from Chapter 4 was used. The seabed shear stress, τ_b, was calculated from the friction velocity, u_*, via $\tau_b = \rho u_*^2$ [37], where ρ is the density of the fluid medium. The CFD computations involved solving the Reynolds averaged form of the incompressible single-phase mass and momentum equations; for further details, the interested reader is referred to Tu *et al.* [130]. The *k*-ω Shear Stress Transport (SST) turbulence model [65] was employed because it is suitable for modelling complex flows which involve separation [89]. In addition, the accuracy of the *k*-ω SST model has been demonstrated by modelling flow around a cylinder (e.g. [91]), as well as flow around a cylinder which was placed on a flat bed (e.g. [39]). The inherent blending functions enable the *k*-ω SST model to switch between the *k*-ω model [90], which is adequate for modelling boundary layer flow, and the *k*-ε model [36], which is appropriate for the fully-turbulent region outside of the boundary layer. In regard to surface roughness, STAR-CCM+ [37] adopted the approach for defining a rough wall boundary condition from Yoon and Patel [93], which is described in Chapter 3.

5.2.2.2 Boundary conditions

The dimensions of the computational domain are presented in Figure 5.1. The dimensions of the domain were set to be very large (i.e. 160 m, or at least 100*D*, from the centreline of the pipe) and held constant, not only to diminish artificial blockage effects but also to maintain the upstream dimensionless seabed shear stress when investigating the effects of varying the external pipe diameter.

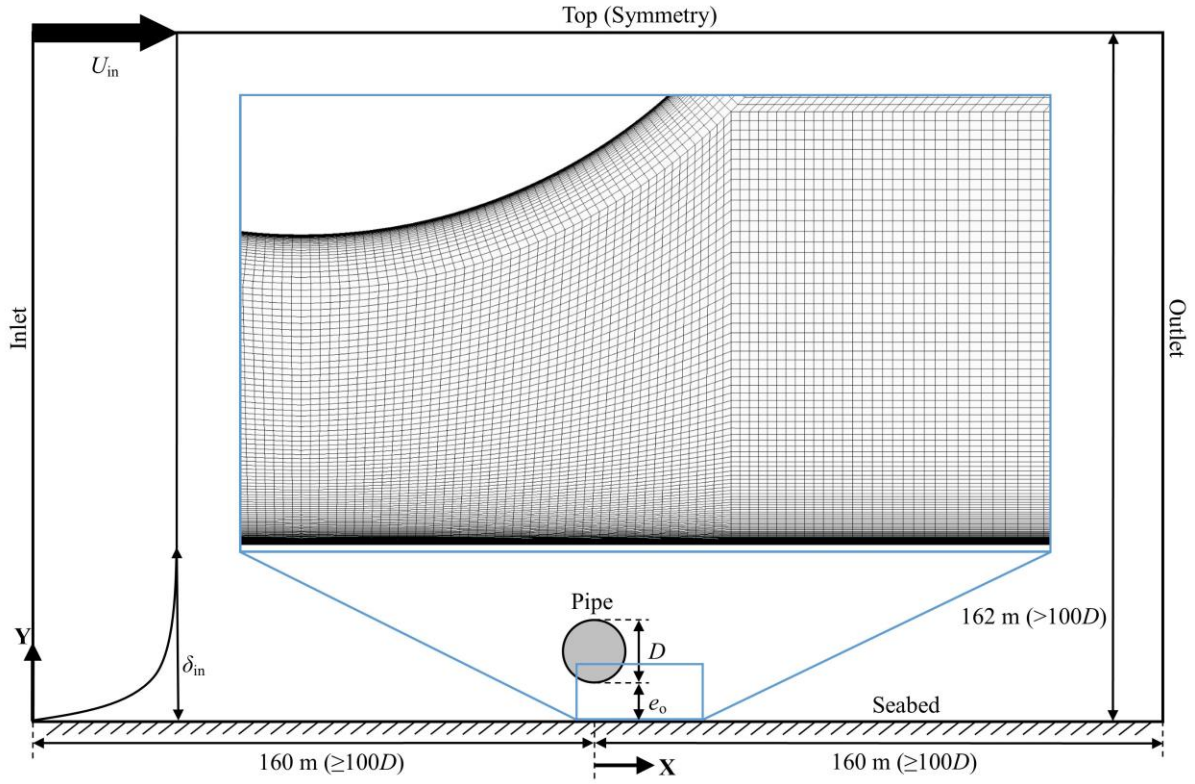

Figure 5.1: A schematic diagram illustrating the 2-D computational domain employed for all CFD computations (not to scale). The blue box shows a close-up view of the mesh between the pipe and the seabed, for e_o/D = 0.28.

An enlarged panel which is outlined in blue shows a sample 2-D structured mesh for the case of e_o/D = 0.28. The mesh resolution corresponded to a maximum wall y^+ value on the pipe and along the seabed of approximately 1.46 among all cases, as Menter [65] recommended a target value of $y^+ < 3$. The intended y^+ value was low, to ensure that the flow around the near-wall region was resolved. In addition, it was not feasible to have a high y^+ while having a very small e_o/D. The low y^+ value is well within the mesh requirements of the roughness

model when used with the all y^+ wall treatment model, provided that the distance from the wall to the centroid of the adjacent cell exceeds the roughness height [37].

Table 5.1 summarises the boundary conditions which were employed for the CFD computations, which are similar to that presented in Chapter 4. At the inlet boundary, a logarithmic velocity profile for a rough seabed was specified for the stream-wise flow velocity using Eq. (5.2) [87]:

$$U_{\mathrm{x}}(y) = \frac{u_*}{\kappa} \ln\left(\frac{y}{z_{\mathrm{o}}}\right) \tag{5.2}$$

where U_{x} is the stream-wise flow velocity; u_* is the friction velocity; the von Kármán constant, $\kappa = 0.4$ [87, 115]; y is the wall-normal distance and was assumed to be bounded by $z_{\mathrm{o}} \leq y \leq \delta_{\mathrm{in}}$, where δ_{in} is the incoming boundary layer thickness; and, z_{o} is the seabed roughness height. Thus, the stream-wise velocity within the boundary layer at the inlet boundary was defined via Eq. (5.2), whilst the stream-wise velocity above the boundary layer was set to equal to the incoming free-stream current velocity, U_{in}, for which the range of values are listed in Table 5.2. The velocity in the y-direction, U_{y}, was set to zero at the inlet boundary. A seawater density, ρ, of 1026.236 kg/m^3 and fluid kinematic viscosity, ν, of 1.2205×10^{-6} m^2/s was used, for a seawater temperature of 14 °C [84]; this was selected based on the average seawater temperature recorded in [127].

The turbulence kinetic energy, k, and the specific turbulence dissipation rate, ω, were calculated in STAR-CCM+ using the specified turbulence intensity, I_{t}, and turbulent viscosity ratio, μ_{t}/μ. A constant inlet turbulence intensity, I_{t} , of 1% was applied, as well as a turbulent viscosity ratio, μ_{t}/μ, of 10, which were the values recommended by STAR-CCM+ while using the k-ω SST model. As the pipe and seabed were set to be rough walls, was specified using the method presented in Section 3.2.1.

The outlet boundary was assigned as a pressure outlet, at which the relative pressure was set to zero. The turbulence intensity and turbulent viscosity ratio were kept similar to that as specified at the inlet boundary. The top boundary was assigned as a symmetry plane, whereby the shear stress is zero, and the velocity and pressure were extrapolated from the adjacent

cells. The inlet, outlet, and top boundaries were all positioned very far away from the pipe (i.e. at least 100*D*) to minimise their influence on the velocity field around the pipe

Table 5.1: Boundary conditions employed for the CFD computations

Boundary	Parameter	Condition/Value
Inlet	Stream-wise velocity	$U_{\mathrm{x}}(y)=\frac{u_*}{\kappa}\ln\left(\frac{y}{z_{\mathrm{o}}}\right)$ for $z_{\mathrm{o}} \le y \le \delta_{\mathrm{in}}$ $U_{\mathrm{x}}(y)=U_{\mathrm{in}}$ for $y > \delta_{\mathrm{in}}$
	Cross-stream velocity	$U_{\mathrm{y}}(y)=0$
	Turbulence intensity	I_{t} = 1%
	Turbulent viscosity ratio	μ_{t}/μ = 10
	Turbulence kinetic energy	Calculated
	Specific turbulence dissipation rate	Calculated
Outlet	Gauge pressure	0 Pa
	Turbulence intensity	I_{t} = 1%
	Turbulent viscosity ratio	μ_{t}/μ = 10
	Turbulence kinetic energy	Calculated
	Specific turbulence dissipation rate	Calculated
Pipe	Shear stress specification	No-slip
	Turbulence kinetic energy	Calculated
	Specific turbulence dissipation rate	$\omega=\frac{u_*^2 S_{\mathrm{r}}}{\nu}$
Seabed	Shear stress specification	No-slip
	Turbulence kinetic energy	Calculated
	Specific turbulence dissipation rate	$\omega=\frac{u_*^2 S_{\mathrm{r}}}{\nu}$
Top	Shear stress specification	Symmetry plane

The pipe and seabed boundaries were assigned as rough, no-slip walls. The influence of marine growth on the pipe was not considered, where the dimensionless pipe roughness, k/D, was held constant at 2×10^{-5}, representing smooth pipes [116]; however, a range of seabed roughness heights, z_{o}, were considered. The seabed roughness height can be estimated via a combination of the following assumptions: (1) where the flow is hydrodynamically rough [87], and hence $z_{\mathrm{o}} = k_{\mathrm{s}}/30$, where k_{s} is the Nikuradse roughness; subsequently, (2) $k_{\mathrm{s}} = 2.5d_{50}$ [95, 115], where d_{50} is the median sediment grain size. Thus, the seabed roughness height was specified based on the equivalent median sediment grain size, whereby $z_{\mathrm{o}} = d_{50}/12$.

5.2.2.3 Parametric study

A range of external pipe diameters, D, elevations of the bottom of the pipe with respect to the far-field seabed, e_o/D, seabed roughness heights, z_o, incoming boundary layer thicknesses, δ_{in}, and incoming free-stream current velocities, U_{in}, were considered, while the size of the computational domain was held constant. The range of values for every parameter is presented in Table 5.2. Three levels were established for each parameter, with reference to the 3^k factorial design [131]. As a total of five parameters were considered, that brought the total number of simulations to 243.

Table 5.2: Parametric study: range of values considered for the CFD computations

Parameter	Values considered
External pipe diameter, D	0.1 m, 0.4 m, 1.6 m
Pipe elevation, e_o/D	0.07, 0.14, 0.28
Seabed roughness height, z_o	7.2×10^{-6} m, 1.8×10^{-5} m, 4.5×10^{-5} m
Equivalent median sediment grain size, d_{50}	0.086 mm, 0.216 mm, 0.540 mm
Dimensionless pipe roughness, z_p/D	2×10^{-5} (i.e. smooth [21])
Incoming boundary layer thickness, δ_{in}	0.16 m, 1.60 m, 16.0 m
Incoming free-stream current velocity, U_{in}	0.05 m/s, 0.25 m/s, 1.25 m/s
Upstream dimensionless seabed shear stress, θ_∞	2.07×10^{-4} — 0.89
Pipe Reynolds number, Re	4.07×10^3 — 1.64×10^6
Maximum non-dimensional wall distance, y^+_{max}	1.46

The range of external pipe diameters considered in the simulation bounded typical subsea pipelines (i.e. 200 mm to 1000 mm [1]). The range of seabed roughness heights represented median sediment grain sizes ranging from very fine sand to coarse sand (i.e. 0.086 mm to 0.540 mm, respectively [33]). This was mainly selected for numerical stability, as the roughness lengths should be smaller than the cell height at the bed and pipe boundaries [37]. A wide range of incoming boundary layer thicknesses, δ_{in}, was considered as it has been shown to have a significant impact on the flow field around the pipe in previous work [19, 38, 132]. Different δ_{in} values, instead of δ_{in}/D were defined, so that the upstream dimensionless seabed shear stress, θ_∞, which is a function of δ_{in}, will be constant while the pipe diameter was varied to investigate the effects of the change in pipe Reynolds number. Finally, the range of incoming current velocities was selected to cover the full range of expected currents.

5.2.2.4 Verification and validation

Verification has been performed to estimate the numerical uncertainty associated with the CFD simulations, by observing the changes in the computed results (i.e. maximum seabed shear stress beneath the pipe, τ_{max}) with an increase in the number of cells (i.e. spatial resolution of the mesh in the x and y directions). The number of mesh points around the pipe was increased by a factor of two, and this was followed by refinement at the region in between the pipe and the seabed. The test conditions and results of the mesh refinement study are presented in Table 5.3.

Table 5.3: Mesh refinement study

Number of cells	Pipe elevation, e_o/D	External pipe diameter, D (m)	Seabed roughness height, z_o (m)	Pipe roughness height, z_p (m)	Incoming free-stream current velocity, U_{in} (m/s)	Max. seabed shear stress, τ_{max} (Pa)	Relative change, $\Delta\tau_{max}$ (%)
44,860	0.14	0.5	2.14×10^{-5}	2.14×10^{-5}	0.20	0.1718	-
148,758	0.14	0.5	2.14×10^{-5}	2.14×10^{-5}	0.20	0.1734	0.90
494,306	0.14	0.5	2.14×10^{-5}	2.14×10^{-5}	0.20	0.1737	0.16

In regard to validation, an experiment conducted by Bearman and Zdravkovich [17] was modelled, to compare the computed and measured pressure distribution along a flat plate beneath a pipe, at an elevation of $e_o/D = 0.1$, and $Re = 4.8 \times 10^4$. A computational domain similar to that as shown in Figure 5.1 was used, whilst adopting the same RANS approach with the k-ω SST model. The mean pressure coefficient, C_{pm}, at different locations along the plate was calculated via:

$$C_{pm} = \frac{p_f - p_\infty}{0.5\rho U_{in}^2} \tag{5.3}$$

where p_f is the normal fluid pressure along the flat plate, p_∞ is the pressure taken at the leading edge of the plate (i.e. 36D upstream from the pipe), and U_{in} is the incoming free-stream flow velocity.

5.2.3 Proposed maximum dimensionless seabed shear stress prediction

The main parameter of interest, in terms of the CFD simulations, was the maximum seabed shear stress or friction velocity beneath the pipe. As a single-phase model with a rigid seabed was adopted in this work, the maximum seabed shear stress, θ_{max}, was non-dimensionalised in the following manner:

$$\theta_{max} = \frac{\tau_{max}}{(\rho_s - \rho) g d_{50}} \tag{5.4}$$

where τ_{max} is the computed local maximum seabed shear stress underneath the pipe; g is gravitational acceleration; and, ρ_s, the sediment density, was assumed to be 2650 kg/m^3 in this paper [87]. However, a change in the density of natural sand (e.g. 2760 kg/m^3) does not influence the final constants in a newly developed equation for predicting θ_{max} by very much (i.e. approximately 0.3% difference). This was followed by fitting the aforementioned newly developed equation, which is an extended form of Eq. (5.1), to the simulation results:

$$\theta_{max} = \theta_{\infty} + \theta_{\infty}^{\alpha_1} \left(\frac{U_o D}{\nu} \right)^{\alpha_2} \left(\frac{1}{\exp(e_o/D)} \right)^{\alpha_3} \tag{5.5}$$

where θ_{∞} is the upstream dimensionless seabed shear stress, which was calculated based on the seabed shear stress sampled at 10D upstream from the pipe, τ_{∞}; U_o is the depth-averaged stream-wise current velocity which was also sampled at 10D upstream from the pipe, and not the value at the inlet boundary; ν is the kinematic viscosity of the fluid; and, α_1, α_2 and α_3, are constants which were obtained via unconstrained nonlinear optimisation. This equation was developed based on Eq. (5.1) from Chapter 4 [127], wherein a good correlation between θ_{∞}, e_o/D, and θ_{max} have been reported. As the influence of the Reynolds number on θ_{max} has not been quantified, the Reynolds number term was added into Eq. (5.5). This endeavour was also motivated by the fact that θ_{∞}, Re, and e_o/D, have been reported to influence the equilibrium scour depth in Sumer and Fredsøe [9]. The rationale behind the formulation of Eq. (5.5) was to ensure that:

- when $e_o/D = 0$, $1/\exp(e_o/D) = 1$, and thus θ_{max} does not equal to zero;
- when e_o/D tends towards infinity, its influence on θ_{max} diminishes as $1/\exp(e_o/D)$ would tend towards zero, and hence θ_{max} would then tend towards θ_∞; and,
- when $U_o = 0$, $\theta_{max} = 0$.

Similar to the process described in Chapter 4 [127], the values of the constants in Eq. (5.5), α_1, α_2 and α_3, were obtained by:

- initially having the constants set to equal to one;
- calculating the difference between θ_{max} obtained via CFD and θ_{max} estimated using Eq. (5.5);
- using unconstrained nonlinear optimisation [125] (i.e. *fminsearch* in MATLAB) to iteratively compute the values for the constants that would result in the smallest squared difference, thus resembling the 'least squares' approach; and,
- assessing the corresponding squared correlation coefficient, R^2, calculated via [26]:

$$R^2 = 1 - \frac{\sum_{i=1}^{N} (f_i - y_i)^2}{\sum_{i=1}^{N} (y_i - \bar{y})^2} \tag{5.6}$$

where f_i is the value of θ_{max} predicted via Eq. (5.5); y_i is the value of θ_{max} computed via CFD; and, $\bar{y}$ is the mean of the values of θ_{max} which were obtained via CFD.

The correlation of Eq. (5.5) with the simulation results was also compared against that of Eq. (5.1) from Chapter 4 [127], with the original constants, and with updated constants based on the present simulation results. Overall, the prediction of the maximum dimensionless seabed shear stress underneath the pipe, θ_{max}, was of interest; because the maximum shear stress can be compared with the critical shear stress to predict the occurrence of scour, which may progress towards an equilibrium state. Although the seabed shear stress amplification factor does portray the extent to which the shear stress beneath the pipe has increased with respect to the upstream shear stress, a high amplification may not necessarily result in scour occurring when the maximum shear stress is below the critical shear stress.

5.2.4 Proposed equilibrium scour depth prediction

An additional equation was developed and fitted to experimental measurements which were obtained from published literature [3, 8, 12], to quantify the influence of θ_∞ and *Re* on the dimensionless equilibrium scour depth, S_{eq}/D:

$$\frac{S_{eq}}{D} = \tanh\left(\beta_1\theta_\infty\right)\cdot\left(\frac{U_o D}{\nu}\right)^{\beta_2}\cdot\coth\left(\beta_3\frac{h}{D}\right)\cdot\left(\beta_4+\operatorname{sech}\left(\beta_5\frac{e_o}{D}\right)\right) \tag{5.7}$$

for which the values for the constants, β_1, β_2, β_3, β_4, and β_5, were determined using the same aforementioned optimisation process (Section 5.2.3). It is worth noting that S_{eq}/D was defined as the equilibrium scour depth directly beneath the vertical centreline of the pipe, instead of the maximum scour depth, S_{max}; refer to Figure 1.2 for the definition of the key terms. This is because the deepest point in a scour hole tends not to be directly underneath the bottom of pipe, and in some cases, the maximum scour depth can occur farther than 2*D* downstream from the pipe's centreline [133]. Eq. (5.7) was proposed based on the observed key variables which have been identified through previous experimental results, through which it was suggested that the equilibrium scour depth is influenced by e_o/D [1, 8], θ_∞ [3, 9] and *Re* [9]. The influence of θ_∞ on S_{eq}/D have been shown to be significant, especially for the clear-water condition [3]. However, this term was not considered in the existing formulae for predicting S_{eq}/D with $e_o/D \geq 0$ [1, 8], because they are only applicable for the live-bed condition. In terms of the influence of *Re* on S_{eq}/D, although it has been reported to be small [8], it has not been quantified in an equation for predicting S_{eq}/D.

Similar to Eq. (5.5), the rationale behind the formulation of Eq. (5.7) was to ensure that:

- when $e_o/D = 0$, $\operatorname{sech}(\beta_5 e_o/D) = 1$, and thus S_{eq}/D does not tend towards zero;
- when e_o/D tends towards infinity, its influence on S_{eq}/D diminishes as $\operatorname{sech}(\beta_5 e_o/D)$ would tend towards zero, and S_{eq}/D would not tend towards infinity;
- when h/D tends towards infinity, its influence on S_{eq}/D diminishes as $\coth(\beta_3 h/D)$ would approach unity; and,
- when $U_o = 0$, $S_{eq}/D = 0$.

The effect of the water depth was taken into consideration for predicting S_{eq}/D, while it was not considered in Eq. (5.5) for the prediction of θ_{max} where only deep-water conditions have been modelled via CFD. A h/D term was included in Eq. (5.7) because a significant portion of the experimental data involved relatively shallow waters, where about 30% of the cases had $h/D < 2$.

The investigation on the influence of pipe roughness or marine growth on S_{eq}/D was not within the scope of this paper. It has been reported that vortex shedding off the pipe is influenced by the pipe roughness [134]. However, the experimental results of Sumer and Fredsøe [9] have suggested that there is a negligible difference between the equilibrium scour depth directly beneath the pipe attained with a smooth pipe and that attained with a rough pipe, for which the dimensionless pipe roughness, $z_p/D = 0.1$. Nonetheless, it is rather interesting that for the case of a rough pipe, the maximum scour depth slightly downstream from the vertical centreline of the pipe and the length of the scour hole were slightly deeper and longer, respectively. Thus, these findings could be attributed to the pipe roughness which may require further investigation.

The correlation of Eq. (5.7) with the experimental data was compared against that of the equation from Sumer and Fredsøe [1], and the equation from Moncada-M and Aguirre-Pe [8] with the original constants as well as updated constants based on the compiled experimental data. Overall, with known constants, Eq. (5.7) can be used to predict the equilibrium scour depth beneath a pipe with an elevation with respect to the far-field seabed, for both clear-water and live-bed conditions.

5.3 Results

This section presents the results of the verification and validation study, parametric study, and the compilation of experimental measurements of S_{eq}/D from literature. Based on these results, the accuracy of the numerical approach adopted in this paper was quantified, and two newly developed equations were proposed for the prediction of the maximum dimensionless seabed shear stress beneath the pipe, θ_{max}, and the equilibrium scour depth beneath the pipe, S_{eq}/D.

5.3.1 Verification and validation

Table 5.3 presents the results of the verification, or mesh refinement study, whereby the relative changes in the maximum seabed shear stress beneath the pipe were seen to be very small (i.e. less than 1%). As the numerical uncertainty, or more specifically, the grid uncertainty associated with the CFD computations was estimated to be 0.35%, the solution was considered to be mesh-independent. In addition, the residuals for continuity, X-momentum and Y-momentum were less than 10^{-4}. As the same CFD simulation setup was employed, further details on verification and validation can be found in Chapter 4 [127].

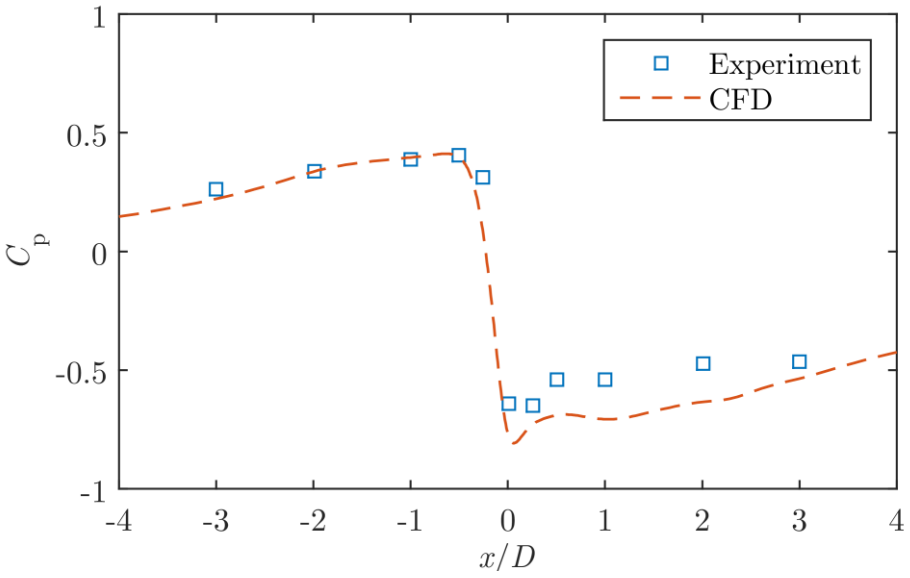

Figure 5.2: Modelling the experiment in Bearman and Zdravkovich [17], from which the non-dimensional pressure distribution along a flat plate beneath a pipe was calculated, where the zero crossing of x/D represents the vertical centreline of the pipe; $e_o/D = 0.1$ and $Re = 4.8 \times 10^4$.

Figure 5.2 presents the result of modelling the experiment of Bearman and Zdravkovich [17]. A good agreement between the experimental and CFD data was observed upstream of the pipe; however, the computed pressure was under-predicted just downstream of the pipe. Nevertheless, the error between the mean pressure coefficient, C_{pm}, calculated via CFD and that measured in Bearman and Zdravkovich [17] at $x/D = 0$ was approximately 18%. This discrepancy can be attributed to modelling uncertainties [120], potentially stemming from the use of the RANS approach along with the k-ω SST turbulence model; however, this was deemed acceptable, because attaining a smaller discrepancy may require partially resolving

the turbulent eddies downstream of the pipe (i.e. Large Eddy Simulation), which will greatly increase the computational load and is not appropriate for performing large parametric studies.

5.3.2 Maximum seabed shear stress prediction

A large parametric study involving 243 CFD simulations, which correspond to the conditions presented in Table 5.2, were performed to compute the maximum seabed shear stresses beneath the pipe. Both, the seabed shear stress amplification factor, τ_{max}/τ_{∞}, and maximum dimensionless seabed shear stress beneath the pipe, θ_{max}, were investigated. Figure 5.3a presents the influence of the pipe elevation with respect to the far-field seabed, e_o/D, on τ_{max}/τ_{∞}. From an overall perspective, τ_{max}/τ_{∞} was seen to decrease with an increase in e_o/D, looking at all of the data in Figure 5.3a. This overall trend was similar to that reported in Griffiths *et al.* [5]. Figure 5.3b shows that θ_{max} also decreased with an increase in e_o/D. e_o/D appeared to be an important variable, and the amplification of the flow between the pipe and the seabed is higher at smaller e_o/D, indicating a higher capacity for scour to occur.

Figure 5.4a presents the correlation between τ_{max}/τ_{∞} and the upstream dimensionless seabed shear stress, θ_{∞}. τ_{max}/τ_{∞} was seen to decrease exponentially with θ_{∞}, and appeared to approach an asymptote. This indicates that the amplification of the shear stress at very low values of θ_{∞} (i.e. the clear-water condition) was several times higher as compared to that at higher values of θ_{∞} (i.e. the live-bed condition). Furthermore, the rate of change of τ_{max}/τ_{∞} for $0 < \theta_{\infty} < 0.3$ was greater than that for $0 < e_o/D < 0.3$ (Figure 5.3a), suggesting that the influence of θ_{∞} for the clear-water condition is greater than that for e_o/D. In contrast, the trend observed in Figure 5.4b for θ_{max} differed significantly from τ_{max}/τ_{∞}, as θ_{max} was seen to increase relatively linearly with θ_{∞}. The potential for scour to occur beneath the pipe appeared to be high, even for the clear-water condition, due to the high amplification of the seabed shear stress. However, for the live-bed condition, the amplification of the shear stress remained relatively constant.

In order to determine whether scour would occur and progress towards an equilibrium condition, the predicted maximum seabed shear stress beneath the pipe can be compared to the critical shear stress for the sediment; thus this chapter focused on predicting θ_{max}, instead of τ_{max}/τ_{∞}. Figure 5.5a shows the correlation of Eq. (5.1) from Chapter 4 [127], with the original constants, with respect to the values of θ_{max} which were obtained via CFD in this

paper. The corresponding squared correlation coefficient, R^2, for Eq. (5.1) was approximately 0.59, indicating that there is a lack of consideration of a key parameter and/or the form of the equation can be improved.

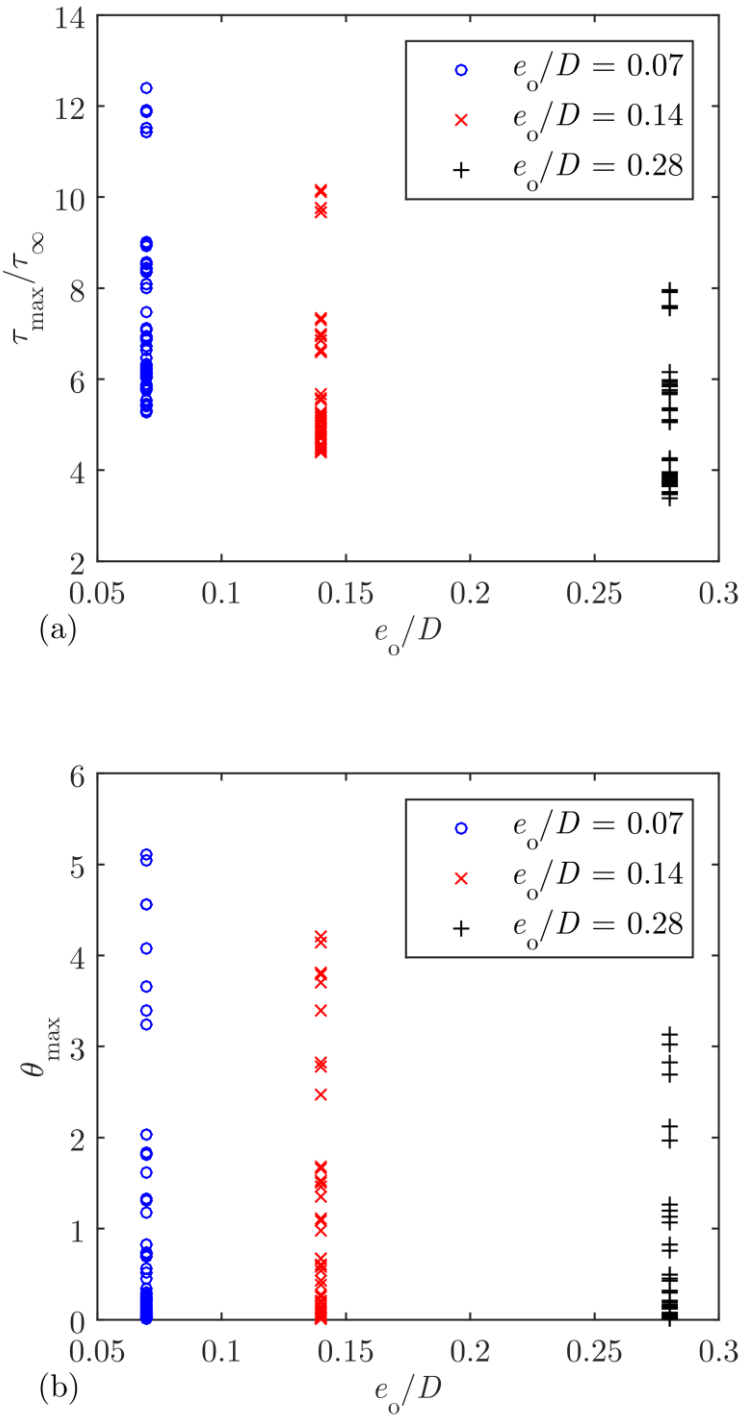

Figure 5.3: Comparison between the influence of e_o/D on: (a) the seabed shear stress amplification factor, τ_{max}/τ_∞, and (b) the maximum dimensionless seabed shear stress beneath the pipe, θ_{max}.

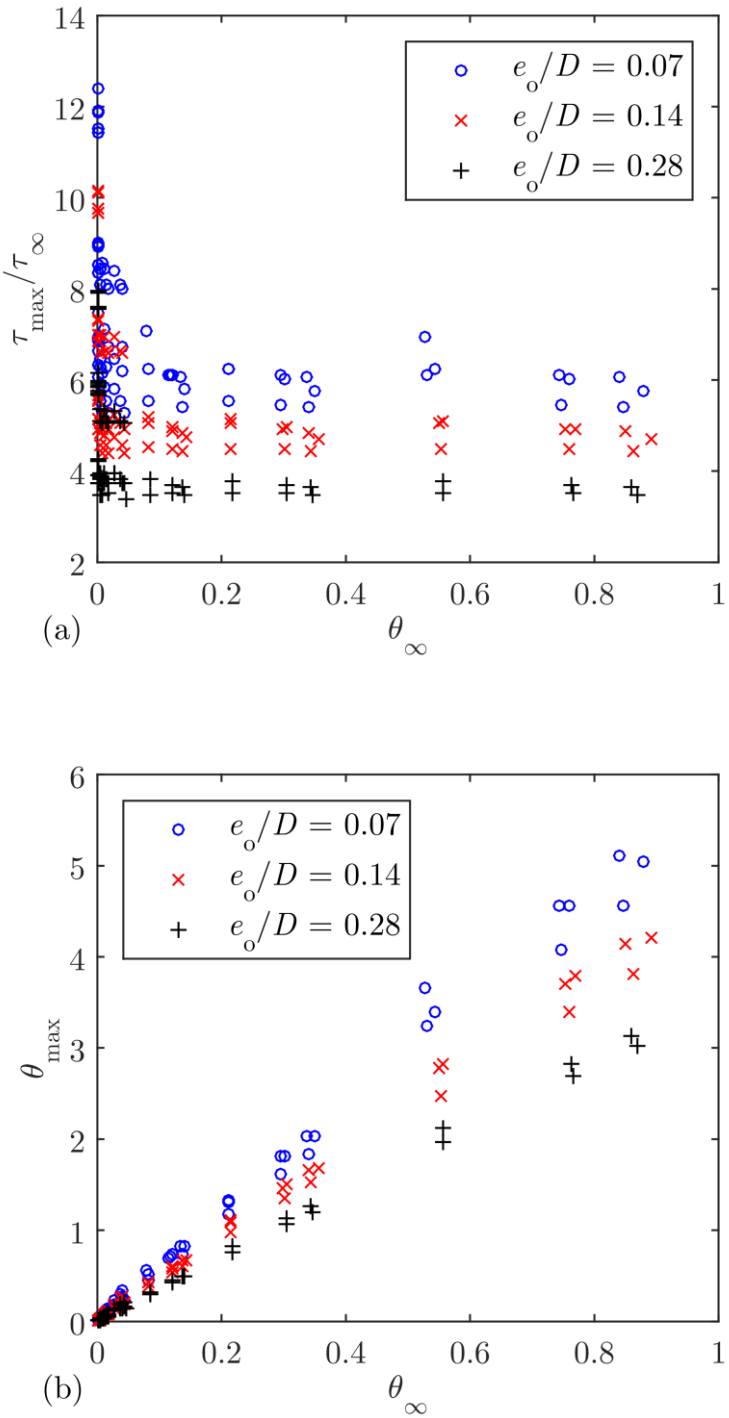

Figure 5.4: Comparison between the influence of θ_∞ on: (a) the seabed shear stress amplification factor, τ_{max}/τ_∞, and (b) the maximum dimensionless seabed shear stress beneath the pipe, θ_{max}.

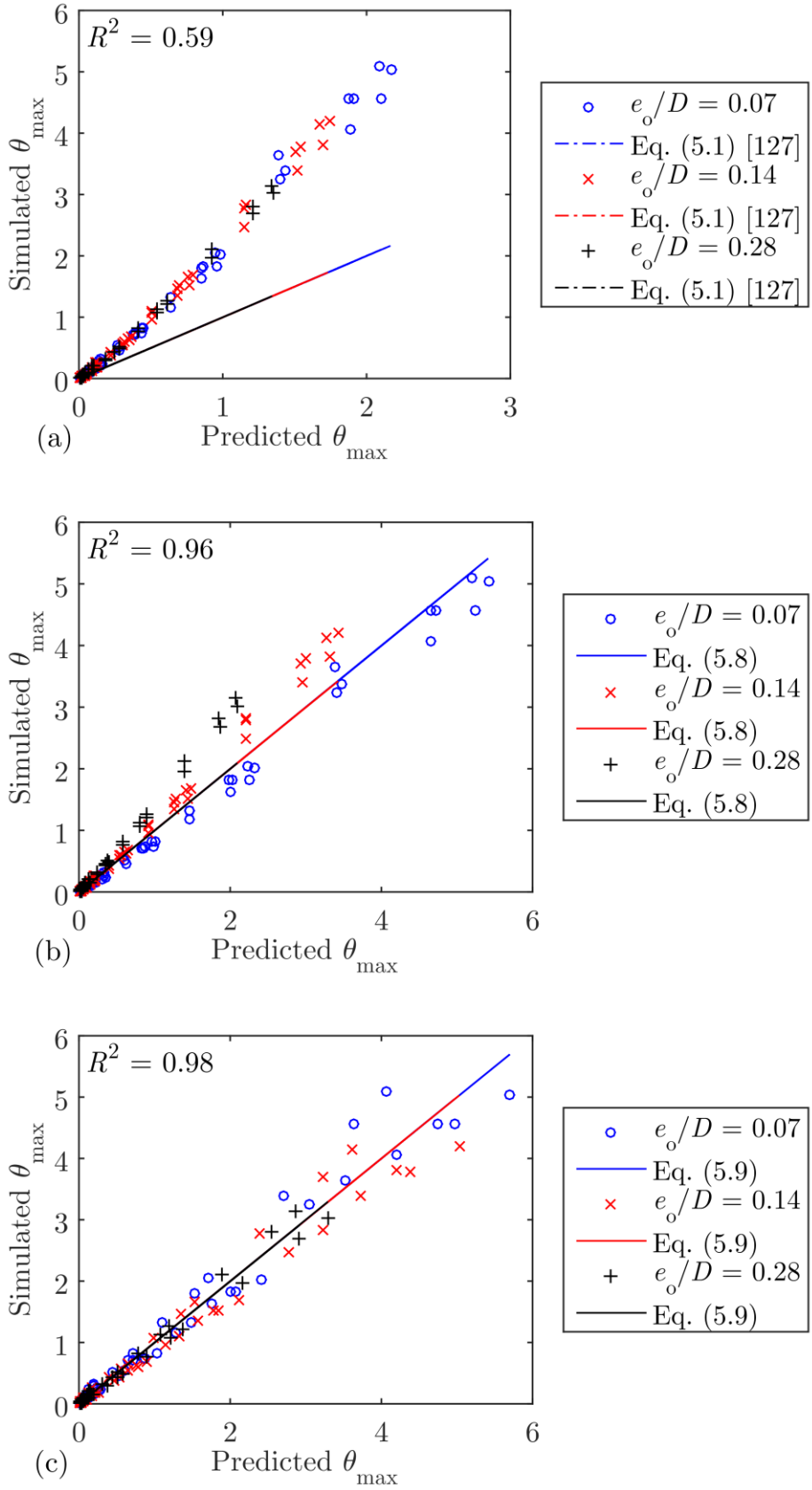

Figure 5.5: Comparing the correlation between θ_{max} simulated via CFD and: (a) θ_{max} calculated using Eq. (5.1) [127]; (b) θ_{max} calculated using Eq. (5.8); (c) θ_{max} calculated using Eq. (5.9).

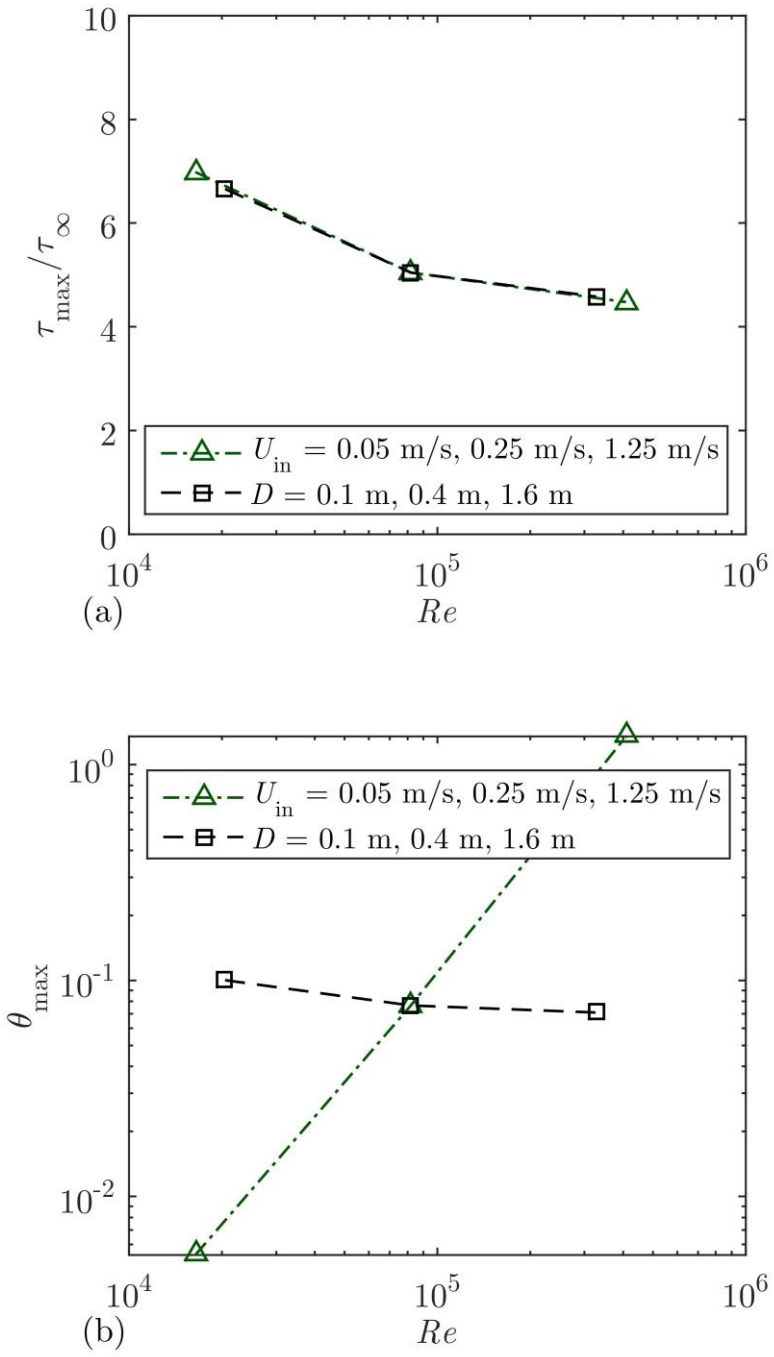

Figure 5.6: Influence of the Reynolds number, *Re*, on: (a) τ_{max}/τ_∞; and, (b) θ_{max}

The constants in Eq. (5.1) were modified using the optimisation process presented in Section 5.2.3 based on the values of θ_{max} simulated via CFD, and the following updated constants were obtained:

$$\theta_{max} = \theta_\infty^{\,0.92} \left(\frac{e_o}{D} \right)^{-0.68} \tag{5.8}$$

where the magnitude of both constants have increased. The correlation of Eq. (5.8) with the simulation results can be visualised in Figure 5.5b, where the corresponding R^2 was approximately 0.96, which was significantly higher than 0.59 for Eq. (5.1). The wider range of parameters that have been considered in this work, compared to Lee *et al.* [127], seemed to have significantly influenced the values of the constants in Eq. (5.8). However, the correlation of Eq. (5.8) with the simulation results was seen to decrease with an increase in e_o/D, suggesting that Eq. (5.8) may not be appropriate for predicting θ_{max} for $e_o/D > 0.14$.

As described in Section 5.2.3, Eq. (5.5) was developed to quantify the influence of the Reynolds number on θ_{max}, as well as to be compared against Eq. (5.1). With reference to Figure 5.5c, fitting Eq. (5.5) to the simulated θ_{max} values was seen to result in the highest R^2 of 0.98, with the following constants:

$$\theta_{max} = \theta_\infty + \theta_\infty^{0.93} \left(\frac{U_o D}{\nu} \right)^{0.13} \left(\frac{1}{\exp\left(e_o/D\right)} \right)^{2.38} \tag{5.9}$$

albeit a small value was obtained for the Reynolds number term, indicating that the influence of the Reynolds number on θ_{max} is small, when compared to θ_∞ and e_o/D. A slight under-prediction of θ_{max} was observed, which was more evident for the case of $e_o/D = 0.07$, at high values of θ_∞ (i.e. high current velocity); thus, a safety factor of 1.5 can be applied to the predictions of θ_{max} made using Eq. (5.9), for which the modelling uncertainty of 18% that was mentioned in Section 5.3.1 was also taken into account. Nevertheless, Eq. (5.9) had the highest correlation with the simulation results.

Figure 5.6a presents the influence of the Reynolds number on τ_{max}/τ_∞, or more specifically, the effects of the variation in external pipe diameter and upstream current velocity. The influence of the incoming free-stream current velocity, U_{in}, was investigated whilst all other parameters were held constant, such that $D = 0.4$ m, $e_o/D = 0.14$, $z_o = 1.8 \times 10^{-5}$ m, and $\delta_{in} = 1.6$ m, though it is worth noting that *Re* was calculated based on the depth-averaged current velocity at $10D$ upstream from the pipe. Similarly, the effect of the change in external pipe diameter, D, was investigated whilst $U_{in} = 0.25$ m/s, $e_o/D = 0.14$, $z_o = 1.8 \times 10^{-5}$ m, and $\delta_{in} = 1.6$ m. It can be seen in Figure 5.6a that both U_{in} and D had the same effect on τ_{max}/τ_∞, whereby τ_{max}/τ_∞ decreased with an increase in U_{in} or D; in contrast, in Figure 5.6b, θ_{max} was

seen to increase significantly with U_{in}, whilst slightly decreasing with an increase in D. This suggested that, for a constant current velocity and e_o/D, a larger pipe diameter would result in a slightly lower capacity for scour to occur beneath the pipe. However, the current velocity posed a significantly greater influence on θ_{max}, as compared to the external pipe diameter. The same trends were observed for other pipe elevations, e_o/D, seabed roughness heights, z_o, and incoming boundary layer thicknesses, δ_{in}.

5.3.3 Equilibrium scour depth prediction

Upon predicting the maximum seabed shear stress beneath the pipe, which can be compared to the critical shear stress to determine whether scour would progress towards an equilibrium state, the corresponding equilibrium scour depth, S_{eq}/D, would be of interest. Published experimental data [3, 8, 12] were compiled, to quantify the influence of the upstream dimensionless seabed shear stress, θ_∞, and the Reynolds number, Re, on S_{eq}/D, which have not been considered in existing formulae for predicting S_{eq}/D; a comparison of existing empirical formulae is presented in Chapter 2.

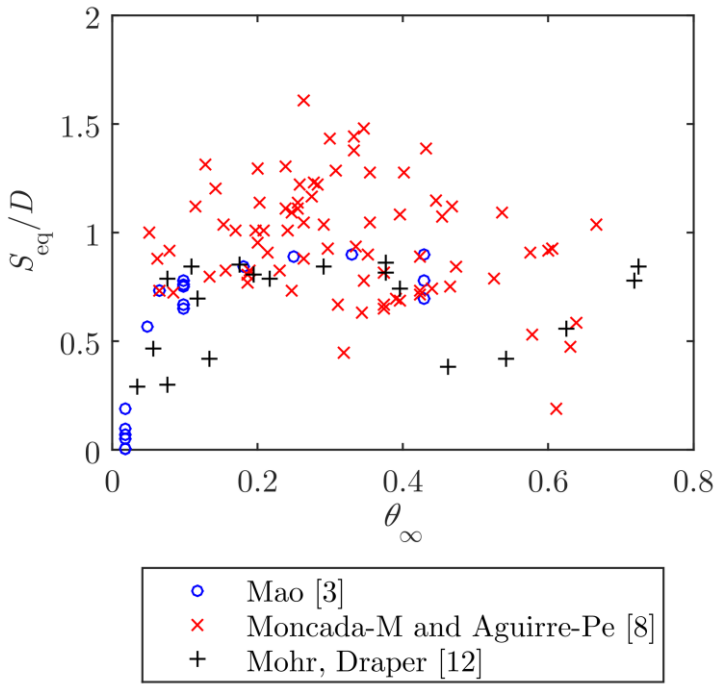

Figure 5.7: Correlation between the equilibrium scour depth, S_{eq}/D, and the upstream dimensionless seabed shear stress, θ_∞.

Figure 5.7 depicts the correlation between S_{eq}/D and θ_∞, in which S_{eq}/D was seen to increase rapidly at low values of θ_∞ (i.e. $\theta_\infty < 0.2$), and then mainly decrease in a more gradual manner. Figure 5.8 presents the correlation between S_{eq}/D and *Re*, wherein the experimental data from the individual sources seemed to suggest that S_{eq}/D slightly increased within a small range of *Re*. However, the overall trend portrayed in Figure 5.8 across a wider range of *Re* appeared to indicate a slight decrease in S_{eq}/D as *Re* increased.

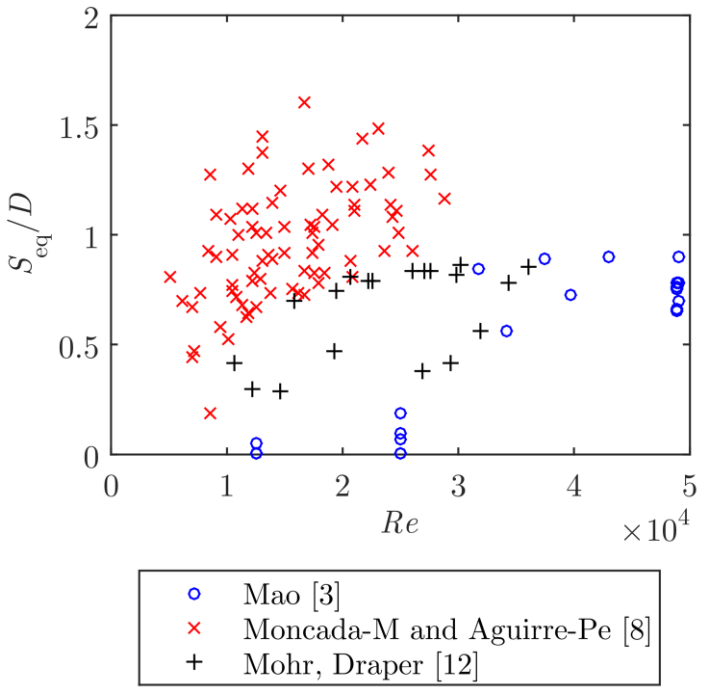

Figure 5.8: Correlation between the equilibrium scour depth, S_{eq}/D, and the Reynolds number, *Re*.

The non-dimensional elevation of the pipe with respect to the far-field seabed, e_o/D, appeared to pose a significant influence on the equilibrium scour depth. In Figure 5.9, S_{eq}/D was seen to decrease with an increase in e_o/D, with a more obvious gradient compared to the gradient observed in Figure 5.8 for *Re*, and that observed in Figure 5.7 at high values of θ_∞. This may have been the main motivation for Sumer and Fredsøe [1] to propose an equation for predicting S_{eq}/D with e_o/D being the only parameter in it. However, Figure 5.10 shows that there is also a rather clear correlation between S_{eq}/D and the water depth, h/D. S_{eq}/D was seen to decrease with an increase in h/D, which may have been largely influenced by the relatively shallow water depths employed in the laboratory experiments, especially Moncada-M and Aguirre-Pe [8], in which scour beneath pipelines in river crossings was of primary interest.

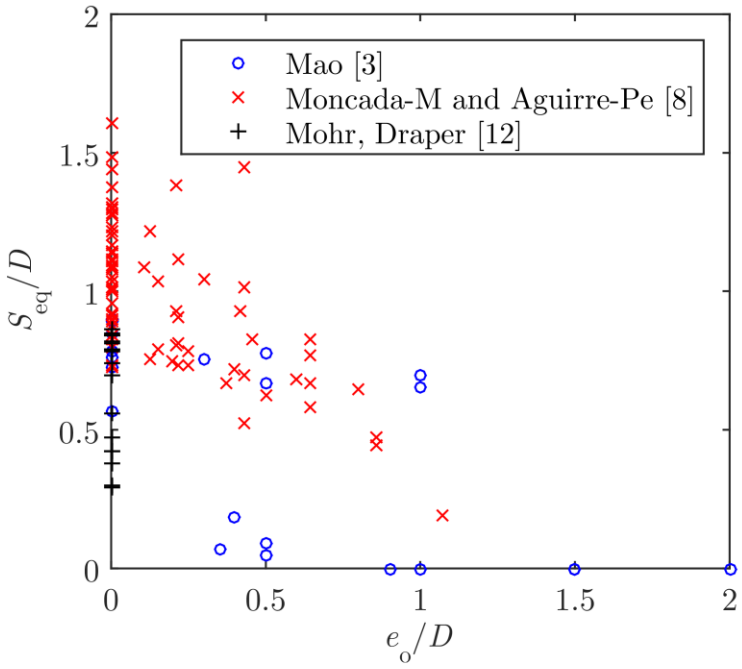

Figure 5.9: Correlation between the equilibrium scour depth, S_{eq}/D, and the non-dimensional pipe elevation with respect to the far-field seabed, e_o/D.

In this work, the correlation of Eq. (5.7) with the experimental measurements were compared against that of the equations from Sumer and Fredsøe [1] and Moncada-M and Aguirre-Pe [8], which are introduced in Chapter 2. The equations without the consideration of the e_o/D term (e.g. [24]) were not included in this comparison, because they predicted the same values of S_{eq}/D for different values of e_o/D, whereas the correlation presented in Figure 5.9 suggested otherwise. In Figure 5.11a, the equation proposed by Sumer and Fredsøe [1] was seen to have a poor correlation to the experimental measurements, despite the strong influence of e_o/D on S_{eq}/D that was observed in Figure 5.9. In addition, this equation is only applicable for the live-bed condition, which was initially logical, since Figure 5.7 showed a relatively weak correlation between S_{eq}/D and θ_∞ for high values of θ_∞, whereby the critical dimensionless shear stress for sand is typically less than 0.11 [33].

The correlation between the equation proposed by Moncada-M and Aguirre-Pe [8] and the experimental data was better than that of Sumer and Fredsøe [1], with a corresponding R^2 of 0.61 (Figure 5.11b). This improved correlation can be attributed to the strong influence of the water depth on S_{eq}/D, which was observed in Figure 5.10. It is interesting to note that, upon modifying the constants in this equation via the same optimisation process presented in

Section 5.2.3, the highest correlation obtained was an R^2 of approximately 0.66 (Figure 5.11c). The updated values for the constants are as follows:

$$\frac{S_{eq}}{D} = 1.84 \cdot \frac{U_o}{\sqrt{gh}} \cdot \text{sech}\left(1.24 \frac{e_o}{D}\right) \tag{5.10}$$

This was one of the motivations to develop a new closed-form equation for the prediction of S_{eq}/D, as there was a lack of consideration of other key parameters and/or the form of the existing formulae can be improved. Thus, Eq. (5.7) was developed in this work, by which the process is described in Section 5.2.4, and the following values for the constants were obtained via the same optimisation process that is presented in Section 5.2.3:

$$\frac{S_{eq}}{D} = \tanh\left(15.15\theta_\infty\right) \cdot \left(\frac{U_o D}{\nu}\right)^{-0.01} \cdot \coth\left(0.62 \frac{h}{D}\right) \cdot \left(-0.11 + \text{sech}\left(-1.08 \frac{e_o}{D}\right)\right) \tag{5.11}$$

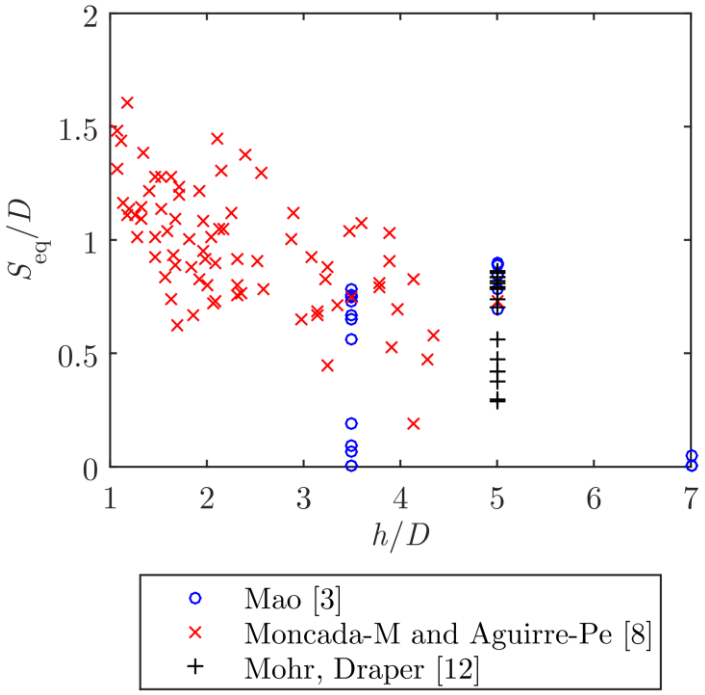

Figure 5.10: Correlation between the equilibrium scour depth, S_{eq}/D, and the dimensionless water depth or blockage ratio, h/D

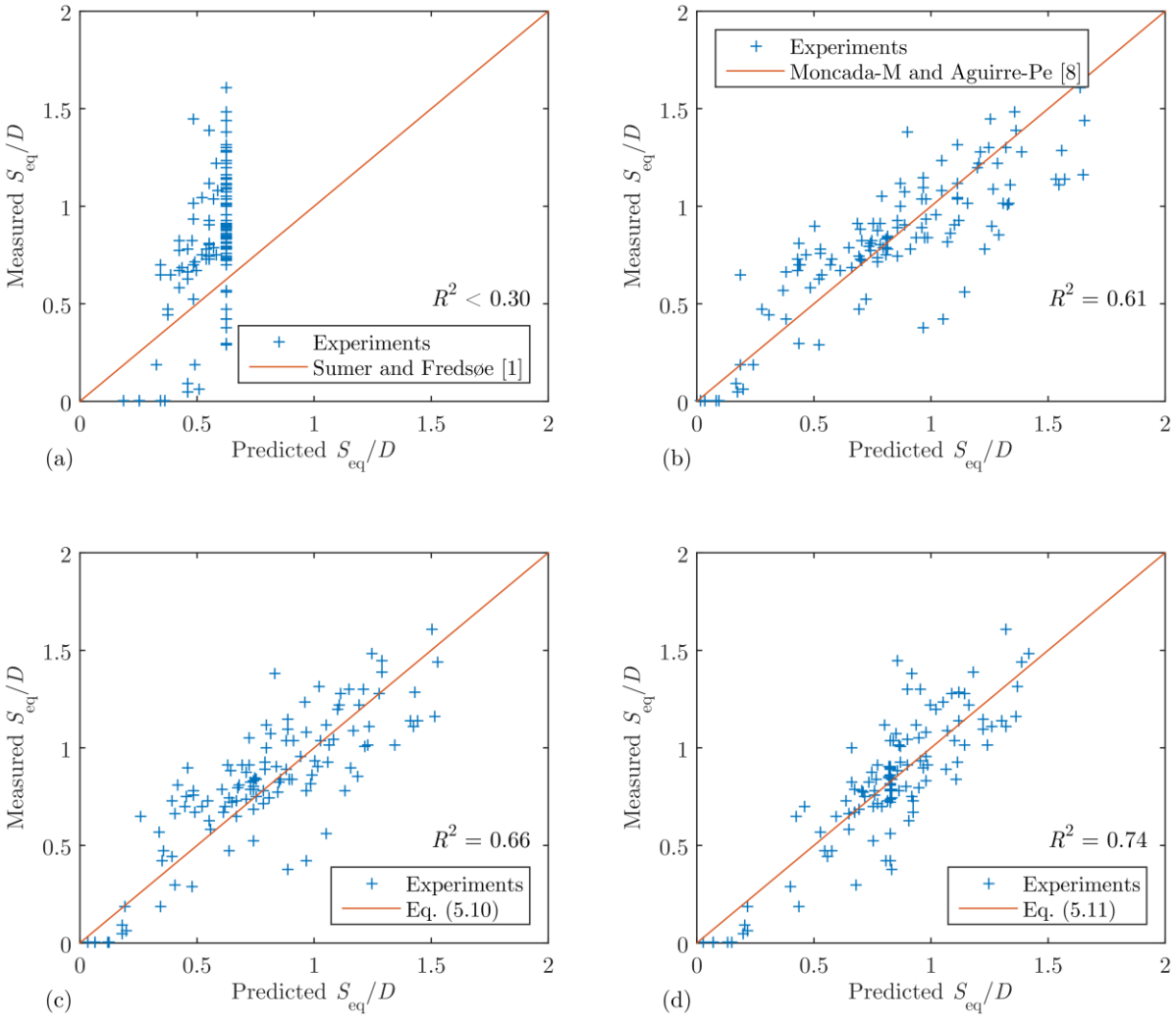

Figure 5.11: Comparing the dimensionless equilibrium scour depth, S_{eq}/D, measured via experiments, and S_{eq}/D predicted using: (a) the equation from Sumer and Fredsøe [1], where $R^2 < 0.3$; (b) the equation from Moncada-M and Aguirre-Pe [8], where $R^2 = 0.61$; (c) Eq. (5.10), where $R^2 = 0.66$; and, (d) Eq. (5.11), where $R^2 = 0.74$.

As seen in Figure 5.11d, the correlation between Eq. (5.11) and the experimental data was high, whereby $R^2 = 0.74$, indicating a step in the right direction, albeit the constant for the Reynolds number term seemed to be small, similar to the case of Eq. (5.9) for the prediction of θ_{max}. Based on the equations listed in Chapter 2, it can be argued that Eq. (5.11) is the most comprehensive one to date, as it was fitted to a wider range of experimental measurements. Furthermore, the influence of θ_∞ has been quantified and thus it is applicable for both clear-water and live-bed conditions.

5.4 Discussion

Additional CFD simulations involving an empty computational domain have been performed to observe the growth of the boundary layer along the length of the domain. Figure 5.12a depicts the computed stream-wise flow velocity profiles at different locations in a domain that has similar dimensions as that shown in Figure 5.1, but without the presence of a pipe, and a hypothetical pipe diameter of 1.6 m was used. Figure 5.12b shows the flow velocity profiles in a domain that has been extended threefold in length.

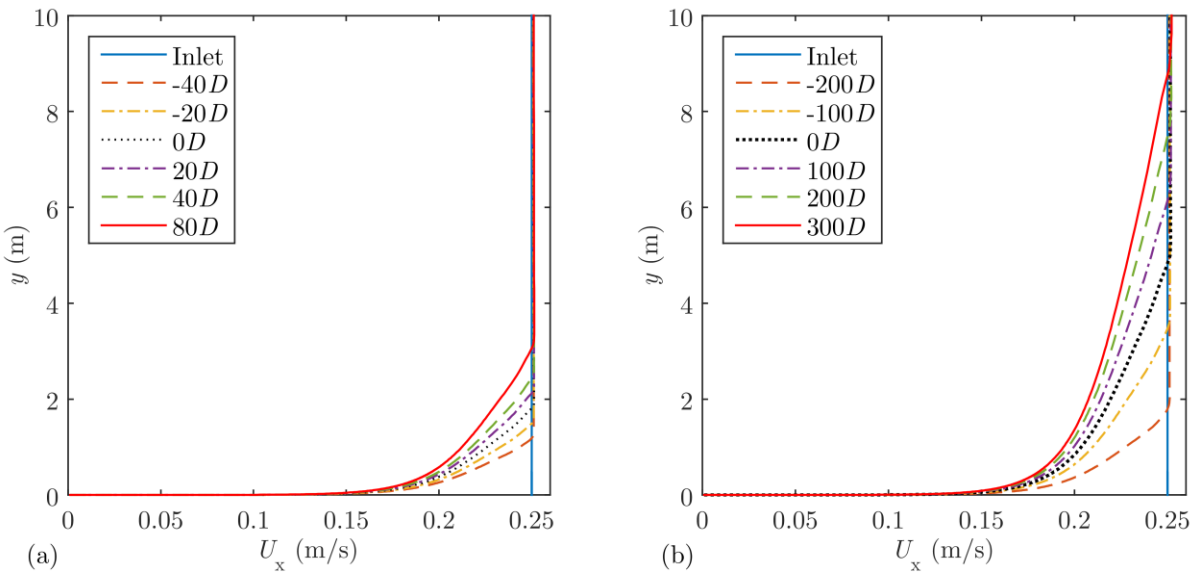

Figure 5.12: (a) Stream-wise flow velocity profiles at various distances from the centre of an empty domain, for a hypothetical pipe diameter, D = 1.6 m; incoming free-stream flow velocity at the inlet, U_{in} = 0.25 m/s; z_o = 1.8 × 10^{-5} m; and, incoming boundary layer thickness at the inlet, δ_{in} = 0 m; (b) Stream-wise flow velocity profiles for a similar case, except the domain length was extended from the centre to 300D on both sides, while the domain height was held constant.

These plots show that the boundary layer flow at the pipe was not at equilibrium, as the boundary layer thickness was seen to increase with the distance from the inlet boundary. Even with a very long domain (i.e. almost 1 km in length), the boundary layer was not at equilibrium. Based on fundamental fluid dynamics, the boundary layer over a flat plate is a continuously dissipative phenomenon in which the thickness is always growing [135]. However, it is hypothesised that that would be the case with an infinite water depth, whilst having a finite water depth may enable the attainment of an equilibrium profile. Nevertheless, for the case that is introduced in Figure 5.12a, the difference between the friction velocity at

10*D* upstream from the pipe and the friction velocity at 0*D* was only approximately 0.65%, with the assumption that *D* = 1.6 m. Hence, the difference in the friction velocities would be smaller for a smaller pipe diameter.

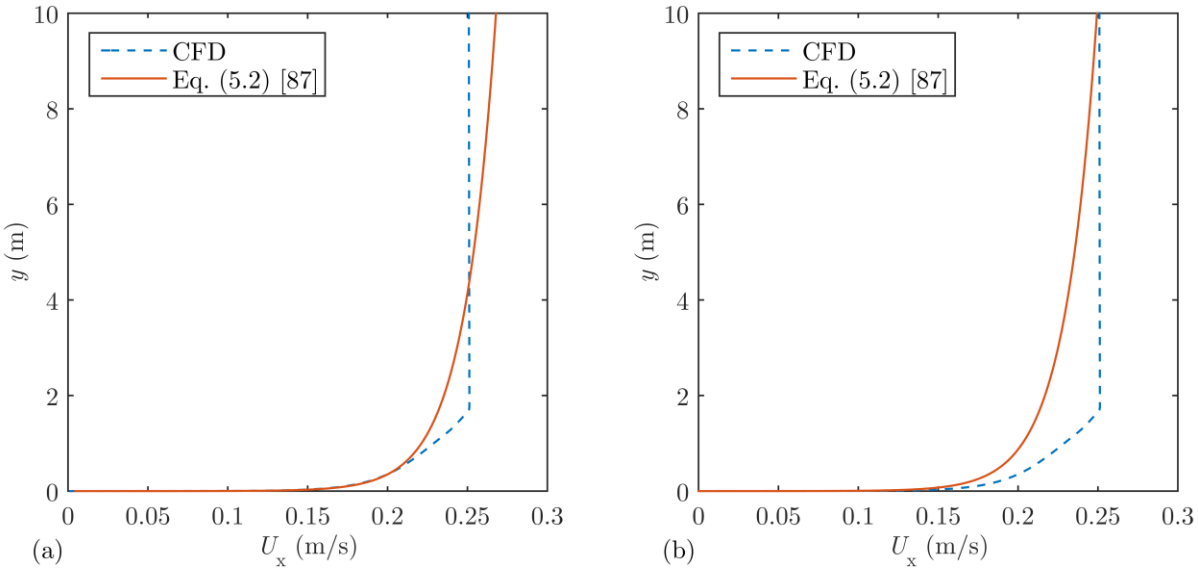

Figure 5.13: (a) Stream-wise flow velocity profiles in an empty domain at 10*D* upstream from a hypothetical pipe with a diameter of 1.6 m; incoming free-stream flow velocity at the inlet, U_{in} = 0.25 m/s; z_o = 1.8 × 10^{-5} m; incoming boundary layer thickness at the inlet, δ_{in} = 0 m; (b) Stream-wise flow velocity profiles for a similar case but with the seabed roughness height, z_o, set to 4.5 × 10^{-5} m.

It can be seen that the flow velocity profiles that were computed via CFD were not in equilibrium as compared to the velocity profiles plotted using Eq. (5.2) from Soulsby [87]. There seem to be a greater difference between the CFD and empirical values in Figure 5.13b, as compared to Figure 5.13a. The influence of the seabed roughness height, z_o, on the flow velocity profile appeared to be more significant based on Eq. (5.2) from Soulsby [87], as compared to the values that were computed via CFD. The difference between the CFD and empirical value in Figure 5.13b, for example, at 1.7 m from the bed, was about 18%, which was similar to the discrepancy between the CFD and experimental values when calculating the pressure distribution along a flat plate beneath a pipe for validation purposes.

The small difference in the velocity profiles predicted via CFD for different seabed roughness heights does not appear to be consistent with Eq. (5.2) from Soulsby [87]; however, the change in the flow velocity profile for a change in z_o was still less than 10% according to the empirical equation nonetheless. It may be worth conducting an investigation into the

roughness model; however, developing a new roughness model for CFD is beyond the scope of this work.

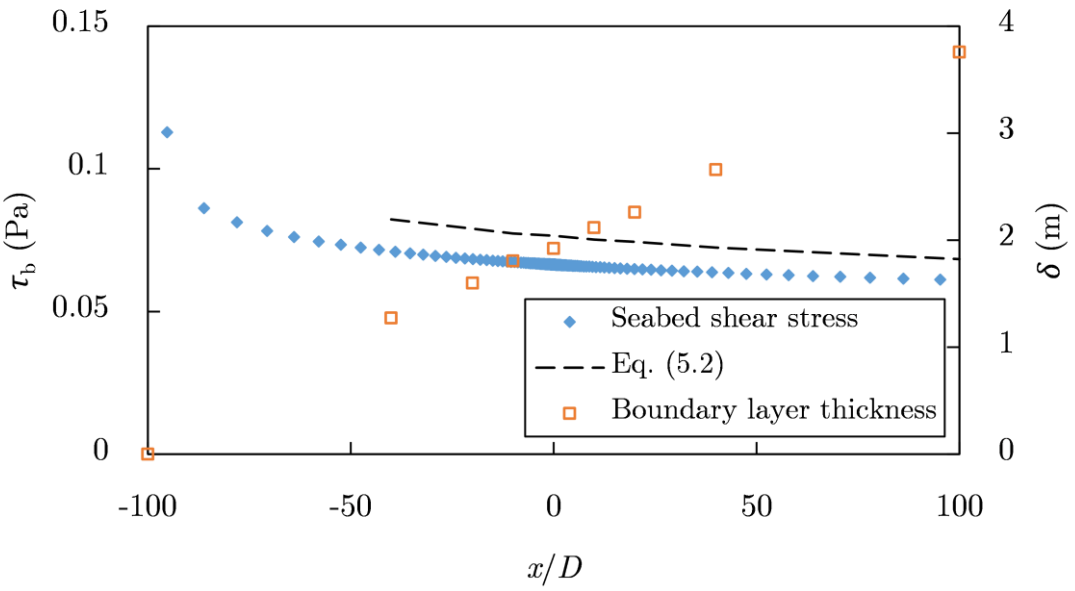

Figure 5.14: Boundary layer thickness, δ, at different locations along an empty domain, which were superimposed on the seabed shear stress, τ_b; a hypothetical pipe diameter, D, is assumed to be 1.6 m.

Figure 5.14 compares the change in the boundary layer thickness, δ, along the empty computational domain (i.e. same domain as that in Figure 5.12a) with the change in the seabed shear stress, τ_b. In this case, the boundary layer thickness was assumed to be the height at which the change in the stream-wise flow velocity was less than 0.1%. The seabed shear stress was computed via CFD, whilst the dashed line was plotted via Eq. (5.2) using the boundary layer thickness at different locations along the length of the domain. There seemed to be a good correlation between these results; whereby at $x/D = 0$, the difference between the computed seabed shear stress and that calculated using Eq. (5.2) was about 15%.

More importantly, although the boundary layer thickness was continuously increasing along the length of the domain, the change in the seabed shear stress was less significant. Between $x = 0D$ and $x = 100D$, the boundary layer thickness increased by more than 95%; however, the computed seabed shear stress only decreased by approximately 8%. This relationship between the boundary layer thickness and seabed shear stress is consistent with the formulation of Eq. (5.2). Thus, the fact that the boundary layer was growing along the length

of the domain may not be a major concern, in terms of investigating the maximum seabed shear stress beneath the pipe.

In addition, the equation for predicting the maximum seabed shear stress, Eq. (5.9), was fitted based on the friction velocity and depth-averaged flow velocity at 10*D* upstream from the pipe, and not the values at the inlet boundary. Furthermore, DNV GL [20] recommended that a height of more than 1 m above the seabed would be sufficient, in terms of defining the height at which the stream-wise flow velocity would only vary slightly. This is within the range of boundary layer thicknesses that have been considered in this work (i.e. 0.16 m, 1.60 m, 16.0 m). Therefore, for all practical purposes of pipeline design, Eq. (5.9) can be used to predict the maximum dimensionless seabed shear stress beneath the pipe.

The amplification of the seabed shear stress with respect to the upstream seabed shear stress, τ_{max}/τ_{∞}, was considered in this paper, as it was deemed to be an important parameter in previous research (e.g. [5]). Interesting trends have been observed, for example, τ_{max}/τ_{∞} slightly decreased with *Re* (Figure 5.6a), whilst S_{eq}/D has also been observed to slightly decrease with *Re* in previous studies (e.g. [9]) and in Eq. (5.11), in which the *Re* term has a small but negative exponent. In addition, τ_{max}/τ_{∞} was seen to decrease at a steeper gradient with an increase in e_o/D (Figure 5.3), whilst this downward trend was also observed in Figure 5.9 for S_{eq}/D.

In terms of the upstream dimensionless seabed shear stress, τ_{max}/τ_{∞} was seen to change rapidly at low values of θ_{∞}, but had an almost flat gradient for $\theta_{\infty} > 0.2$ (Figure 5.4), and likewise for S_{eq}/D (Figure 5.7), albeit a slight decrease in S_{eq}/D with an increase in θ_{∞} for $\theta_{\infty} > 0.2$. There seemed to be a correlation between τ_{max}/τ_{∞} and S_{eq}/D. However, a high amplification may not necessarily result in scour occurring when the maximum shear stress is below the critical shear stress. Therefore, this work mainly focused on the prediction of the maximum dimensionless seabed shear stress beneath the pipe, θ_{max}, which can be compared to the critical dimensionless seabed shear stress for a given sediment, θ_{cr}, based on various methods available in literature (e.g. [33, 34, 86]).

Eq. (5.9) was formulated in a different manner, as compared to Eq. (5.1), to quantify the effects of the Reynolds number, and to ensure that θ_{max} would not be equal to zero or tend towards infinity when e_o/D equals to zero or tend towards infinity. Using the same set of θ_{max}

values simulated via CFD and optimisation procedure described in Section 5.2.3, Eq. (5.9) attained a stronger correlation to the simulation results, as compared to Eq. (5.8), which was Eq. (5.1) but with updated coefficients. Furthermore, based on Figure 5.5b, Eq. (5.8) may be limited to small values of e_o/D (e.g. $e_o/D < 0.14$) for high current velocities, which is a rather narrow range, albeit the high squared correlation coefficient (i.e. $R^2 = 0.96$). Therefore, Eq. (5.9) was proposed for the prediction of θ_{max} for various Reynolds numbers, or more specifically, for a wide range of external pipe diameters. However, it is worth noting that Eq. (5.9) is valid for $e_o/D < 0.3$, at which there would initially be no regular vortex shedding in the wake of the pipe [3, 17], and the friction velocity beneath the pipe would be constant over time [40, 41]. The case of having a small e_o/D is of particular interest, because the capacity for scour to occur would increase significantly for a decrease in e_o/D (Figure 5.3), for which a deeper scour hole can be expected, based on the trend observed in Figure 5.9.

Interestingly, the influence of the Reynolds number on θ_{max} seemed to be largely dominated by the current velocity, as the effect of the external pipe diameter was significantly weaker (Figure 5.6b). For a constant pipe diameter, an increase in the current velocity was seen to result in a significant increase in θ_{max}. This could be the reason why the Reynolds number term in Eq. (5.9) had a positive exponent, despite the fact that both, τ_{max}/τ_∞ and S_{eq}/D, were seen to slightly decrease with *Re*. The influence of the upstream current velocity on θ_{max} was straightforward, whereby having higher current velocities would be expected to result in higher friction velocities on the seabed underneath the pipe. However, with a constant upstream flow condition, an increase in the external pipe diameter led to a decrease in θ_{max} instead. This can be attributed to the fact that, when the pipe diameter was increased while e_o/D was held constant, this resulted in a larger dimensional pipe elevation, e_o. Thus, there was less flow amplification underneath the pipe, and hence less amplification of the seabed shear stress. In summary, with a constant upstream flow condition and e_o/D, an increase in the external pipe diameter would result in a lower capacity for scour to occur underneath the pipe. In contrast, the capacity for scour to occur beneath a pipeline would increase significantly with an increase in the current velocity.

In terms of non-dimensionalising the seabed shear stress, an alternative can be considered:

$$\theta = \frac{u_*^2}{g k_s} \tag{5.12}$$

When this relationship was substituted into Eq. (5.9) with the same constants to predict the maximum seabed shear stress beneath the pipe, a very high correlation with the simulation results (i.e. R^2 = 0.97) could still be attained. In comparison to the conventional Shields parameter [34], Eq. (5.12) offered a relationship that is independent of the specific gravity of the sediment. The specific gravity may not have been adequately taken into consideration in the CFD simulations which involved a single-phase rigid bed model that was driven by a pressure gradient. However, it is worth mentioning that the CFD simulations were primarily focused on the initiation of the scour process, as opposed to modelling the development of scour and the equilibrium condition.

The rationale behind formulating Eq. (5.11) in such a manner was similar to that of Eq. (5.9), that being S_{eq}/D would not be equal to zero or tend towards infinity when e_o/D equals to zero or tend towards infinity. The reason for the adoption of the hyperbolic tangent function to describe the correlation between θ_∞ and S_{eq}/D was that, in a study conducted by Mao [3], wherein θ_∞ was varied while all other parameters were held constant, S_{eq}/D was reported to increase rapidly when $\theta_\infty < 0.1$, but then approach a constant value despite a further increase in θ_∞ when $\theta_\infty > 0.1$. Therefore, it was reported that S_{eq}/D had a strong correlation with θ_∞ for the clear-water condition, but that correlation would diminish for the live-bed condition, since the critical dimensionless shear stress, θ_{cr}, for sand is typically less than 0.11 [33]. This may be the reason why the equation proposed by Sumer and Fredsøe [1] was reported to only be applicable for the live-bed condition.

Similarly, this would have been the case for the equation proposed by Moncada-M and Aguirre-Pe [8] as well, based on the absence of the θ_∞ term, and the fact that the experiments were conducted under a live-bed condition. Nevertheless, it is also rather intriguing that an equilibrium scour depth can be obtained when $\theta_\infty > \theta_{cr}$, at which sediment transport will be prevalent over the entire bed, including the region upstream of the pipeline. One possible explanation for this is that an equivalent amount of sediment is transported into and out of the scour hole, so that the net transport rate underneath the pipe is practically zero [9]. This could be attributed to the relatively constant shear stress amplification factor when $\theta_\infty > 0.2$, which was observed in Figure 5.4a.

Although the exponent for the Reynolds number term in Eq. (5.11) appeared to be small when compared to that of the other parameters, it may still be of interest to investigate the

effects of having a wider Reynolds number range, as the pipe diameters in the experiments only ranged between 23 mm and 100 mm, whilst it may exceed 1,000 mm in the field [1]. The numerical results from Liang *et al.* [6], which involved pipe diameters of 100 mm and 800 mm, was not taken into consideration in this work, because the associated water depth of 3.5D is hypothesised to result in predictions of S_{eq}/D that are mainly influenced by h/D. Hence, it may not be an accurate representation of subsea pipelines in deep waters. In addition, the influence of h/D on S_{eq}/D may not be significant for deep-sea pipelines, and may have arisen mainly due to the physical limitations associated with laboratory experiments in terms of the water depth.

On that note, it is worth mentioning that the equation in Sumer and Fredsøe [1] was proposed for subsea pipelines; thus, it may not be appropriate to use this equation to predict the experimental results of Moncada-M and Aguirre-Pe [8], which were obtained for pipelines in river crossings with relatively shallow water depths. Therefore, it would also be interesting to investigate the equilibrium scour depths at large water depths. Nevertheless, Eq. (5.11) can be used to predict the equilibrium scour depth beneath pipelines with zero or an elevation with respect to the far-field seabed, and it is applicable for both clear-water and live-bed conditions.

5.5 Summary

This work provides an update on the prediction of the criteria for determining whether scour would progress towards an equilibrium condition, as well as the equilibrium scour depth beneath the pipe. An extensive parametric study was conducted via a total of 243 2-D RANS simulations using the k-ω SST turbulence model to compute the maximum dimensionless seabed shear stress beneath the pipe, θ_{max}. Based on the simulation results, a newly developed equation was proposed for the prediction of θ_{max}, whilst quantifying the influence of the pipe Reynolds number, Re. Subsequently, experimental measurements have been compiled from literature to develop an additional equation for the prediction of the equilibrium scour depth, S_{eq}/D, whilst quantifying the influence of the upstream dimensionless shear stress, θ_{∞}, and Re on S_{eq}/D. The following main conclusions can be drawn from this work:

- Eq. (5.9) can be used for a more accurate prediction of θ_{max} for $0 < e_o/D < 0.3$ for various Reynolds numbers, as compared to Eq. (5.1) [127].
- θ_{max} increases significantly with an increase in current velocity; however, for the same upstream flow condition and e_o/D, θ_{max} would slightly decrease for a pipe with a larger external diameter.
- Eq. (5.11) can be used for predicting S_{eq}/D, with a high correlation to experimental data as compared to existing formulae, which accounts for pipelines with $e_o/D \geq 0$.
- The influence of θ_∞ on S_{eq}/D is significant, especially for the clear-water condition, and the correlation of Eq. (5.11) appeared to have improved with the inclusion of θ_∞.
- The influence of Re on S_{eq}/D is small when compared to the other key parameters.

Chapter 6
Development of current-induced scour beneath elevated subsea pipelines[3]

This chapter focused on predicting the development of the scour depth beneath subsea pipelines with an elevation under steady flow conditions. A range of pipe elevation-to-diameter ratios (i.e. $0 \leq e_o/D \leq 0.5$) have been considered for laboratory experiments conducted in a sediment flume. The corresponding equilibrium scour depths and scour time scale are obtained; experimental data from published literature have been collected and added to the present work to produce a more complete analysis database. The correlation between existing empirical formulae for predicting the time scale and the experimental data are assessed. A new manner of converting the scour time scale into a non-dimensional form is found to aid the empirical formulae in attaining a better correlation to the experimental data. Subsequently, a new empirical formula has also been proposed in this work, which accounts for the influence of e_o/D on the non-dimensional scour time scale. It is found to have the best overall correlation with the experimental data. Finally, full-scale predictions of the seabed gaps and time scales have been made for the Tasmanian Gas Pipeline (TGP); for which the field data has been presented in Chapter 4, and the equation for predicting the equilibrium scour depth is proposed in Chapter 5.

[3] A version of this chapter has been published as: Lee, J. Y., Forrest, A. L., Hardjanto, F. A., Chai, S., Cossu, R., & Leong, Z. Q. (2018). Development of current-induced scour beneath elevated subsea pipelines. *Journal of Ocean Engineering and Science*, 3(4), 265-281. DOI: 10.1016/j.joes.2018.09.001.

6.1 Introduction

A pipeline may be found at a certain elevation from the seabed, e_o [1], and pipeline free spans can be permanent [113]. If the span length, hydrodynamic loads and pipe characteristics are such that unacceptable fatigue damage can develop or, even worse, the critical bending moment is exceeded, intervention works to mitigate these occurrences shall be undertaken. For a smaller pipe elevation, e_o, a larger amplification of the seabed shear stress beneath the pipe can be expected, and hence a deeper scour hole [136]. It is of technical interest to predict the development of the scour hole beneath the pipeline, or more specifically, the time required to reach a significant scour depth, where for example, storm events may not last as long as the period required for the scour hole to reach an equilibrium state [6]. Although the influence of e_o/D had been considered for predicting the maximum seabed shear stress and equilibrium scour depth beneath the pipe, it had not been considered in terms of predicting the scour time scale. This chapter focused on predicting the time scale of two-dimensional scour occurring beneath an elevated pipe under steady currents. A review of the existing empirical formulae which have been proposed for predicting the scour time scale was presented in Chapter 2.

6.2 Methods

Sediment flume experiments were conducted to obtain the equilibrium scour depths and scour time scales were obtained for a range of pipe elevation ratios under steady currents. Subsequently, experimental data from published literature were compiled, and the scour time scale was converted to a non-dimensional form. Existing and newly developed empirical formulae were used to predict the dimensionless equilibrium scour depths and scour time scales, where the predictions were compared with experimental measurements. Finally, full-scale predictions of the equilibrium scour depth and time scale were also made for a natural gas pipeline (i.e. Tasmanian Gas Pipeline), which were compared against field measurements of the seabed gaps from Chapter 4 [127].

6.2.1 Sediment flume experiments

Experiments were conducted in a sediment flume at the University of California, Davis (Figure 6.1), of which the setup was introduced in Section 3.1.1. A smooth PVC pipe with an external diameter, D, of 48 mm and thickness of 2 mm was rigidly positioned at various elevations above a sandbox of 2.62 m in length (i.e. ≈ 54D), 0.46 m in width (i.e. ≈ 9D), and 0.15 m in depth (i.e. ≈ 3D). The sandbox was filled with Cemex #0/30 sand with a median grain size, d_{50}, of approximately 0.52 mm. For every test case, the ADV was positioned 10D upstream from the pipe, to measure the flow velocities at various heights (i.e. 10 mm vertical intervals). The mean stream-wise flow velocities at each vertical position were attained by averaging the velocities which were recorded for over one minute.

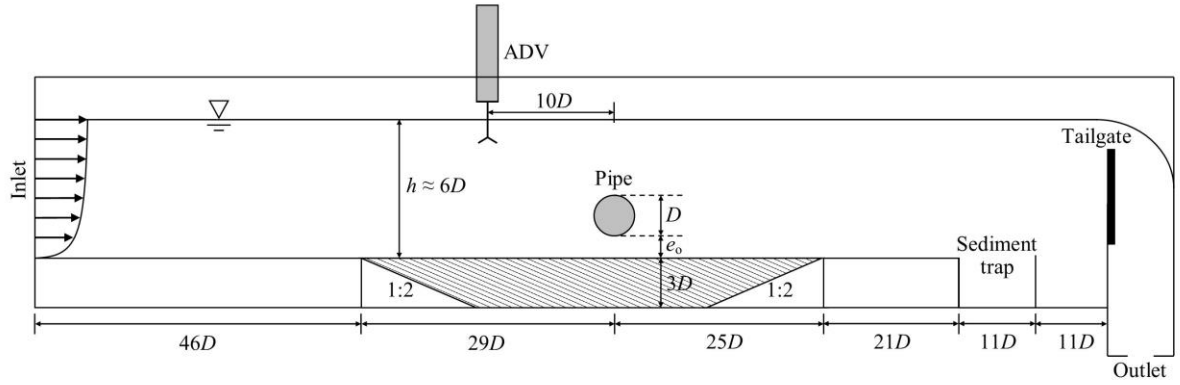

Figure 6.1: Sketch of the sediment flume experimental setup, where the external pipe diameter, D, is 48 mm.

The test conditions are listed in Table 6.1. A range of pipe elevation ratios, e_o/D, was investigated for the clear-water condition, with a particular focus on relatively small elevations (i.e. $e_o/D \leq 0.3$), where the capacity for scour to occur was expected to be higher [127]. The experiments were primarily conducted for the clear-water condition, where the upstream dimensionless bed shear stress is below the critical value, due to the lack of published experimental data for the clear-water condition, and to avoid having the effects of scour developing upstream of the pipe at the beginning of the sandbox on the development of the scour hole directly underneath the pipe.

The corresponding pipe Reynolds number may be small due to the low flow velocities for the clear-water condition. However, a previous study has reported the influence of the Reynolds number on the maximum dimensionless seabed shear stress beneath the pipe and the equilibrium scour depth to be small [136]. The measured water depths listed in Table 6.1 may not appear to be precisely constant; however, the standard deviation was only less than 2% of the mean value of approximately 6.04. Larger water depths were not investigated due to physical limitations of the flume. It is also worth mentioning that no small initial hole was made beneath the pipe, whereby the scour process was left to be initiated naturally for every test case.

Table 6.1: Sediment flume experimental test conditions; D = 48 mm, d_{50} = 0.52 mm and θ_{cr} = 0.030.

Test number	Pipe elevation, e_o/D	Depth-averaged current velocity, U_o (m/s)	Upstream dimensionless bed shear stress, θ_∞	Reynolds number, Re	Water depth, h/D
1	0.0	0.11	0.004	0.53×10^4	5.87
2	0.0	0.22	0.015	1.12×10^4	6.04
3	0.0	0.29	0.026	1.47×10^4	6.21
4	0.0	0.35	0.037	1.74×10^4	6.12
5	0.1	0.13	0.006	0.68×10^4	5.90
6	0.1	0.22	0.015	1.10×10^4	5.92
7	0.1	0.28	0.025	1.42×10^4	5.96
8	0.1	0.35	0.038	1.75×10^4	6.08
9	0.2	0.13	0.005	0.64×10^4	6.15
10	0.2	0.23	0.016	1.14×10^4	5.98
11	0.2	0.30	0.028	1.50×10^4	6.08
12	0.2	0.34	0.036	1.72×10^4	6.10
13	0.3	0.13	0.006	0.67×10^4	5.96
14	0.3	0.22	0.014	1.08×10^4	6.04
15	0.3	0.30	0.028	1.51×10^4	6.10
16	0.3	0.35	0.039	1.77×10^4	6.08
17	0.5	0.14	0.006	0.70×10^4	6.04
18	0.5	0.23	0.016	1.14×10^4	5.85
19	0.5	0.27	0.022	1.35×10^4	6.17
20	0.5	0.34	0.035	1.69×10^4	6.19

6.2.2 Time scale formulation

The main parameters of interest with regards to the sediment flume experiments were the equilibrium scour depth and the scour time scale under steady currents. Upon obtaining the experimental data, published data [3, 12] have also been compiled, with the aim of developing an equation for predicting the scour time scale. Firstly, the following equation was fitted to every test case to estimate the scour time scale, T_p [2, 26]:

$$S(t) = S_{eq}\left\{1 - \exp\left[-\left(\frac{t}{T_p}\right)^{C_p}\right]\right\} \tag{6.1}$$

where C_p is a constant, and the values of T_p and C_p were determined for each case via:

- initially having its value set to one;
- calculating the difference between the measured values of S obtained via the experiments and S estimated using Eq. (6.1);
- using unconstrained nonlinear optimisation [125] (i.e. *fminsearch* in MATLAB) to iteratively compute the value for the constant that would result in the smallest squared difference, thus resembling the 'least squares' approach; and,
- assessing the corresponding squared correlation coefficient, R^2, calculated via [26]:

$$R^2 = 1 - \frac{\sum_{i=1}^{N}(f_i - y_i)^2}{\sum_{i=1}^{N}(y_i - \bar{y})^2} \tag{6.2}$$

where f_i is the value of S predicted via Eq. (6.1); y_i is the measured value of S obtained from the experiments; and, $\bar{y}$ is the mean of the measured values of S which were obtained via experiments. A unique value of C_p was attained for each test case in order to achieve high R^2 values overall, and thus Eq. (6.1) was able to produce a more accurate estimate of the scour time scale as compared to the original equation from Fredsøe *et al.* [13], which was the equivalent of Eq. (6.1) with $C_p = 1$.

Subsequently, the estimated scour time scale, T_p, was converted into a non-dimensional form, T_p^*, with reference to Eq. (2.2) derived in Fredsøe *et al.* [13]:

$$T_p^* = \frac{\left[g\left(\frac{\rho_s}{\rho} - 1\right)d_{50}{}^3\right]^{1/2}}{D^2} T_p \tag{6.3}$$

where ρ_s is sediment density and ρ is fluid density. Finally, several equations were compared for predicting the dimensionless scour time scale, where their correlation to the experimental data were quantified. With reference to the equations proposed in Fredsøe *et al.* [13] and Zhang *et al.* [26], a general form was used as follows:

$$T_p^* = \varepsilon_1 \theta_\infty^{\ \varepsilon_2} \tag{6.4}$$

where the values of the constants, ε_1 and ε_2, were computed using the aforementioned optimisation process. A general form of the equation proposed in Zang *et al.* [32] was also included in this comparison:

$$T_p^* = \zeta_1 \theta_\infty^{\ \zeta_2} \exp\left(\left(\zeta_3 \frac{e_o}{D}\right)^{\zeta_4}\right) \tag{6.5}$$

where the values of the constants, ζ_1, ζ_2, ζ_3, and ζ_4, were computed using the same optimisation process. e_o/D is defined as the dimensionless pipe elevation in this work, even though Eq. (6.5) was initially proposed in Zang *et al.* [32] for predicting the scour time scale for pipelines with a partial embedment. Hence, it was thought that an update of the constants would be required.

As it was found that Eq. (6.4) and Eq. (6.5) did not yield a high squared correlation coefficient, R^2, a new relationship was proposed for normalising the scour time scale, instead of using Eq. (6.3):

$$T_q^* = \frac{g\left(\frac{\rho_s}{\rho} - 1\right) d_{50}}{U_o D} T_p \tag{6.6}$$

where U_o is the depth-averaged current velocity. Eq. (6.6) was found to enable a better correlation with the experimental data to be attained, in terms of developing an equation for predicting the dimensionless scour time scale. Therefore, Eq. (6.4) and Eq. (6.5) were subsequently modified into the following equations, whilst maintaining the same general forms as before:

$$T_{\mathrm{q}}^{*} = \eta_1 \theta_{\infty}^{\ \eta_2} \tag{6.7}$$

$$T_{\mathrm{q}}^{*} = \lambda_1 \theta_{\infty}^{\ \lambda_2} \exp\left(\left(\lambda_3 \frac{e_{\mathrm{o}}}{D}\right)^{\lambda_4}\right) \tag{6.8}$$

In addition to the aforementioned equations with updated constants, the following equation was proposed in an effort to attain the highest possible correlation to the experimental data:

$$T_{\mathrm{q}}^{*} = \coth\left(\psi_1 \theta_{\infty}\right) \cdot \cosh^{-1}\left(\psi_2 Re\right) \cdot \left(1 - \mathrm{sech}\left(\psi_3 \frac{h}{D} + \psi_4\right)\right) \cdot \cosh\left(\psi_5 \frac{e_{\mathrm{o}}}{D}\right) \tag{6.9}$$

The Reynolds number, albeit posing a small influence on the maximum bed shear stress beneath the pipe and the equilibrium scour depth [136], was nonetheless an interesting parameter to investigate. Hence, this work aimed to quantify the influence of *Re* on the scour time scale. The *h*/*D* term was included in Eq. (6.9) because it had previously been reported to have an influence on the scour time scale [46]. In this work, the rationale behind the formulation of Eq. (6.9) was to ensure that:

- when $e_{\mathrm{o}}/D = 0$, $\cosh(\Psi_5 e_{\mathrm{o}}/D) = 1$, and thus T_{q}^{*} does not tend towards zero or infinity;
- when h/D tends towards infinity, $1 - \mathrm{sech}(\Psi_3 h/D + \Psi_4)$ does not tend towards zero or infinity, and thus T_{q}^{*} does not tend towards zero or infinity.

Further discussions regarding the formulation of Eq. (6.9) are presented in subsequent sections of this chapter.

6.3 Results

Experiments were conducted in a sediment flume facility to investigate the development of scour underneath a pipeline with an elevation with respect to the far-field seabed. This work particularly focused on the clear-water condition, for which the upstream shear stress is below the critical shear stress, because there seemed to be a lack of clear-water data in

published literature. Nevertheless, live-bed data from multiple sources have been included as well.

Figure 6.2 shows the flow velocities that were measured at different distances upstream from the pipe for one case, wherein the lines were plotted using [87]:

$$U_{\mathrm{x}}\left(y\right)=\frac{u_{*}}{\kappa}\ln\left(\frac{y}{z_{\mathrm{o}}}\right) \tag{6.10}$$

where U_{x} is the mean stream-wise flow velocity; u_{*} is the friction velocity; the von Kármán constant, κ = 0.4 [87, 115]; y is the elevation from the sand bed; and, z_{o} is the bed roughness height. There were discrepancies between the calculated and measured velocities in the regions that were close to the sand bed, because Eq. (6.10) was reported to only be valid from a few centimetres above the bed [87].

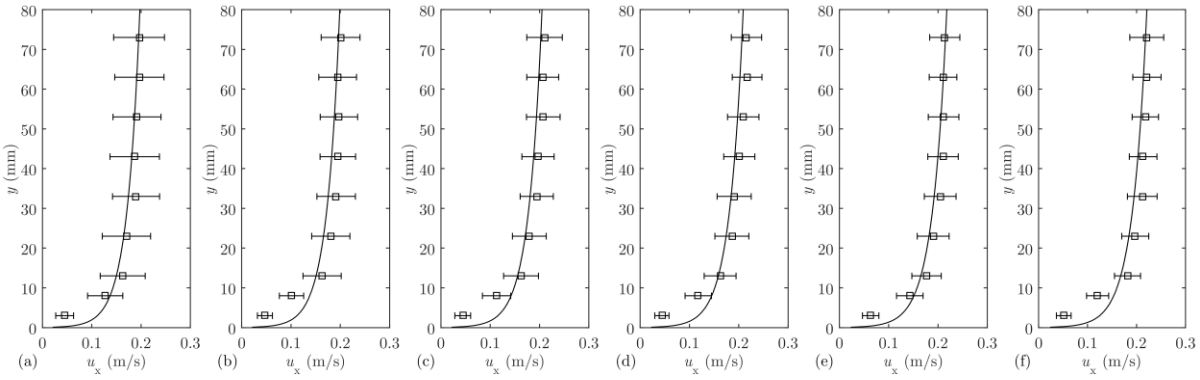

Figure 6.2: Stream-wise flow velocity profiles measured at: (a) 2.8 m upstream from the pipe; (b) 2.3 m from the pipe; (c) 1.8 m from the pipe; (d) 1.4 m from the pipe; (e) 1.0 m from the pipe; and, (f) 0.5 m or 10*D* from the pipe. The error bars represent the standard deviation, and the lines were plotted using Eq. (6.10).

Overall, there seemed to be small differences in the boundary layer thickness and velocities for different locations, especially at the locations which were close to the pipe. For example, at y = 73 mm from the sand bed, the difference between the mean velocity at 10*D* from the pipe and that at 1 m from the pipe was approximately 3.4%; while at y = 43 mm from the sand bed, the difference between the mean velocity at 10*D* from the pipe and that at 1 m from the pipe was approximately 1.5%. In addition, for the locations that were closer to the pipe,

the standard deviations were seen to decrease and approach a relatively constant value. Furthermore, the CFD simulation result presented in Section 5.4 suggests that, even if the boundary layer thickness was still growing slightly when the flow encountered the pipe, the change in the bed shear stress would be significantly smaller as compared to the change in the boundary layer thickness.

6.3.1 Equilibrium scour depth

Figure 6.3 depicts the relationship between the upstream dimensionless seabed shear stress, θ_∞, and the equilibrium scour depth beneath the pipe, S_{eq}/D, where experimental data from [3, 8, 12] were compiled and plotted with results from the present study. The present experimental results was observed to agree with the findings in Mao [3], whereby S_{eq}/D increased rapidly with θ_∞ for the clear-water condition. However, the live-bed data suggest that the relationship between S_{eq}/D and θ_∞ became less significant at high values of θ_∞.

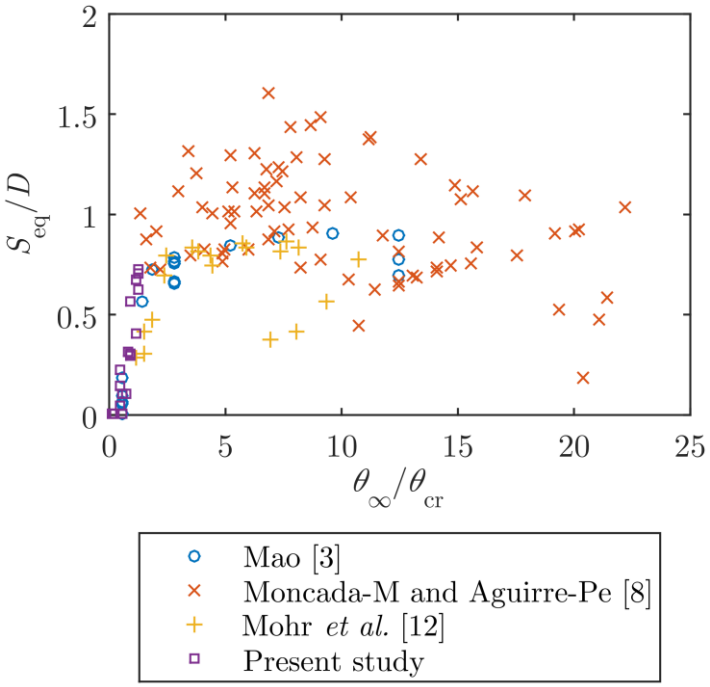

Figure 6.3: Compilation of experimental data [3, 8, 12] showing the correlation between the equilibrium scour depth, S_{eq}/D, and the upstream dimensionless seabed shear stress, θ_∞, normalised by the critical dimensionless seabed shear stress, θ_{cr}.

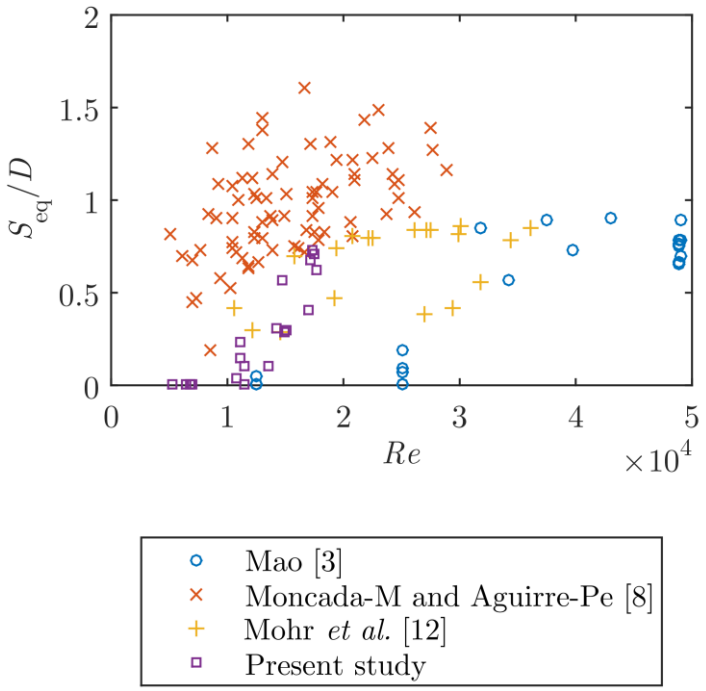

Figure 6.4: Compilation of experimental data [3, 8, 12] showing the correlation between the equilibrium scour depth, S_{eq}/D, and the Reynolds number, Re.

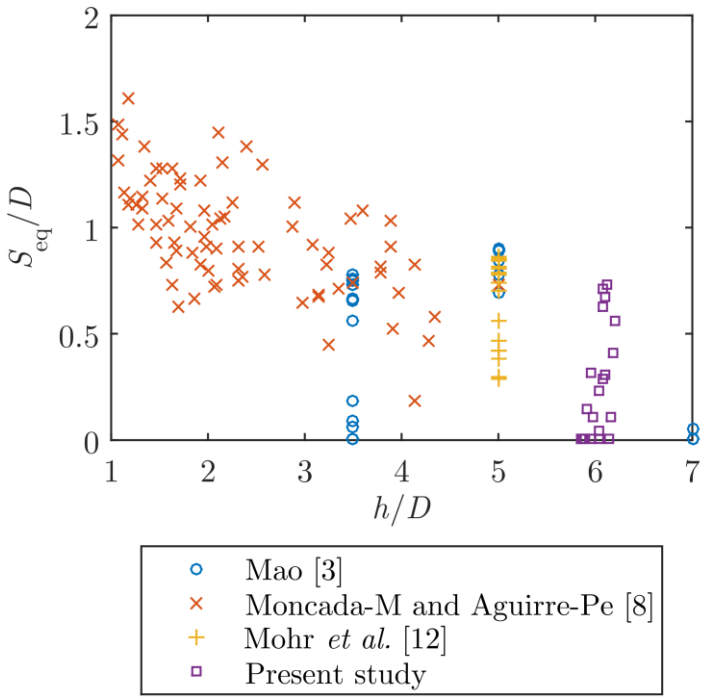

Figure 6.5: Compilation of experimental data [3, 8, 12] showing the correlation between the equilibrium scour depth, S_{eq}/D, and the water depth or blockage ratio, h/D.

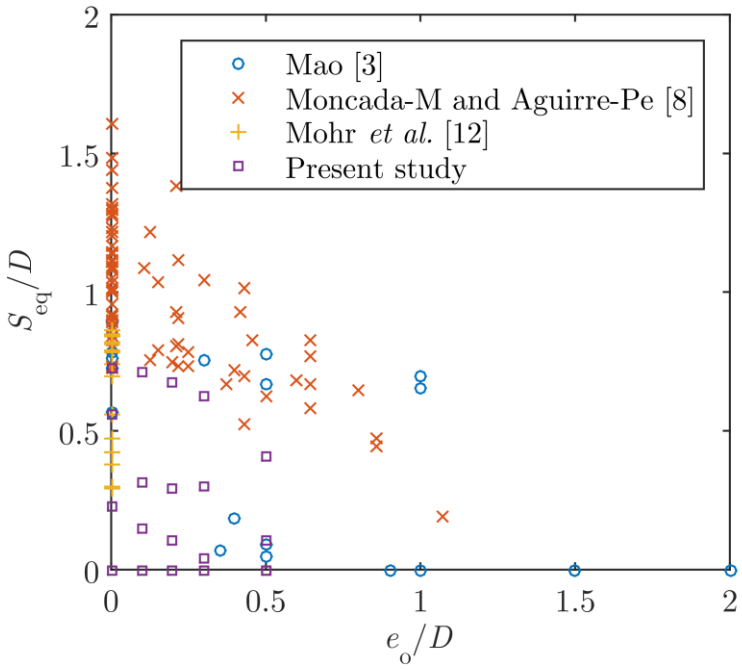

Figure 6.6: Compilation of experimental data [3, 8, 12] showing the correlation between the equilibrium scour depth, S_{eq}/D, and the pipe elevation ratio, e_o/D.

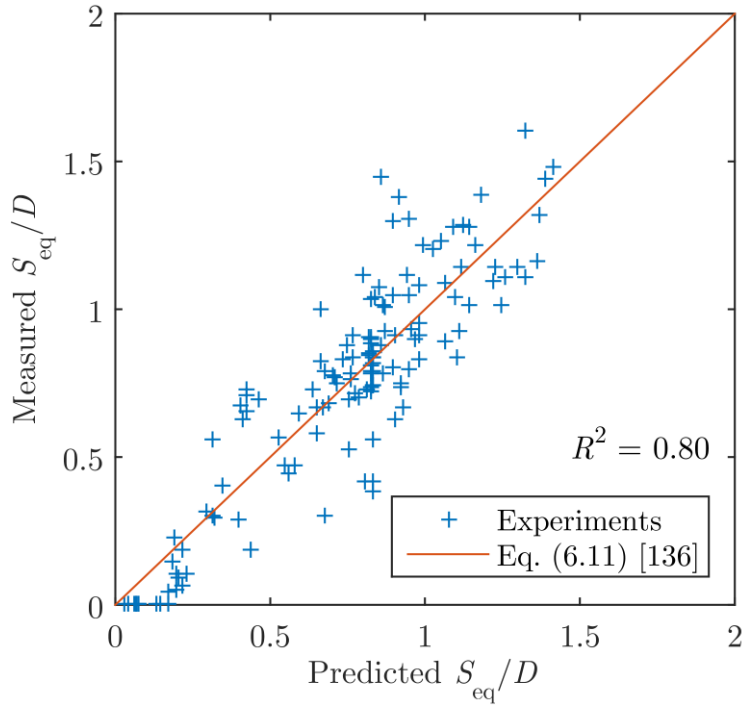

Figure 6.7: Correlation between Eq. (6.11) [136] and the compiled experimental data.

With reference to Figure 6.4, S_{eq}/D was seen to increase with the Reynolds number, Re, in the present study (i.e. mostly clear-water). However, the overall relationship between S_{eq}/D and

Re, which includes both clear-water and live-bed data, was observed to be weak when the data from other sources were put into perspective.

In terms of the water depth or blockage ratio, h/D, the results in Figure 6.5 suggest that deeper scour depths can be expected at very shallow water depths. However, the influence of h/D on S_{eq}/D appeared to be diminishing as h/D increased. Figure 6.6 suggests that the pipe elevation ratio, e_o/D, was seen to have a strong influence on S_{eq}/D, whereby S_{eq}/D was observed to decrease with an increase in e_o/D for both clear-water and live-bed conditions; thus reinforcing the importance of investigating the effects of e_o/D. This relationship can also be seen in Table 6.2 for the clear-water condition, wherein for the same depth-averaged current velocity, the resulting S_{eq}/D generally decreased with an increase in e_o/D.

Figure 6.7 portrays the correlation between the measured values S_{eq}/D, which included results from the present study (Table 6.2) and from published literature [3, 8, 12], and the values predicted using the following equation from Chapter 5 [136]:

$$\frac{S_{eq}}{D} = \tanh\left(15.15\theta_{\infty}\right) \cdot Re^{-0.01} \cdot \coth\left(0.62\frac{h}{D}\right) \cdot \left(-0.11 + \operatorname{sech}\left(-1.08\frac{e_o}{D}\right)\right) \qquad (6.11)$$

where a very good agreement was observed (i.e. $R^2 = 0.80$). In addition, the aforementioned observations based on the experimental data were also consistent with the formulation of Eq. (6.11): (1) the initial rapid increase of S_{eq}/D with θ_{∞}, followed by a weak trend at higher values of θ_{∞}, resembled a hyperbolic tangent curve (Figure 6.3); (2) the overall weak relationship between S_{eq}/D and *Re* can serve as an explanation for the small coefficient for the *Re* term (Figure 6.4); (3) the diminishing influence of h/D on S_{eq}/D resembled a hyperbolic cotangent curve (Figure 6.5); and, (4) inverse relationship between S_{eq}/D and e_o/D resembled a hyperbolic secant curve (Figure 6.6).

Table 6.2 included a dimensionless seabed shear stress ratio, θ_{max}/θ_{cr}, which was used to predict the initiation of scour beneath the pipe. The maximum dimensionless seabed shear stress beneath the pipe, θ_{max}, was calculated using the following equation from Chapter 5 [136]:

$$\theta_{\max} = \theta_{\infty} + \theta_{\infty}^{0.93} Re^{0.13} \left(\frac{1}{\exp\left(e_o / D\right)} \right)^{2.38} \tag{6.12}$$

which was normalised by the critical dimensionless shear stress, θ_{cr}, at which significant sediment transport beneath the pipe would occur.

Table 6.2: Experimental results.

Test number	Pipe elevation, e_o/D	Dimensionless shear stress ratio, θ_{max}/θ_{cr}	Equilibrium scour depth, S_{eq}/D	Scour time scale, T_p (s)	Constant, C_p	Squared correlation coefficient, R^2
1	0.0	0.6	0.00	-	-	-
2	0.0	2.7	0.23	140	0.46	0.99
3	0.0	4.6	0.56	616	0.68	0.99
4	0.0	6.4	0.73	396	0.49	0.97
5	0.1	0.8	0.00	-	-	-
6	0.1	2.2	0.15	209	0.42	0.96
7	0.1	3.6	0.31	283	0.51	0.98
8	0.1	5.4	0.71	439	0.62	0.99
9	0.2	0.6	0.00	-	-	-
10	0.2	2.0	0.10	457	0.63	0.96
11	0.2	3.3	0.29	221	0.64	0.99
12	0.2	4.4	0.68	764	0.58	0.97
13	0.3	0.6	0.00	-	-	-
14	0.3	1.5	0.04	130	4.42	0.99
15	0.3	2.9	0.30	495	0.63	0.99
16	0.3	3.8	0.63	578	0.62	0.98
17	0.5	0.5	0.00	-	-	-
18	0.5	1.2	0.00	-	-	-
19	0.5	1.7	0.10	1211	1.08	0.98
20	0.5	2.7	0.41	645	0.69	0.99

Eq. (6.12) was proposed in Chapter 5 [136] to predict the occurrence of scour. This equation was developed based on numerical data, where a large parametric study was performed to compute the maximum seabed shear stress beneath a pipe under various conditions. θ_{cr} was estimated using [87]:

$$\theta_{cr} = \frac{0.30}{1+1.2D_*} + 0.055\left[1 - \exp\left(-0.02D_*\right)\right] \tag{6.13}$$

where D_*, which is the dimensionless form of the sediment grain size, was calculated using [87]:

$$D_* = \left[\frac{g(s-1)}{\nu^2}\right]^{1/3} d_{50} \tag{6.14}$$

When $\theta_{max}/\theta_{cr} > 1$, scour can be expected to occur beneath the pipe. With reference to Table 6.2, the dimensionless seabed shear stress ratio, θ_{max}/θ_{cr}, was seen to correlate well with the equilibrium scour depth beneath the pipe, S_{eq}/D, whereby a scour depth was generally not observed when $\theta_{max}/\theta_{cr} < 1$. The exception would be test number 18, for which θ_{max}/θ_{cr} was approximately 1.2, whilst no scour was observed. This exception could be attributed to the reliability of Eq. (6.12) and Eq. (6.13); nonetheless, the adoption of the θ_{max}/θ_{cr} ratio to predict the occurrence of scour was seen to be relatively accurate, especially for small e_o/D ratios.

6.3.2 Time scale

Figure 6.8 presents the development of the scour depths beneath the pipe for the test cases wherein scour have occurred underneath the pipe. The best fit curves were plotted using Eq. (6.1), for which the associated values, such as the estimated dimensional scour time scale, T_p, the constant C_p, and the corresponding squared correlation coefficients, R^2, are listed in Table 6.2. In this work, the method of calculating the area under the curve in order to estimate the scour time scale, which was used in previous studies [13, 26], was not adopted for the sake of consistency, where only Eq. (6.1) was used to estimate the scour time scale.

The high R^2 values that were observed in Table 6.2 (i.e. $R^2 \geq 0.96$) suggest that Eq. (6.1) was able to produce a very good correlation with the experimental data, which would not have been achievable with the equation from Fredsøe *et al.* [13], whereby $C_p = 1$. Higher scour depths were observed for higher current velocities. However, the scour time scale did not necessarily increase with the increase in current velocity. An occasional decrease in the scour time scale was observed, which was also reported in Fredsøe *et al.* [13]. There seemed to be a clearer influence of e_o/D, where S_{eq}/D decreased with an increase in e_o/D, and T_p increased with an increase in e_o/D.

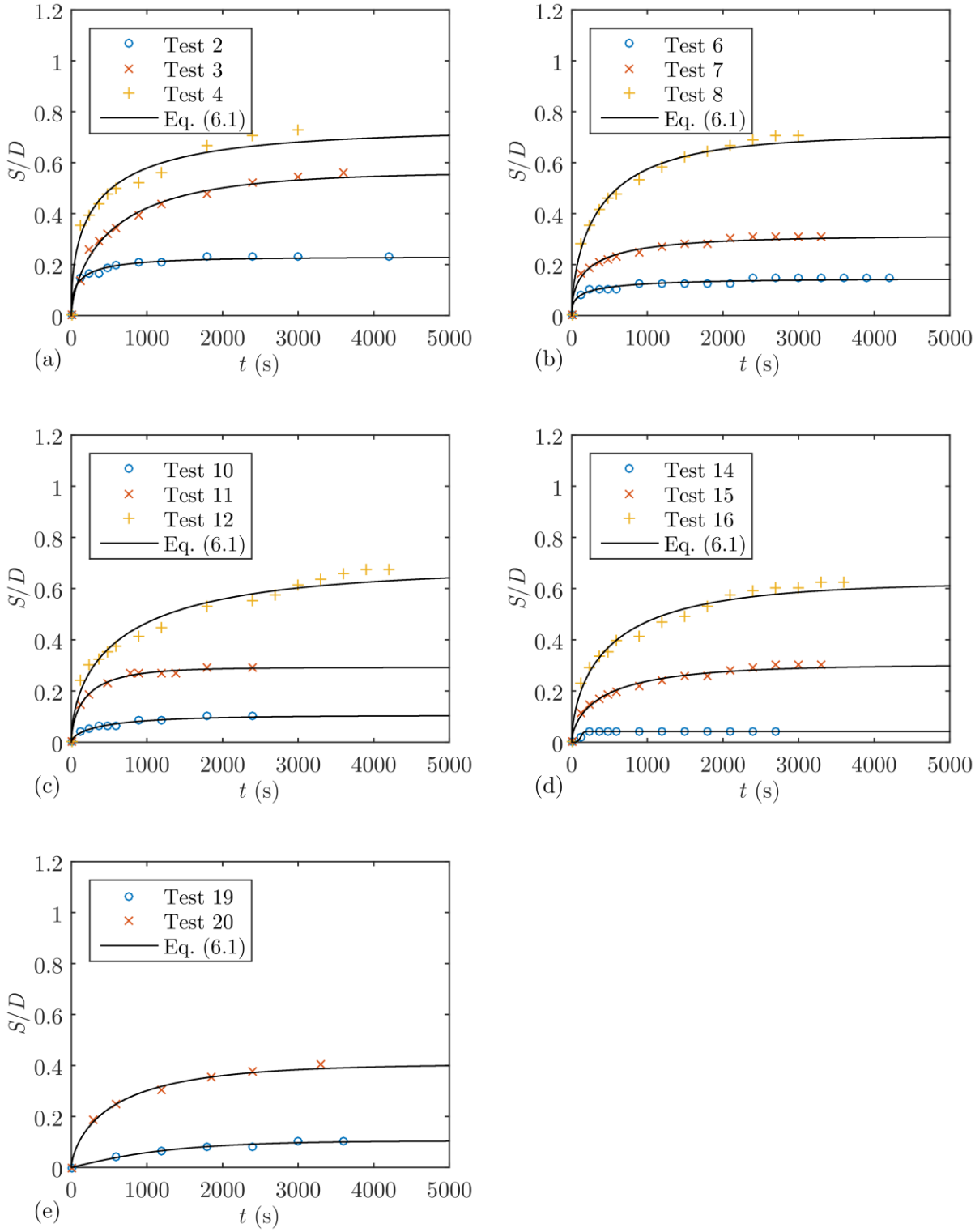

Figure 6.8: Development of the absolute scour depth ratio, *S*/*D*, over time, where the best fit curves were plotted using Eq. (6.1).

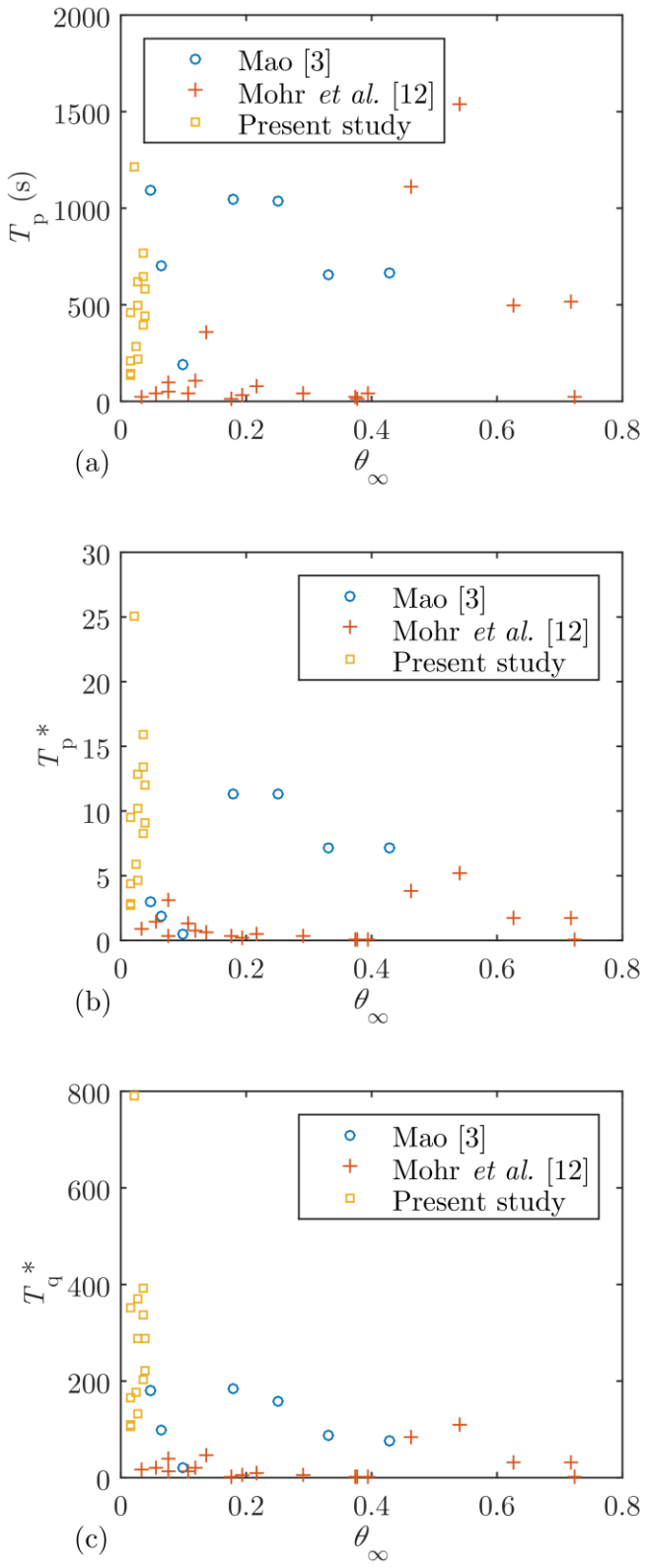

Figure 6.9: Correlation between the upstream dimensionless seabed shear stress, θ_∞, and: (a) the dimensional scour time scale, T_p, which was estimated using Eq. (6.1) [2, 26]; (b) the non-dimensional scour time scale, T_p^*, which was calculated using Eq. (6.3) [13]; and, (c) a new non-dimensional form of the scour time scale, T_q^*, which was calculated using Eq. (6.6).

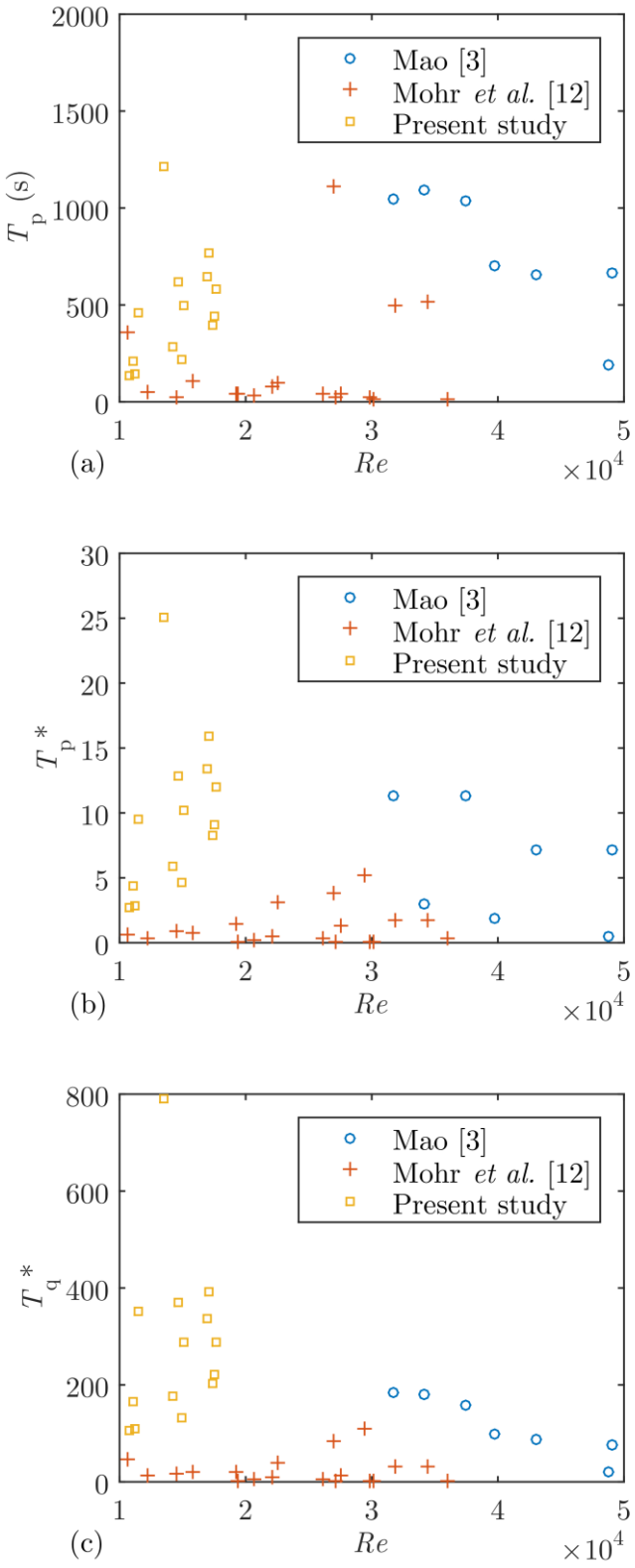

Figure 6.10: Correlation between the Reynolds number, *Re*, and: (a) the dimensional scour time scale, T_p, which was estimated using Eq. (6.1) [2, 26]; (b) the non-dimensional scour time scale, T_p^*, which was calculated using Eq. (6.3) [13]; and, (c) a new non-dimensional form of the scour time scale, T_q^*, which was calculated using Eq. (6.6).

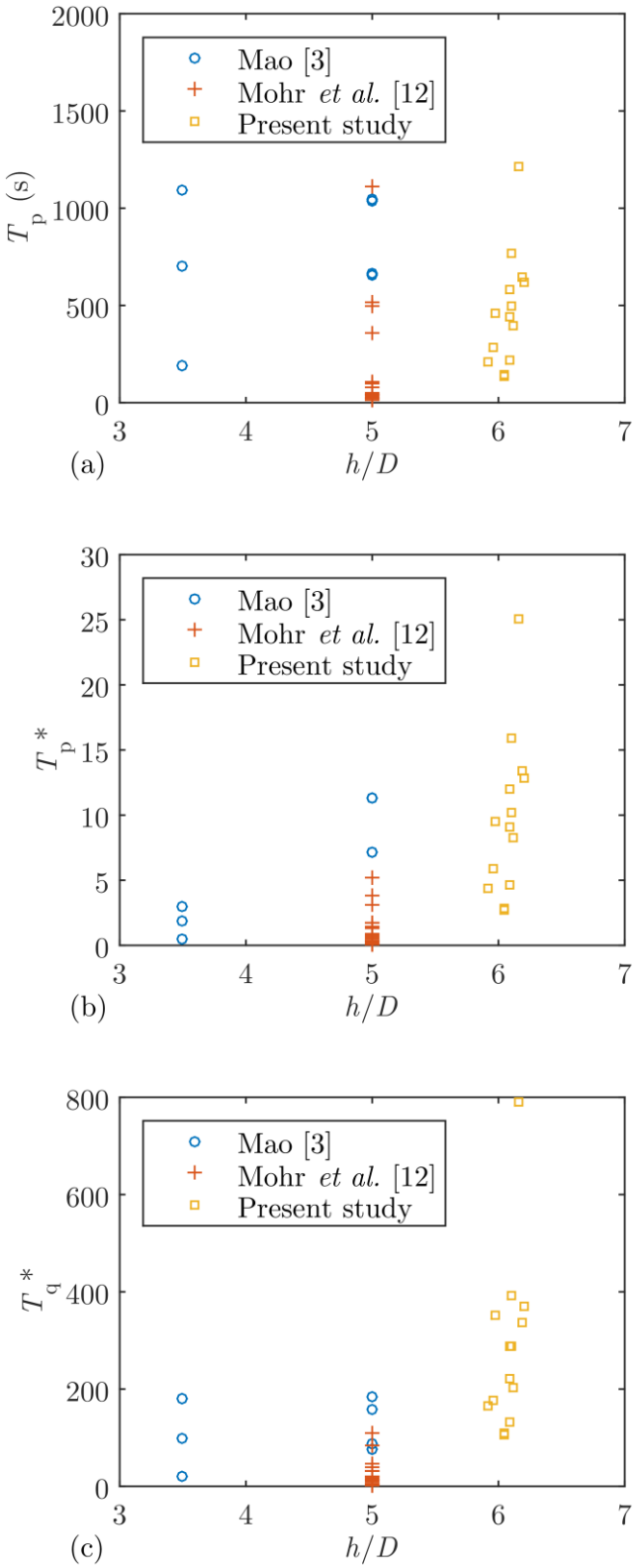

Figure 6.11: Correlation between the water depth or blockage ratio, *h*/*D*, and: (a) the dimensional scour time scale, T_p, which was estimated using Eq. (6.1) [2, 26]; (b) the non-dimensional scour time scale, T_p^*, which was calculated using Eq. (6.3) [13]; and, (c) a new non-dimensional form of the scour time scale, T_q^*, which was calculated using Eq. (6.6).

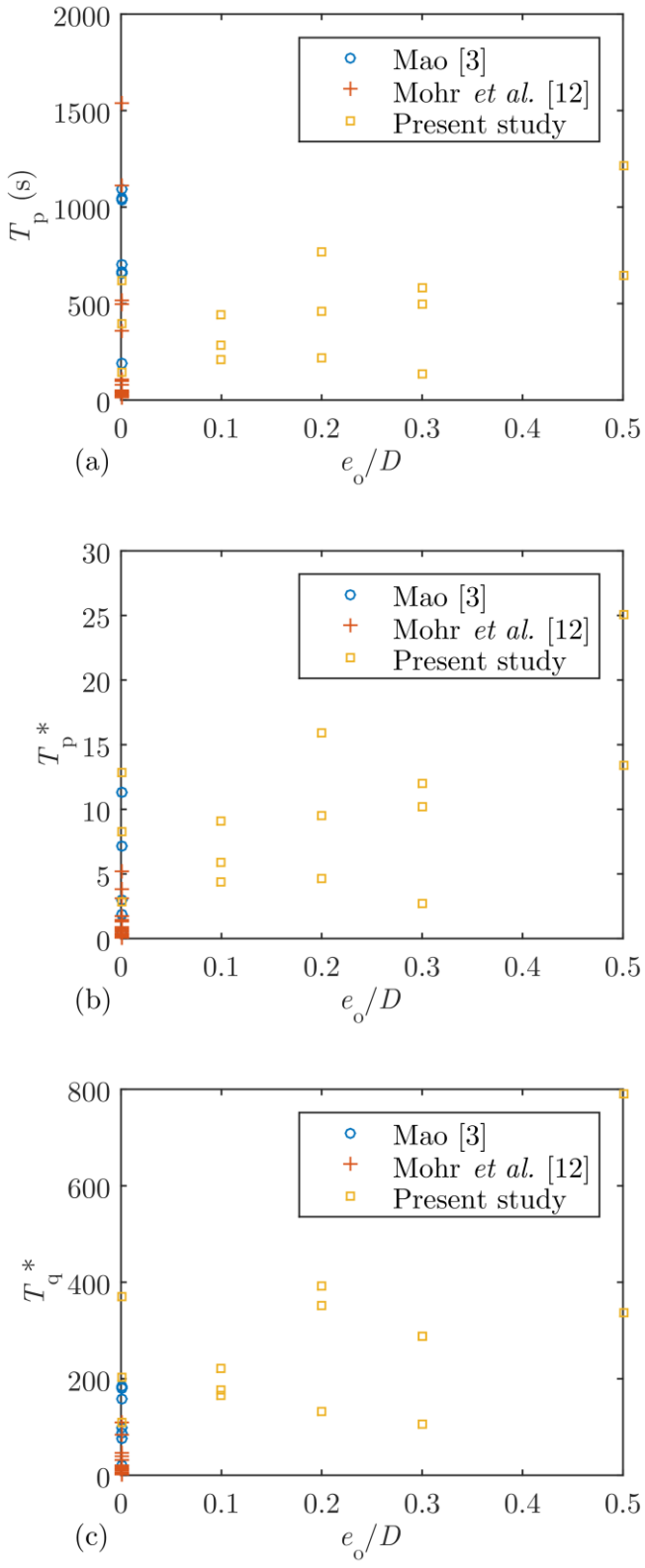

Figure 6.12: Correlation between the pipe elevation ratio, e_o/D, and: (a) the dimensional scour time scale, T_p, which was estimated using Eq. (6.1) [2, 26]; (b) the non-dimensional scour time scale, T_p^*, which was calculated using Eq. (6.3) [13]; and, (c) a new non-dimensional form of the scour time scale, T_q^*, which was calculated using Eq. (6.6).

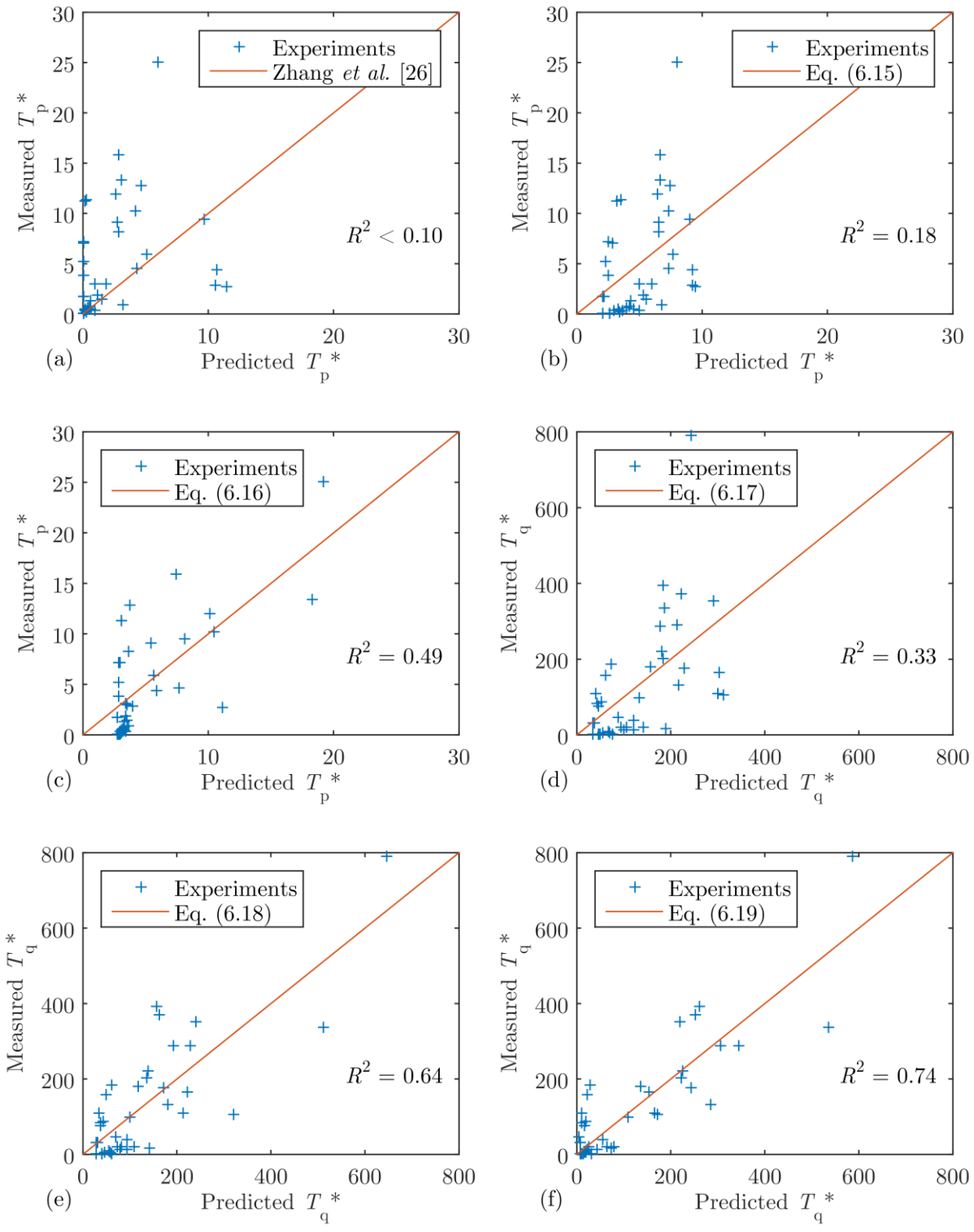

Figure 6.13: Comparing the non-dimensional scour time scale, T_p^*, based on experimental data, with the values predicted using: (a) the equation proposed in Zhang *et al.* [26]; (b) Eq. (6.15); and, (c) Eq. (6.16). Subsequently, a new non-dimensional form of the scour time scale, T_q^*, was applied, and the experimental values were compared with the values predicted using: (d) Eq. (6.17); (e) Eq. (6.18); and, (f) Eq. (6.19), which was seen to attain the highest correlation.

In order to better understand the relationship between the manipulated variables and the scour time scale, the time scale was non-dimensionalised. In Figure 6.9, the non-dimensional time scale, T_p^*, was calculated using Eq. (6.3), which is proposed in Fredsøe *et al.* [13], whilst T_q^* was calculated using Eq. (6.6), which is proposed in this work. A clear relationship between the dimensional time scale, T_p, and the upstream dimensionless bed shear stress, θ_∞, was not observed (Figure 6.9a). However, an overall downward trend can be observed in both Figure 6.9b and Figure 6.9c, wherein the non-dimensional scour time scale was seen to decrease with an increase in θ_∞. This overall downward trend is consistent with the findings in previous studies (e.g. [13, 26]).

Figure 6.10 depicts the influence of the Reynolds number on the scour time scale. Similar to the case for θ_∞, a clear relationship between T_p and *Re* was not observed in Figure 6.10a; however, both Figure 6.10b and Figure 6.10c portray a slight downward trend. Although the gradients were not as steep as that seen in Figure 6.9b and Figure 6.9c, it is still evident that *Re* had an influence on the scour time scale, and thus the *Re* term was included in Eq. (6.9) for predicting the non-dimensional scour time scale, which has not been considered in previous studies.

Figure 6.11 shows the effect of the water depth ratio, h/D, on the scour time scale. There seemed to be an increase in the non-dimensional time scale with an increase in h/D, which agreed with the numerical results in Zhao and Cheng [46]. Due to physical limitations, it was not possible to consider higher water depths.

Figure 6.12 shows the effect of e_o/D on the scour time scale, where the time scale appeared to be increasing with an increase in e_o/D from an overall perspective, in terms of the dimensional as well as the non-dimensional time scales. It is worth noting that S_{eq}/D was observed to decrease with an increase in e_o/D (Figure 6.6).

Figure 6.13 presents the correlation between the empirical formulae with all clear-water and live-bed experimental data, which were obtained in the present study and from published literature [3, 12]. Figure 6.13a shows that fitting the equation proposed in Zhang *et al.* [26] (introduced in Table 2.3), with the original coefficients, to the experimental data had resulted in a low squared correlation coefficient. Figure 6.13b shows the correlation between the

equation proposed in Zhang *et al.* [26], but with the constants updated via the optimisation process described in Section 6.2.2, with the experimental data:

$$T_{\mathrm{p}}^{*} = 1.83\theta_{\infty}^{-0.39} \tag{6.15}$$

where R^2 = 0.18, suggesting that there is a lack of consideration of other essential parameters and/or the formulation of the equation can be improved. Figure 6.13c shows the correlation of Eq. (6.5) with the experimental data, where the original equation was proposed in Zang *et al.* [32], but for predicting the scour time scale beneath pipelines with a partial embedment; hence, the constants have been updated to better reflect the influence of the pipe elevation, e_o/D:

$$T_{\mathrm{p}}^{*} = 2.65\theta_{\infty}^{-0.10} \exp\left(\left(3.42\frac{e_{\mathrm{o}}}{D}\right)^{0.88}\right) \tag{6.16}$$

where the corresponding R^2 was approximately 0.49. Subsequently, Eq. (6.6) was proposed in this work and was used to non-dimensionalise the time scale, instead of using Eq. (6.3) which was proposed in Fredsøe *et al.* [13]. Figure 6.13d shows the correlation between the following equation and the experimental data:

$$T_{\mathrm{q}}^{*} = 28.02\theta_{\infty}^{-0.57} \tag{6.17}$$

whereby the formulation of this equation was similar to that of Eq. (6.15), but the way in which the scour time scale was non-dimensionalised was modified (i.e. using T_{q}^{*} instead of T_{p}^{*}), and by using the same optimisation process described in Section 6.2.2, new values for the constants were computed to attain the best possible correlation (i.e. R^2 = 0.33). Although the corresponding R^2 of 0.33 for Eq. (6.17) was still relatively low, it was significantly improved as compared to that of Eq. (6.15) (i.e. R^2 = 0.18). In Figure 6.13e, the following equation was also seen to produce a much improved correlation with the experimental data:

$$T_{\mathrm{q}}^{*} = 24.63\theta_{\infty}^{-0.52} \exp\left(\left(2.23\frac{e_{\mathrm{o}}}{D}\right)^{2.42}\right) \tag{6.18}$$

where R^2 = 0.64. The formulation of Eq. (6.18) was adopted from Eq. (6.16), for which it was similar to the case for Eq. (6.17) where T_q^* was used instead of T_p^*, and a higher correlation was achieved. This trend has been the motivation behind developing a new equation for predicting the non-dimensional scour time scale, which was based on T_q^* instead of T_p^*. The following equation was formulated, as described in Section 6.2.2:

$$T_q^* = \coth\left(0.11\theta_\infty\right)\cdot\cosh^{-1}\left(9.50\times10^{-4}Re\right)\cdot\left(1-\operatorname{sech}\left(1.34\frac{h}{D}-5.78\right)\right)\cdot\cosh\left(2.98\frac{e_o}{D}\right) \tag{6.19}$$

where a good correlation with the experimental data was achieved (i.e. R^2 = 0.74), as seen in Figure 6.13f. It appeared that Eq. (6.19) can be used to predict the scour time scale for elevated pipelines for both clear-water and live-bed conditions. Although the constant associated with the Reynolds number seemed to be small, this is the first time where the influence of the Reynolds number on the time scale had been quantified. However, due to the inverse hyperbolic cosine function (i.e. ArcCosh) that was used for the Reynolds number term, Eq. (6.19) would only be valid for Re > 1,052.

6.3.3 Field predictions

Figure 6.14 compares the range of measured seabed gaps, which were obtained for the Tasmanian Gas Pipeline (TGP) [127], with the seabed gaps that were predicted by adding the pipe elevation and the predicted equilibrium scour depths (i.e. $G_s = e_o + S_{eq}$); the term definitions are illustrated in Figure 1.2.

The predictions for the equilibrium scour depth were made by inputting a range of current velocities and the pipe elevation ratio into Eq. (6.11), based on an external pipe diameter, D, of 0.5 m, median sediment grain size, d_{50}, of 0.257 mm, mean water depth of 23 m, and boundary layer thickness of 1 m. Unfortunately, as the boundary layer profile was not available, a boundary layer thickness of 1 m was selected as it was assumed to be a typical boundary layer thickness over the seabed [20].

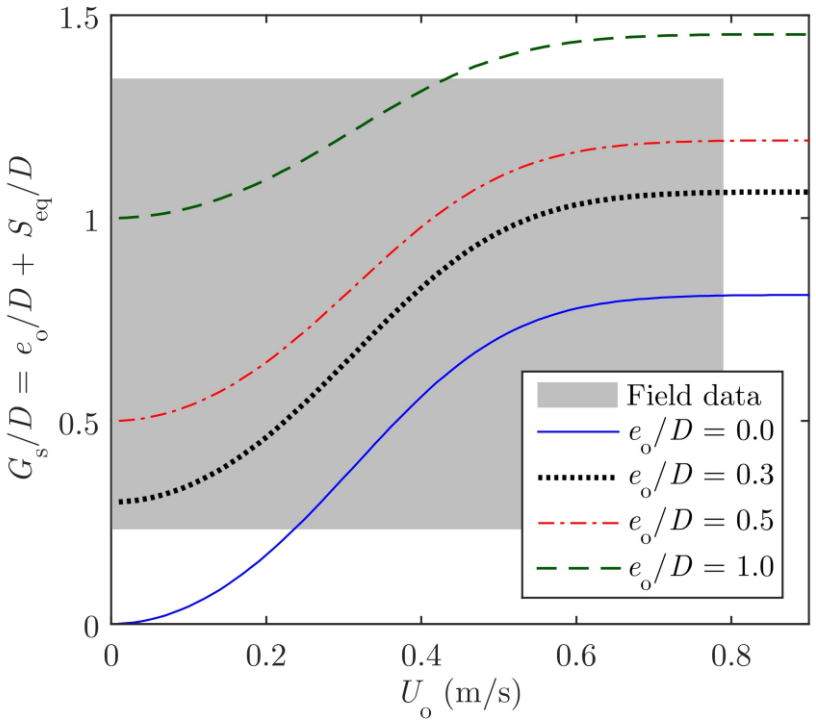

Figure 6.14: Seabed gaps, G_s/D, predicted using Eq. (6.11), which are superimposed on the range of measured seabed gaps for the Tasmanian Gas Pipeline (TGP) [127] (shaded in grey); the upper limit of the current speed (i.e. 0.79 m/s) is the maximum speed for five year return period storms [107].

The vertical limits of the shaded area in Figure 6.14 represents the range of maximum seabed gaps for every detected free span along the surveyed section of the TGP. The horizontal limit of the shaded area corresponded to a current speed of 0.79 m/s, which is the maximum speed for five year return period storms in the Bass Strait [107]. A large portion of the predicted values appear to be within the range of measured seabed gaps, and the predicted seabed gaps seem to remain constant after 0.8 m/s, at which the equilibrium scour depth would no longer increase with higher current speeds.

Figure 6.15 presents the predicted scour time scales for the TGP for different current speeds and pipe elevations, which were calculated using Eq. (6.19), and converted into a dimensional form via Eq. (6.6). The assumptions made were similar to the aforementioned assumptions which were used to predict the seabed gaps. It is worth mentioning that it was not practical to physically measure the scour time scale beneath the TGP, and hence the predicted time scales could not be compared with field measurements. Nevertheless, the time

required for substantial scour to develop beneath the TGP was predicted to be generally longer for larger e_o/D ratios, and shorter for higher current speeds.

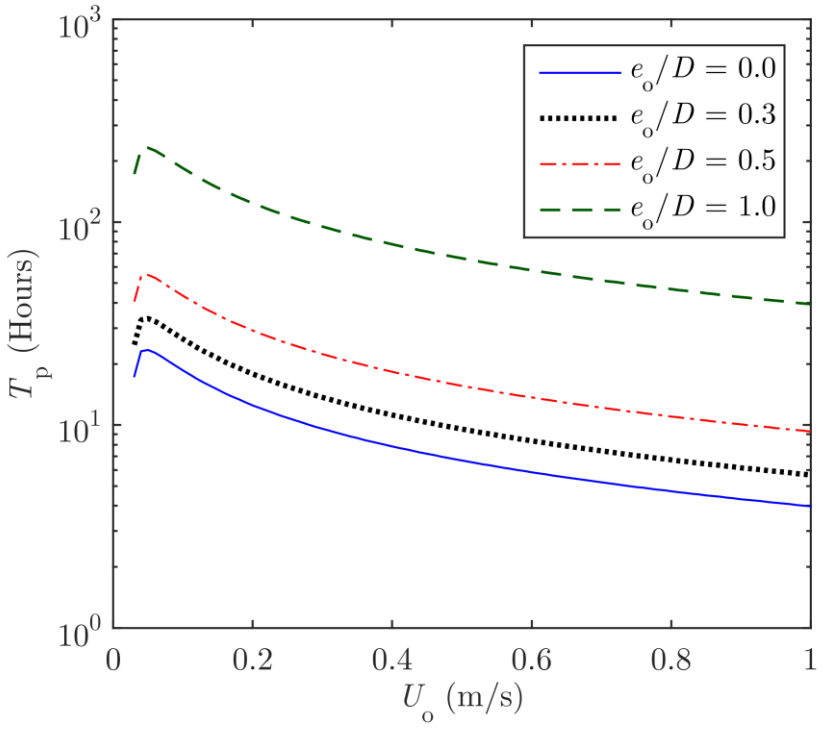

Figure 6.15: Dimensional scour time scales, T_p, predicted using Eq. (6.19) and Eq. (6.6) for the TGP.

The predicted scour time scale for the TGP was seen to be on the order of hours, instead of minutes, which has been observed in the sediment flume experiments. Qualitatively, this difference in the scour time scales between the model-scale and full-scale conditions is consistent with the finding in Liang *et al.* [6], wherein a numerical model was employed to model scour at different scales.

6.4 Discussion

The experimental results suggest that the pipe elevation ratio, e_o/D, does have a significant influence on the development of scour beneath subsea pipelines under steady currents (i.e. both the equilibrium scour depth and the scour time scale). When e_o/D was increased, higher equilibrium scour depths were observed, whilst the maximum scour depth occurred at e_o/D = 0. This can be correlated to weaker flow amplification underneath the pipe as e_o/D increased, and thus leading to a decrease in the maximum seabed shear stress beneath the pipe [127,

136]. In terms of the scour time scale, a general increase was observed with the increase in e_o/D. This could also be attributed to the decrease in the amplified seabed shear stresses underneath the pipe as e_o/D increased. A reduction in the seabed shear stress would result in a lower sediment transport rate, as they are directly proportional to each other [137, 138]. In addition, the sediment transport rate had been linked to the scour time scale [26].

With reference to Figure 6.12, it is interesting to note that both the dimensional and non-dimensional scour time scales were observed to be slightly higher when $e_o/D = 0$, as compared to the time scale for the case of $e_o/D = 0.1$. This could have stemmed from the different mechanics of scour, or the way in which scour was initiated, for these two conditions. When $e_o/D \leq 0$, there would initially be a flow-induced pressure difference between the upstream and downstream sides of the pipe, which promotes fluid flow through the voids in between the sediment particles beneath the pipe (i.e. seepage flow). Eventually, a mixture of water and sediment will be discharged at the immediate downstream side of the pipe (i.e. piping) [16]. This is followed by a "jet period" (i.e. tunnel erosion) where sediment is syphoned violently through the gap between the pipe and the sand bed [3], as seen in Figure 6.16 below.

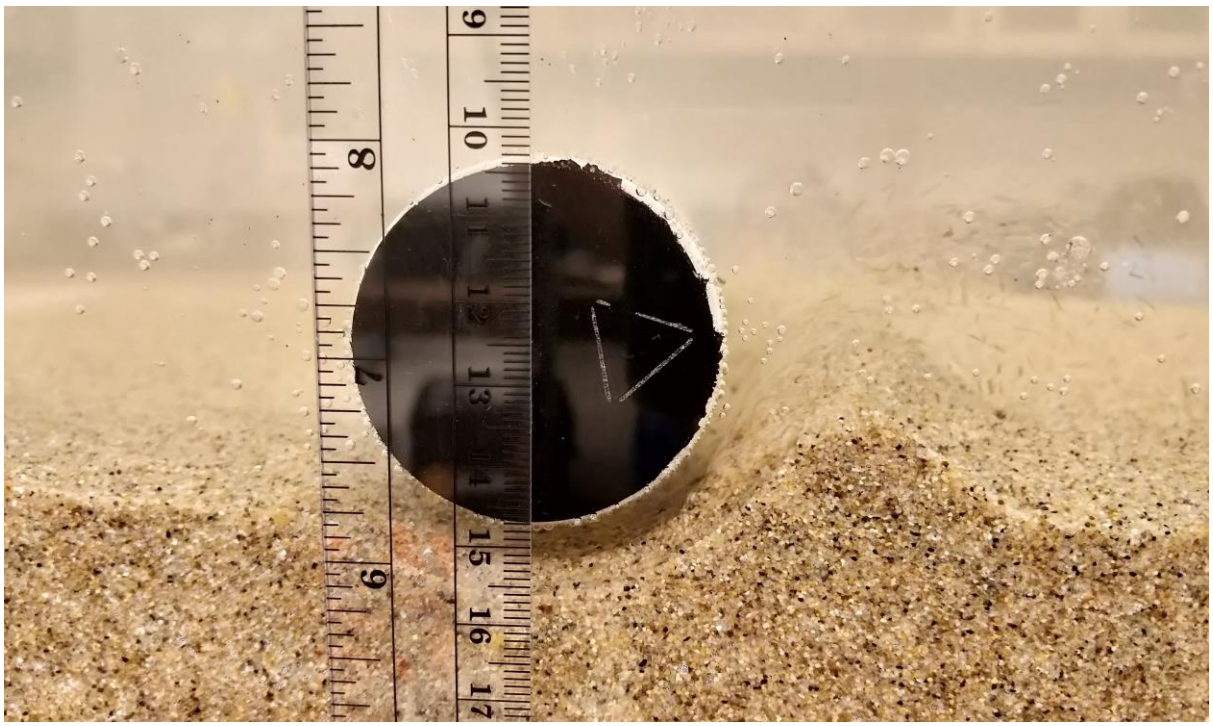

Figure 6.16: Tunnel erosion.

As more sediment is eroded, the scour hole will deepen. However, when $e_o/D > 0$, the existing gap in between the pipe and the seabed would induce flow amplification. Subsequently, scour would occur underneath the pipe, provided that the local amplified seabed shear stress had exceeded the critical shear stress for the sediment. Therefore, the difference in the aforementioned mechanisms at play is thought to result in the difference in the scour time scale, where a longer period would be required for the scouring rate to reach a significant level for $e_o/D = 0$, as compared to the case of $e_o/D = 0.1$.

There seem to be a significant scatter in the results in Figure 6.12. This could be attributed to other parameters that pose a strong influence on the scour time scale. For example, the upstream dimensionless seabed shear stress, θ_∞. A nonlinear decrease in the scour time scale was observed as θ_∞ increased, as shown in Figure 6.9, whilst the scour time scale would generally increase with an increase in e_o/D. On the subject of θ_∞, the overall trends shown in Figure 6.9 agreed with previous findings [13, 26]. This strong relationship between the scour time scale and θ_∞ had led to the development of previous empirical formulae [13, 26, 32], in which the θ_∞ term was always present. This downward trend can be related to the aforementioned relationship between the seabed shear stress and the sediment transport rate, whereby an increase in θ_∞ would lead to an increase in the seabed shear stress underneath the pipe, and hence a higher sediment transport rate.

In this work, the adoption of a hyperbolic cotangent function in Eq. (6.19) for describing the relationship between the newly-derived dimensionless scour time scale, T_q^*, and θ_∞ was seen to contribute towards achieving a good correlation with the experimental data overall (i.e. $R^2 = 0.74$). As this work had contributed significant clear-water experimental data, whilst previous work [13, 26, 32] largely focused on the live-bed condition, Eq. (6.19), which was fitted to both conditions, can therefore be used for predicting the scour time scale both under clear-water and live-bed conditions. Eq. (6.19) is introduced in an attempt of simplification, whereby a single equation is proposed for both clear-water and live-bed conditions. In contrast, Dogan and Arisoy [29] found different dependencies of the non-dimensional scour time scale, and proposed two separate equations for the clear-water and live-bed conditions. Therefore, a possible improvement in the correlation between the equation proposed in this work and the experimental data may be attainable by having two separate equations.

In addition to the strong relationship between the scour time scale and θ_∞, the θ_∞ term was also included in Eq. (6.19), as it has been successfully adopted for scaling laboratory experiments that involve sediment transport for many years [124]. On the topic of scale effects, another important parameter to consider is the Reynolds number, *Re* [4]. However, a relatively weak relationship between T_q^* and the Reynolds number was observed in Figure 6.10, and also based on the small constant in Eq. (6.19). This occurrence was expected, as *Re* was previously found to pose a small influence on the maximum seabed shear stress beneath the pipe and the equilibrium scour depth [136].

The water depth ratio, h/D, was seen to have an effect on the non-dimensional scour time scale. Although the relationship between the dimensional scour time scale, T_p, and h/D was relatively unclear (Figure 6.11a), the non-dimensional scour time scale was seen to increase with the increase in h/D (Figure 6.11b and Figure 6.11c). A previous numerical study [46], in which the influence of h/D was investigated, independent of other variables, reported that the time required for the equilibrium scour depth to be achieved was approximately 2.9 times higher when $h/D = 10$, as compared to $h/D = 2.5$. However, it seemed that this could not be validated with experimental data due to the physical limitations associated with laboratory setups, where having high h/D ratios would not be possible. In addition, higher h/D ratios were neither investigated experimentally nor numerically, and the upper limit at which h/D no longer poses an influence on the dimensionless scour time scale is still an unknown, whilst the equilibrium scour depth was seen to initially decrease and tend towards a constant value despite a further increase in h/D (Figure 6.5). Nevertheless, Eq. (6.19) was formulated in such a way that the non-dimensional scour time scale will not tend towards infinity when h/D approaches infinity. It is hypothesised that a comprehensive multi-phase numerical model would be required to systematically study the effect of having large water depths on the scour time scale beneath full-scale subsea pipelines (e.g. $h/D > 100$).

A new manner of non-dimensionalising the scour time scale, via Eq. (6.6), was seen to improve the correlation of existing empirical formulae to the compilation of experimental data (Figure 6.13). In comparison to Eq. (6.3) [13], Eq. (6.6) proposed the removal of the indices, or powers (e.g. D^2), which would alter the units of certain parameters (e.g. from m to m^2). However, a flux parameter (i.e. U_o) was introduced in Eq. (6.6), which was not present in Eq. (6.3). This flux parameter, U_o, was mainly introduced to normalise the time scale

without relying on indices. The presence of multiple powers in Eq. (6.3) is hypothesised to result in "overfitting" in a sense.

With reference to Figure 6.15, the dimensional scour time scale for the Tasmanian Gas Pipeline (TGP) was predicted to increase with e_o/D, suggesting that the time required for substantial scour to develop would be longer for higher pipe elevations, which can be related to the reduction in the aforementioned seabed shear stress amplification factor. The time scale was seen to generally decrease with an increase in the current speed, and approach a certain value. However, there was an initial increase in the time scale at low current speeds, which was followed by a rapid change, at which a maximum value was reached. This could be related to the formulation of Eq. (6.19), wherein an increase in the current speed would influence both θ_∞ and *Re*. The time scale would tend to decrease with an increase in θ_∞, whilst the time scale would tend to increase with an increase in *Re*, but the constants in Eq. (6.19) suggest that the influence of θ_∞ is more significant than that of *Re*. In addition, the increase in the scour time scale with the flow velocity was also observed in the sediment flume experimental results (Table 6.2), where an occasional decrease in the scour time scale was observed; this inconsistency was also observed in [13]. Nevertheless, the increase in the scour time scale was observed to occur at very low current speeds in Figure 6.15 (i.e. less than 0.1 m/s), and thus, it can be deduced that the dimensional scour time scale would generally decrease with the current speed.

Although the scour time scale could not be compared with field measurements, the influence of the pipe elevation on the scour time scale had not been investigated in previous work. In addition, full-scale predictions have also been made for the seabed gaps (Figure 6.14), for which the predictions made using Eq. (6.11) appeared to be mostly within the range of measured values in Lee *et al.* [127]. It is worth mentioning that the highest incidence in terms of the measured seabed gaps was found to be $G_s/D = 0.5$, at more than 35%, which was followed by $G_s/D = 0.6$, and subsequently, smaller ratios (i.e. $G_s/D < 0.5$) [127]. However, the scour depths beneath the TGP may not necessarily be in an equilibrium state. Therefore, it can only be deduced that there seemed to be a correlation between the predictions made using Eq. (6.11) and the measured values, and that the scour depth may deepen if it is not in equilibrium. In addition, along the surveyed section of the TGP, the seabed has been observed to be mostly comprised of uniform sand, but occasionally, rocks have been

observed. Thus, the seabed gaps could be present due to scouring beneath the pipe and/or feature mobility where the seabed is uneven.

In summary, the compilation of experimental data in this work suggests that the non-dimensional scour time scale is significantly influenced by the upstream dimensionless seabed shear stress, θ_∞, and the pipe elevation ratio, e_o/D. The effect of the Reynolds number is small, and the effect of the water depth or blockage ratio, h/D, can be further investigated with sophisticated numerical models without physical restrictions in terms of the size of the computational domain. As previous experimental investigations on the scour time scale largely focused on live-bed conditions and bottom-seated or partially embedded pipelines, this work presents Eq. (6.19), in which the scour time scale was non-dimensionalised using a new formulation as shown in Eq. (6.6), that is found to result in a high correlation to the experimental data. Eq. (6.19) is applicable for both clear-water and live-bed conditions, as well as pipelines with an elevation with respect to the far-field seabed under steady currents.

6.5 Summary

This work focused on predicting the development of scour beneath subsea pipelines with an initial elevation with respect to the far-field seabed under steady currents. A range of pipe elevation ratios, $0 \leq e_o/D \leq 0.5$, were considered for the sediment flume experiments, and additional experimental data from published literature were compiled as well. Multiple equations have been formulated to non-dimensionalise the scour time scale, and to predict the time scale as a function of the upstream seabed shear stress, θ_∞, Reynolds number, Re, water depth ratio, h/D, and e_o/D. The following major conclusions can be drawn from the results presented in this work:

- A general increase in the scour time scale was observed as e_o/D increased.
- The effect of Re on the time scale was small.
- The non-dimensional time scale was seen to increase with an increase in h/D; however, the dimensional time scale appear to be weakly correlated with h/D.
- A new form of the non-dimensional scour time scale, which is calculated using Eq. (6.6), was found to result in a better correlation with the experimental data

- A new empirical formula, Eq. (6.19), is proposed for predicting the non-dimensional scour time scale beneath elevated pipelines under steady currents, which has a good correlation with experimental data, and is applicable for both clear-water and live-bed conditions.
- As the scour time scale for the TGP was not known, the measured scour depths beneath the full-scale pipeline may not be at equilibrium. Nevertheless, the comparison between the seabed gaps predicted using Eq. (6.11) and the field measurements did not indicate that the full-scale predictions are erroneous.

Chapter 7 has been removed for copyright or proprietary reasons.

It has been published as: Lee, J. Y., McInerney, J. B., Hardjanto, F. A., Chai, S., Cossu, R., Leong, Z. Q., Forrest, A. L., 2018. Two-phase model for simulating current-induced scour beneath subsea pipelines at different initial elevations, in, ASME 2018 37th International Conference on Ocean, Offshore and Arctic Engineering (pp. V009T10A021-V009T10A021). American Society of Mechanical Engineers.

Chapter 8
Conclusions

This chapter concludes the research that has been conducted, by summarising the research questions and objectives, highlighting the key findings, and discussing the implications of the contributions in this thesis as well as recommendations for the future.

8.1 Research summary

This thesis focused on predicting two-dimensional scour beneath elevated subsea pipelines under steady currents. This consisted of the maximum seabed shear stress beneath the pipe, the equilibrium scour depth and the scour time scale. In addition to a review of existing empirical formulae, which were developed for scour prediction, a review of relevant numerical modelling techniques was undertaken to identify practical options for predicting the initiation and development of scour. Subsequently, experimental, numerical and field investigations were conducted in this work; through which, the effects of the pipe-elevation-to-diameter ratio, e_o/D, upstream dimensionless seabed shear stress, θ_∞, and Reynolds number, Re, were quantified.

The research conducted in this thesis stemmed from addressing the first research question: "*how would having a small initial pipe elevation or seabed gap affect the occurrence of scour beneath a pipe?*". A field survey was conducted for a natural gas pipeline to gauge the presence of small seabed gaps along the surveyed section. This was followed by performing full-scale computational fluid dynamics (CFD) simulations, which involved modelling the flow and seabed shear stress beneath a two-dimensional pipe close to a rough seabed. The key findings here were:

- The field data (Chapter 4), revealed multiple incidences of free spanning, whereby a significant number of spans had small maximum seabed gaps (i.e. less than the equivalent of 30% of the external pipe diameter).
- The simulation results showed that there are highly nonlinear changes in the seabed shear stress in the vicinity of the pipe. A peak in the seabed shear stress beneath the pipe, which was significantly higher than the upstream seabed shear stress, was observed in all cases. For the same upstream flow condition, the maximum seabed shear stress beneath the pipe was observed to increase with a decrease in the pipe elevation with respect to the far-field seabed. A new equation was proposed in Chapter 4 for predicting the maximum dimensionless seabed shear stress beneath the pipe:

$$\theta_{\max} = \theta_{\infty}^{0.864}\left(\frac{e_o}{D}\right)^{-0.333} \tag{8.1}$$

  where the predicted maximum dimensionless seabed shear stress, $\theta_{\max}$, can be compared to the critical shear stress, θ_{cr}, to estimate whether scour would occur beneath the pipe; θ_{∞} is the upstream dimensionless seabed shear stress, whilst e_o/D is the normalised pipe elevation.

The influence of e_o/D on the initiation of scour has not been quantified in existing empirical formulae. The author then built on this work by addressing scale effects, or more specifically: "*to what extent does θ_{∞} and Re influence the maximum seabed shear stress and equilibrium scour depth underneath a pipe for $e_o/D > 0$?*". A large parametric study, which involved numerous CFD simulations, were performed at various scales, to quantify the influence of the pipe Reynolds number on the maximum seabed shear stress. This was performed using the same single-phase rigid seabed model. In addition, experimental data were compiled from published literature to derive a new empirical formula for predicting the equilibrium scour depth, whilst quantifying the influence of θ_{∞} and *Re*, which have not been considered in existing formulae. It was found that:

- For the same upstream flow condition, the change in the external pipe diameter was observed to result in a decrease in the maximum seabed shear stress beneath the pipe.

However, the Reynolds number effects were small as compared to that of θ_∞ and e_o/D. The aforementioned Eq. (8.1) was modified to include a Reynolds number term in Chapter 5, and the result was:

$$\theta_{max} = \theta_\infty + \theta_\infty^{0.93} Re^{0.13} \left(\frac{1}{\exp(e_o/D)} \right)^{2.38} \tag{8.2}$$

where *Re* is the pipe Reynolds number.

- The equilibrium scour depth was seen to increase rapidly with θ_∞ for the clear-water condition, but slightly decrease for the live-bed condition. Similar to Eq. (8.2), there is a strong influence of θ_∞ and e_o/D on the equilibrium scour depth, whilst the Reynolds number effects appeared to be small. In Chapter 5, the following equation was proposed:

$$\frac{S_{eq}}{D} = \tanh(15.15\theta_\infty) \cdot Re^{-0.01} \cdot \coth\left(0.62\frac{h}{D}\right) \cdot \left(-0.11 + \operatorname{sech}\left(-1.08\frac{e_o}{D}\right)\right) \tag{8.3}$$

where S_{eq}/D is the equilibrium scour depth, and h/D is the normalised water depth. An additional term was added, which was the water depth or blockage ratio, h/D. It was also of interest to quantify the influence of this parameter, because the experimental data that was used to develop this equation involved a significant number of tests in relatively shallow water. Interestingly, the equilibrium scour depth was seen to initially decrease but approach a relatively constant value as h/D increased.

Subsequently, sediment flume experiments were conducted to investigate the development of scour beneath elevated subsea pipelines, as the third research question was: "*to what extent does θ_∞, Re and e_o/D affect the scour time scale?*". Scour depth measurements attained in this work as well as from published literature were also used to develop a new empirical formula for predicting the scour time scale, whereby the influence of e_o/D on the scour time scale has not been quantified in existing formulae. Furthermore, there appeared to be a lack of clear-water data (i.e. the condition for which $\theta_\infty < \theta_{cr}$) in the literature. The key findings here can be summarised as:

- The influence of the parameters of interest were similar to that for the equilibrium scour depth. The Reynolds number also had a small influence on the dimensionless scour time scale. The scour time scale was seen to decrease with an increase in θ_∞, but increase with an increase in e_o/D and h/D. In Chapter 6, the following equation was proposed:

$$T_q^* = \coth\left(0.11\theta_\infty\right)\cdot\cosh^{-1}\left(9.50\times10^{-4}Re\right)\cdot\left(1-\operatorname{sech}\left(1.34\frac{h}{D}-5.78\right)\right)\cdot\cosh\left(2.98\frac{e_o}{D}\right), \quad \text{for } Re > 1052 \tag{8.4}$$

  where T_q^* is the non-dimensional scour time scale. Eq. (8.4) was fitted to experimental data for both clear-water and live-bed conditions, whilst existing formulae largely focused on the live-bed condition.
- It was possible to attain a high correlation coefficient with Eq. (8.4) by adopting a new approach to normalise the scour time scale:

$$T_q^* = \frac{g\left(\frac{\rho_s}{\rho}-1\right)d_{50}}{U_o D}T_p \tag{8.5}$$

  where g is gravitational acceleration; ρ_s is sediment density; ρ is fluid density; d_{50} is the median sediment grain size; U_o is the depth-averaged current velocity; D is the external pipe diameter; and, T_p is the dimensional scour time scale. The use of Eq. (8.5) enabled existing empirical formulae and Eq. (8.4) to attain higher correlation coefficients, as compared to using the conventional manner of normalising the scour time scale.

Finally, this thesis explored the practicality of an open-source two-phase numerical model, *twoPhaseEulerFoam*, to take a closer look into multiphase modelling. This aimed to address the question of: "*what is the state-of-the-art in terms of practical numerical modelling techniques for simulating scour beneath subsea pipelines?*". The assessment of the capabilities of *twoPhaseEulerFoam* was preceded by a comprehensive review of existing numerical modelling techniques (Section 2.2). *twoPhaseEulerFoam* has been used to

simulate experiments to compare the numerical predictions with published experimental and numerical data. The findings suggest that:

- The equilibrium scour depths predicted using *twoPhaseEulerFoam* was seen to be in a good agreement with published experimental and numerical data, as well as the predictions that were made using Eq. (8.3). However, similar to a recent study which involved another two-phase Eulerian-Eulerian model, the scour time scale was under-predicted, whereby the rate at which scour occurred beneath the pipe was more rapid than that recorded in the experiments.
- Nevertheless, relatively short computational times were achieved (e.g. several hours) whilst using inexpensive hardware (e.g. a single desktop computer). This may have partly been achievable due to the relatively coarse mesh that was required to attain reasonably accurate equilibrium scour depths. In addition, it was found that a small initial scour hole was not required to initiate the scour process, which has been reported to be necessary in previous studies.

8.2 Conclusions

The pipe elevation with respect to the far-field seabed has a significant influence on the initiation and development of scour beneath a subsea pipeline. The aforementioned key findings imply that having a small pipe-elevation-to-diameter ratio would increase the capacity for scour to occur and develop at a rapid rate, after which a deep scour depth can be expected. In addition, field observations showed that it is possible for a pipeline to have relatively small gaps between the bottom of the pipe and the seabed.

The capacity for scour to occur would be higher for a smaller seabed gap, due to a higher amplification of the seabed shear stress beneath the pipe, with respect to the upstream seabed shear stress. The influence of the pipe elevation on the amplification of the seabed shear stress has been investigated in previous studies. However, the results in this work suggest that having a high amplification of the seabed shear stress may not necessarily lead to the occurrence of scour, especially for the clear-water condition, for which the maximum seabed shear stress may not exceed the critical shear stress for the sediment. Therefore, it may be

more beneficial to focus on comparing the maximum seabed shear stress to the critical shear stress.

The small constants associated with the Reynolds number terms in the equations, which were proposed in this work, suggest that fluid viscous effects may be negligible. Nevertheless, high correlation coefficients were attainable with the inclusion of the Reynolds number term, which has not been quantified in existing formulae. Similarly, the influence of the upstream dimensionless seabed shear stress is also worth considering, even though it is not present in existing formulae for predicting the equilibrium scour depth. In terms of scale effects, it appears that for a full-scale pipe, scour may take much longer to develop, but may arrive at a slightly smaller dimensionless equilibrium scour depth, as compared to a laboratory-scale pipe.

With regards to numerical modelling, the initiation of scour can be predicted using a single-phase rigid seabed model. This can be achieved by comparing the calculated maximum seabed shear stress with the critical shear stress. For the development of scour, a two-phase Eulerian-Eulerian model such as *twoPhaseEulerFoam* has been shown to be a practical option, to be used for predicting the equilibrium scour depth with reasonable accuracy. However, this open-source model under-predicted the scour time scale, and modifications to the code may be required to improve its accuracy.

8.3 Implications

Existing formulae that were developed for predicting the initiation of scour have not considered the pipe elevation with respect to the seabed, e_o/D. Although the influence of e_o/D on the amplification of the seabed shear stress has been investigated, this work showed that having a high amplification factor may not necessarily lead to the occurrence of scour beneath the pipe. Eq. (8.2) was proposed in this work for predicting the local maximum dimensionless seabed shear stress beneath subsea pipelines, θ_{max}, wherein the effects of e_o/D, the upstream dimensionless seabed shear stress, θ_∞, and the pipe Reynolds number, Re, were quantified. Hence, the capacity for scour to occur underneath the pipe can be estimated by comparing θ_{max} with the critical shear stress for the sediment, θ_{cr}. This may be particularly

useful when a pipeline could have multiple free spans with small seabed gaps, which have been observed in the field.

The ability to predict the equilibrium scour depth directly beneath the pipe, S_{eq}/D, enables one to estimate the severity of scour. When the gap between the bottom of the pipe and the seabed exceeds the equivalent of 30% of the external pipe diameter, regular vortex shedding may occur in the wake of the pipe, potentially leading to vortex-induced vibrations which may compromise the structural integrity of the pipeline. Existing formulae that included a e_o/D term have been developed for the live-bed condition (i.e. $\theta_\infty > \theta_{cr}$). However, scour can occur under the clear-water condition (i.e. $\theta_\infty < \theta_{cr}$) as well. Thus, Eq. (8.3) was proposed in this work to quantify the influence of θ_∞. Furthermore, the influence of *Re* and the water depth ratio, h/D, were quantified as well, which were not present in existing formulae. Therefore, Eq. (8.3) may be applicable for pipelines in both shallow and deep waters, and of various external pipe diameters.

The ability to predict the scour time scale would allow pipeline engineers to estimate the time required for a substantial scour depth to develop, which can be compared to the period of a storm event, to gauge the corresponding development of a scour hole underneath the pipeline. Unfortunately, existing empirical formulae that were developed for predicting the time scale have not considered the influence of e_o/D and *Re* as well. In this work, Eq. (8.4) was proposed, wherein the effects of e_o/D and *Re* were quantified. In addition, Eq. (8.5) was suggested as a new manner of non-dimensionalising the scour time scale, because it was shown to enable existing formulae as well as Eq. (8.4) to attain higher correlation coefficients.

With regards to numerical modelling, there seemed to be a lack of a comprehensive review of existing numerical models. This work reviewed the numerical models that were used to simulate scour beneath pipelines to identify the practical options for industrial and/or academic research purposes. In terms of predicting the seabed shear stress, it was found that a single-phase rigid seabed model would be appropriate, especially for performing large parametric studies. A two-phase Eulerian-Eulerian model can be a practical option for modelling the equilibrium scour depth, even for bottom-seated pipelines. However, modifications to the code may be required to accurately predict the scour time scale. The ability to employ a numerical model to obtain accurate predictions of scour development

within a reasonable time frame may be beneficial for the design and maintenance of subsea pipelines.

8.4 Recommendations for the future

This thesis is a step in the direction towards improving the existing methods of predicting scour beneath subsea pipelines. The long-term objective of this body of work would be to improve the design and management of subsea pipelines, which may incidentally further develop the understanding of the natural environment encompassing such subsea structures. Nevertheless, there is room for improvement, whereby the work that have been presented in this thesis can be further extended.

It was mentioned in Section 1.4 that investigating the influence of waves was not within the scope of this work. There have been studies that focused on scour in waves (e.g. [9, 30]) and a combination of currents and waves (e.g. [31, 32]). However, it seems that the influence of the pipe elevation has not been considered in these studies. Although unidirectional currents were found to result in deeper scour depths as compared to that under the effect of waves or a combination of current and wave action [15], the effects of oscillatory flow may be of interest in relatively shallow waters. Sumer and Fredsøe [9] showed that there was a significant correlation between the equilibrium scour depth and the *KC* number for the live-bed condition, and proposed the following equation:

$$\frac{S_{eq}}{D} = 0.1\sqrt{KC} \tag{8.6}$$

Recently, Dogan *et al.* [148] conducted experiments in both clear-water and live-bed conditions, and proposed the following equation:

$$\frac{S_{eq}}{D} = 0.004KC^{1.88}\theta_{\infty}^{1/3} \tag{8.7}$$

where it was found that the equilibrium scour depth had a significant correlation with θ_∞ for the live-bed condition, but not the clear-water condition. Interestingly, this is in contrast with

scour under steady currents, for which S_{eq}/D correlated well with θ_∞ for the clear-water condition and not the live-bed condition. In addition, the influence of the pipe elevation has not been quantified, even though the effect of the vertical position of the pipe was investigated in Sumer and Fredsøe [9]. As the amplitude of the oscillatory motion is directly proportional to the *KC* number, the aforementioned equations suggest that higher amplitudes would result in deeper scour depths. Therefore, it may be of interest to build on this work by quantifying the influence of e_o/D on scour in waves.

The influence of oscillatory flow on the scour time scale has also become increasingly popular in recent years (e.g. [26, 29, 32]). A high correlation with experimental data was seen to be achievable with equations that include a modified Shields parameter term, which incorporated both the friction velocity due to current action and that due to waves; or, θ_∞ and *KC* number (refer to Table 2.3). However, it appears that the influence of the water depth has yet to be quantified for scour in waves. Although the *KC* number term in the equation from Dogan and Arisoy [29] did include the water depth, *h*, it seems that the mean water level was held constant in the experiments. Thus, it may be worth investigating a wide range of mean water depth ratios, *h*/*D*, in addition to the effects of oscillatory flow, especially for shallow water cases whereby the influence of waves would be important.

As the results in this work showed that the dimensionless scour time scale did vary with *h*/*D*, it would also be interesting to determine the upper limit at which *h*/*D* no longer has an influence on the scour time scale. However, this may require a sufficiently large experimental facility or computational domain. Due to physical limitations, it may often be more feasible to employ numerical models for such purposes. This was a key motivation to review existing numerical modelling techniques, to identify the practical options for simulating scour.

In this thesis, a single-phase CFD model was used to compute the seabed shear stress for predicting the initiation of scour, while a two-phase CFD model was employed to simulate the development of scour beneath a pipe. The single-phase model appeared to have room for improvement in terms of the roughness model. As discussed in Chapter 5, although the change in the velocity profile due to a change in the seabed roughness is expected to be small with reference to the law of the wall (i.e. less than 10%), the change in the velocity profile predicted via CFD was an order of magnitude smaller (i.e. less than 1%). Thus, it may be

worth to consider adopting or developing a new roughness model to simulate the seabed shear stress beneath the pipe.

The two-phase Eulerian-Eulerian model which was used in this work, *twoPhaseEulerFoam*, was found to be able to predict the equilibrium scour depth with a reasonable level of accuracy; however, it was inadequate in terms of predicting the scour time scale. Modifications to the code may be required to improve the accuracy of *twoPhaseEulerFoam*; or, if there were abundant computational resources, it may be worth employing an Eulerian-Lagrangian model. In addition, although the aforementioned numerical models have been validated against several studies from the published literature, it may be beneficial to perform further validation. For example, for the case of clear-water scour where the scour time scale is on the order of minutes or hours, and not 168 s.

With some notable exceptions (e.g. [6]), it seems that few studies have simulated scour around full-scale pipelines, especially when it comes to investigating the effects of h/D. Numerical models can also be used to simulate three-dimensional scour around a pipeline, where the development of free spans is of interest. Three-dimensional scour has been investigated via experiments (e.g. [149, 150]), through which empirical formulae have been developed for predicting the scour propagation velocity (i.e. rate of scour propagating along the length of the pipe). However, it seems that the influence of the pipe elevation has not been considered as well. Furthermore, for three-dimensional scour, the structural responses of the pipe itself may play a significant role (e.g. bending, vibration, etc.). The significant increase in the complexity of the problem may be the reason behind the sparsity of such studies in the literature. Further validation may be required before one can proceed to select a numerical model to simulate three-dimensional scour around pipelines, especially when fluid-structure interaction were to be included to model the structural responses of the pipe.

Bibliography

[1] Sumer B.M., Fredsøe J. The Mechanics of Scour in the Marine Environment. Singapore: World Scientific; 2002.

[2] Whitehouse R. Scour at marine structures: A manual for practical applications. London: Thomas Telford; 1998.

[3] Mao Y. The interaction between a pipeline and an erodible bed (PhD Thesis). Lyngby, Denmark: Technical University of Denmark; 1986.

[4] Fredsøe J. Pipeline–Seabed Interaction. J. Waterw. Port Coast. Ocean Eng. 142 (6) (2016) 03116002.

[5] Griffiths T., Zhao F., Kalkhoven M., Shen W., Xu M., Zan Z., et al. Seabed shear stress amplification around subsea pipelines: Part 1, 2D parametric study with currents. Scour and Erosion: Proceedings of the 7th International Conference on Scour and Erosion, Perth, Australia, 2-4 December 2014: CRC Press; 2014. p. 317.

[6] Liang D., Cheng L., Yeow K. Numerical study of the Reynolds-number dependence of two-dimensional scour beneath offshore pipelines in steady currents. Ocean Eng. 32 (13) (2005) 1590-607.

[7] Leckie S.H., Draper S., White D.J., Cheng L., Fogliani A. Lifelong embedment and spanning of a pipeline on a mobile seabed. Coast. Eng. 95 (2015) 130-46.

[8] Moncada-M A.T., Aguirre-Pe J. Scour below pipeline in river crossings. J. Hydraul. Eng. 125 (9) (1999) 953-8.

[9] Sumer B.M., Fredsøe J. Scour below pipelines in waves. J. Waterw. Port Coast. Ocean Eng. 116 (3) (1990) 307-23.

[10] Hughes S.A. Physical models and laboratory techniques in coastal engineering: World Scientific; 1993.

[11] Masselink G., Hughes M.G. Introduction to coastal processes and geomorphology. London: Hodder Arnold; 2003.

[12] Mohr H., Draper S., Cheng L., White D. Predicting the rate of scour beneath subsea pipelines in marine sediments under steady flow conditions. Coast. Eng. 110 (2016) 111-26.

[13] Fredsøe J., Sumer B., Arnskov M. Time scale for wave/current scour below pipelines. Int. J. Offshore Polar Eng. 2 (1) (1992).

[14] Azamathulla H.M., Yusoff M., Hasan Z. Scour below submerged skewed pipeline. J. Hydrol. 509 (2014) 615-20.

[15] Chiew Y.M. Prediction of maximum scour depth at submarine pipelines. J. Hydraul. Eng. 117 (4) (1991) 452-66.

[16] Chiew Y.M. Mechanics of local scour around submarine pipelines. J. Hydraul. Eng. 116 (4) (1990) 515-29.

[17] Bearman P.W., Zdravkovich M.M. Flow around a circular cylinder near a plane boundary. J. Fluid Mech. 89 (1) (1978) 33-47.

[18] Sumer B.M., Truelsen C., Sichmann T., Fredsøe J. Onset of scour below pipelines and self-burial. Coast. Eng. 42 (4) (2001) 313-35.

[19] Zang Z., Cheng L., Zhao M., Liang D., Teng B. A numerical model for onset of scour below offshore pipelines. Coast. Eng. 56 (4) (2009) 458-66.

[20] DNV GL. Recommended Practice DNVGL-RP-F109: On-bottom stability design of submarine pipelines. 2017.

[21] DNV GL. Recommended Practice DNVGL-RP-F105: Free spanning pipelines. 2017.

[22] DNV GL. Recommended Practice DNVGL-RP-F114: Pipe-soil interaction for submarine pipelines. 2017.

[23] Kjeldsen S., Gjorsvik O., Bringaker K., Jacobsen J. Local scour near offshore pipelines. Paper available only as part of the complete Proceedings of the Second International Conference on Port and Ocean Engineering Under Arctic Conditions (POAC), August 27-30, 1973.1973.

[24] Bijker E., Leeuwestein W. Interaction between pipelines and the seabed under the influence of waves and currents. Seabed mechanics: Springer; 1984. p. 235-42.

[25] Ibrahim A., Nalluri C. Scour prediction around marine pipelines. Proc., 5th Int. Symp. on Offshore Mechanics and Arctic Engineering, American Society of Mechanical Engineers1986. p. 679-84.

[26] Zhang Q., Draper S., Cheng L., An H. Time Scale of Local Scour around Pipelines in Current, Waves, and Combined Waves and Current. J. Hydraul. Eng. (2016) 04016093.

[27] Chao J., Hennessy P. Local scour under ocean outfall pipelines. Journal (Water Pollution Control Federation) 44 (7) (1972) 1443-7.

[28] Dey S., Singh N.P. Clear-water scour depth below underwater pipelines. Journal of Hydro-Environment Research 1 (2) (2007) 157-62.

[29] Dogan M., Arisoy Y. Scour regime effects on the time scale of wave scour below submerged pipes. Ocean Eng. 104 (2015) 673-9.

[30] Çevik E., Yüksel Y. Scour under submarine pipelines in waves in shoaling conditions. J. Waterw. Port Coast. Ocean Eng. 125 (1) (1999) 9-19.

[31] Larsen B.E., Fuhrman D.R., Sumer B.M. Simulation of Wave-Plus-Current Scour beneath Submarine Pipelines. J. Waterw. Port Coast. Ocean Eng. (2016) 04016003.

[32] Zang Z., Tang G., Cheng L. Time Scale of Scour Below Submarine Pipeline Under Combined Waves and Currents With Oblique Incident Angle. ASME 2017 36th International Conference on Ocean, Offshore and Arctic Engineering: American Society of Mechanical Engineers; 2017. p. V009T10A19-VT10A19.

[33] Barton G.J., McDonald R.R., Nelson J.M., Dinehart R.L. Simulation of Flow and Sediment Mobility Using a Multidimensional Flow Model for the White Sturgeon Critical-Habitat Reach, Kootenai River near Bonners Ferry, Idaho. Scientific Investigations Report 2005-5230. Virginia: U.S. Geological Survey; 2005.

[34] Shields A. Anwendung der Aehnlichkeitsmechanik und der Turbulenzforschung auf die Geschiebebewegung (Dissertation Doktor-Ingenieur). Berlin: Preussischen Versuchsanstalt für Wasserbau; 1936.

[35] Pinna R., Weatherald A., Grulich J., Ronalds B.F. Field Observations and Modelling of the Self-Burial of a North West Shelf Pipeline. ASME 2003 22nd International Conference on Offshore Mechanics and Arctic Engineering: American Society of Mechanical Engineers; 2003. p. 591-9.

[36] Launder B., Sharma B. Application of the energy-dissipation model of turbulence to the calculation of flow near a spinning disc. Letters in heat and mass transfer 1 (2) (1974) 131-7.

[37] CD-adapco. STAR-CCM+ User Guide Version 10.02. 2015.

[38] Abrahamsen Prsic M., Ong M.C., Pettersen B., Myrhaug D. Large Eddy Simulations of flow around a circular cylinder close to a flat seabed. Mar. Struct. 46 (2016) 127-48.

[39] Akoz M.S., Kirkgoz M.S. Numerical and experimental analyses of the flow around a horizontal wall-mounted circular cylinder. Transactions of the Canadian Society for Mechanical Engineering 33 (2) (2009) 189-215.

[40] Ong M.C., Utnes T., Holmedal L.E., Myrhaug D., Pettersen B. Numerical simulation of flow around a circular cylinder close to a flat seabed at high Reynolds numbers using a k–ε model. Coast. Eng. 57 (10) (2010) 931-47.

[41] Ong M.C., Utnes T., Holmedal L.E., Myrhaug D., Pettersen B. Near-Bed Flow Mechanisms Around a Circular Marine Pipeline Close to a Flat Seabed in the Subcritical Flow Regime Using a k-e Model. J. Offshore Mech. Arct. Eng. 134 (021803) (2012) 1-11.

[42] Zhao M., Cheng L., Teng B. Numerical modeling of flow and hydrodynamic forces around a piggyback pipeline near the seabed. J. Waterw. Port Coast. Ocean Eng. 133 (4) (2007) 286-95.

[43] Shen W., Griffiths T., Xu M., Leggoe J. 2D and 3D CFD Investigations of Seabed Shear Stresses around Subsea Pipelines. ASME 2013 32nd International Conference on Ocean, Offshore and Arctic Engineering: American Society of Mechanical Engineers; 2013. p. V04ATA048-V04AT04A.

[44] Zhao M., Cheng L., Teng B., Dong G. Hydrodynamic forces on dual cylinders of different diameters in steady currents. Journal of fluids and structures 23 (1) (2007) 59-83.

[45] Li F., Cheng L. Effect of Pipeline Sagging on Local Scour Below Pipelines. 20th International Conference of Offshore Mechanics and Arctic Engineering2001. p. 1-6.

[46] Zhao M., Cheng L. Numerical investigation of local scour below a vibrating pipeline under steady currents. Coast. Eng. 57 (4) (2010) 397-406.

[47] Zhao M., Vaidya S., Zhang Q., Cheng L. Local scour around two pipelines in tandem in steady current. Coast. Eng. 98 (2015) 1-15.

[48] Liang D., Cheng L., Li F. Numerical modeling of flow and scour below a pipeline in currents: Part II. Scour simulation. Coast. Eng. 52 (1) (2005) 43-62.

[49] Smagorinsky J. General circulation experiments with the primitive equations. Mon. Weather Rev. 91 (3) (1963) 99-164.

[50] Paola C., Voller V. A generalized Exner equation for sediment mass balance. Journal of Geophysical Research: Earth Surface 110 (F4) (2005).

[51] Engelund F., Fredsøe J. A sediment transport model for straight alluvial channels. Hydrology Research 7 (5) (1976) 293-306.

[52] Sumer B.M. A review of recent advances in numerical modelling of local scour problems. Scour and Erosion: Proceedings of the 7th International Conference on Scour and Erosion. Perth, Australia: CRC Press; 2015. p. 61-70.

[53] Bohorquez P. Study and numerical simulation of sediment transport in free-surface flow (PhD Thesis): University of Malaga, Spain; 2008.

[54] Ahilan R., Sleath J.F. Sediment transport in oscillatory flow over flat beds. J. Hydraul. Eng. 113 (3) (1987) 308-21.

[55] Lun C., Savage S.B., Jeffrey D., Chepurniy N. Kinetic theories for granular flow: inelastic particles in Couette flow and slightly inelastic particles in a general flowfield. J. Fluid Mech. 140 (1984) 223-56.

[56] Wen C.Y., Yu Y.H. Mechanics of fluidization. Chem. Eng. Prog. Symp. Ser.1966. p. 100-1.

[57] Srivastava A., Sundaresan S. Analysis of a frictional–kinetic model for gas–particle flow. Powder technology 129 (1) (2003) 72-85.

[58] Van Wachem B., Schouten J., Van den Bleek C., Krishna R., Sinclair J. Comparative analysis of CFD models of dense gas–solid systems. AIChE Journal 47 (5) (2001) 1035-51.

[59] Zhao Z., Fernando H. Numerical simulation of scour around pipelines using an Euler–Euler coupled two-phase model. Environmental Fluid Mechanics 7 (2) (2007) 121-42.

[60] Yeganeh-Bakhtiary A., Kazeminezhad M.H., Etemad-Shahidi A., Baas J.H., Cheng L. Euler–Euler two-phase flow simulation of tunnel erosion beneath marine pipelines. Appl Ocean Res 33 (2) (2011) 137-46.

[61] Schaeffer D.G. Instability in the evolution equations describing incompressible granular flow. Journal of differential equations 66 (1) (1987) 19-50.

[62] Savage S. Analyses of slow high-concentration flows of granular materials. J. Fluid Mech. 377 (1998) 1-26.

[63] Johnson P.C., Jackson R. Frictional–collisional constitutive relations for granular materials, with application to plane shearing. J. Fluid Mech. 176 (1987) 67-93.

[64] Cheng Z., Hsu T.-J., Calantoni J. SedFoam: A multi-dimensional Eulerian two-phase model for sediment transport and its application to momentary bed failure. Coast. Eng. 119 (2017) 32-50.

[65] Menter F.R. Two-equation eddy-viscosity turbulence models for engineering applications. AIAA J. 32 (8) (1994) 1598-605.

[66] Yeganeh-Bakhtiary A., Zanganeh M., Kazemi E., Cheng L., Wahab A.A. Euler–Lagrange two-phase model for simulating live-bed scour beneath marine pipelines. J. Offshore Mech. Arct. Eng. 135 (3) (2013) 031705.

[67] Zhu H., Zhou Z., Yang R., Yu A. Discrete particle simulation of particulate systems: theoretical developments. Chemical Engineering Science 62 (13) (2007) 3378-96.

[68] Zhang Y., Zhao M., Kwok K., Liu M. Computational fluid dynamics–discrete element method analysis of the onset of scour around subsea pipelines. Appl. Math. Model. 39 (23) (2015) 7611-9.

[69] Di Felice R. The voidage function for fluid-particle interaction systems. International Journal of Multiphase Flow 20 (1) (1994) 153-9.

[70] Crowe C., Sommerfeld M., Tsuji Y. Multiphase flows with particles and droplets. CRC Press, New York; 1998.

[71] Yang J., Low Y.M., Lee C.-H., Chiew Y.-M. Numerical simulation of scour around a submarine pipeline using computational fluid dynamics and discrete element method. Appl. Math. Model. 55 (2018) 400-16.

[72] van Wachem B.G.M. Derivation, implementation, and validation of computer simulation models for gas-solid fluidized beds (PhD Thesis). Netherlands: Delft University of Technology; 2000.

[73] Brumby P.E., Sato T., Nagao J., Tenma N., Narita H. Coupled LBM–DEM Micro-scale Simulations of Cohesive Particle Erosion Due to Shear Flows. Transport in Porous Media (2015) 1-18.

[74] Alam M.S., Cheng L. A parallel three-dimensional scour model to predict flow and scour below a submarine pipeline. Central European Journal of Physics 8 (4) (2010) 604-19.

[75] Viggen E.M. The lattice Boltzmann method: Fundamentals and acoustics (PhD Thesis). Trondheim: Norwegian University of Science and Technology; 2014.

[76] Schlichting H., Gersten K. Boundary-Layer Theory. Berlin: Springer-Verlag; 2000.

[77] Koda Y., Lien F.-S. The Lattice Boltzmann Method Implemented on the GPU to Simulate the Turbulent Flow Over a Square Cylinder Confined in a Channel. Flow, Turbulence and Combustion 94 (3) (2015) 495-512.

[78] Löhner R., Corrigan A., Wichmann K.-R., Wall W. Comparison of Lattice-Boltzmann and Finite Difference Solvers. 52nd Aerospace Sciences Meeting2014. p. 1439.

[79] Goodarzi M., Safaei M., Karimipour A., Hooman K., Dahari M., Kazi S., et al. Comparison of the finite volume and lattice Boltzmann methods for solving natural convection heat transfer problems inside cavities and enclosures. Abstract and Applied Analysis: Hindawi Publishing Corporation; 2014.

[80] Najafzadeh M., Barani G.-A., Azamathulla H.M. Prediction of pipeline scour depth in clear-water and live-bed conditions using group method of data handling. Neural Computing and Applications 24 (3-4) (2014) 629-35.

[81] Maren A.J., Harston C.T., Pap R.M. Handbook of neural computing applications: Academic Press; 2014.

[82] Voulgaris G., Trowbridge J.H. Evaluation of the acoustic Doppler velocimeter (ADV) for turbulence measurements. J. Atmos. Ocean Tech. 15 (1) (1998) 272-89.

[83] Nortek AS. Vector Current Meter User Manual. Vangkroken, Norway. 2004.

[84] ITTC. Fresh Water and Seawater Properties. International Towing Tank Conference: Recommended Procedures and Guidelines. 2011.

[85] SonTek/YSI. SonTek/YSI ADVField/Hydra Acoustic Doppler Velocimeter (Field) Technical Documentation. San Diego, California. 2001.

[86] Miedema S. Constructing the Shields curve, a new theoretical approach and its applications. WODCON XIX, Beijing China (2010).

[87] Soulsby R. Dynamics of marine sands: a manual for practical applications: Thomas Telford; 1997.

[88] Boussinesq J. Théorie de l'écoulement tourbillant. Mem. Présentés par Divers Savants Acad. Sci. Inst. Fr 23 (46-50) (1877) 6.5.

[89] Bardina J., Huang P., Coakley T. Turbulence modeling validation, testing. and development, technical report, NASA, US. NASA Technical Memorandum; 1997.

[90] Wilcox D.C. Reassessment of the scale-determining equation for advanced turbulence models. AIAA J. 26 (11) (1988) 1299-310.

[91] Stringer R., Zang J., Hillis A. Unsteady RANS computations of flow around a circular cylinder for a wide range of Reynolds numbers. Ocean Eng. 87 (2014) 1-9.

[92] Menter F.R. Review of the shear-stress transport turbulence model experience from an industrial perspective. Int. J. Comput. Fluid D. 23 (4) (2009) 305-16.

[93] Yoon J., Patel V. Numerical model of turbulent flow over sand dune. J. Hydraul. Eng. 122 (1) (1996) 10-8.

[94] Wilcox D.C. Turbulence modeling for CFD: DCW industries La Canada, CA; 1993.

[95] Soulsby R., Humphery J. Field observations of wave-current interaction at the sea bed. Water wave kinematics: Springer; 1990. p. 413-28.

[96] Liu Y., Hinrichsen O. CFD simulation of hydrodynamics and methanation reactions in a fluidized-bed reactor for the production of synthetic natural gas. Industrial & Engineering Chemistry Research 53 (22) (2014) 9348-56.

[97] Basirat S., Neyshabouri S.A.A.S. Eulerian–Eulerian Model Application to Simulate Scouring Downstream of Sluice Gate. Iranian Journal of Science and Technology, Transactions of Civil Engineering 41 (2) (2017) 197-203.

[98] Liu Y., Hinrichsen O. Numerical simulation of tube erosion in a bubbling fluidized bed with a dense tube bundle. Chemical Engineering & Technology 36 (4) (2013) 635-44.

[99] Rusche H. Computational fluid dynamics of dispersed two-phase flows at high phase fractions (PhD Thesis). London: Imperial College London (University of London); 2002.

[100] Johnson P.C., Nott P., Jackson R. Frictional–collisional equations of motion for participate flows and their application to chutes. J. Fluid Mech. 210 (1990) 501-35.

[101] Sinclair J., Jackson R. Gas‐particle flow in a vertical pipe with particle‐particle interactions. AIChE Journal 35 (9) (1989) 1473-86.

[102] Gidaspow D. Multiphase flow and fluidization: continuum and kinetic theory descriptions: Academic press; 1994.

[103] Louge M., Mastorakos E., Jenkins J. The role of particle collisions in pneumatic transport. J. Fluid Mech. 231 (1991) 345-59.

[104] Zhang D., Rauenzahn R. A viscoelastic model for dense granular flows. J. Rheol. 41 (6) (1997) 1275-98.

[105] Tretola G., Marra F. Validation of the twoPhaseEulerFoam solver for jet inlet fluidized bed. XXXVIII Meeting of the Italian Section of The Combustion Institute. Lecce: Associazione Sezione Italiana del Combustion Institute; 2015.

[106] Ranz W., Marshall W. Evaporation from drops. Chem. Eng. Prog 48 (3) (1952) 141-6.

[107] OSDAS. Environment Plan (EP) Summary. Perth, Australia: National Offshore Petroleum Safety and Environmental Management Authority; 2014. p. 50.

[108] Teledyne RD Instruments. Sentinel V Self-Contained 20m, 50m, 100m Profiling ADCP. Poway, California. 2011.

[109] Gostnell C., Yoos J. Efficacy of an Interferometric Sonar for Hydrographic Surveying: Do interferometers warrant an in-depth examination? Hydrographic Journal 118 (2005) 17.

[110] McInerney J., Forrest A.L., Lee J.Y., Hardjanto F., Cossu R. Scour propagation beneath a subsea pipeline in high and low energy environments. OCEANS 16 Monterey. Monterey, California. 2016.

[111] Akyildiz I.F., Pompili D., Melodia T. Underwater acoustic sensor networks: research challenges. Ad hoc networks 3 (3) (2005) 257-79.

[112] Panish R., Taylor M. Achieving high navigation accuracy using inertial navigation systems in autonomous underwater vehicles. OCEANS 2011 IEEE-Spain: IEEE; 2011. p. 1-7.

[113] Drago M., Mattioli M., Bruschi R., Vitali L. Insights on the design of free-spanning pipelines. Philos. Trans. R. Soc. London, Ser. A 373 (2033) (2015) 20140111.

[114] Jensen B.L., Sumer B.M., Jensen H.R., Fredsoe J. Flow around and forces on a pipeline near a scoured bed in steady current. J. Offshore Mech. Arct. Eng. 112 (3) (1990) 206-13.

[115] Det Norske Veritas. Recommended Practice DNV-RP-E305: On-Bottom Stability Design of Submarine Pipelines. Oslo, Norway1988.

[116] Det Norske Veritas. Recommended Practice DNV-RP-F105: Free Spanning Pipelines. Høvik, Norway2006.

[117] International Towing Tank Conference. Uncertainty Analysis in CFD Verification and Validation Methodology and Procedures. ITTC – Recommended Procedures and Guidelines2008.

[118] Jin Y., Duffy J., Chai S., Chin C., Bose N. URANS study of scale effects on hydrodynamic manoeuvring coefficients of KVLCC2. Ocean Eng. 118 (2016) 93-106.

[119] Simonsen C.D., Otzen J.F., Klimt C., Larsen N.L., Stern F. Maneuvering predictions in the early design phase using CFD generated PMM data. 29th symposium on naval hydrodynamics2012. p. 26-31.

[120] Stern F., Wilson R.V., Coleman H.W., Paterson E.G. Comprehensive approach to verification and validation of CFD simulations—part 1: methodology and procedures. J. Fluids Eng. 123 (4) (2001) 793-802.

[121] Wilson R.V., Stern F., Coleman H.W., Paterson E.G. Comprehensive approach to verification and validation of CFD simulations—Part 2: Application for RANS simulation of a cargo/container ship. J. Fluids Eng. 123 (4) (2001) 803-10.

[122] Eça L., Vaz G., Rosetti G., Pereira F. On the Numerical Prediction of the Flow Around Smooth Circular Cylinders. ASME 2014 33rd International Conference on Ocean, Offshore and Arctic Engineering: American Society of Mechanical Engineers; 2014. p. 1-11.

[123] Hansen E.A. Scour Below Pipelines and Cables, A Simple Model. Proceedings of the International Conference on Offshore Mechanics and Arctic Engineering: American Society of Mechanical Engineers; 1992. p. 133-.

[124] Sumer B.M., Whitehouse R.J., Tørum A. Scour around coastal structures: a summary of recent research. Coast. Eng. 44 (2) (2001) 153-90.

[125] Lagarias J.C., Reeds J.A., Wright M.H., Wright P.E. Convergence Properties of the Nelder-Mead Simplex Method in Low Dimensions. SIAM J Optimiz. 9 (1) (1998) 112-47.

[126] White F.M. Fluid Mechanics. 7th ed. New York: McGraw-Hill; 2011.

[127] Lee J.Y., McInerney J., Cossu R., Leong Z.Q., Forrest A.L. Predicting scour beneath subsea pipelines from existing small free span depths under steady currents. Journal of Ocean Engineering and Science 2 (2) (2017) 61–75.

[128] Zhang Q., Draper S., Cheng L., An H. Effect of limited sediment supply on sedimentation and the onset of tunnel scour below subsea pipelines. Coast. Eng. 116 (2016) 103-17.

[129] Zhang Q., Draper S., Cheng L., An H., Shi H. Revisiting the Mechanics of Onset of Scour Below Subsea Pipelines in Steady Currents. ASME 2013 32nd International Conference on Ocean, Offshore and Arctic Engineering. Nantes: American Society of Mechanical Engineers; 2013. p. V04BTA039-V04BT04A.

[130] Tu J., Yeoh G.H., Liu C. Computational Fluid Dynamics: A Practical Approach. 1st ed. Oxford: Butterworth-Heinemann; 2008.

[131] Montgomery D.C. Design and Analysis of Experiments. 8th ed: John Wiley and Sons; 2013.

[132] Zdravkovich M. Forces on a circular cylinder near a plane wall. Appl Ocean Res 7 (4) (1985) 197-201.

[133] Sumer B.M., Jensen H.R., Mao Y., Fredsøe J. Effect of lee-wake on scour below pipelines in current. J. Waterw. Port Coast. Ocean Eng. 114 (5) (1988) 599-614.

[134] Summer M., Fredsøe J. Hydrodynamics around circular cylinders. volume; 1997.

[135] Clauser F.H. The turbulent boundary layer. Adv. Appl. Mech.: Elsevier; 1956. p. 1-51.

[136] Lee J.Y., Hardjanto F.A., Cossu R., Chai S., Leong Z.Q., Forrest A.L. Current-induced scour beneath initially elevated subsea pipelines. Appl Ocean Res 82 (2019) (2019) 309-24.

[137] Van Rijn L.C. Unified view of sediment transport by currents and waves. I: Initiation of motion, bed roughness, and bed-load transport. J. Hydraul. Eng. 133 (6) (2007) 649-67.

[138] Meyer-Peter E., Müller R. Formulae for bed-load transport. IAHSR 2nd meeting, Stockholm, appendix 2: IAHR; 1948.

[139] Lee J.Y., Forrest A.L., Hardjanto F.A., Chai S., Cossu R., Leong Z.Q. Development of current-induced scour beneath elevated subsea pipelines. Journal of Ocean Engineering and Science 3 (4) (2018) 265-81.

[140] Lee C.-H., Low Y.M., Chiew Y.-M. Multi-dimensional rheology-based two-phase model for sediment transport and applications to sheet flow and pipeline scour. Physics of Fluids (1994-present) 28 (5) (2016) 053305.

[141] ANSYS. ANSYS Fluent User's Guide 15.0 2015.

[142] Van Leer B. Towards the ultimate conservative difference scheme. II. Monotonicity and conservation combined in a second-order scheme. J. Comput. Phys. 14 (4) (1974) 361-70.

[143] Warming R., Beam R.M. Upwind second-order difference schemes and applications in aerodynamic flows. AIAA J. 14 (9) (1976) 1241-9.

[144] Barrett R., Berry M.W., Chan T.F., Demmel J., Donato J., Dongarra J., et al. Templates for the solution of linear systems: building blocks for iterative methods: Siam; 1994.

[145] Van der Vorst H.A. Bi-CGSTAB: A fast and smoothly converging variant of Bi-CG for the solution of nonsymmetric linear systems. SIAM Journal on scientific and Statistical Computing 13 (2) (1992) 631-44.

[146] Issa R.I. Solution of the implicitly discretised fluid flow equations by operator-splitting. J. Comput. Phys. 62 (1) (1986) 40-65.

[147] Caretto L., Gosman A., Patankar S., Spalding D. Two calculation procedures for steady, three-dimensional flows with recirculation. Proceedings of the third international conference on numerical methods in fluid mechanics: Springer; 1973. p. 60-8.

[148] Dogan M., Aksoy A.O., Arisoy Y., Guney M.S., Abdi V. Experimental investigation of the equilibrium scour depth below submerged pipes both in live-bed and clear-water regimes under the wave effect. Appl Ocean Res 80 (2018) 49-56.

[149] Cheng L., Yeow K., Zang Z., Li F. 3D scour below pipelines under waves and combined waves and currents. Coast. Eng. 83 (2014) 137-49.

[150] Cheng L., Yeow K., Zhang Z., Teng B. Three-dimensional scour below offshore pipelines in steady currents. Coast. Eng. 56 (5) (2009) 577-90.

Appendix A

Settings for *twoPhaseEulerFoam*

The following are settings (i.e. boundary conditions, solver settings, etc.) which have been specified for the case shown in Figure 7.4 in Chapter 7.

```
/*--------------------------------*- C++ -*----------------------------------
--*\
| =========                 |
|
| \\      /  F ield         | OpenFOAM: The Open Source CFD Toolbox
|
|  \\    /   O peration     | Version:  plus
|
|   \\  /    A nd           | Web:      www.OpenFOAM.com
|
|    \\/     M anipulation  |
|
\*---------------------------------------------------------------------------
--*/
FoamFile
{
    version     2.0;
    format      ascii;
    class       volScalarField;
    object      alpha.particles;
}
// * * * * * * * * * * * * * * * * * * * * * * * * * * * * * * * * * * * * *
* //

dimensions      [0 0 0 0 0 0 0];

internalField   uniform 0;

boundaryField
{
    fluidBedAftWall
    {
        type            zeroGradient;
    }
    fluidBedFwdWall
    {
        type            zeroGradient;
    }
```

```
    fluidInlet
    {
        type            fixedValue;
        value           uniform 0;
    }
    fluidOutlet
    {
        type            inletOutlet;
        inletValue      $internalField;
        value           $internalField;
    }
    fluidTopWall
    {
        type            symmetryPlane;
    }
    pipe
    {
        type            zeroGradient;
    }
    sedAftWall
    {
        type            zeroGradient;
    }
    sedBedWall
    {
        type            zeroGradient;
    }
    sedFwdWall
    {
        type            zeroGradient;
    }
    symSides
    {
        type            empty;
    }
}

//
*********************************************************************************
//
```

```
/*--------------------------------*- C++ -*----------------------------------
--*\
| =========                 |
|
| \\      /  F ield         | OpenFOAM: The Open Source CFD Toolbox
|
|  \\    /   O peration     | Version:  plus
|
|   \\  /    A nd           | Web:      www.OpenFOAM.com
|
|    \\/     M anipulation  |
|
\*---------------------------------------------------------------------------
--*/
FoamFile
{
    version     2.0;
    format      ascii;
    class       volScalarField;
    object      alpha.water;
}
// * * * * * * * * * * * * * * * * * * * * * * * * * * * * * * * * * * * * *
* //

dimensions      [0 0 0 0 0 0 0];

internalField   uniform 1;

boundaryField
{
    fluidBedAftWall
    {
        type            zeroGradient;
    }
    fluidBedFwdWall
    {
        type            zeroGradient;
    }
    fluidInlet
    {
        type            fixedValue;
        value           uniform 1;
    }
    fluidOutlet
    {
        type            inletOutlet;
        inletValue      $internalField;
        value           $internalField;
    }
    fluidTopWall
    {
        type            symmetryPlane;
    }
    pipe
    {
        type            zeroGradient;
    }
    sedAftWall
    {
        type            zeroGradient;
    }
```

```
    sedBedWall
    {
        type            zeroGradient;
    }
    sedFwdWall
    {
        type            zeroGradient;
    }
    symSides
    {
        type            empty;
    }
}

//
*********************************************************************************
//
```

```
/*--------------------------------*- C++ -*----------------------------------
--*\
| =========                 |
|
| \\      /  F ield         | OpenFOAM: The Open Source CFD Toolbox
|
|  \\    /   O peration     | Version:  plus
|
|   \\  /    A nd           | Web:      www.OpenFOAM.com
|
|    \\/     M anipulation  |
|
\*---------------------------------------------------------------------------
--*/
FoamFile
{
    version     2.0;
    format      ascii;
    class       volScalarField;
    object      alphat.particles;
}
// * * * * * * * * * * * * * * * * * * * * * * * * * * * * * * * * * * * * *
* //

dimensions      [1 -1 -1 0 0 0 0];

internalField   uniform 0;

boundaryField
{
    fluidBedAftWall
    {
        type            calculated;
        value           $internalField;
    }
    fluidBedFwdWall
    {
        type            calculated;
        value           $internalField;
    }
    fluidInlet
    {
        type            calculated;
        value           $internalField;
    }
    fluidOutlet
    {
        type            calculated;
        value           $internalField;
    }
    fluidTopWall
    {
        type            symmetryPlane;
    }
    pipe
    {
        type            calculated;
        value           $internalField;
    }
```

```
    sedAftWall
    {
        type            calculated;
        value           $internalField;
    }
    sedBedWall
    {
        type            calculated;
        value           $internalField;
    }
    sedFwdWall
    {
        type            calculated;
        value           $internalField;
    }
    symSides
    {
        type            empty;
    }
}

//
// ************************************************************************* //
```

```
/*--------------------------------*- C++ -*----------------------------------
--*\
| =========                 |
|
| \\      /  F ield         | OpenFOAM: The Open Source CFD Toolbox
|
|  \\    /   O peration     | Version:  plus
|
|   \\  /    A nd           | Web:      www.OpenFOAM.com
|
|    \\/     M anipulation  |
|
\*---------------------------------------------------------------------------
--*/
FoamFile
{
    version     2.0;
    format      ascii;
    class       volScalarField;
    object      alphat.water;
}
// * * * * * * * * * * * * * * * * * * * * * * * * * * * * * * * * * * * * *
* //

dimensions      [1 -1 -1 0 0 0 0];

internalField   uniform 0;

boundaryField
{
    fluidBedAftWall
    {
        type            calculated;
        value           $internalField;
    }
    fluidBedFwdWall
    {
        type            calculated;
        value           $internalField;
    }
    fluidInlet
    {
        type            calculated;
        value           $internalField;
    }
    fluidOutlet
    {
        type            calculated;
        value           $internalField;
    }
    fluidTopWall
    {
        type            symmetryPlane;
    }
    pipe
    {
        type            calculated;
        value           $internalField;
    }
```

```
    sedAftWall
    {
        type            calculated;
        value           $internalField;
    }
    sedBedWall
    {
        type            calculated;
        value           $internalField;
    }
    sedFwdWall
    {
        type            calculated;
        value           $internalField;
    }
    symSides
    {
        type            empty;
    }
}

//
// ************************************************************************* //
```

```
/*--------------------------------*- C++ -*----------------------------------
--*\
| =========                 |
|
| \\      /  F ield         | OpenFOAM: The Open Source CFD Toolbox
|
|  \\    /   O peration     | Version:  plus
|
|   \\  /    A nd           | Web:      www.OpenFOAM.com
|
|    \\/     M anipulation  |
|
\*---------------------------------------------------------------------------
--*/
FoamFile
{
    version     2.0;
    format      ascii;
    class       volScalarField;
    object      k.water;
}
// * * * * * * * * * * * * * * * * * * * * * * * * * * * * * * * * * * * * *
* //

dimensions          [0 2 -2 0 0 0 0];

internalField       uniform 1e-12;

boundaryField
{
    fluidBedAftWall
    {
        type            kqRWallFunction;
        value           uniform 1e-12;
    }
    fluidBedFwdWall
    {
        type            kqRWallFunction;
        value           uniform 1e-12;
    }
    fluidInlet
    {
        type            uniformFixedValue;
        uniformValue    table
        (
                (0      0)
                (4      1.375392e-03)
        );
    }
    fluidOutlet
    {
        type            inletOutlet;
        inletValue      $internalField;
        value           $internalField;
    }
    fluidTopWall
    {
        type            symmetryPlane;
    }
```

```
    pipe
    {
        type            kqRWallFunction;
        value           uniform 1e-12;
    }
    sedAftWall
    {
        type            kqRWallFunction;
        value           uniform 1e-12;
    }
    sedBedWall
    {
        type            kqRWallFunction;
        value           uniform 1e-12;
    }
    sedFwdWall
    {
        type            kqRWallFunction;
        value           uniform 1e-12;
    }
    symSides
    {
        type            empty;
    }
}

// * * *
```

```
/*--------------------------------*- C++ -*----------------------------------
--*\
| =========                 |
|
| \\      /  F ield         | OpenFOAM: The Open Source CFD Toolbox
|
|  \\    /   O peration     | Version:  plus
|
|   \\  /    A nd           | Web:      www.OpenFOAM.com
|
|    \\/     M anipulation  |
|
\*---------------------------------------------------------------------------
--*/
FoamFile
{
    version     2.0;
    format      ascii;
    class       volScalarField;
    object      nut.particles;
}
// * * * * * * * * * * * * * * * * * * * * * * * * * * * * * * * * * * * * *
* //

dimensions          [0 2 -1 0 0 0 0];

internalField       uniform 0;

boundaryField
{
    fluidBedAftWall
    {
        type            calculated;
        value           $internalField;
    }
    fluidBedFwdWall
    {
        type            calculated;
        value           $internalField;
    }
    fluidInlet
    {
        type            calculated;
        value           $internalField;
    }
    fluidOutlet
    {
        type            calculated;
        value           $internalField;
    }
    fluidTopWall
    {
        type            symmetryPlane;
    }
    pipe
    {
        type            calculated;
        value           $internalField;
    }
```

```
    sedAftWall
    {
        type            calculated;
        value           $internalField;
    }
    sedBedWall
    {
        type            calculated;
        value           $internalField;
    }
    sedFwdWall
    {
        type            calculated;
        value           $internalField;
    }
    symSides
    {
        type            empty;
    }
}

// * * *
```

```
/*--------------------------------*- C++ -*----------------------------------
--*\
| =========                 |
|
| \\      /  F ield         | OpenFOAM: The Open Source CFD Toolbox
|
|  \\    /   O peration     | Version:  plus
|
|   \\  /    A nd           | Web:      www.OpenFOAM.com
|
|    \\/     M anipulation  |
|
\*---------------------------------------------------------------------------
--*/
FoamFile
{
    version     2.0;
    format      ascii;
    class       volScalarField;
    object      nut.water;
}
// * * * * * * * * * * * * * * * * * * * * * * * * * * * * * * * * * * * * *
* //

dimensions          [0 2 -1 0 0 0 0];

internalField       uniform 0;

boundaryField
{
    fluidBedAftWall
    {
        type            nutKWallFunction;
        value           uniform 0;
    }
    fluidBedFwdWall
    {
        type            nutKWallFunction;
        value           uniform 0;
    }
    fluidInlet
    {
        type            fixedValue;
        value           uniform 9.0306e-09;
    }
    fluidOutlet
    {
        type            calculated;
        value           uniform 0;
    }
    fluidTopWall
    {
        type            symmetryPlane;
    }
    pipe
    {
        type            nutKWallFunction;
        value           uniform 0;
    }
```

```
    sedAftWall
    {
        type            nutKWallFunction;
        value           uniform 0;
    }
    sedBedWall
    {
        type            nutKWallFunction;
        value           uniform 0;
    }
    sedFwdWall
    {
        type            nutKWallFunction;
        value           uniform 0;
    }
    symSides
    {
        type            empty;
    }
}

// * * *
```

```
/*--------------------------------*- C++ -*----------------------------------
--*\
| =========                 |
|
| \\      /  F ield         | OpenFOAM: The Open Source CFD Toolbox
|
|  \\    /   O peration     | Version:  plus
|
|   \\  /    A nd           | Web:      www.OpenFOAM.com
|
|    \\/     M anipulation  |
|
\*---------------------------------------------------------------------------
--*/
FoamFile
{
    version     2.0;
    format      ascii;
    class       volScalarField;
    object      omega.water;
}
// * * * * * * * * * * * * * * * * * * * * * * * * * * * * * * * * * * * * *
* //


dimensions      [0 0 -1 0 0 0 0];

internalField   uniform 4.205588;

boundaryField
{
    fluidBedAftWall
    {
        type            omegaWallFunction;
        value           uniform 721.3274377;
    }
    fluidBedFwdWall
    {
        type            omegaWallFunction;
        value           uniform 721.3274377;
    }
    fluidInlet
    {
        type            uniformFixedValue;
        uniformValue    table
        (
                (0      0)
                (4      4.205588)
        );
    }
    fluidOutlet
    {
        type            inletOutlet;
        inletValue      $internalField;
        value           $internalField;
    }
    fluidTopWall
    {
        type            symmetryPlane;
    }
```

```
    pipe
    {
        type            omegaWallFunction;
        value           uniform 591.6787513;
    }
    sedAftWall
    {
        type            omegaWallFunction;
        value           uniform 46.6485777;
    }
    sedBedWall
    {
        type            omegaWallFunction;
        value           uniform 92.04331705;
    }
    sedFwdWall
    {
        type            omegaWallFunction;
        value           uniform 47.02282879;
    }
    symSides
    {
        type            empty;
    }
}


//
*********************************************************************************
//
```

```
/*--------------------------------*- C++ -*----------------------------------
--*\
| =========                 |
|
| \\      /  F ield         | OpenFOAM: The Open Source CFD Toolbox
|
|  \\    /   O peration     | Version:  plus
|
|   \\  /    A nd           | Web:      www.OpenFOAM.com
|
|    \\/     M anipulation  |
|
\*---------------------------------------------------------------------------
--*/
FoamFile
{
    version     2.0;
    format      ascii;
    class       volScalarField;
    object      p;
}
// * * * * * * * * * * * * * * * * * * * * * * * * * * * * * * * * * * * * *
* //

dimensions          [1 -1 -2 0 0 0 0];

internalField       uniform 101325;

boundaryField
{
    fluidBedAftWall
    {
        type            calculated;
        value           $internalField;
    }
    fluidBedFwdWall
    {
        type            calculated;
        value           $internalField;
    }
    fluidInlet
    {
        type            calculated;
        value           $internalField;
    }
    fluidOutlet
    {
        type            calculated;
        value           $internalField;
    }
    fluidTopWall
    {
        type            symmetryPlane;
    }
    pipe
    {
        type            calculated;
        value           $internalField;
    }
```

```
    sedAftWall
    {
        type            calculated;
        value           $internalField;
    }
    sedBedWall
    {
        type            calculated;
        value           $internalField;
    }
    sedFwdWall
    {
        type            calculated;
        value           $internalField;
    }
    symSides
    {
        type            empty;
    }
}

// * * *
```

```
/*--------------------------------*- C++ -*----------------------------------
--*\
| =========                 |
|
| \\      /  F ield         | OpenFOAM: The Open Source CFD Toolbox
|
|  \\    /   O peration     | Version:  plus
|
|   \\  /    A nd           | Web:      www.OpenFOAM.com
|
|    \\/     M anipulation  |
|
\*---------------------------------------------------------------------------
--*/
FoamFile
{
    version     2.0;
    format      ascii;
    class       volScalarField;
    object      p_rgh;
}
// * * * * * * * * * * * * * * * * * * * * * * * * * * * * * * * * * * * * *
* //

dimensions          [1 -1 -2 0 0 0 0];

internalField       uniform 101325;

boundaryField
{
    fluidBedAftWall
    {
        type            fixedFluxPressure;
        value           $internalField;
    }
    fluidBedFwdWall
    {
        type            fixedFluxPressure;
        value           $internalField;
    }
    fluidInlet
    {
        type            fixedFluxPressure;
        value           $internalField;
    }
    fluidOutlet
    {
        type            prghPressure;
        p               $internalField;
        value           $internalField;
    }
    fluidTopWall
    {
        type            symmetryPlane;
    }
    pipe
    {
        type            fixedFluxPressure;
        value           $internalField;
    }
```

```
    sedAftWall
    {
        type            fixedFluxPressure;
        value           $internalField;
    }
    sedBedWall
    {
        type            fixedFluxPressure;
        value           $internalField;
    }
    sedFwdWall
    {
        type            fixedFluxPressure;
        value           $internalField;
    }
     symSides
    {
        type            empty;
    }
}

// * * *
```

```
/*--------------------------------*- C++ -*----------------------------------
--*\
| =========                 |
|
| \\      /  F ield         | OpenFOAM: The Open Source CFD Toolbox
|
|  \\    /   O peration     | Version:  plus
|
|   \\  /    A nd           | Web:      www.OpenFOAM.com
|
|    \\/     M anipulation  |
|
\*---------------------------------------------------------------------------
--*/
FoamFile
{
    version     2.0;
    format      ascii;
    class       volScalarField;
    object      Theta.particles;
}
//
*****************************************************************************
//

dimensions          [0 2 -2 0 0 0 0];

internalField       uniform 0;

referenceLevel      1e-4;

boundaryField
{
    fluidBedAftWall
    {
        type            zeroGradient;
    }
    fluidBedFwdWall
    {
        type            zeroGradient;
    }
    fluidInlet
    {
        type            zeroGradient;
    }
    fluidOutlet
    {
        type            inletOutlet;
        inletValue      $internalField;
        value           $internalField;
    }
    fluidTopWall
    {
        type            symmetryPlane;
    }
    pipe
    {
        type            zeroGradient;
    }
```

```
    sedAftWall
    {
        type            zeroGradient;
    }
    sedBedWall
    {
        type            zeroGradient;
    }
    sedFwdWall
    {
        type            zeroGradient;
    }
    symSides
    {
        type            empty;
    }
}

//
// ************************************************************************* //
```

```
/*--------------------------------*- C++ -*----------------------------------
--*\
| =========                 |
|
| \\      /  F ield         | OpenFOAM: The Open Source CFD Toolbox
|
|  \\    /   O peration     | Version:  plus
|
|   \\  /    A nd           | Web:      www.OpenFOAM.com
|
|    \\/     M anipulation  |
|
\*---------------------------------------------------------------------------
--*/
FoamFile
{
    version     2.0;
    format      ascii;
    class       volScalarField;
    object      T.particles;
}
// * * * * * * * * * * * * * * * * * * * * * * * * * * * * * * * * * * * * *
* //

dimensions          [0 0 0 1 0 0 0];

internalField       uniform 293.15;

boundaryField
{
    fluidBedAftWall
    {
        type            fixedValue;
        value           uniform 293.15;
    }
    fluidBedFwdWall
    {
        type            fixedValue;
        value           uniform 293.15;
    }
    fluidInlet
    {
        type            fixedValue;
        value           uniform 293.15;
    }
    fluidOutlet
    {
        type            fixedValue;
        value           uniform 293.15;
    }
    fluidTopWall
    {
        type            symmetryPlane;
    }
    pipe
    {
        type            fixedValue;
        value           uniform 293.15;
    }
```

```
    sedAftWall
    {
        type            fixedValue;
        value           uniform 293.15;
    }
    sedBedWall
    {
        type            fixedValue;
        value           uniform 293.15;
    }
    sedFwdWall
    {
        type            fixedValue;
        value           uniform 293.15;
    }
    symSides
    {
        type            empty;
    }
}

// * * *
```

```
/*--------------------------------*- C++ -*----------------------------------
--*\
| =========                 |
|
| \\      /  F ield         | OpenFOAM: The Open Source CFD Toolbox
|
|  \\    /   O peration     | Version:  plus
|
|   \\  /    A nd           | Web:      www.OpenFOAM.com
|
|    \\/     M anipulation  |
|
\*---------------------------------------------------------------------------
--*/
FoamFile
{
    version     2.0;
    format      ascii;
    class       volScalarField;
    object      T.water;
}
// * * * * * * * * * * * * * * * * * * * * * * * * * * * * * * * * * * * * *
* //

dimensions          [0 0 0 1 0 0 0];

internalField       uniform 293.15;

boundaryField
{
    fluidBedAftWall
    {
        type            fixedValue;
        value           uniform 293.15;
    }
    fluidBedFwdWall
    {
        type            fixedValue;
        value           uniform 293.15;
    }
    fluidInlet
    {
        type            fixedValue;
        value           uniform 293.15;
    }
    fluidOutlet
    {
        type            fixedValue;
        value           uniform 293.15;
    }
    fluidTopWall
    {
        type            symmetryPlane;
    }
    pipe
    {
        type            fixedValue;
        value           uniform 293.15;
    }
```

```
    sedAftWall
    {
        type            fixedValue;
        value           uniform 293.15;
    }
    sedBedWall
    {
        type            fixedValue;
        value           uniform 293.15;
    }
    sedFwdWall
    {
        type            fixedValue;
        value           uniform 293.15;
    }
    symSides
    {
        type            empty;
    }
}

// * * *
```

```
/*--------------------------------*- C++ -*----------------------------------
--*\
| =========                 |
|
| \\      /  F ield         | OpenFOAM: The Open Source CFD Toolbox
|
|  \\    /   O peration     | Version:  plus
|
|   \\  /    A nd           | Web:      www.OpenFOAM.com
|
|    \\/     M anipulation  |
|
\*---------------------------------------------------------------------------
--*/
FoamFile
{
    version     2.0;
    format      ascii;
    class       volVectorField;
    object      U.particles;
}
// * * * * * * * * * * * * * * * * * * * * * * * * * * * * * * * * * * * * *
* //

dimensions      [0 1 -1 0 0 0 0];

internalField   uniform (0 0 0);

boundaryField
{
    fluidBedAftWall
    {
        type            fixedValue;
        value           uniform (0 0 0);
    }
    fluidBedFwdWall
    {
        type            fixedValue;
        value           uniform (0 0 0);
    }
    fluidInlet
    {
        type            fixedValue;
        value           uniform (0 0 0);
    }
    fluidOutlet
    {
        type            inletOutlet;
        inletValue      uniform (0 0 0);
        value           $internalField;
    }
    fluidTopWall
    {
        type            symmetryPlane;
    }
    pipe
    {
        type            fixedValue;
        value           uniform (0 0 0);
    }
```

```
    sedAftWall
    {
        type            fixedValue;
        value           uniform (0 0 0);
    }
    sedBedWall
    {
        type            fixedValue;
        value           uniform (0 0 0);
    }
    sedFwdWall
    {
        type            fixedValue;
        value           uniform (0 0 0);
    }
    symSides
    {
        type            empty;
    }
}

//
************************************************************************
//
```

```
/*--------------------------------*- C++ -*----------------------------------
--*\
| =========                 |
|
| \\      /  F ield         | OpenFOAM: The Open Source CFD Toolbox
|
|  \\    /   O peration     | Version:  plus
|
|   \\  /    A nd           | Web:      www.OpenFOAM.com
|
|    \\/     M anipulation  |
|
\*---------------------------------------------------------------------------
--*/
FoamFile
{
    version     2.0;
    format      ascii;
    class       volVectorField;
    object      U.water;
}
// * * * * * * * * * * * * * * * * * * * * * * * * * * * * * * * * * * * * *
* //

dimensions      [0 1 -1 0 0 0 0];

internalField   uniform (0 0 0);

boundaryField
{
    fluidBedAftWall
    {
        type            fixedValue;
        value           uniform (0 0 0);
    }
    fluidBedFwdWall
    {
        type            fixedValue;
        value           uniform (0 0 0);
    }
    fluidInlet
    {
        type            uniformFixedValue;
        uniformValue    table
        (
                (0      (0 0 0))
                (4      (0.87 0 0))
        );
    }
    fluidOutlet
    {
        type            inletOutlet;
        inletValue      uniform (0 0 0);
        value           $internalField;
    }
    fluidTopWall
    {
        type            symmetryPlane;
    }
```

```
    pipe
    {
        type            fixedValue;
        value           uniform (0 0 0);
    }
    sedAftWall
    {
        type            fixedValue;
        value           uniform (0 0 0);
    }
    sedBedWall
    {
        type            fixedValue;
        value           uniform (0 0 0);
    }
    sedFwdWall
    {
        type            fixedValue;
        value           uniform (0 0 0);
    }
    symSides
    {
        type            empty;
    }
}

//
************************************************************************
//
```

```
/*--------------------------------*- C++ -*----------------------------------
--*\
| =========                 |
|
| \\      /  F ield         | OpenFOAM: The Open Source CFD Toolbox
|
|  \\    /   O peration     | Version:  plus
|
|   \\  /    A nd           | Web:      www.OpenFOAM.com
|
|    \\/     M anipulation  |
|
\*---------------------------------------------------------------------------
--*/
FoamFile
{
    version     2.0;
    format      ascii;
    class       uniformDimensionedVectorField;
    location    "constant";
    object      g;
}
// * * * * * * * * * * * * * * * * * * * * * * * * * * * * * * * * * * * * *
* //

dimensions      [0 1 -2 0 0 0 0];
value           (0 -9.81 0);


//
************************************************************************
//
```

```
/*--------------------------------*- C++ -*----------------------------------
--*\
| =========                 |
|
| \\      /  F ield         | OpenFOAM: The Open Source CFD Toolbox
|
|  \\    /   O peration     | Version:  plus
|
|   \\  /    A nd           | Web:      www.OpenFOAM.com
|
|    \\/     M anipulation  |
|
\*---------------------------------------------------------------------------
--*/
FoamFile
{
    version     2.0;
    format      ascii;
    class       dictionary;
    location    "constant";
    object      phaseProperties;
}
// * * * * * * * * * * * * * * * * * * * * * * * * * * * * * * * * * * * * *
* //

phases (particles water);

particles
{
    residualAlpha   1e-06;
    diameterModel constant;
    constantCoeffs
    {
        d               0.00036;
    }
    alphaMax        0.62;
    residualAlpha   1e-06;
}

water
{
    residualAlpha   0;
    diameterModel constant;
    constantCoeffs
    {
        d               1;
    }
    residualAlpha   0;
}

blending
{
    default
    {
        type            none;
        continuousPhase water;
    }
}

sigma
(
```

```
    (particles and water) 0
);

aspectRatio
(
);

drag
(
    (particles in water)
    {
        type            WenYu;
        residualRe      1e-03;
        swarmCorrection
        {
            type        none;
        }
    }
);

virtualMass
(
    (particles in water)
    {
        type            none;
    }
);

heatTransfer
(
    (particles in water)
    {
        type            RanzMarshall;
        residualAlpha   1e-03;
    }
);

lift
(
    (particles in water)
    {
        type            none;
    }
);

wallLubrication
(
);

turbulentDispersion
(
);

pMin            10000;


//
// ************************************************************************
//
```

```
/*--------------------------------*- C++ -*----------------------------------
--*\
| =========                 |
|
| \\      /  F ield         | OpenFOAM: The Open Source CFD Toolbox
|
|  \\    /   O peration     | Version:  plus
|
|   \\  /    A nd           | Web:      www.OpenFOAM.com
|
|    \\/     M anipulation  |
|
\*---------------------------------------------------------------------------
--*/
FoamFile
{
    version     2.0;
    format      ascii;
    class       dictionary;
    location    "constant";
    object      thermophysicalProperties.particles;
}
// * * * * * * * * * * * * * * * * * * * * * * * * * * * * * * * * * * * * *
* //

thermoType
{
    type            heRhoThermo;
    mixture         pureMixture;
    transport       const;
    thermo          hConst;
    equationOfState rhoConst;
    specie          specie;
    energy          sensibleInternalEnergy;
}
mixture
{
    specie
    {
        nMoles      1;
        molWeight   60.083;
    }
    equationOfState
    {
        rho         2600;
    }
    thermodynamics
    {
        Cp          1483;
        Hf          0;
    }
    transport
    {
        mu          0;
        Pr          1;
    }
}

//
************************************************************************
//
```

```
/*--------------------------------*- C++ -*----------------------------------
--*\
| =========                 |
|
| \\      /  F ield         | OpenFOAM: The Open Source CFD Toolbox
|
|  \\    /   O peration     | Version:  plus
|
|   \\  /    A nd           | Web:      www.OpenFOAM.com
|
|    \\/     M anipulation  |
|
\*---------------------------------------------------------------------------
--*/
FoamFile
{
    version     2.0;
    format      ascii;
    class       dictionary;
    location    "constant";
    object      thermophysicalProperties.water;
}
// * * * * * * * * * * * * * * * * * * * * * * * * * * * * * * * * * * * * *
* //
thermoType
{
    type            heRhoThermo;
    mixture         pureMixture;
    transport       const;
    thermo          hConst;
    equationOfState perfectFluid;
    specie          specie;
    energy          sensibleInternalEnergy;
}
mixture
{
    specie
    {
        nMoles      1;
        molWeight   18.01528;
    }
    equationOfState
    {
        R           3000;
        rho         998.2072;
        rho0        998.2072;
    }
    thermodynamics
    {
        Cp          4182;
        Hf          0;
    }
    transport
    {
        mu          1.002e-03;
        Pr          7.01;
    }
}
//
************************************************************************
//
```

```
/*--------------------------------*- C++ -*----------------------------------
--*\
| =========                 |
|
| \\      /  F ield         | OpenFOAM: The Open Source CFD Toolbox
|
|  \\    /   O peration     | Version:  plus
|
|   \\  /    A nd           | Web:      www.OpenFOAM.com
|
|    \\/     M anipulation  |
|
\*---------------------------------------------------------------------------
--*/
FoamFile
{
    version     2.0;
    format      ascii;
    class       dictionary;
    location    "constant";
    object      turbulenceProperties.particles;
}
// * * * * * * * * * * * * * * * * * * * * * * * * * * * * * * * * * * * * *
* //

simulationType  RAS;

RAS
{
    RASModel kineticTheory;

    turbulence      on;
    printCoeffs     on;

    kineticTheoryCoeffs
    {
        equilibrium             off;
        e                       0.91;
        alphaMax                0.62;

        alphaMinFriction        0.5;
        residualAlpha           1e-04;

        viscosityModel          Gidaspow;
        conductivityModel       Gidaspow;
        granularPressureModel   Lun;

        frictionalStressModel   JohnsonJacksonSchaeffer;
        radialModel             SinclairJackson;

        JohnsonJacksonSchaefferCoeffs
        {
            Fr                      0.05;
            eta                     2;
            p                       5;
            phi                     28.5;
            alphaDeltaMin           0.05;
        }
    }
```

```
    phasePressureCoeffs
    {
        preAlphaExp     500;
        expMax          1000;
        alphaMax        0.62;
        g0              1000;
    }
}


//
// ************************************************************************* //
```

```
/*--------------------------------*- C++ -*----------------------------------
--*\
| =========                 |
|
| \\      /  F ield         | OpenFOAM: The Open Source CFD Toolbox
|
|  \\    /   O peration     | Version:  plus
|
|   \\  /    A nd           | Web:      www.OpenFOAM.com
|
|    \\/     M anipulation  |
|
\*---------------------------------------------------------------------------
--*/
FoamFile
{
    version     2.0;
    format      ascii;
    class       dictionary;
    location    "constant";
    object      turbulenceProperties.water;
}
// * * * * * * * * * * * * * * * * * * * * * * * * * * * * * * * * * * * * *
* //

simulationType  RAS;

RAS
{
    RASModel kOmegaSST;

    turbulence      on;
    printCoeffs     on;
}

LES
{
    LESModel Smagorinsky;

    turbulence      on;
    printCoeffs     on;

    delta cubeRootVol;

    cubeRootVolCoeffs
    {
        deltaCoeff 1;
    }

    SmagorinskyCoeffs
    {
        Ck                  0.094;
        Ce                  1.048;
    }

}


//
************************************************************************
//
```

```
/*--------------------------------*- C++ -*----------------------------------
--*\
| =========                 |
|
| \\      /  F ield         | OpenFOAM: The Open Source CFD Toolbox
|
|  \\    /   O peration     | Version:  plus
|
|   \\  /    A nd           | Web:      www.OpenFOAM.com
|
|    \\/     M anipulation  |
|
\*---------------------------------------------------------------------------
--*/
FoamFile
{
    version     2.0;
    format      ascii;
    class       dictionary;
    note        "mesh renumbering dictionary";
    object      renumberMeshDict;
}
// * * * * * * * * * * * * * * * * * * * * * * * * * * * * * * * * * * * * *
* //

method          CuthillMcKee;

CuthillMcKeeCoeffs
{
    reverse true;
}

manualCoeffs
{
    dataFile "cellMap";
}

structuredCoeffs
{
    patches (movingWall);

    method  random;

    depthFirst true;

    reverse false;
}

springCoeffs
{
    maxCo 0.01;

    freezeFraction 0.999;

    maxIter 1000;
}

blockCoeffs
{
    method          scotch;
}
```

```
zoltanCoeffs
{
    ORDER_METHOD    LOCAL_HSFC;
}

//
// ************************************************************************* //
```

```
/*--------------------------------*- C++ -*----------------------------------
--*\
| =========                 |
|
| \\      /  F ield         | OpenFOAM: The Open Source CFD Toolbox
|
|  \\    /   O peration     | Version:  plus
|
|   \\  /    A nd           | Web:      www.OpenFOAM.com
|
|    \\/     M anipulation  |
|
\*---------------------------------------------------------------------------
--*/
FoamFile
{
    version     2.0;
    format      ascii;
    class       dictionary;
    location    "system";
    object      controlDict;
}
// * * * * * * * * * * * * * * * * * * * * * * * * * * * * * * * * * * * * *
* //

application             twoPhaseEulerFoam;

startFrom               latestTime;

startTime               0;

stopAt                  endTime;

endTime                 60;

deltaT                  1e-06;

writeControl            adjustableRunTime;

writeInterval           5;

purgeWrite              0;

writeFormat             binary;

writePrecision          6;

writeCompression        yes;

timeFormat              general;

timePrecision           6;

runTimeModifiable       yes;

adjustTimeStep          yes;

maxCo                   0.9;

maxDeltaT               1;
```

```
functions
{
    elevation
    {
        interpolationScheme     cellPoint;
        type                    surfaces;
        libs
        (
            "libsampling.so"
            "libfieldFunctionObjects.so"
        );
        writeControl   writeTime;
        surfaceFormat  raw;
        fields
        (
            alpha.particles
        );
        surfaces
        (
            topFreeSurface
            {
                type            isoSurface;
                isoField        alpha.particles;
                isoValue        0.5;
                interpolate     true;
            }
        );
    }
}
libs
(
        "libOpenFOAM.so"
        "libsimpleSwakFunctionObjects.so"
        "libswakFunctionObjects.so"
        "libgroovyBC.so"
        "libgenericPatchFields.so"
);
//
************************************************************************
//
```

```
/*--------------------------------*- C++ -*----------------------------------
--*\
| =========                 |
|
| \\      /  F ield         | OpenFOAM: The Open Source CFD Toolbox
|
|  \\    /   O peration     | Version:  plus
|
|   \\  /    A nd           | Web:      www.OpenFOAM.com
|
|    \\/     M anipulation  |
|
\*---------------------------------------------------------------------------
--*/
FoamFile
{
    version     2.0;
    format      ascii;
    class       dictionary;
    location    "system";
    object      decomposeParDict;
}
// * * * * * * * * * * * * * * * * * * * * * * * * * * * * * * * * * * * * *
* //

numberOfSubdomains  6;

method          scotch;

simpleCoeffs
{
    n           (2 2 1);
    delta       0.001;
}

hierarchicalCoeffs
{
    n           (2 2 1);
    delta       0.001;
    order       xyz;
}

scotchCoeffs
{
}

manualCoeffs
{
    dataFile    "decompositionData";
}

//
************************************************************************
//
```

```
/*--------------------------------*- C++ -*----------------------------------
--*\
| =========                 |
|
| \\      /  F ield         | OpenFOAM: The Open Source CFD Toolbox
|
|  \\    /   O peration     | Version:  plus
|
|   \\  /    A nd           | Web:      www.OpenFOAM.com
|
|    \\/     M anipulation  |
|
\*---------------------------------------------------------------------------
--*/
FoamFile
{
    version     2.0;
    format      ascii;
    class       dictionary;
    location    "system";
    object      setFieldsDict;
}
// * * * * * * * * * * * * * * * * * * * * * * * * * * * * * * * * * * * * *
* //

defaultFieldValues
(
    volScalarFieldValue alpha.water 1
    volScalarFieldValue alpha.particles 0
);

regions
(
    boxToCell
    {
        box (-8 -0.15 0) (2 0 0.01);
        fieldValues
        (
            volScalarFieldValue alpha.water 0.44
            volScalarFieldValue alpha.particles 0.56
        );
    }
);


//
************************************************************************
//
```

```
/*--------------------------------*- C++ -*----------------------------------
--*\
| =========                 |
|
| \\      /  F ield         | OpenFOAM: The Open Source CFD Toolbox
|
|  \\    /   O peration     | Version:  plus
|
|   \\  /    A nd           | Web:      www.OpenFOAM.com
|
|    \\/     M anipulation  |
|
\*---------------------------------------------------------------------------
--*/
FoamFile
{
    version     2.0;
    format      ascii;
    class       dictionary;
    location    "system";
    object      fvSchemes;
}
// * * * * * * * * * * * * * * * * * * * * * * * * * * * * * * * * * * * * *
* //

ddtSchemes
{
    default     Euler;
}

gradSchemes
{
    default     Gauss linear;
}

divSchemes
{
    default                         none;

    "div\(phi,alpha.*\)"            Gauss outletStabilised vanLeer;
    "div\(phir,alpha.*\)"           Gauss outletStabilised vanLeer;
    "div\(alphaRhoPhi.*,U.*\)"      Gauss outletStabilised vanLeer;
    "div\(phi.*,U.*\)"              Gauss outletStabilised vanLeer;
    "div\(alphaRhoPhi.*,(h|e).*\)"  Gauss outletStabilised vanLeer;
    "div\(alphaRhoPhi.*,K.*\)"      Gauss outletStabilised vanLeer;
    "div\(alphaPhi.*,p\)"           Gauss outletStabilised vanLeer;

    div(alphaRhoPhi.particles,Theta.particles) Gauss outletStabilised
vanLeer;

    "div\(alphaRhoPhi.*,(k|epsilon|omega).*\)"  Gauss outletStabilised
vanLeer;

div((((alpha.water*thermo:rho.water)*nuEff.water)*dev2(T(grad(U.water)))))
Gauss linear;

div((((thermo:rho.particles*nut.particles)*dev2(T(grad(U.particles))))+(((t
hermo:rho.particles*lambda.particles)*div(phi.particles))*I)))  Gauss
linear;
}
```

```
laplacianSchemes
{
    default     Gauss linear corrected;
    bounded     Gauss linear corrected;
}

interpolationSchemes
{
    default     linear;
}

snGradSchemes
{
    default     corrected;
    bounded     corrected;
}

wallDist
{
    method meshWave;
}

//
************************************************************************
//
```

```
/*--------------------------------*- C++ -*----------------------------------
--*\
| =========                 |
|
| \\      /  F ield         | OpenFOAM: The Open Source CFD Toolbox
|
|  \\    /   O peration     | Version:  plus
|
|   \\  /    A nd           | Web:      www.OpenFOAM.com
|
|    \\/     M anipulation  |
|
\*---------------------------------------------------------------------------
--*/
FoamFile
{
    version     2.0;
    format      ascii;
    class       dictionary;
    location    "system";
    object      fvSolution;
}
// * * * * * * * * * * * * * * * * * * * * * * * * * * * * * * * * * * * * *
* //

solvers
{
    "alpha.*"
    {
        nAlphaCorr              1;
        nAlphaSubCycles         2;
        smoothLimiter           0.1;
        implicitPhasePressure   yes;
        solver                  smoothSolver;
        smoother                DICGaussSeidel;
        tolerance               1e-09;
        relTol                  0;
        minIter                 1;
    }

    p_rgh
    {
        solver          GAMG;
        tolerance       1e-07;
        relTol          0.1;

        smoother        DICGaussSeidel;
        nPreSweeps      0;
        nPostSweeps     2;
        nFinestSweeps   2;
        nCellsInCoarsestLevel 1000;
        agglomerator    faceAreaPair;
        mergeLevels     1;
        minIter         1;
    }

    p_rghFinal
    {
        solver         PCG;
        preconditioner
        {
```

```
            preconditioner  GAMG;
            tolerance       1e-07;
            relTol          0.1;

            nVcycles        2;

            smoother        DICGaussSeidel;
            nPreSweeps      0;
            nPostSweeps     2;
            nFinestSweeps   2;
            nCellsInCoarsestLevel 20;
            agglomerator    faceAreaPair;
            mergeLevels     1;
        }
        tolerance       1e-07;
        relTol          0;
        minIter         1;
    }
    "U.*"
    {
        solver          PBiCGStab;
        preconditioner  DILU;
        tolerance       1e-05;
        relTol          0;
        minIter         1;
    }

    "(Theta|k|epsilon|omega).*"
    {
        solver          PBiCGStab;
        preconditioner  DILU;
        tolerance       1e-05;
        relTol          0;
        minIter         1;
    }

    "(h|e).*"
    {
        solver          PBiCGStab;
        preconditioner  DILU;
        tolerance       1e-05;
        relTol          0;
        minIter         0;
        maxIter         0;
    }
}

PIMPLE
{
    nOuterCorrectors            1;
    nCorrectors                 1;
    nNonOrthogonalCorrectors    1;

    residualControl
    {
        p_rgh
        {
                relTol     0;
                tolerance  1e-04;
        }
```

```
        "alpha.*"
        {
                relTol      0;
                tolerance   1e-04;
        }
    }
}

//
// ************************************************************************* //
```